



HAL
open science

Le patrimoine de la nébuleuse protosolaire : le rapport isotopique de l'azote des nuages interstellaires à des systèmes planétaires

Victor de Souza Magalhaes

► To cite this version:

Victor de Souza Magalhaes. Le patrimoine de la nébuleuse protosolaire : le rapport isotopique de l'azote des nuages interstellaires à des systèmes planétaires. Solar and Stellar Astrophysics [astro-ph.SR]. Université Grenoble Alpes, 2017. English. NNT : 2017GREAY095 . tel-01824304

HAL Id: tel-01824304

<https://theses.hal.science/tel-01824304>

Submitted on 27 Jun 2018

HAL is a multi-disciplinary open access archive for the deposit and dissemination of scientific research documents, whether they are published or not. The documents may come from teaching and research institutions in France or abroad, or from public or private research centers.

L'archive ouverte pluridisciplinaire **HAL**, est destinée au dépôt et à la diffusion de documents scientifiques de niveau recherche, publiés ou non, émanant des établissements d'enseignement et de recherche français ou étrangers, des laboratoires publics ou privés.

THÈSE

Pour obtenir le grade de

DOCTEUR DE LA COMMUNAUTÉ UNIVERSITÉ GRENOBLE ALPES

Spécialité : **Astrophysique et Milieux Dilués**

Arrêté ministériel : 25 mai 2016

Présentée par

Victor de Souza Magalhães

Thèse dirigée par **Pierre Hily-Blant**

préparée au sein de l'**Institut de Planétologie et d'Astrophysique de Grenoble**
et de l'**École Doctorale de Physique**

The protosolar nebula heritage: The nitrogen isotopic ratio from interstellar clouds to planetary systems

Thèse soutenue publiquement le **20 décembre 2017**,
devant le jury composé de :

Stephane Guilloteau

Directeur de recherche, Rapporteur
Laboratoire d'Astrophysique de Bordeaux

Evelyne Roueff

Astronome, Rapporteur
Observatoire de Paris

Paola Caselli

Professor, Examinatrice
Max-Planck-Institut für extraterrestrische Physik

Pierre Lesaffre

Chargé de recherche, Examineur
LERMA/L.R.A., Paris

Claudine Kahane

Professeur, Président
Université Grenoble Alpes

Alexandre Faure

Chargé de recherche, Examineur
CNRS délégation Alpes



ABSTRACT

The existence of interstellar molecules raises the question, are these molecules the same molecules we see on the Solar system today? This is still an open question with far reaching consequences. Some light may be shed on this issue if we are able to trace the heritage of a group of chemically linked molecules, a so-called reservoir. The best tool to trace the heritage of reservoirs are isotopic ratios. The element that shows the largest isotopic ratio variations in the Solar system is nitrogen. Which is an indication that the isotopic ratio of nitrogen is sensitive to the physical conditions during star formation.

The main objective of this thesis is to identify the reservoirs of nitrogen at different stages of star and planet formation. The first step in this endeavour was to identify the isotopic ratio of the bulk of nitrogen in the local ISM today. This was determined to be 323 ± 30 from the $\text{CN}/\text{C}^{15}\text{N}$ ratio in the protoplanetary disk around TW Hya. Along with it we also measured the $\text{HCN}/\text{HC}^{15}\text{N} = 128 \pm 36$ in the protoplanetary disk around MWC 480. This very distinct nitrogen isotopic ratios on protoplanetary disks are a clear indication that there are at least two reservoirs of nitrogen in them. How these reservoirs get separated is however unknown. This could possibly happen due to chemical fractionation reactions taking place in prestellar cores. We therefore aimed to obtain an accurate direct measurement of the nitrogen isotopic ratio of HCN in the prestellar core L1498.

To obtain this measurement the most important hurdle to overcome were the hyperfine anomalies of HCN. These hyperfine anomalies arise due to the overlap of hyperfine components. They are especially sensitive to the column density of HCN, but also to the velocity field and line widths. Thus hyperfine anomalies are a tool to measure the abundance of HCN and to probe the kinematics of prestellar cores.

To accurately reproduce the hyperfine anomalies, and thus measure accurate column densities for HCN, we needed to explore a degenerate parameter space of 15 dimensions. To minimise the degeneracies we have derived a density profile based on continuum maps of L1498. This reduced the parameter space to 12 dimensions. The exploration of this parameter space was done through the use of a MCMC minimisation method. Through this exploration we obtained $\text{HCN}/\text{HC}^{15}\text{N} = 338 \pm 28$ and $\text{HCN}/\text{H}^{13}\text{CN} = 45 \pm 3$. The uncertainties on these values are calibration limited and determined non-arbitrarily by the MCMC method. Implications of these results are discussed in the concluding chapter, where we also present some future perspectives.

CONTENTS

1	INTRODUCTION	1
1.1	The process of low mass star formation	1
1.1.1	The prestellar phase	1
1.1.2	The protostellar phase	5
1.1.3	The Protoplanetary disk phase	5
1.2	The results of the star formation process	8
1.2.1	Stars	8
1.2.2	Planets	11
1.2.3	Asteroids and comets	12
1.3	The interstellar heritage of planetary systems	13
1.3.1	Whats is a reservoir?	13
1.3.2	What are the different reservoirs that we see in the Solar system today	14
1.3.3	What are the different reservoirs that we see in the dense interstellar medium	14
1.4	How do we trace the heritage of reservoirs?	17
1.4.1	Isotopic ratios as a tool to follow reservoirs	17
1.4.1.1	D/H ratio as a tracer of interstellar heritage	18
1.4.1.2	Using Carbon Isotopic ratio to elucidate formation mechanisms of carbon chains	18
1.4.2	The puzzle of the isotopic ratio of nitrogen in the Solar System	19
1.4.3	The PhD project	19
2	THE ISOTOPIC RATIO OF NITROGEN	23
2.1	Nucleosynthesis of nitrogen	23
2.2	Nitrogen in the ISM and circumstellar environments	24
2.3	Measuring the isotopic ratio of nitrogen in the ISM	26
2.3.1	Direct methods	26
2.3.2	Indirect methods	28
2.4	Review of existing $^{14}\text{N}/^{15}\text{N}$ measurements	28
2.4.1	Measurements in the Solar system	29
2.4.2	Measurements in the local ISM	29
2.4.3	Protostellar envelopes	32
2.4.4	Protoplanetary disks	32
2.4.5	The big picture	33
3	SOFTWARE TOOLS	35
3.1	NSLAB	35
3.1.1	Implementation	36
3.1.2	Benchmarking	37
3.1.3	Perspectives	42

3.2	Accelerated Lambda Iteration COde, ALICO	43
3.2.1	Model cloud	44
3.2.2	ALICO gridding software	45
3.2.3	The ALICO model and observation classes	45
3.2.4	Perspectives	46
3.3	MCMC TOOLKIT	47
3.3.1	ALICO MCMC	48
3.3.2	Perspectives	54
3.4	Summary of radiative transfer tools	54
4	MEASURING $^{14}\text{N}/^{15}\text{N}$ IN PRESTELLAR CORES	55
4.1	The hyperfine anomalies of HCN	55
4.1.1	What are Hyperfine Anomalies?	56
4.1.2	Possible mechanisms for the origins of the hyperfine anomalies	58
4.1.2.1	Rotational spectroscopy of HCN	59
4.1.2.2	Self-absorption	63
4.1.2.3	Radiative trapping caused by the overlap of hyperfine components	63
4.1.3	Testing the possible mechanisms	67
4.1.3.1	Four slabs Toy model	67
4.1.3.2	Tests with ALICO	73
4.1.4	Conclusions	85
4.2	HCN and its isotopologues in L1498	85
4.2.1	Observations	86
4.2.1.1	Spectral observations	86
4.2.1.2	Continuum observations	86
4.2.2	HCN/HC ^{15}N under the single excitation temperature hypothesis	89
4.2.3	Measuring the isotopic ratio of HCN with the escape probability formalism	89
4.2.4	Density profile of L1498	94
4.2.5	ALICO/MCMC fitting of HCN, H ^{13}CN and HC ^{15}N spectra	106
4.2.6	Article on HCN/HC ^{15}N in L1498	111
5	THE $^{14}\text{N}/^{15}\text{N}$ RATIO IN PROTOSOLAR NEBULA ANALOGS	125
5.1	Interferometric observations	125
5.1.1	Self-calibration	128
5.2	Direct evidence of multiple reservoirs of volatile nitrogen in a protosolar nebula analogue	129
6	$^{14}\text{N}/^{15}\text{N}$ IN PROTOSTELLAR ENVIRONMENTS	147
6.1	NH $_2$ D in IRAS03282	148
6.2	The nitrogen isotopic ratio in VLA1623 and IRAS16293	148
7		159
7.1	HCN hyperfine anomalies	160
7.2	Accurate measurements of isotopic ratios	161
7.3	HCN isotopic ratios in L1498	163

7.4	Where when and how are the two reservoirs of nitrogen seen in protoplanetary disks separated?	164
I	APPENDIX	165
A	SOFTWARE WRITTEN AND EXAMPLE INPUT FILES	167
A.1	Nslab	167
A.1.1	Source code for Nslab	167
A.1.2	Nslab input	171
A.1.3	Nslab output	171
A.1.4	Nslab help	175
A.2	ALICO/1DART	176
A.2.1	1DART input files	176
A.2.1.1	Physical model input file	176
A.2.1.2	Beam convolution input file	181
A.2.2	Model cloud input file	182
A.2.2.1	Model cloud help	183
A.2.3	ALICO gridding software	183
A.2.3.1	Source file	183
A.2.3.2	Molecular file	184
A.2.3.3	Grid file	184
A.2.3.4	Gridding software help	185
A.2.4	ALICO classes	186
A.2.4.1	Model class	186
A.2.4.2	Observation class	193
A.2.4.3	Example code using observation and model classes	195
A.3	MCMC toolkit	198
A.3.1	MCMC toolkit code	198
A.3.2	MCMC toolkit example input file	203
B	DATA TABLES	205
C	APPROVED TELESCOPE TIME PROPOSALS	207
D	HC₃N/HC₃¹⁵N IN L1544	209
	BIBLIOGRAPHY	223

LIST OF FIGURES

- Figure 1.1 Evolution of core structure with time. The x axis denote the logarithm of the core radius in cm while the y axis denote the logarithm of the pressure in dyne/cm^2 . The different model times are indicated in units of 10^{13} s. Note that the core pressure distribution approaches a r^{-2} distribution with the passage of time. Figure extracted from Larson (1969). 3
- Figure 1.2 False colour maps of the Taurus-Auriga molecular cloud complex, red is Herschel-SPIRE 500 μm , green is Herschel-SPIRE 350 μm and blue is Herschel-SPIRE 250 μm . These Herschel-SPIRE images were obtained in the Gould Belt Survey key program (André et al., 2010). a) The entire Taurus-Auriga molecular cloud complex; b)The prestellar core L1544 and its surroundings; c) The prestellar core L1498 and its surroundings. 4
- Figure 1.3 The multiple protostar system IRAS 16293 – 2422 located in the ρ Ophichi complex at a distance of 120 pc, as viewed by ALMA at 110 GHz. The main components A and B are marked by white crosses. Data from ALMA project: 2016.1.01468.S, P.I.: V. S. Magalhães. 6
- Figure 1.4 a) Cartoon of the physical structure of a protoplanetary disk showing on the right the three main layers of a protoplanetary disk with emphasis on the species that can be found in each layer: The atmosphere; The warm molecular layer and the cold and dense mid plane. On the left we have an sketch of where different instruments are able to probe a protoplanetary disk b) A detailed physical structure for a protoplanetary disk such as DM Tau. Z/R denotes the height over the mid plane (Z) divided by the radial distance to the central star (R). a) was extracted from van Dishoeck (2014) and b) was extracted from Henning and Semenov (2013). 7

- Figure 1.5 Integrated intensity map of the optically thin hyperfine component of the CN $N=3 \rightarrow 2$ transition at 340.020 GHz towards TW Hydra. The white circle in the image represents the size of Neptune's orbit around the Sun. Note that the emission of CN $N=3 \rightarrow 2$ comes from an annular region similar in size to the Solar system's Kuiper's belt. Data from ALMA project: 2013.1.00196.S, P.I.: P. Hily-Blant. 9
- Figure 1.6 Channel maps of the optically thin hyperfine component of the CN $N=3 \rightarrow 2$ transition at 340.020 GHz towards TW Hydra. Here we can see that different velocities have different spatial distributions. This effect is caused by the keplerian rotation of the protoplanetary disk. The white cross marks the position of TW Hydra. Data from ALMA project: 2013.1.00196.S, P.I.: P. Hily-Blant. 10
- Figure 1.7 NASA/ESA Hubble Space Telescope stunning view of the bright α Centauri A (on the left) and α Centauri B (on the right). The third component of the system, Proxima Centauri is too far away from the main components (A and B) to be seen in this scale. The field of view is 0.85×0.56 arc minutes in width and height respectively. Image extracted from: *Best image of Alpha Centauri A and B (2016)*. 11
- Figure 1.8 a) Example of a rocky planet: Earth. This image was taken from the Apollo 17 crew during their way back from the Moon. b) Example of a giant planet: Jupiter. Image obtained in visible light with Ultraviolet Aurora capture superimposed on its north pole, Origin: NASA, ESA, and J. Nichols (University of Leicester). 12

Figure 1.9 Approximate sequence of equilibrium condensation drawn from the information given in Lewis (1997). The white boxes show the approximate transitions of various elements into minerals and ices from the gaseous state assuming solar nebula disk pressures (10^{-2} bar). While the blue boxes provide the formation sequence as gas cools (see text for discussion of condensation vs. evaporation). Some modifications include a question as to whether N is found as NH_3 or as N_2 or even N, as the latter two have lower condensation temperatures. Thus a range has been shown. The green dashed line roughly delineates the line between refractory solids and ices, while the yellow line notes species that remain in the gas. Note that C and N straddle this line. O in the form of H_2O will also be found both in the gas and ice at various radial positions in a protoplanetary disk. A fraction of C, H, O, and N will also be bound in organics which, depending on the form, have condensation/sublimation temperatures in the range of 50-150 K (Öberg et al., 2009). Image extracted from Bergin (2014). 15

Figure 1.10 Proposed evolution of ices during star formation and formation of complex molecules. Pink indicates an H_2O -dominated ice and blue a CO-dominated ice. Early during cloud formation (a) an H_2O -rich ice forms, with minor amounts of CH_4 and NH_3 through hydrogenation of O, C and N. Once a critical density is reached CO freezes out catastrophically (b), providing reactants for CH_3OH ice formation through hydrogenation of CO (oth generation complex organic molecules). In the cold outer envelope (c), photo processing of the CO-rich ice results in the production of, e.g., HCOOCH_3 (1st generation). Closer to the protostar (d), following sublimation of CO, other complex molecules become abundant. Finally, all ices may desorb thermally close to the protostar >100 K (e) (2nd generation). Figure from Öberg et al. (2010). 16

- Figure 1.11 Compilation of all measurements of the nitrogen isotopic ratio in comets. The observed carrier is indicated above each measurement. Although it is clear that NH_2 is a photo dissociation product of ammonia in the coma, the origin of CN is still debated. Data were taken from Jehin et al. (2009) and Bockelée-Morvan et al. (2015). The weighted average ratio is 144 ± 3 . For each carrier, the average ratios for Jupiter Family Comets (JFC) and Oort Cloud Comets (OCC), are indicated (thick dots), where the distinction between JFC and OCC was based only on the periodicity of the comets being respectively lower and higher than 200 years (Shinnaka et al., 2016). Figure extracted from Hily-Blant et al. (2017) 20
- Figure 2.1 Plot of $^{14}\text{N}/^{15}\text{N}$ isotope ratios as a function of galactocentric distance, D_{GC} (kpc). The filled circles indicate direct measurement of the ratios using the hyperfine components of the CN isotopologues. The open circles represent the ratios calculated using $\text{HN}^{13}\text{C}/\text{H}^{15}\text{NC}$ and the $^{12}\text{C}/^{13}\text{C}$ ratio measured in CN by Milam et al. (2005). The triangles are the ratios obtained from the HCN data of Dahmen, Wilson, and Matteucci (1995), combined with the $^{12}\text{C}/^{13}\text{C}$ ratios of Milam et al. (2005). The dashed line is the gradient from the model 3n of Romano and Matteucci (2003), where ^{15}N is treated as a secondary element and produced in novae. The rectangular box represents the range of values found in comet measurements of $^{14}\text{N}/^{15}\text{N}$, and the star is the value in Earth's atmosphere. A linear fit of these three sets of data results in the expression: $^{14}\text{N}/^{15}\text{N} = 21.1D_{\text{GC}} + 123.8$. Figure extracted from Adande and Ziurys (2012). 25

- Figure 2.2 Nitrogen isotopic ratios measured in the Solar system. Different symbols stand for different papers: HB2017 refers to Hily-Blant et al. (2017), BU2006 refers to Busemann et al. (2006), OW2001 refers to Owen et al. (2001), SE2002 refers to Sephton et al. (2002), FL2006 refers to Floss et al. (2006), FU2015 refers to Füri, Chaussidon, and Marty (2015), AL2007 refers to Alexander et al. (2007), MK2007 refers to Meibom et al. (2007), BO2010 refers to Bonal et al. (2010) and FO2000 refers to Fouchet et al. (2000). IDP stands for interplanetary dust particle. 30
- Figure 2.3 Nitrogen isotopic ratio measured in the local diffuse ISM. The quoted value for Adande and Ziurys (2012) (AZ2012) comes from the interpolation of their galactic gradient. Different symbols stand for different papers: LL1998 refers to Lucas and Liszt (1998) and RI2015 refers to Ritchey, Federman, and Lambert (2015). 31
- Figure 2.4 Nitrogen isotopic ratio measured in the local dense ISM. Black markers stand for direct measurements, while red markers stand for double isotopologue measurements. Different symbols stand for different papers: DG2013 refers to Daniel et al. (2013), DF2016 refers to Daniel et al. (2016), HB2013a refers to Hily-Blant et al. (2013a), GM2009 refers to Gerin et al. (2009), HB2013b refers to Hily-Blant et al. (2013b), BC2013 refers to Bizzocchi et al. (2013), LW2010 refers to Lis et al. (2010), TS2017 refers to Taniguchi and Saito (2017) and IH2002 refers to Ikeda, Hirota, and Yamamoto (2002). 31
- Figure 2.5 Nitrogen isotopic ratio measured in protostellar envelopes. WA2014 stands for Wampfler et al. (2014), while TW stands for this work. 32
- Figure 2.6 Nitrogen isotopic ratio measured in the nearby protoplanetary disks. Black markers stand for direct measurements, while red markers stand for double isotopologue measurements. Different symbols stand for different papers: GO2017 refers to Guzmán et al. (2017) and HB2017 refers to Hily-Blant et al. (2017). 33

- Figure 2.7 The big picture of the nitrogen isotopic ratio. In the Solar system and in protoplanetary disks two reservoirs have been identified. The difference in isotopic ratios between these two sets of reservoirs are consistent with the evolution of the nitrogen isotopic ratio with time. The remaining question is where and when does the fractionation of the minor reservoir happens. 34
- Figure 3.1 Automatically generated plot by NSLAB from the output file in Section A.1.3 with spectral resolution of 0.1 km/s. 37
- Figure 3.2 NSLAB parameters as function of the slabs as produced automatically by NSLAB. The input file contains 4 slabs and 3 spectral lines, which are reflected in the x axis and legend respectively. 38
- Figure 3.3 Spectrum computed by NSLAB for a single slab experiment (test 1, see Table 3.1). The labels from A to E denote the different experiments in Table 3.1. 39
- Figure 3.4 Results of the second benchmarking test of NSLAB, testing the propagation of spectral lines through two slabs. The labels F to J correspond to the spectral lines described in Table 3.2. 41
- Figure 3.5 Results of the third benchmarking test of NSLAB, testing the propagation of spectral lines through two slabs with different velocities. The labels K to O correspond to the spectral lines described in Table 3.2. 42
- Figure 3.6 HCN $J = 1 \rightarrow 0$ spectra produced by the model class along with HCN $J = 1 \rightarrow 0$ observations as plotted by the function `plot_with_obs` from the model class (see Section A.2.4.1). 46
- Figure 3.7 Evolution of the walkers in a Markov chain as a function of the steps taken. For the three parameters displayed it is possible to see that the MCMC walkers rapidly converge to the correct values for the parameters (within ~ 100 steps). 49

- Figure 3.8 Cross histograms of the parameters for a model Gaussian. A is the peak intensity, X_0 is the Gaussian centre and σ is its dispersion. From this plot we can learn which parameters are not correlated with each other as the is the case between the centre of the Gaussian and its amplitude (the cross histogram is circular) and which parameters do present a correlation with each other like the amplitude of the Gaussian and its dispersion (The cross histogram is elliptical and inclined). The dashed vertical lines in the histograms indicate the 0.16, 0.5 and 0.86 fractional quantiles and are used to automatically compute the best fit parameters and their uncertainties. 50
- Figure 3.9 Results of the MCMC fit to a Gaussian with a RMS noise of 2.5. The fit clearly converges and presents a good agreement with the mock up observations. 51
- Figure 3.10 Time for ALICO execution as a function of molecular abundance for CO, HCN, N_2H^+ and NH_2D . 53
- Figure 4.1 HCN $J = 1 \rightarrow 0$ spectrum presenting hyperfine anomalies (bottom) and $H^{13}CN$ $J = 1 \rightarrow 0$ spectrum displaying no hyperfine anomalies (top). Both HCN and $H^{13}CN$ have the same resolved hyperfine structure, therefore the $H^{13}CN$ $J = 1 \rightarrow 0$ transition is a proxy for non anomalous HCN $J = 1 \rightarrow 0$. The hyperfine splitting caused by the presence of ^{13}C is not resolved in $H^{13}CN$. The hyperfine components of the $J = 1 \rightarrow 0$ transition of both HCN and $H^{13}CN$ are labeled with their respective relative intensities. Both spectra were obtained towards the continuum peak of L1498. 57
- Figure 4.2 R_{12} vs. R_{02} ($R_{12} = F = 1 \rightarrow 1/F = 2 \rightarrow 1$, $R_{02} = F = 0 \rightarrow 1/F = 2 \rightarrow 1$) for several sources in the dense ISM. The red polygon indicates the region where hyperfine ratios are not anomalous. There is only one set of ratios that is completely inconsistent with hyperfine anomalies, that of L234-ES. The hyperfine ratios were extracted from the data in Sohn et al. (2007) and are listed in Table B.1. 57

- Figure 4.3 Top panel: Observed HCN $J = 3 \rightarrow 2$ spectrum towards the continuum peak of L1498; Bottom panel: Synthetic HCN $J = 3 \rightarrow 2$ spectrum build by NSLAB (Section 3.1) using the relative intensities of the hyperfine components of the $J = 3 \rightarrow 2$ rotational transition. 58
- Figure 4.4 Rotational curves of growth for HCN transitions $J = 1 \rightarrow 0$, $J = 2 \rightarrow 1$ and $J = 3 \rightarrow 2$. These curves of growth were computed with the usage of RADEX for a kinetic temperature $T_k = 10$ K, a HCN column density $N(\text{HCN})=10^{14} \text{ cm}^{-2}$ and using the latest hyperfine collisional coefficients for HCN (Lique et al. private communication). 59
- Figure 4.5 Spectroscopy of HCN for $J = 0, 1, 2, 3$ including allowed radiative transitions between these levels, F denotes the nuclear spin state. Splitting not to scale. 60
- Figure 4.6 Collisional and radiative de-excitation rates for HCN $J, F = 2, 2$ at a temperature of 10 K and a density of 10^5 cm^{-3} . 65
- Figure 4.7 Collisional and radiative de-excitation rates for HCN $J, F = 2, 3$ at a temperature of 10 K and a density of 10^5 cm^{-3} . 65
- Figure 4.8 Left: Schematic representation of the spectroscopy of HCN for $J \leq 2$. Right: Schematic description of the radiative trapping mechanism. The transition labels follow the scheme in Table 4.1. Solid black arrows represent the allowed collisional transitions, Sinusoidal blue lines represent the allowed radiative transitions and the red sinusoidal lines represent the effects of the overlap between transitions #6 and #7. The red arrows indicate the net flux of population. 66
- Figure 4.9 Evolution of the HCN $J = 1 \rightarrow 0$ hyperfine ratios as a function of HCN abundance for a simplified model with $n_{\text{H}_2} = 10^5 \text{ cm}^{-3}$, $T_{\text{kin}} = 10$ K and a non thermal dispersion of velocities, $\sigma = 0.05$ km/s. Hyperfine ratios computed with ALICO. 66
- Figure 4.10 Schematic description of the toy model. Slabs are numbered according to Table 4.2. 68
- Figure 4.11 HCN hyperfine ratios as a function of total opacity for grid G1. The non anomalous optically thin values for R_{02} , R_{01} and R_{12} are 0.2, 0.333, and 0.6 respectively. 70

- Figure 4.12 HCN hyperfine ratios as a function of total opacity in the envelope for grid G2. Here $T_{ex,A}^{21} = 1.2T_{ex,A}^{01}$ and $T_{ex,A}^{11} = 0.8T_{ex,A}^{01}$ mimicking an excitation temperature imbalance such as what would be expected from the hyperfine overlap mechanism. The non anomalous optically thin values for R_{02} , R_{01} and R_{12} are 0.2, 0.333, and 0.6 respectively. 72
- Figure 4.13 HCN hyperfine ratios as a function of total opacity in the envelope for grid G2, with B slabs suppressed. Here $T_{ex,A}^{21} = 1.2T_{ex,A}^{01}$ and $T_{ex,A}^{11} = 0.8T_{ex,A}^{01}$ mimicking an excitation temperature imbalance such as what would be expected from the hyperfine overlap mechanism. The non anomalous optically thin values for R_{02} , R_{01} and R_{12} are 0.2, 0.333, and 0.6 respectively. 74
- Figure 4.14 Comparison between the emergent spectra for the $J = 1 \rightarrow 0$ transition of HCN produced by ALICO with (black) and without (orange) hyperfine overlap taken into account. 76
- Figure 4.15 Same as Figure 4.14 for HCN $J = 3 \rightarrow 2$. 77
- Figure 4.16 Profile for the physical quantities in the reference model. Top: H_2 number density as a function of the fraction of the model size. Middle: Non thermal velocity dispersion as a function of the projected distance from the model centre in arc seconds. Bottom: Collapse velocity profile as a function of the distance from the model centre in cm. 80
- Figure 4.17 Spectra produced by ALICO towards the model centre along with HCN observations towards the continuum peak of L1498. Left: $J = 1 \rightarrow 0$ spectra; Right: $J = 3 \rightarrow 2$ spectra. 81
- Figure 4.18 Dependency of the hyperfine ratios on the non thermal velocity dispersion profile parameters. Top left: Hyperfine ratios as a function of σ_0 ; Top Right: Hyperfine ratios as a function of σ_{ext} ; Bottom left: Hyperfine ratios as a function of r_j ; Bottom right: Hyperfine ratios as a function of Δr_j . 81
- Figure 4.19 Dependency of the hyperfine ratios on the collapse velocity profile parameters. Top: Hyperfine ratios as a function of the maximal collapse velocity V_c ; Middle: Hyperfine ratios as a function of r_V ; Bottom: Hyperfine ratios as a function of Δr_V . 83

- Figure 4.20 Hyperfine ratios as a function of the abundance of HCN. 84
- Figure 4.21 Histogram of intensities for the 1250 μm MAMBO map along with the best Gaussian fit to it. 87
- Figure 4.22 Top panel: histogram of intensities for the 250 μm Herschel SPIRE low signal region map along with the best 2 Gaussian fit to it. Middle panel: histogram of intensities for the 350 μm Herschel SPIRE low signal region map along with the best 2 Gaussian fit to it. bottom panel: histogram of intensities for the 500 μm Herschel SPIRE low signal region map along with the best 2 Gaussian fit to it. 88
- Figure 4.23 The CLASS HFS fit (blue) to the $\text{H}^{13}\text{CN } J = 1 \rightarrow 0$ transition towards the continuum peak of L1498 (thick black) along with the residuals of this fit (thin black lines). The vertical axis is in the main beam temperature scale in K. 89
- Figure 4.24 Schematics of the inner workings of the RADEX+NSLAB LVG model. 90
- Figure 4.25 HCN $J = 1 \rightarrow 0$ observations towards the continuum peak of L1498 (blue) along with the best fit from RADEX+NSLABMCMC (red) and the residuals of this fit (orange). 92
- Figure 4.26 HCN $J = 3 \rightarrow 2$ observations towards the continuum peak of L1498 (blue) along with the best fit from RADEX+NSLABMCMC (red) and the residuals of this fit (orange). Notice the very poor quality of the fit caused by the inability of RADEX to process hyperfine overlaps. 92
- Figure 4.27 $\text{H}^{13}\text{CN } J = 1 \rightarrow 0$ observations towards the continuum peak of L1498 (blue) along with the best fit from RADEX+NSLABMCMC (red) and the residuals of this fit (orange). 93
- Figure 4.28 $\text{HC}^{15}\text{N } J = 1 \rightarrow 0$ observations towards the continuum peak of L1498 (blue) along with the best fit from RADEX+NSLABMCMC (red) and the residuals of this fit (orange). 93

- Figure 4.29 Color composite map of L1498. 1.25 mm is Red, 500 μm is green and 250 μm is blue. Black circles indicate where the $J = 1 \rightarrow 0$ of all HCN isotopologues was observed, green circles indicate the positions that were only observed in HCN $J = 1 \rightarrow 0$, the blue circle indicates the position that was observed only on HCN and H^{13}CN $J = 1 \rightarrow 0$ and the white circles indicate the positions where HCN $J = 3 \rightarrow 2$ was observed. The sizes of the circles indicate the HPBW of the IRAM-30m telescope at the observed frequencies, 28'' for the $J = 1 \rightarrow 0$ transitions and 9'' for the HCN $J = 3 \rightarrow 2$ transition. 95
- Figure 4.30 Radial profile of the continuum emission along the SW axis of L1498. The offsets refer to the continuum peak of L1498 at $\alpha=4:10:52.2$, $\delta=25:10:20$ (J2000). The 1250 μm emission was multiplied by 10 so that it could be displayed on the same linear scale as the other continuum wavelengths. Notice the bump in emission at an offset of 220 arc seconds. 97
- Figure 4.31 Single dust temperature fit to the continuum emission at 1250 μm . Here we can see that the single dust temperature fit underestimates the emission at 1250 μm by a factor of ~ 2 . 98
- Figure 4.32 Top panel: Single dust temperature fit to the continuum emission at 250 μm . Middle panel: Single dust temperature fit to the continuum emission at 350 μm . Bottom panel: Single dust temperature fit to the continuum emission at 500 μm . Here we can see that the best fit with a single dust temperature falls short of accurately reproducing the dust emission profiles at the Herschel SPIRE wavelengths. 99
- Figure 4.33 Top panel: Dust emission at 4 different wavelengths as a function of distance along the line of sight towards the centre of the model. Bottom panel: Dust emission at 350 μm as a function of distance along the line of sight for different impact parameters, b . It is possible to see that the emission at small impact parameters is approximately two orders of magnitude more intense than the emission with larger impact parameters. 100

- Figure 4.34 Top panel: best fit continuum dust emission model along with the Herschel SPIRE observations at $250\ \mu\text{m}$. Bottom panel: best fit continuum dust emission model along with the Herschel SPIRE observations at $350\ \mu\text{m}$. 102
- Figure 4.35 Top panel: best fit continuum dust emission model along with the Herschel SPIRE observations at $500\ \mu\text{m}$. Bottom panel: best fit continuum dust emission model along with MAMBO observations at $1250\ \mu\text{m}$. 103
- Figure 4.36 Density and dust temperature profiles for the best fit dust continuum emission profile. 104
- Figure 4.37 Cross histograms for the parameters in the continuum fit. 105
- Figure 4.38 Best fit HCN $J = 1 \rightarrow 0$ (red) spectra along the HCN $J = 1 \rightarrow 0$ observations (blue) and the residuals of the fit (orange) for different offsets from the continuum peak of L1498: top left (0,0)", top centre: (-10,-20)", top right (-20,-40)", bottom left (-30,-60)", bottom centre: (-50,-100)", bottom right (-60,-120)" 109
- Figure 4.39 Best fit HCN $J = 3 \rightarrow 2$ (red) spectra along the HCN $J = 3 \rightarrow 2$ observations (blue) and the residuals of the fit (orange) for different offsets from the continuum peak of L1498: top left (0,0)", top centre: (-5,-10)", top right (-10,-20)", bottom left (-20,-40)", bottom centre: (-30,-60)", bottom right (-40,-80)" 109
- Figure 4.40 Best fit H^{13}CN $J = 1 \rightarrow 0$ (red) spectra along the H^{13}CN $J = 1 \rightarrow 0$ observations (blue) and the residuals of the fit (orange) for different offsets from the continuum peak of L1498: top left (0,0)", top centre: (-10,-20)", top right (-20,-40)", bottom left (-30,-60)", bottom centre: (-50,-100)", bottom right (-60,-120)". 110
- Figure 4.41 Best fit HC^{15}N $J = 1 \rightarrow 0$ (red) spectra along the HC^{15}N $J = 1 \rightarrow 0$ observations (blue) and the residuals of the fit (orange) for different offsets from the continuum peak of L1498: top left (0,0)", top centre: (-10,-20)", top right (-20,-40)", bottom left (-30,-60)", bottom centre: (-50,-100)". 110

- Figure 5.1 *uv* coverage of an artificial interferometer (top panel) and the resulting dirty beam obtained from the Fourier transform of the *uv* coverage. Notice the side lobes produced in the dirty beam by the blanks in *uv* coverage. Images produced with *APSYNSIM* (Marti-Vidal, 2017). 126
- Figure 5.2 Dirty image produced by the synthetic observation of two point sources with the *uv* coverage in Figure 5.1. Image produced with *APSYNSIM* (Marti-Vidal, 2017). 127
- Figure 5.3 Results of CLEAN when applied to the dirty image in Figure 5.2. Image produced with *APSYNSIM* (Marti-Vidal, 2017). 128
- Figure 5.4 Continuum emission of TW Hya at 340 GHz before and after self-calibration (top and bottom panels respectively). Notice the reduction of residuals and the increase in flux after self-calibration. Maps in Jy/beam. 130
- Figure 6.1 Top panel: $o - \text{NH}_2\text{D } 1_{1,1} \rightarrow 1_{1,0}$ integrated intensity map towards IRAS03282 along with contours indicating the continuum emission of IRAS03282 at 86 GHz. Intensity of the integrated intensity map in Jy/beam. The continuum contours start at 2 mJy/Beam and go up to 18 mJy/beam in 4 mJy/beam intervals. Middle panel: $o - \text{NH}_2\text{D } 1_{1,1} \rightarrow 1_{1,0}$ spatially integrated spectrum inside the black circle in the top panel. Bottom panel: $o - ^{15}\text{NH}_2\text{D } 1_{1,1} \rightarrow 1_{1,0}$ spatially integrated spectrum inside the black circle in the top panel. 149
- Figure 6.2 Top panel: $\text{H}^{13}\text{CN } J = 1 \rightarrow 0$ integrated intensity map towards IRAS03282 along with contours indicating the continuum emission of IRAS03282 at 86 GHz. Intensity of the integrated intensity map in Jy/beam. The continuum contours start at 2 mJy/Beam and go up to 18 mJy/beam in 4 mJy/beam intervals. Middle panel: $\text{H}^{13}\text{CN } J = 1 \rightarrow 0$ spatially integrated spectrum inside the black circle in the top panel. Bottom panel: $\text{HC}^{15}\text{N } J = 1 \rightarrow 0$ spatially integrated spectrum inside the black circle in the top panel. 150

- Figure 6.3 $o - \text{NH}_2\text{D } 1_{1,1} \rightarrow 1_{1,0}$ integrated intensity map towards VLA 1623 along with contours indicating the continuum emission of VLA 1623 at 110 GHz. Intensity of the integrated intensity map in Jy/beam. The continuum contours start at 5 mJy/Beam and go up to 40 mJy/beam in 5 mJy/beam intervals. The black circle indicates the region of strong NH_2D emission in the envelope of VLA 1623, over which spectra of NH_2D and $^{15}\text{NH}_2\text{D}$ were integrated. The black circle indicates the region around VLA 1623 where ice sublimation is expected, over which spectra of NH_2D and $^{15}\text{NH}_2\text{D}$ were integrated. 151
- Figure 6.4 Left panels: spatially integrated spectra towards the sublimation region of VLA 1623. Right: spatially integrated spectra towards NH_2D emission peak in the envelope of VLA 1623. Top: $o - \text{NH}_2\text{D } 1_{1,1} \rightarrow 1_{1,0}$. Middle: $p - \text{NH}_2\text{D } 1_{1,1} \rightarrow 1_{1,0}$. Bottom: $o - ^{15}\text{NH}_2\text{D } 1_{1,1} \rightarrow 1_{1,0}$. 152
- Figure 6.5 Left panels: spatially integrated spectra towards the sublimation region of VLA 1623. Right: spatially integrated spectra towards NH_2D emission peak in the envelope of VLA 1623. Top: $\text{H}^{13}\text{CN } J = 1 \rightarrow 0$. Bottom: $\text{HC}^{15}\text{N } J = 1 \rightarrow 0$. 152
- Figure 6.6 Top panel Integrated intensity map of $o - \text{NH}_2\text{D } 1_{1,1} \rightarrow 1_{1,0}$ towards IRAS16293. Middle left panel: spatially integrated spectrum of $o - \text{NH}_2\text{D } 1_{1,1} \rightarrow 1_{1,0}$ towards the A component of IRAS16293 (blue circle in the top panel). Middle left panel: spatially integrated spectrum of $o - \text{NH}_2\text{D } 1_{1,1} \rightarrow 1_{1,0}$ towards the B component of IRAS16293 (yellow circle in the top panel). Bottom left panel: spatially integrated spectrum of $o - \text{NH}_2\text{D } 1_{1,1} \rightarrow 1_{1,0}$ towards the NH_2D peak in the envelope of IRAS16293 (black circle in the top panel). Bottom left panel: spatially integrated spectrum of $o - ^{15}\text{NH}_2\text{D } 1_{1,1} \rightarrow 1_{1,0}$ towards the NH_2D peak in the envelope of IRAS16293. 154

- Figure 6.7 Top panel Integrated intensity map of p -NH₂D $1_{1,1} \rightarrow 1_{1,0}$ towards IRAS16293. Middle left panel: spatially integrated spectrum of p -NH₂D $1_{1,1} \rightarrow 1_{1,0}$ towards the A component of IRAS16293 (blue circle in the top panel). Middle left panel: spatially integrated spectrum of p -NH₂D $1_{1,1} \rightarrow 1_{1,0}$ towards the B component of IRAS16293 (yellow circle in the top panel). Bottom panel: spatially integrated spectrum of p -NH₂D $1_{1,1} \rightarrow 1_{1,0}$ towards the NH₂D peak in the envelope of IRAS16293 (black circle in the top panel). 155
- Figure 6.8 Top panel Integrated intensity map of H¹³CN $J = 1 \rightarrow 0$ towards IRAS16293. Middle left panel: spatially integrated spectrum of H¹³CN $J = 1 \rightarrow 0$ towards the A component of IRAS16293 (blue circle in the top panel). Middle left panel: spatially integrated spectrum of H¹³CN $J = 1 \rightarrow 0$ towards the B component of IRAS16293 (yellow circle in the top panel). Bottom panel: spatially integrated spectrum of H¹³CN $J = 1 \rightarrow 0$ towards the NH₂D peak in the envelope of IRAS16293 (black circle in the top panel). 156
- Figure 6.9 Top panel Integrated intensity map of HC¹⁵N $J = 1 \rightarrow 0$ towards IRAS16293. Middle left panel: spatially integrated spectrum of HC¹⁵N $J = 1 \rightarrow 0$ towards the A component of IRAS16293 (blue circle in the top panel). Middle left panel: spatially integrated spectrum of HC¹⁵N $J = 1 \rightarrow 0$ towards the B component of IRAS16293 (yellow circle in the top panel). Bottom panel: spatially integrated spectrum of HC¹⁵N $J = 1 \rightarrow 0$ towards the NH₂D peak in the envelope of IRAS16293 (black circle in the top panel). 157

LIST OF TABLES

Table 3.1	Parameters for the lines in test 1, along with analytically predicted brightness temperatures and NSLAB computed brightness temperatures. Opacities quoted refer to line centre opacities.	39
-----------	--	----

Table 3.2	Parameters for the lines in test 2. Opacities quoted refer to line centre opacities. 40	
Table 3.3	Parameters for the lines in test 3. Opacities quoted refer to line centre opacities. 41	
Table 3.4	Physical parameters for the time benchmarking of ALICO/1DART. 52	
Table 3.5	Summary of the radiative transfer codes developed in this thesis along typical execution times. The execution times have been measured in a 2.2 GHz intel i7 processor, with either 1 or 8 cores, except for ALICO/MCMC which had its execution time measured in FROGGY. 54	
Table 4.1	Spectroscopic properties of the hyperfine components of the HCN $J = 1 \rightarrow 0$, $J = 2 \rightarrow 1$ and $J = 3 \rightarrow 2$ rotational transitions. Transitions are numbered according to increasing frequency. 61	
Table 4.2	Parameters of the toy model. Slabs are numbered from the background to the observer. 68	
Table 4.3	default 75	
Table 4.4	Excitation temperatures for the hyperfine components of the $J = 1 \rightarrow 0$ and $J = 3 \rightarrow 2$ transitions of HCN for two different models: a model where the hyperfine overlaps have been taken into account, and another where hyperfine overlaps have not been taken into account. 75	
Table 4.5	Values for the parameters in the reference model. Some of the parameters were chosen from an already published value. 79	
Table 4.6	Expected hyperfine ratios for HCN $J = 1 \rightarrow 0$ and $J = 3 \rightarrow 2$. Hyperfine transitions numbered according to the notation in Table 4.1. 82	
Table 4.7	RMS noise and intensity offsets applied to the continuum maps, along with the Half Power at Beam Width of the observations. 87	
Table 4.8	H^{13}CN and HC^{15}N column densities along with the $\text{HCN}/\text{H}^{13}\text{CN}$ ratio compute for different values of $^{12}\text{C}/^{13}\text{C}$. 90	
Table 4.9	Best fit results to the observations of HCN and its isotopologues by RADEX+NSLAB MCMC. We also present the fixed parameters used in the fit. 91	

Table 4.10	Column densities for HCN and its isotopologues and the isotopic ratios between this isotopologues and HCN as computed from the results of the MCMC fit with RADEX+NSLAB. 94	
Table 4.11	Best fit parameters for our continuum dust emission model. 101	
Table 4.12	Best fit values for the ALICO/MCMC fit to the emission of HCN and its isotopologues in L1498. 108	
Table 6.1	Detected species and transitions with NOEMA towards IRAS 03282. 148	
Table 6.2	Detected species and transitions with ALMA towards VLA1623. 153	
Table 6.3	Detected species and transitions with ALMA towards IRAS16293. 153	
Table B.1	Integrated intensities for the hyperfine components of the HCN $J = 1 \rightarrow 0$ transition along with the ratios between them, $R_{02} = F = 0 \rightarrow 1/F = 2 \rightarrow 1$, $R_{12} = F = 1 \rightarrow 1/F = 2 \rightarrow 1$. Data extracted from Sohn et al. (2007). 206	
Table C.1	Approved telescope time proposals submitted by V. S. Magalhães during this thesis. 207	

INTRODUCTION

In this chapter we describe the concepts that will be referenced in the remaining chapters of this thesis. The first concept to be introduced is star formation, especially the low mass case (Section 1.1), followed by a description of what are the results of this process, i.e. a formed star system (Section 1.2). Next we explore what stellar systems inherit from their parental interstellar clouds (Section 1.3) and lastly how we can trace this heritage (Section 1.4).

1.1 THE PROCESS OF LOW MASS STAR FORMATION

Star formation is the process that converts interstellar material (gas and dust) into stars. The phases of this process are well defined but its physical and chemical conditions are still not yet completely understood.

The process of star formation can be divided in three main phases:

1. The prestellar phase: Where regions inside molecular cloud complex have condensed enough to form what we call prestellar cores, objects with central densities larger than 10^4 cm^{-3} and kinetic temperatures close to 10 K, and have not yet formed a central object. Some prototypical examples are L1544, L1498 and TMC1 (Keto and Caselli, 2010; Tafalla et al., 2004; Sohn et al., 2007).
2. The protostellar phase: Where a compact dense object, bound to form a star but that has not yet started to fusion hydrogen, called a protostar, has formed inside a core but is still shrouded by it. Prototypical examples are IRAS 16293 – 2422, VLA 1623 – 2417 (Zapata et al., 2013; Murillo et al., 2015).
3. The protoplanetary disk phase: Where the protostar has already accreted most of its mass but there is still a disk of gas and dust orbiting it, which will eventually lead to the formation of planets, asteroids and comets. Two examples of objects in this stage are TW Hydra and V4046 Sagittarius (Kastner et al., 2014).

1.1.1 *The prestellar phase*

Star formation takes place in molecular clouds. These clouds are molecular in nature as they are protected from the harsh UV light in the interstellar medium (ISM) due to high extinction ($A_V > 3$ Snow and McCall, 2006). The temperature balance is maintained by the opposing effects of the cooling (mainly the CO $J = 1 \rightarrow 0$ transition)

and heating (dominated by cosmic rays) mechanisms (e.g. Snow and McCall, 2006), this leads to typical temperatures of the order of 10 K in the densest parts of the cloud (e.g. Tafalla et al., 2004; Keto and Caselli, 2010). These densest parts can evolve into small condensations called starless cores (e.g. Belloche et al., 2011; Keto and Burkert, 2014).

These starless cores are regions where the hydrogen number density gets an order of magnitude higher ($n_{\text{H}_2} > 10^4 \text{ cm}^{-3}$) than that of the surrounding cloud ($n_{\text{H}} \sim 500 \text{ cm}^{-3}$, Hily-Blant and Falgarone, 2007). Their central density measured through the fitting of continuum maps (Tafalla et al., 2004; Keto and Caselli, 2010, e.g.) or through the analysis of the excitation of molecular lines (Lee et al., 2007, e.g.) usually exceeds $5 \times 10^4 \text{ cm}^{-3}$. These objects are usually found inside molecular cloud complexes (e.g. Belloche et al., 2011; Sohn et al., 2007), where they are usually found along filamentary structures (André et al., 2010). These objects may also be found isolated from molecular clouds (e.g. Bourke, Hyland, and Robinson, 1995), in which case they are called Bok globules (Bok and Reilly, 1947). When these structures exceed the Jean's mass and thus become gravitationally unstable they are called instead prestellar cores, as these objects will give rise to stellar objects. How this collapse is triggered is still an open question (Stahler and Palla, 2005), but numerical simulations suggest that the collapse starts in the outskirts of the core (e.g. Foster and Chevalier, 1993; Lesaffre et al., 2005), in contrast with the classical inside out picture (Shu, 1977). During the collapse the central density increases with time increasing the pressure and therefore providing some support for the core slowing the collapse down to times slower than the free fall time (see Figure 1.1, Larson, 1969). The lifetime of these cores is estimated to be more than 10^6 years (Brünken et al., 2014). When the central density has sufficiently increased the core starts being optically thick to the dust emission and therefore starts to heat up, forming the first hydrostatic core, this marks the birth of a protostar. Some dense cores, such as L1512, do not present clear signs of collapse and may be in very early stages of their evolution (Lee, Myers, and Tafalla, 2001).

Figure 1.2 shows the complete Taurus-Auriga molecular cloud complex along with two prototypical prestellar cores that have been identified in this molecular cloud complex: L1498 a young prestellar core with a flattened density structure with some signs of collapse (Tafalla et al., 2004; Sohn et al., 2007) and L1544 a more evolved prestellar core with signs of collapse even in its denser parts of the core (Caselli et al., 2012; Keto, Caselli, and Rawlings, 2015).

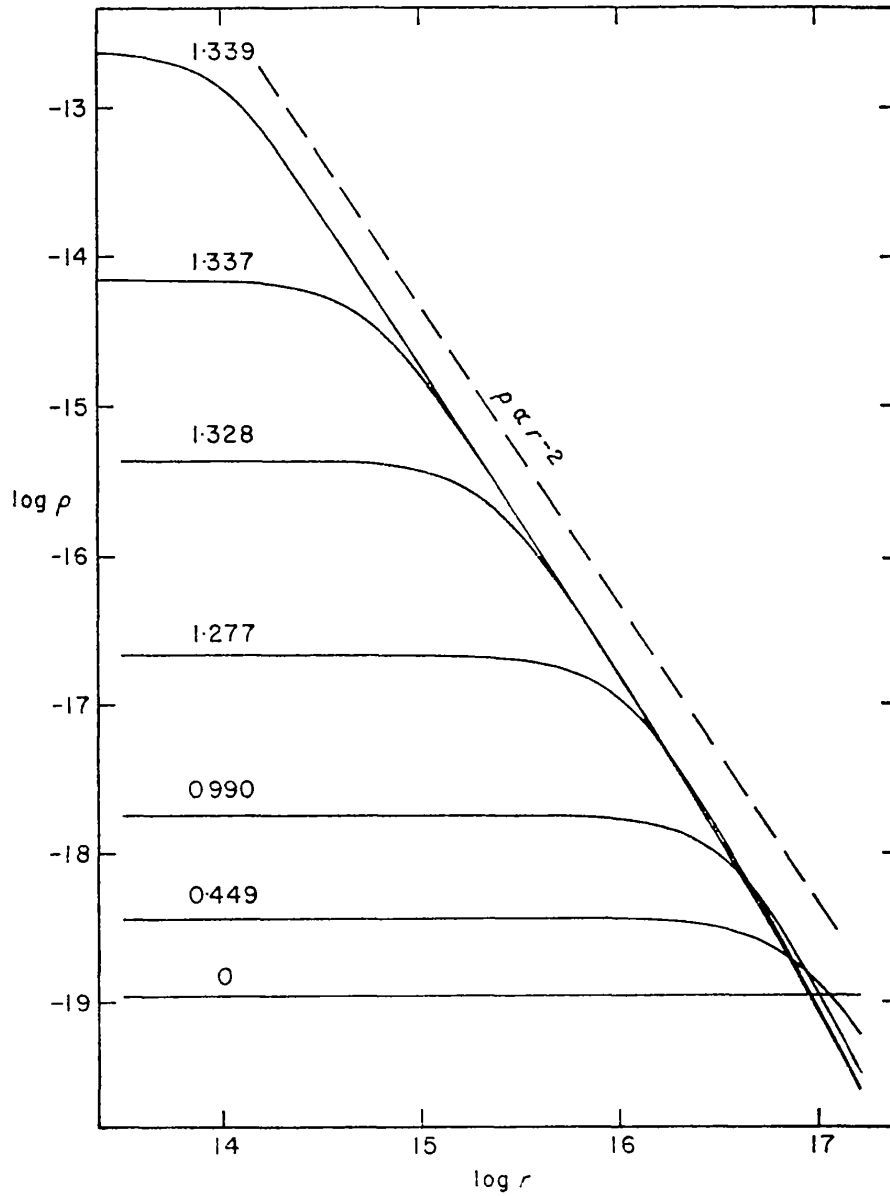


Figure 1.1 – Evolution of core structure with time. The x axis denote the logarithm of the core radius in cm while the y axis denote the logarithm of the pressure in dyne/cm^2 . The different model times are indicated in units of 10^{13} s. Note that the core pressure distribution approaches a r^{-2} distribution with the passage of time. Figure extracted from Larson (1969).

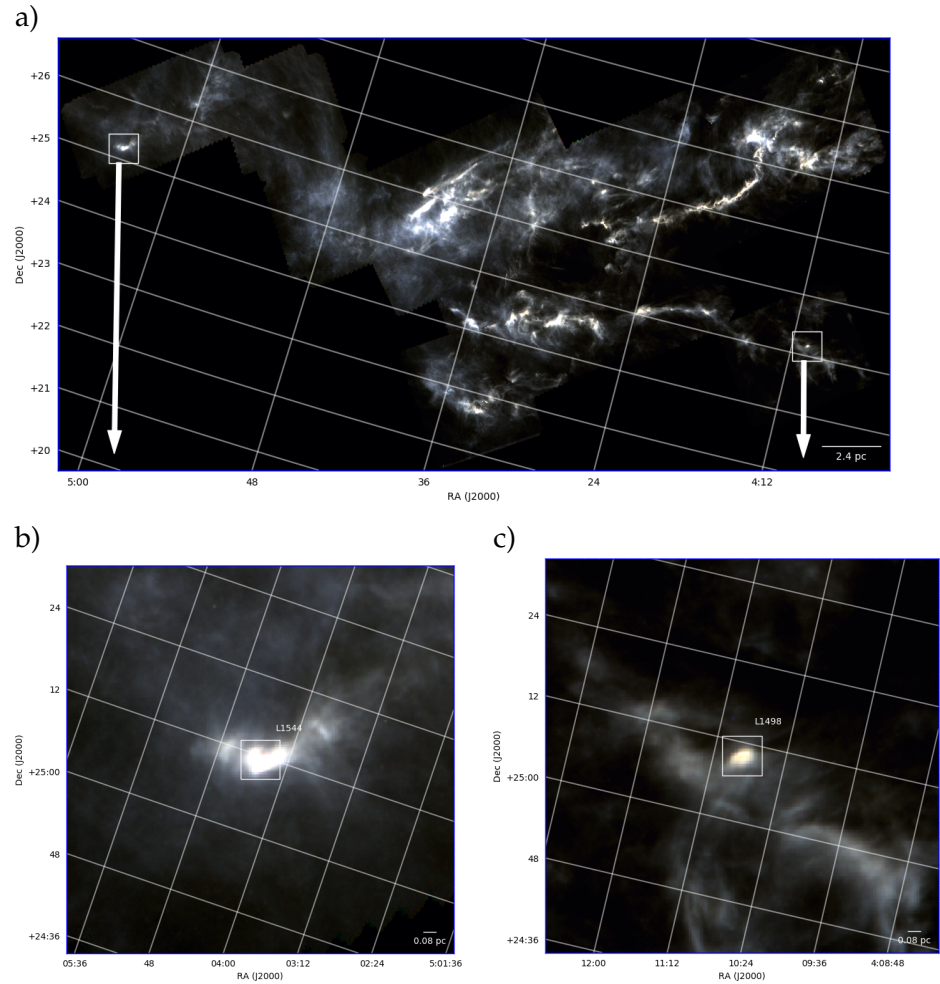


Figure 1.2 – False colour maps of the Taurus-Auriga molecular cloud complex, red is Herschel-SPIRE 500 μm , green is Herschel-SPIRE 350 μm and blue is Herschel-SPIRE 250 μm . These Herschel-SPIRE images were obtained in the Gould Belt Survey key program (André et al., 2010). a) The entire Taurus-Auriga molecular cloud complex; b) The prestellar core L1544 and its surroundings; c) The prestellar core L1498 and its surroundings.

1.1.2 *The protostellar phase*

After the formation of the first hydrostatic core the protostar continues to accrete mass from its surrounding envelope, increasing in size and in temperature. The radiation produced by the new born protostar starts to heat the material around it. This dense and warm conditions allow chemistry to proceed at a much higher pace, producing or liberating from the icy mantles of dust grains relatively large molecules (10 or more atoms) in a region called a hot core or hot corino depending on its mass (e.g. Kurtz et al., 2000; Barone et al., 2015; van Dishoeck, 2014). During this phase the protostar remains shrouded by its envelope which makes it difficult to directly observe it and its accretion disk in the optical or near infrared regimes. The best way to peer through the dust is to look through the millimetre window. The duration of the protostellar phase depends on its mass, more massive protostars go through the protostellar phase quicker than lower mass protostars, a star similar in mass to the Sun spends usually half a million years in this protostellar phase (Bergin, 2014).

Due to the immense distances to this objects (several tenths of pc) and the small size of their heated envelopes ($\lesssim 100$ AU) this objects appear very small in the sky (100 AU at 100 pc appear as $1''$ in the sky). This small size precludes single dish telescopes from being able to resolve the regions close to the protostar and therefore are not able to distinguish the emission that comes from the heated region close to the protostar from the surrounding cold envelope and cloud. Therefore the best tool to study this kind of objects are interferometers as they are able to filter out the emission from the surrounding cloud (large spacial scales) leaving only the emission from the circumstellar envelope and that of the protostar while also providing good spatial resolution (synthesised beam, $\theta_s \sim 1''$).

Figure 1.3 displays the continuum image at 110 GHz of the multiple protostar system IRAS 16293 – 2422 and its surroundings. One interesting thing to notice is the different scales between the prestellar cores in Figure 1.2 and the protostellar environment in Figure 1.3. Prestellar cores have a diameter of the order of 2×10^4 AU while the envelope of a protostar is typically only a 1000 AU.

1.1.3 *The Protoplanetary disk phase*

During the accretion process onto the protostar, the conservation of angular momentum leads to the formation of an accretion disk around the protostar (Pringle, 1981). After the envelope around the protostar has dissipated, either through accretion or ejection, the only remaining gaseous component is the protoplanetary disk. This disk is the place where planets, comets and asteroids form, being analogous to the protosolar nebula phase during the formation of the Solar

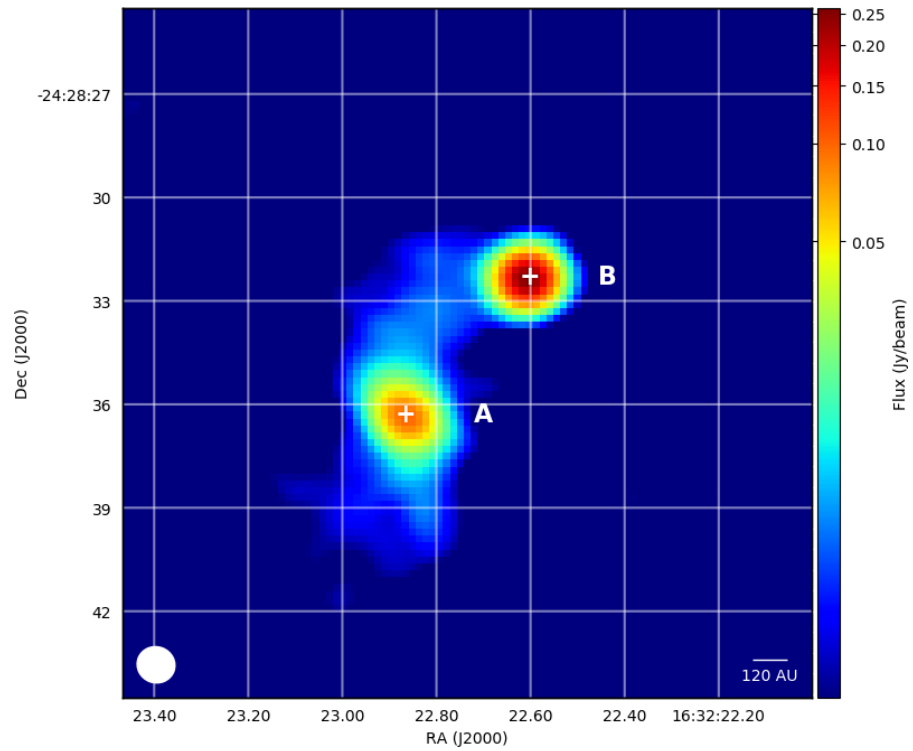


Figure 1.3 – The multiple protostar system IRAS 16293 – 2422 located in the ρ Ophichi complex at a distance of 120 pc, as viewed by ALMA at 110 GHz. The main components A and B are marked by white crosses. Data from ALMA project: 2016.1.01468.S, P.I.: V. S. Magalhães.

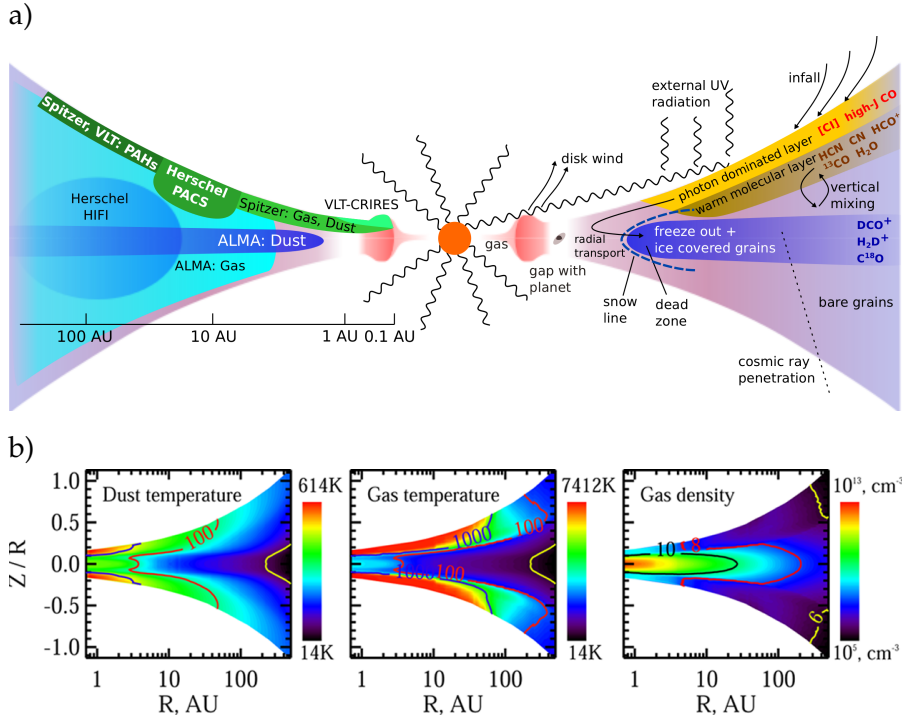


Figure 1.4 – a) Cartoon of the physical structure of a protoplanetary disk showing on the right the three main layers of a protoplanetary disk with emphasis on the species that can be found in each layer: The atmosphere; The warm molecular layer and the cold and dense mid plane. On the left we have an sketch of where different instruments are able to probe a protoplanetary disk b) A detailed physical structure for a protoplanetary disk such as DM Tau. Z/R denotes the height over the mid plane (Z) divided by the radial distance to the central star (R). a) was extracted from van Dishoeck (2014) and b) was extracted from Henning and Semenov (2013).

system. The mass of a protoplanetary disk is usually around a few percent of its parent stars mass, in the case of TW Hydra system the disk has a mass of $0.04 M_{\odot}$ while the star has a mass of $0.8 M_{\odot}$ ($\sim 5\%$, Qi et al., 2013). From chemical point of view a protoplanetary disk can be divided in three layers: A photon dominated region usually named atmosphere; a warm and molecular intermediary layer and a cold and dense layer close to the mid plane where depletion of molecules into the grains is likely very pronounced (Henning and Semenov, 2013), Figure 1.4.

The atmosphere is mainly composed of atomic species that have been photo dissociated from species in the warm molecular layer due to the light of the central star. Here the temperature can go up to $T_k \sim 1000$ K, and the density is a few 10^5 cm^{-3} . The grains in this

layer are usually very small ($< 0.1 \mu\text{m}$) due to the loss of all volatiles (Henning and Semenov, 2013).

The intermediate layer, called the molecular layer is hot enough for molecules to have been desorbed from the grains ($T_k \sim 20 - 100 \text{ K}$) but not enough to dissociate them. Here the density is high ($n_{\text{H}_2} \sim 10^6 - 10^{10} \text{ cm}^{-3}$) and the molecules are partially shielded by the atmosphere from the UV light and X-rays from the central star, protecting them from immediate dissociation. Due to the high density and the availability of UV radiation this is a place of active chemistry.

The third layer is the so called mid plane. Here the density is so high ($n_{\text{H}_2} > 10^7 \text{ cm}^{-3}$) that most species deplete to the grains surfaces, the fact the temperature is low ($T_k \sim 20 \text{ K}$) ensures that there is little desorption so most volatiles are kept frozen onto the grains in ice mantles.

In Figures 1.5 and 1.6 we see the protoplanetary disk of TW Hydra as seen through the emission of the CN $N=3 \rightarrow 2$ transition at 340.02 GHz. In Figure 1.5 we can see that the size of the protoplanetary disk of TW Hydra as seen in CN is larger than the current size of Neptune's orbit. The nearly circular aspect of the disk is due to its being almost face on when seen from Earth (inclination of 6° , Qi et al., 2013). In Figure 1.6 we can see the effects of Keplerian rotation in the CN $N=3 \rightarrow 2$ emission from the disk.

1.2 THE RESULTS OF THE STAR FORMATION PROCESS

When all is done and finished we are left with the products of the star formation:

- 1.2.1 one or more main objects.
- 1.2.2 several planets.
- 1.2.3 an almost innumerable quantity of comets and asteroids.

1.2.1 Stars

The main object formed is either one or more brown dwarfs or stars. A star is an object that is capable of fusing protons into helium in its core and uses this as its main source of energy. A brown dwarf is a smaller object ($8 M_{\oplus} < M < 80 M_{\oplus}$) that is capable of deuterium fusion but is not capable of igniting the PP chain. The most common situation is that in which a multiple system is born (Stahler and Palla, 2005), which means that there might be one or several brown dwarfs or stars gravitationally bound to one another in the formed system. The Solar system is an example of a system formed with only one star while α Centauri is an example of system formed with three stars (Figure 1.7).

Stars dominate the budget of their systems, in the solar system more than 99% of the mass that was not dispersed during the proto-

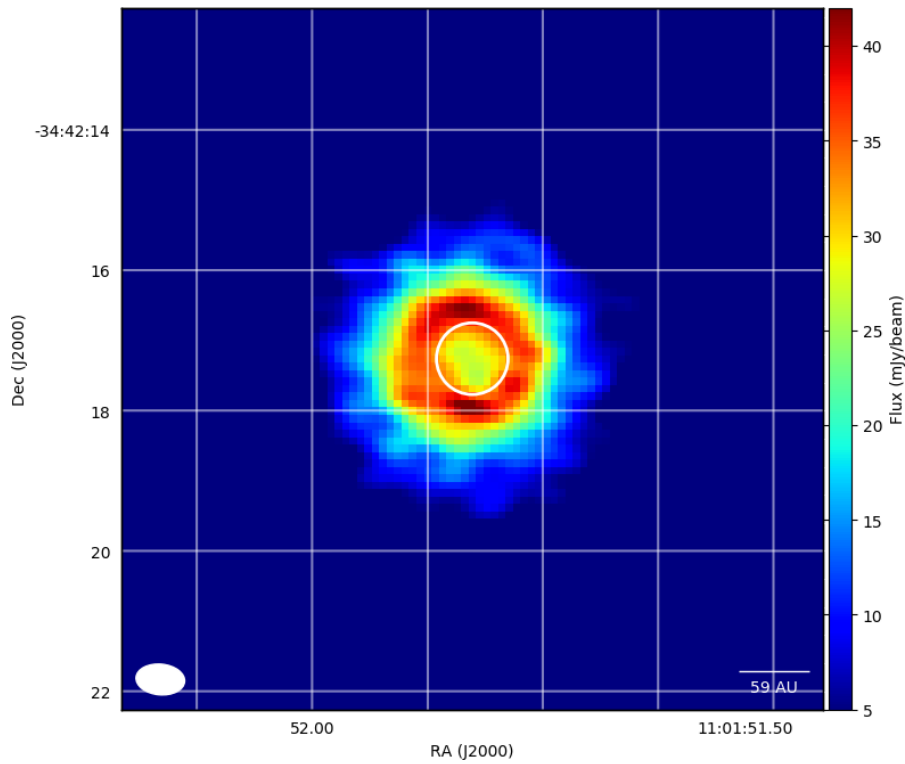


Figure 1.5 – Integrated intensity map of the optically thin hyperfine component of the CN $N=3 \rightarrow 2$ transition at 340.020 GHz towards TW Hydra. The white circle in the image represents the size of Neptune’s orbit around the Sun. Note that the emission of CN $N=3 \rightarrow 2$ comes from an annular region similar in size to the Solar system’s Kuiper’s belt. Data from ALMA project: 2013.1.00196.S, P.I.: P. Hily-Blant.

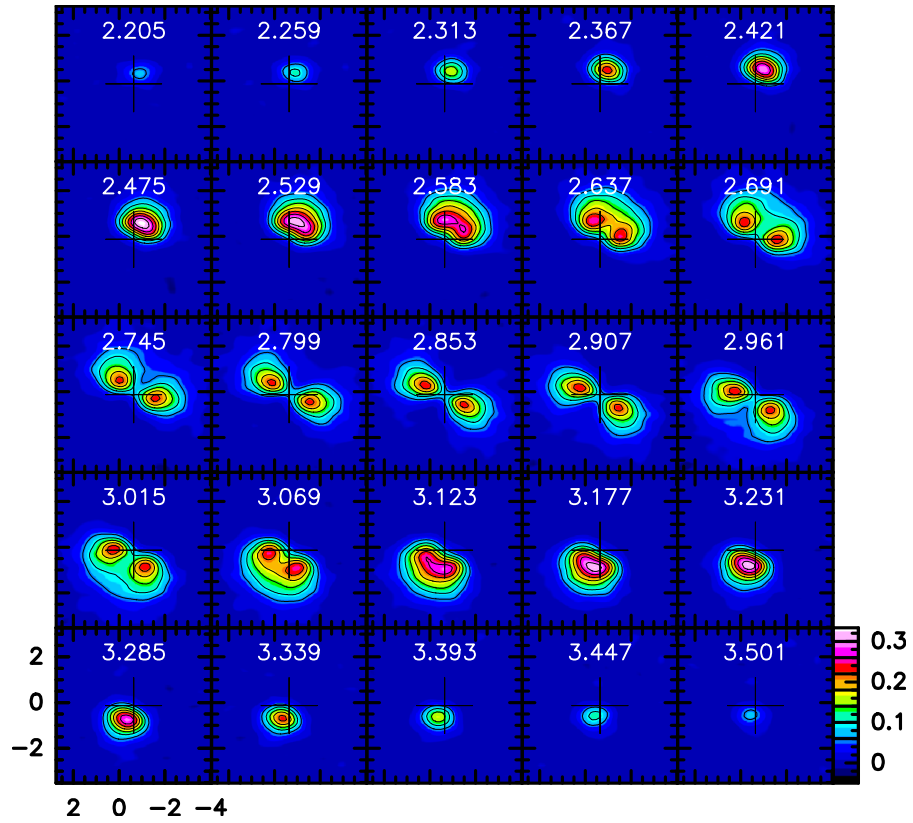


Figure 1.6 – Channel maps of the optically thin hyperfine component of the CN $N=3 \rightarrow 2$ transition at 340.020 GHz towards TW Hydra. Here we can see that different velocities have different spatial distributions. This effect is caused by the keplerian rotation of the protoplanetary disk. The white cross marks the position of TW Hydra. Data from ALMA project: 2013.1.00196.S, P.I.: P. Hily-Blant.



Figure 1.7 – NASA/ESA Hubble Space Telescope stunning view of the bright α Centauri A (on the left) and α Centauri B (on the right). The third component of the system, Proxima Centauri is too far away from the main components (A and B) to be seen in this scale. The field of view is 0.85×0.56 arc minutes in width and height respectively. Image extracted from: *Best image of Alpha Centauri A and B* (2016).

stellar and protoplanetary disk stages is the Sun. This means that the composition of the Sun, or of the stars in other systems, is representative of the prestellar environment that formed it. In the end the take home message is that all composition variations in the solar system should be compared to the Sun instead of the Earth in order to give us some light in the possible mechanisms behind it.

1.2.2 Planets

The most massive byproducts of star formation are planets. These are divided into two categories of planets: rocky planets like the Earth or Mars and gas giants like Jupiter or Saturn. Gas giants are formed early and quickly from material beyond the snow line of water, meaning they are rich in the material that was trapped in the ices. This very rapid formation enable these planets to sample the protoplanetary disk when it is still rich in gas, allowing them to accrete immense atmospheres of H_2 and He (Lissauer and Stevenson, 2007). Since they sampled all the different materials available in the protoplanetary disk their composition is very similar to the initial composition of the Solar system. This in turn makes the giant planets a good environment to investigate the primordial composition of the Solar system (e.g. Füri, Chaussidon, and Marty, 2015).

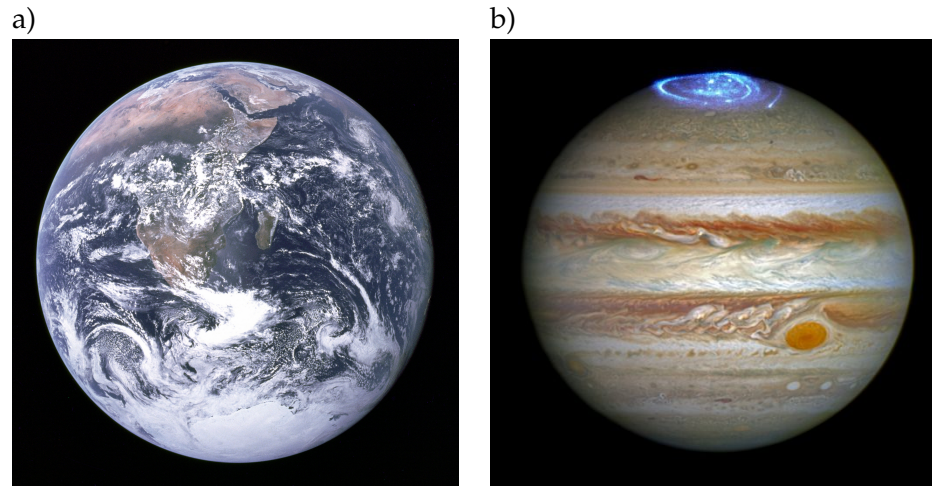


Figure 1.8 – a) Example of a rocky planet: Earth. This image was taken from the Apollo 17 crew during their way back from the Moon. b) Example of a giant planet: Jupiter. Image obtained in visible light with Ultraviolet Aurora capture superimposed on its north pole, Origin: NASA, ESA, and J. Nichols (University of Leicester).

Rocky planets on the other hand form mainly from material inside the snow line of protoplanetary disks (Morbidelli et al., 2012). This makes these worlds very deficient in light elements if compared to the Sun or the gas giants, and yet these worlds still possess some light elements as evidenced by Earth's oceans. Indeed the water content of Earth even though very small ($\sim 0.1\text{-}0.2\%$ in mass) is much larger than what should be expected from such worlds (Lécuyer, Gillet, and Robert, 1998; Marty, 2012). The solution nowadays proposed for this conundrum is the Grand Tack scenario in which during the late stages of planet formation the gas giants migrate radially (Walsh et al., 2011). This proposed migration of the gas giants would stir up the planetary embryos in the inner disk adding some material beyond the snow line to the infant terrestrial planets (O'Brien et al., 2010). In the end the rocky planets would be a sort of mixed repository of inner disk material with very little abundances of the light elements along with some contribution (2-3% in mass) from material beyond the snow line of water.

1.2.3 Asteroids and comets

Asteroids and comets are the left overs from the formation of planets, the remains of the building blocks of the planets, the so-called planetesimals. Comets are set apart from asteroids because they eject a large quantity of material when they are close to the Sun. These ejecta are basically composed of water, ammonia, some other com-

pounds made from lighter elements, and some silicates. While asteroids are expected to be basically dryer rocks being formed inside to the water snow line or close to it. The distinction between comet and asteroid has been somewhat blurred in recent years as some main belt asteroids demonstrate cometary activity (e.g. Hsieh and Jewitt, 2006). The Grand Tack scenario see these ice rich asteroids as the main source for the light elements seen in rocky planets (Walsh et al., 2011).

1.3 THE INTERSTELLAR HERITAGE OF PLANETARY SYSTEMS

Throughout the process of star formation what is lost and what is preserved? This is the main question surrounding the interstellar heritage of planetary systems. Comets are specially relevant to this subject as they are thought to have preserved the conditions in the protosolar nebula (Bockelée-Morvan et al., 2015). Specially since recent findings from the ROSETTA mission have demonstrated that the presence and abundance of O_2 (Bieler et al., 2015; Mousis et al., 2016b) and S_2 (Mousis et al., 2017) in the coma of 67P/Churyumov-Gerasimenko (67P) are consistent with an interstellar origin for these molecules. Two scenarios are possible for the origin of these molecules in the ices of 67P: one in which even the grain structure is preserved during comet formation, in this scenario O_2 and S_2 would be produced by radiolysis of H_2O and H_2S respectively, during the prestellar phase, in the other scenario during comet formation the icy components rearrange themselves in clathrates trapping gases from the PSN inside the grains Mousis et al., 2016a; Mousis et al., 2016b. In the first scenario comets preserve prestellar ices without any processing while on the second there is some mixing between the ice and the gas phase during comet formation. This points to the question of what exactly has been preserved in comets, to understand that we need the concept of reservoirs.

1.3.1 *Whats is a reservoir?*

A reservoir is a source from which a resource can be obtained. For example, on Earth it can be said the ocean is a reservoir of water, as it is possible to obtain water from the ocean. On chemical terms we refer to a reservoir of certain element as a source for that element. For example for Earth's biosphere the reservoir of nitrogen is the atmosphere, as all the nitrogen incorporated into biological compounds comes from the atmosphere. It can be the case that there are multiple reservoirs for a single resource, as example, on Earth fresh water can be obtained from three reservoirs: The atmosphere (in the form of clouds), rivers and lakes, and ice caps. When we look at the chemistry of the interstellar medium matters become more complicated as

it is difficult to assert the origin of most molecules, giving rise to the field of astrochemistry (Langer et al., 1978).

Therefore if we want to understand what is preserved and what is created during the formation of planetary systems we need first to understand which are the reservoirs that exist in the Solar system and in the interstellar medium. So that we are able to trace links between them.

1.3.2 *What are the different reservoirs that we see in the Solar system today*

The reservoirs that we see in the solar system can be divided in two simple categories based on the boiling point of the materials. Low boiling point materials, such as water ammonia, carbon monoxide and other are considered volatiles. While high melting point material such as silicon dioxide, iron and other metals are considered refractory materials.

Refractories are the dominant reservoir in the inner Solar system, (near Earth asteroids, Earth, mercury, Venus, and mars). It is also present in the outer Solar system as well, but its mass fraction is smaller compared to the inner Solar system. These materials are the dominant reservoir in the inner Solar system because they are the materials with the highest melting points, therefore being solid, even in the hot inner system (Figure 1.9).

Going further out, to beyond the main asteroid belt, volatile materials become the dominant reservoir in mass. This is the case because the water and ammonia snow lines are located within the asteroid belt, so bodies beyond this line have preserved their water and ammonia content over the age of the Solar system. The situation for the main belt objects is somewhat mixed as they are constantly shuffled by Jupiter's gravity and therefore we see objects rich in volatiles closer to the Sun than would otherwise be expected (Morbidelli et al., 2012). The situation is even more complicated due to the discovery of main belt comets (Elst et al., 1996). Gas giants have accreted the most volatile of reservoirs H_2 and He, with Jupiter and Saturn having chemical compositions similar to the Sun (Asplund et al., 2009).

1.3.3 *What are the different reservoirs that we see in the dense interstellar medium*

The dense interstellar medium reservoirs on the other hand have to be categorised in three categories based on their boiling points: gas phase only, ices and refractory materials.

The gas phase reservoir is composed of the substances that never deplete onto the dust grains. The principal species in this category are H_2 and the noble gases (He, Ne, Ar, etc). This species never deplete

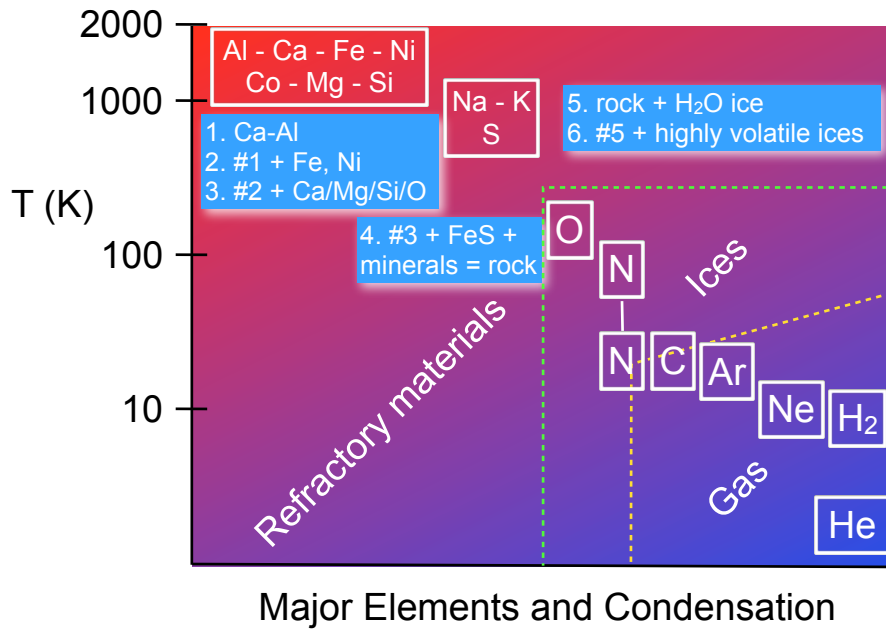


Figure 1.9 – Approximate sequence of equilibrium condensation drawn from the information given in Lewis (1997). The white boxes show the approximate transitions of various elements into minerals and ices from the gaseous state assuming solar nebula disk pressures (10^{-2} bar). While the blue boxes provide the formation sequence as gas cools (see text for discussion of condensation vs. evaporation). Some modifications include a question as to whether N is found as NH_3 or as N_2 or even N, as the latter two have lower condensation temperatures. Thus a range has been shown. The green dashed line roughly delineates the line between refractory solids and ices, while the yellow line notes species that remain in the gas. Note that C and N straddle this line. O in the form of H_2O will also be found both in the gas and ice at various radial positions in a protoplanetary disk. A fraction of C, H, O, and N will also be bound in organics which, depending on the form, have condensation/sublimation temperatures in the range of 50-150 K (Öberg et al., 2009). Image extracted from Bergin (2014).

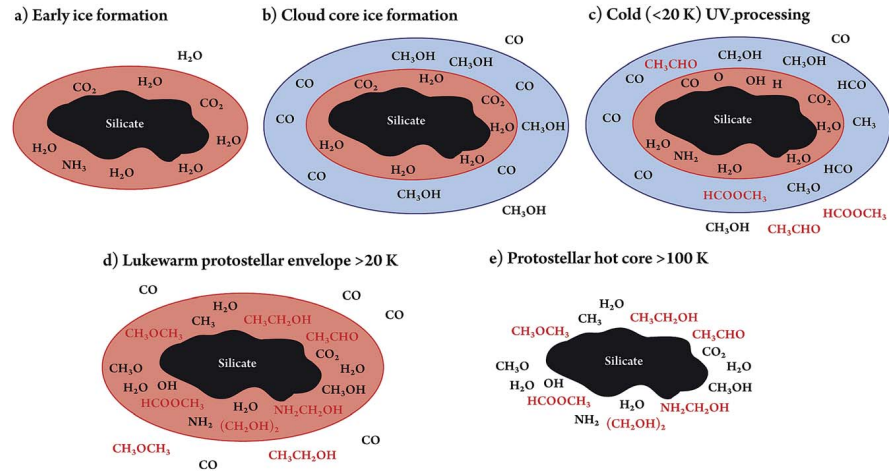


Figure 1.10 – Proposed evolution of ices during star formation and formation of complex molecules. Pink indicates an H₂O-dominated ice and blue a CO-dominated ice. Early during cloud formation (a) an H₂O-rich ice forms, with minor amounts of CH₄ and NH₃ through hydrogenation of O, C and N. Once a critical density is reached CO freezes out catastrophically (b), providing reactants for CH₃OH ice formation through hydrogenation of CO (other generation complex organic molecules). In the cold outer envelope (c), photo processing of the CO-rich ice results in the production of, e.g., HCOOCH₃ (1st generation). Closer to the protostar (d), following sublimation of CO, other complex molecules become abundant. Finally, all ices may desorb thermally close to the protostar >100 K (e) (2nd generation). Figure from Öberg et al. (2010).

onto the dust grains are their sublimation points remain below of 10 K.

The interstellar ices are a fleeting reservoir of volatile material. The first ice to form is water ice, it forms when the optical depth of the dust is enough to start protecting the recently formed water from the interstellar UV field (when the opacity of the 9.7 μm silicate feature exceeds 0.15, Whittet et al., 2013). The different species that are part of the ice mantles are deposited when different conditions are attained in the ISM, thus giving the grains a layered appearance Figure 1.10. CO ice the second most abundant ice in grains depletes to the grains when $A_V \gtrsim 10$, being therefore frozen out into grains in prestellar cores (Whittet, Goldsmith, and Pineda, 2010). In the grain surfaces these species interact and give rise to intricate surface chemistry (van Dishoeck, 2014).

The main reservoir of refractory materials in the interstellar medium are silicate grains, they comprise 76% of the total grain mass and 60% of the total grain volume (Draine, 2011). These grains exist in all phases of the interstellar medium and are thought to be created on

the death of stars (van Dishoeck, 2014). These grains are also important as they are the hosts for the formation of H_2 and also to the interstellar ices that form at higher densities.

1.4 HOW DO WE TRACE THE HERITAGE OF RESERVOIRS?

To trace the heritage of reservoirs we need to identify characteristics of each reservoir that do not change over time. Individual species are not great at this because during the star formation process, the prevalent species of a reservoir may change, thus requiring a very reliable chemical model. Another problem that we may run into is that the prevalent species of a reservoir is unobservable.

One thing that remains constant in a reservoir is the isotopic ratio of stable isotopes of elements present in that reservoir. Yet different reservoirs may present different isotopic ratios for a given element. During the formation of a minor reservoir three processes can make it have a different isotopic ratio to that of the main reservoir: selective photo dissociation, chemical mass fractionation and spallation. The action of these processes could leave imprints in the minor reservoirs making them distinguishable from the main reservoir by their isotopic ratios.

1.4.1 *Isotopic ratios as a tool to follow reservoirs*

I propose a thought experiment, let's assume that there are two hypothetical reservoirs of water A and B that contain all the oxygen atoms in our experiment. Let's further assume that the process that separated the two water reservoirs is isotopically selective on oxygen. Let's also assume that the elemental isotopic ratio of oxygen, $^{16}\text{O}/^{18}\text{O}$ over all the water available is 600, and that we are not contaminated by ^{17}O . When the two reservoirs are separated we have: water from reservoir A has an $^{16}\text{O}/^{18}\text{O}$ ratio of 600 while water from reservoir B has an $^{16}\text{O}/^{18}\text{O}$ ratio of 2000. Now we leave these two reservoirs evolve in time in contact with a substrate.

After some time we check the species that are available. We encounter two major species CO and H_2O_2 . We measure the oxygen isotopic ratio of CO and it is 2000, while the oxygen isotopic ratio in H_2O_2 is 600. From this simple measurement we can infer that CO was formed from water from reservoir B and that H_2O_2 was formed from reservoir A. Which means we were able to follow the heritage of reservoirs A and B even though the original species, water, is not present anymore.

One other interesting fact that can be grasped from this thought experiment is that we can infer that reservoir B must be much less abundant than reservoir A. This follows from the fact that even though we see an extreme divergence from the elemental ratio in reservoir B,

reservoir A still has the elemental ratio. This can only be achieved if the abundance of reservoir B is so minor that we don't see the effects of isotopic segregation in reservoir A.

1.4.1.1 *D/H ratio as a tracer of interstellar heritage*

This method was used to trace the origin of water in the Solar system today to the interstellar medium (Cleeves et al., 2014). The deuterium to hydrogen ratio of water in the Solar system had been noted to be markedly different from the deuterium to hydrogen ratio in the Sun (Eberhardt et al., 1995; Bockelée-Morvan et al., 1998; Alexander et al., 2012; Usui et al., 2012). Interstellar ices also are very enriched in deuterium even several times more than terrestrial water (Dartois et al., 2003; Coutens et al., 2012; Persson, Jørgensen, and van Dishoeck, 2012; Persson et al., 2014). Cleeves et al., 2014 argue from that, that only part of the water ice was reprocessed during the formation of the Solar system. Therefore at least some part of the ice from the interstellar reservoirs survived and was incorporated into planets and comets. The method used by Cleeves et al. (2014) remain controversial as it requires the protoplanetary disk to be shielded from cosmic rays. Even with this caveat Cleeves et al. (2014) demonstrate that isotopic ratios can be used to follow reservoirs during the star formation process.

1.4.1.2 *Using Carbon Isotopic ratio to elucidate formation mechanisms of carbon chains*

The formation pathways of simple carbon chains in the ISM such as C_2H , $c-C_3H_2$ or the cyanopolyynes ($HC_{2n+1}N$) is still not completely understood. Since different carbon atoms in these carbon chains may not be equivalent chemically (e.g. Sakai and Yamamoto, 2013), the carbon isotopic ratio in each of the atoms may help define from which species each of these atoms came, elucidating the formation pathway of the carbon chains. This technique has been explored to suggest pathways to the formation of the two simplest cyanopolyynes and also CCH. Araki et al. (2016) suggest the equal carbon isotopic ratios of the first two carbon atoms but not of the carbon atom linked to nitrogen in HC_3N suggest a formation pathway through C_2H_2 and $C_2H_2^+$. Taniguchi et al. (2016) propose that the formation of HC_5N should come from the reaction of atomic nitrogen with hydrocarbon ions with 5 carbon atoms such as $C_5H_4^+$ based on the fact that the isotopic ratios of all carbon atoms are the same ($^{12}C/^{13}C \sim 94$) and slightly depleted when compared to the $^{12}C/^{13}C$ ratio in the local interstellar medium ($^{12}C/^{13}C = 68$ Milam et al., 2005). Sakai et al. (2010) claim that the difference in abundance between $C^{13}CH$ and ^{13}CCH can only be explained if the two carbon atoms in CCH are not equivalent. This restrains the possible formation pathways of CCH to

pathways that have non equivalent carbon atoms such as the neutral neutral reaction: $C + CH_2$.

1.4.2 *The puzzle of the isotopic ratio of nitrogen in the Solar System*

The isotopic ratio of nitrogen in Solar system comets is basically uniform, $^{14}N/^{15}N \approx 144$, independent of the molecular carrier (NH_2 , CN, HCN) and comet family (See Figure 1.11 Mumma and Charnley, 2011; Shinnaka et al., 2016; Hily-Blant et al., 2017). This value is markedly different from the nitrogen isotopic ratio measured in the Solar wind, $^{14}N/^{15}N = 441 \pm 5$ (Füri, Chaussidon, and Marty, 2015). The isotopic ratio measured in the Solar wind is also a measurement of the nitrogen isotopic ratio of the bulk of the Solar system as the Sun has sampled all reservoirs of the protosolar nebula (PSN, the birth place of the Solar system) and is also not expected to have synthesised neither ^{15}N nor ^{14}N (See Section 2.1). Such discrepancy suggests that there possibly were at least two distinct reservoirs of nitrogen in the PSN, a primary one, sampled by the Sun and Jupiter, and a fractionated secondary one, sampled by the comets. But this could also be a result of isotopic exchanges happening in the ices since the formation of the comets. These two reservoirs may have an interstellar origin or the secondary reservoir may have been created *in-situ* during the comet formation stage.

1.4.3 *The PhD project*

The main objective of this thesis is to identify the different reservoirs of nitrogen at the different stages of star and planet formation. We plan to identify these reservoirs by obtaining accurate isotopic ratios, using different nitrogen carriers observed in prestellar cores, protostars, and protoplanetary disks. Among our primary objectives is a comprehensive study of the internal structure—density, velocity—of the L1498 prestellar core, including a significant step further in the derivation of the abundance of HCN and its isotopologues with respect to earlier studies, especially that of Daniel et al., 2013. We anticipate that the challenge will be to quantitatively reproduce the hyperfine anomalies of HCN, hence improving on the seminal studies of Guilloteau and Baudry, 1981 and Gonzalez-Alfonso and Cernicharo, 1993. We expect to provide accurate isotopic ratios to be compared to the theoretical predictions based on the most recent astrochemical fractionation network of Roueff, Loison, and Hickson, 2015.

In this thesis, we will use various nitrogen-bearing molecules belonging to two broad families, nitriles—HCN, HC_3N —and hydrides (NH_2D), and the somewhat ambivalent CN radical. Among the motivations for our study of HCN is the HCN/ $HC^{15}N$ ratio which was indirectly measured to be between 140 and 340 in prestellar cores (Hily-

Blant et al., 2013a) and 111 ± 19 in protoplanetary disks (Guzmán et al., 2017). Such measurements rely on the so-called double isotopologue method (Section 2.3.2) but were questioned by recent chemical models Roueff, Loison, and Hickson, 2015. In their comprehensive study of the nitrogen isotopic ratio in the B1 core, Daniel et al. (2013) did obtain a low HCN/HC¹⁵N ratio (165^{+30}_{-25}) not going through the double isotopic method. However, these authors discarded this value under the assumption that the column density of HCN could not be reliably measured, thus illustrating the challenge in deriving the column density of HCN. It is one goal of this thesis to solve this issue at least in the case of L1498.

One strength of Daniel et al. (2013) is the consistent analysis of several species. However, this could only be done at the expense of important features that had to be neglected. In particular, Daniel et al. (2013) considered an oversimplified profile for the velocity field and the velocity dispersion. However, as will be shown in the following, these parameters are crucial to reproduce the HCN line intensities, due to overlapping hyperfine transitions (Guilloteau and Baudry, 1981; Gonzalez-Alfonso and Cernicharo, 1993). To accurately take the line profiles into account requires an efficient way to explore the parameter space, that cannot be achieved with χ^2 minimisation. This is another step further with respect to the study of Daniel et al. (2013). Another limitation of their study was the use of the collisional excitation coefficients of Ben Abdallah et al. (2012) for HCN. These collisional coefficients assume that H₂ can be assumed to be a sphere which can alter significantly the collisional coefficients. In this thesis, we will use collision rate coefficients at the hyperfine levels for HCN in collisions with ortho and para-H₂ (Lique et al. in preparation).

Another chief objective of this thesis is to identify the isotopic reservoirs of nitrogen present in evolved protoplanetary disks such as in the TW Hya system, to investigate the origin of the cometary reservoir of nitrogen. In the process, the elemental isotopic ratio of nitrogen in the present-day local interstellar medium will be needed.

Finally, the possibility that nitrogen can be fractionated in ices before being incorporated within cometary nuclei in protoplanetary disks will also be investigated using ALMA and IRAM-NOEMA observations of protostars.

THE ISOTOPIC RATIO OF NITROGEN

As seen in the previous chapter the isotopic ratio of nitrogen may be key to disentangling the mystery of the heritage of the protosolar nebula. To be able to understand the measurements that we have of $^{14}\text{N}/^{15}\text{N}$ in the ISM today we need to understand the sources of the two isotopes of nitrogen ^{14}N and ^{15}N (Section 2.1). With that knowledge in hand we need to choose our target molecules between the multitude of molecules seen in the ISM (Section 2.2) to carry out the measurements of the nitrogen isotopic ratio (Section 2.3). From these measurements (Section 2.4), a big picture is emerging which will be the framework for this thesis (Section 2.4.5).

2.1 NUCLEOSYNTHESIS OF NITROGEN

During the big bang nucleosynthesis only the lightest atomic nuclei were produced: H, He, Li and Be (Alpher, Bethe, and Gamow, 1948). All the other elements in the universe have been created by stars long after the big bang either in their cores (Hoyle, 1946) or in supernova explosions (Hoyle et al., 1956). The first stable atomic nucleus produced in stars is ^4He through the proton-proton chain (Eddington, 1920; Bethe, 1939). The next nuclei to be produced are those that can be built directly from helium nuclei (ex: ^{12}C , ^{16}O , ^{20}Ne , etc). Other atomic nuclei that can be build from this elements simply by the addition of D or H are also produced (ex: ^{14}N , ^{22}Na), but in much lower quantities as they require an extra step to be produced. These nuclei are called primary isotopes as they can be built directly from hydrogen and helium in one single star. Other nuclei, such as ^{13}C , ^{18}O , ^{15}N , require that the stars that produce them are born with a non negligible amount of nuclei heavier than ^4He to be efficiently produced, and are thus called secondary isotopes. Since their production depend on the abundance of the elements built previously their abundances are generally 2 to 3 orders of magnitude inferior to the primary isotopes of the same element (ex: $^{14}\text{N}/^{15}\text{N} = 441$ in the Solar system, $^{12}\text{C}/^{13}\text{C}=70$ in the local ISM, Füri, Chaussidon, and Marty, 2015; Milam et al., 2005, respectively).

Nitrogen has two stable isotopes: ^{14}N is a primary isotope, and ^{15}N is a secondary isotope. The details behind the production of these two isotopes are still debated (Clayton, 2003; Prantzos, 2003; Romano and Matteucci, 2003; Wiescher et al., 2010), but the main processes have been identified (Wilson and Rood, 1994). ^{14}N is produced by both the cold and hot CNO cycles, as well as in the so-

called hot bottom burning process in asymptotic giant branch (AGB) stars, although massive, rotating stars may be sources as well (Prantzos, 2011). In contrast, it is thought that ^{15}N can only be produced through the hot CNO cycle, during nova outburst or in Type Ia and Type II supernovae (Romano and Matteucci, 2003). The differences in primary and secondary origins of the two nitrogen isotopes are predicted to lead to an increase in the $^{14}\text{N}/^{15}\text{N}$ ratio with distance from the galactic centre. Indeed Adande and Ziurys (2012) have measured a positive gradient with increasing distance from the galactic centre, $^{14}\text{N}/^{15}\text{N} = 21.1D_{\text{GC}} + 123.8$, where D_{GC} is the distance from the galactic centre in kpc. As can be seen in Figure 2.1 the observed galactic gradient is compatible with current galactic evolution models for the $^{14}\text{N}/^{15}\text{N}$ ratio.

2.2 NITROGEN IN THE ISM AND CIRCUMSTELLAR ENVIRONMENTS

Nitrogen is an atom capable of a very rich chemistry, and being the seventh most abundant element in the universe it is readily available to form a multitude of compounds, specially with hydrogen carbon and oxygen. Nitrogen has been detected in the diffuse ISM in several forms, atomic, mainly through its UV absorption bands (Nieva and Przybilla, 2012), or in molecular carriers (HCN N_2 e.g. Liszt and Lucas, 2001; Knauth et al., 2004; Li et al., 2013). CN was among the first molecules to have ever been identified in the diffuse ISM (McKellar, 1940; Swings and Rosenfeld, 1937).

In the dense ISM Nitrogen can be found in a variety of species, from very simple ones such as CN, to big complex ones like HC_{11}N . This rich chemistry is a result of the much denser gas and the presence of ions that allow fast ion-neutral reactions to take place (Terzieva and Herbst, 2000). It is theorised that the main reservoir of nitrogen in the dense ISM should be either atomic N or N_2 , with some part of it being locked in ices as NH_3 (Herbst and Klemperer, 1973). Of these three main reservoirs only NH_3 in ices is observable, and is measured to be an important component of interstellar ices $\text{NH}_3/\text{H}_2\text{O} \sim 5 - 20\%$ Boogert, Gerakines, and Whittet, 2015. The other two reservoirs, N_2 and N are not observable in the dense ISM (Herbst, Schubert, and Certain, 1977). Atomic nitrogen by being a single atom presents only fine structure transitions and electronic transitions. Both types of transitions have upper levels that are not excitable in the dense ISM, due to the low temperatures. The possibility remains to use those transitions as absorption probes through the use of background sources of continuum radiation. The problem is that the electronic lines fall in the ultraviolet which is strongly affected by the extinction of dust in the dense ISM, and that stars do not emit sufficient light in the wavelengths of the fine structure lines to be used in as an absorption probe. For N_2 the electronic lines are also not available

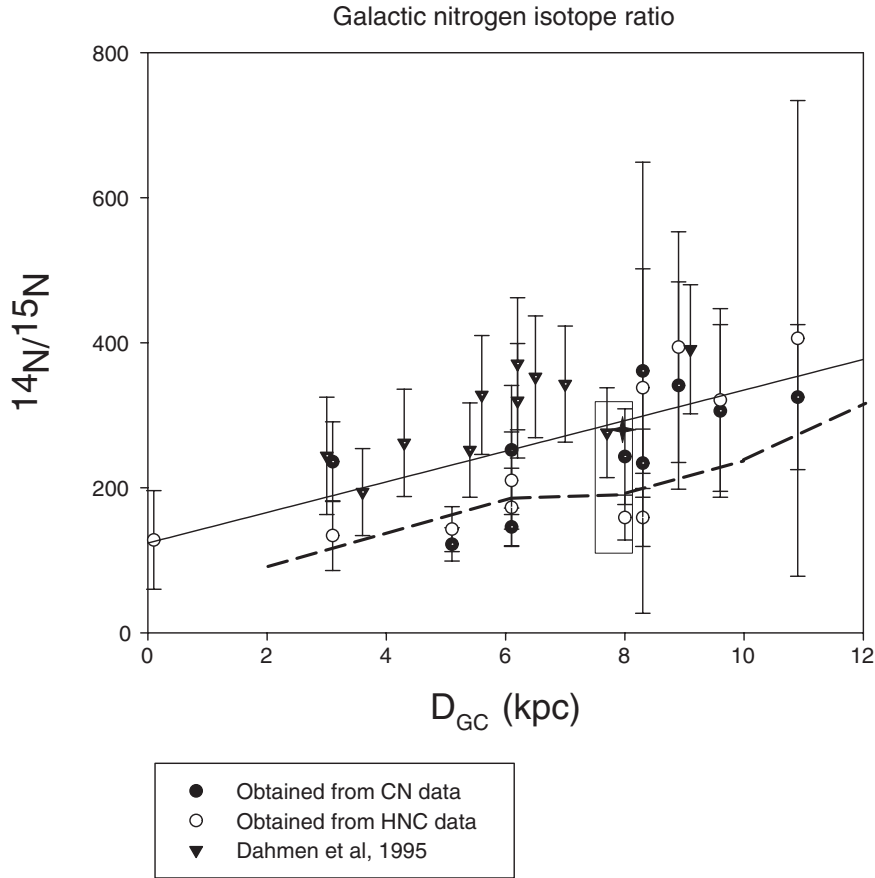


Figure 2.1 – Plot of $^{14}\text{N}/^{15}\text{N}$ isotope ratios as a function of galactocentric distance, D_{GC} (kpc). The filled circles indicate direct measurement of the ratios using the hyperfine components of the CN isotopologues. The open circles represent the ratios calculated using $\text{HN}^{13}\text{C}/\text{H}^{15}\text{NC}$ and the $^{12}\text{C}/^{13}\text{C}$ ratio measured in CN by Milam et al. (2005). The triangles are the ratios obtained from the HCN data of Dahmen, Wilson, and Matteucci (1995), combined with the $^{12}\text{C}/^{13}\text{C}$ ratios of Milam et al. (2005). The dashed line is the gradient from the model 3n of Romano and Matteucci (2003), where ^{15}N is treated as a secondary element and produced in novae. The rectangular box represents the range of values found in comet measurements of $^{14}\text{N}/^{15}\text{N}$, and the star is the value in Earth’s atmosphere. A linear fit of these three sets of data results in the expression: $^{14}\text{N}/^{15}\text{N} = 21.1D_{\text{GC}} + 123.8$. Figure extracted from Adande and Ziurys (2012).

for the same reasons and being a closed shell molecule there are no dipole fine structure transitions allowed. The hope should remain on its rotational or vibrational transitions, but since it is a mono atomic species there is no permanent dipole moment therefore there are no dipolar radiative rotational transitions.

The picture that can be built from this is that the two candidates for the main reservoir of Nitrogen in the dense ISM are unobservable. We therefore must rely on the study of the trace species that are detectable in the dense ISM and use their abundances to reverse engineer the properties of the main reservoirs of nitrogen in the dense ISM, and also trying to identify which is the dominant one. The reverse engineering is done through the use of theoretical chemistry simulations using the so-called chemical networks. Chemical networks are databases of possible chemical reactions and their effective rates.

In circumstellar environments nitrogen is seen in a larger multitude of molecules, ranging from simple ones like CN to big organic molecules like $\text{CH}_3\text{CH}_2\text{CN}$ (Cazaux et al., 2003). This complex chemistry is still not completely understood but may be related to the sublimation of ice mantles close to the protostars (van Dishoeck, 2014) or in the case of formamide (NH_2CHO) be a product of gas phase reactions only (Barone et al., 2015). In disks fewer species have been detected, but nevertheless nitrogen carriers are commonly observed. Chapillon et al. (2012b) demonstrate that CN and HCN are ubiquitous in protoplanetary disks. A few complex molecules have been detected in disks, such as HC_3N (Chapillon et al., 2012a) and CH_3CN (Öberg et al., 2015).

2.3 MEASURING THE ISOTOPIC RATIO OF NITROGEN IN THE ISM

The methods to measure the $^{14}\text{N}/^{15}\text{N}$ ratio can be divided in two broad categories: direct methods and indirect methods. The direct methods are called so because $^{14}\text{N}/^{15}\text{N}$ is computed is taken as the ratio of the column densities of the main and rare isotopologue measured directly. Whereas the indirect methods use the ratio between the rare isotopologue and a third species to estimate the ratio between the main and the rare isotopologue. The most used method in this category is called the double isotopologue method Section 2.3.2.

2.3.1 Direct methods

To measure the isotopic ratio directly it is necessary to have a reliable way to measure the column density of the main isotopologue. The simplest case would be that in which the emission of the main isotopologue is optically thin, but this usually means that the rare isotopologue is undetectable. Yet due to the hyperfine struc-

ture displayed by molecules containing nitrogen, sometimes one of the hyperfine components of the main isotopologue is indeed optically thin. One example of such a measurement is the measurement of the $^{14}\text{N}/^{15}\text{N}$ in CN in the protoplanetary disk around TW Hydra by Hily-Blant et al. (2017) ($^{14}\text{N}/^{15}\text{N} = 323 \pm 30$).

Another way of directly measuring the column density of the main isotopologue is through hyperfine fits to the rotational spectra to obtain the total opacity of the rotational transition. The caveat of this method is that the hyperfine fit assumes that the hyperfine components of rotational transition have the same excitation temperature, which may not be true. One example of such a measurement is the measurement of the $^{14}\text{N}/^{15}\text{N}$ in NH_2D towards a few prestellar cores by Gerin et al. (2009) ($^{14}\text{N}/^{15}\text{N} = 350 - 850$).

The column density may also be estimated through a local thermodynamical equilibrium analysis which assumes that the different radiative transitions observed can be described by a single excitation temperature. This approach is better suited for molecules which have several transitions available, like the cyanopolyynes or organic molecules like CH_3CN . The problem with this method is that this assumption is rarely valid. Despite this problem this method has been used to compute the isotopic ratio of nitrogen in cyanopolyynes, one example of such an endeavour is Taniguchi and Saito (2017). The authors have measured the isotopic ratio of nitrogen in HC_5N in TMC1 through this method to obtain $^{14}\text{N}/^{15}\text{N} = 323 \pm 80$.

The isotopic ratio of nitrogen can also be measured in the diffuse ISM by measuring the opacity of absorption lines of molecules containing nitrogen against a strong background source. This has been carried out for example for HCN which had its $^{14}\text{N}/^{15}\text{N}$ ratio measured in the line of sight towards B0415 + 379 (Lucas and Liszt, 1998). The main caveat here is that emission in the line of sight might hamper the measurements by diminishing the perceived absorption.

The remaining method to measure the column density of the main isotopologue directly is through the usage of complex radiative transfer models. In this case a complex source model is assumed and line profiles are computed in order to compare them to observations in search for the best fit. The main difficulty in this method resides in the necessity of an accurate source model which is prone to have correlations between its parameters (Keto et al., 2004). Despite this difficulty there are some examples of such measurements such as in Daniel et al. (2013). These authors have measured the abundances of several species along with their isotopologues in the B1 dark cloud. These abundances were then used to compute the isotopic ratio of nitrogen in several molecules.

2.3.2 Indirect methods

Indirect methods to measure the nitrogen isotopic ratio consist in measuring the column density of the ^{15}N isotopologue and a third species. This third species is a species for which there is an expected ratio between it and the ^{14}N isotopologue. Usually this third species is taken as a rare isotopologue on another element such as carbon. In such cases this method is called the double isotopologue method (Dahmen, Wilson, and Matteucci, 1995).

This method has been usually used to derive the isotopic ratio of nitrogen in species of the nitrile family (species containing the CN group, HCN, CN, HNC, etc). In such a case the abundance of the ^{13}C and the ^{15}N isotopologues is measured and is subsequently multiplied by an assumed $^{12}\text{C}/^{13}\text{C}$:

$$\frac{\text{XCN}}{\text{XC}^{15}\text{N}} = \frac{\text{X}^{13}\text{CN}}{\text{XC}^{15}\text{N}} \times \frac{^{12}\text{C}}{^{13}\text{C}} \quad (2.1)$$

where X stand for any chemical group bound to the CN group. This method has been extensively used to measure the isotopic ratio of nitrogen (e.g. Adande and Ziurys, 2012; Hily-Blant et al., 2013a; Guzmán et al., 2017), but a lot of uncertainties remain as the $^{12}\text{C}/^{13}\text{C}$ is usually unknown and therefore adopted to be the elemental one ($^{12}\text{C}/^{13}\text{C}=70$, Milam et al., 2005). This may indeed not be the case, as there is observational evidence that this ratio may be lower than the elemental ratio (HCN/ $\text{H}^{13}\text{CN} \sim 30$ Daniel et al., 2013), and theoretical expectations that it could be higher than the elemental ratio (HCN/ $\text{H}^{13}\text{CN}=90 - 140$ Roueff, Loison, and Hickson, 2015). Due to this incredible discrepancies, it is hard to judge the uncertainties in double isotopologue measurements.

2.4 REVIEW OF EXISTING $^{14}\text{N}/^{15}\text{N}$ MEASUREMENTS

To better comprehend what new information would be brought by new measurements of the isotopic ratio of nitrogen we need to make a review of the measurements that are already available in the literature. This review of the available measurements is divided in 4 subsections: the measurements in the Solar system, the measurements in the local ISM; the measurements in protostellar envelopes and the measurements in protoplanetary disks. The measurements are divided in this manner as the main idea of this thesis is to comprehend what we see in the Solar system in respect to the nitrogen isotopic ratio, with what can be observed during the phases of star formation.

2.4.1 *Measurements in the Solar system*

In the Solar system today we see a marked difference between the main mass reservoirs (the Sun and Jupiter) and the smaller mass reservoirs (asteroids, comets, interplanetary dust, inner planets). The Sun as the dominant mass reservoir displays the value of the $^{14}\text{N}/^{15}\text{N}$ at the moment and location of the birth of the Sun. All the other reservoirs that show isotopic ratios that differ from that of the Sun have been fractionated by some unknown physical process.

Material extracted from meteorites presents differing degrees of fractionation. The most refractory substance containing nitrogen, osbornite (TiN), has an isotopic ratio very similar to the bulk of the Solar system ($^{14}\text{N}/^{15}\text{N} = 424 \pm 3$ Meibom et al., 2007), while other reservoirs of nitrogen inside meteorites can show incredibly low isotopic ratios ($^{14}\text{N}/^{15}\text{N} \approx 50$, Bonal et al., 2010). On the other hand measurements of $^{14}\text{N}/^{15}\text{N}$ on the gases in the coma of comets are remarkably homogeneous, with all the values very close to 150 and a weighted average which gives $^{14}\text{N}/^{15}\text{N} = 144 \pm 3$ (see Figure 1.11 Hily-Blant et al., 2017).

For the inner planets the situation appears to be somewhat mixed with the Earth displaying a nitrogen isotopic ratio that is close to half way between that of comets and of the Sun. Füri, Chaussidon, and Marty (2015) argue that this is an evidence that the Earth sampled a third reservoir of nitrogen during its formation. We on the other hand believe that this isotopic ratio is the result of the mixing of the two reservoirs of nitrogen. This scenario is consistent with the Grand Tack scenario for the late stages of planet that predicts that the Earth has sampled volatile rich (cometary like in $^{14}\text{N}/^{15}\text{N}$) and volatile poor (Sun like in $^{14}\text{N}/^{15}\text{N}$) material (e.g. Morbidelli et al., 2012). Mars on the other hand has no records of its primordial nitrogen isotopic ratio, as its atmospheric loss is isotopic selective (Mahaffy, 2016). In Figure 2.2 we have a compilation of the most relevant measurements of the isotopic ratio of nitrogen in the Solar system.

2.4.2 *Measurements in the local ISM*

In the local ISM there are several measurements of the Nitrogen Isotopic ratio. Some of these measurements are focused on the diffuse interstellar medium. These measurements target the species that exist at low densities ($n_H \leq 10^3 \text{ cm}^{-3}$) and lukewarm temperatures ($T_{\text{kin}} \sim 100 \text{ K}$). Most of this measurements are carried out using the absorption technique as molecular emission in this physical conditions is very feeble. Figure 2.3 displays the available measurements of the nitrogen isotopic ratio in the local diffuse ISM, along with the expected value from the galactic gradient of Adande and Ziurys (2012). All the values in the diffuse ISM are more or less con-

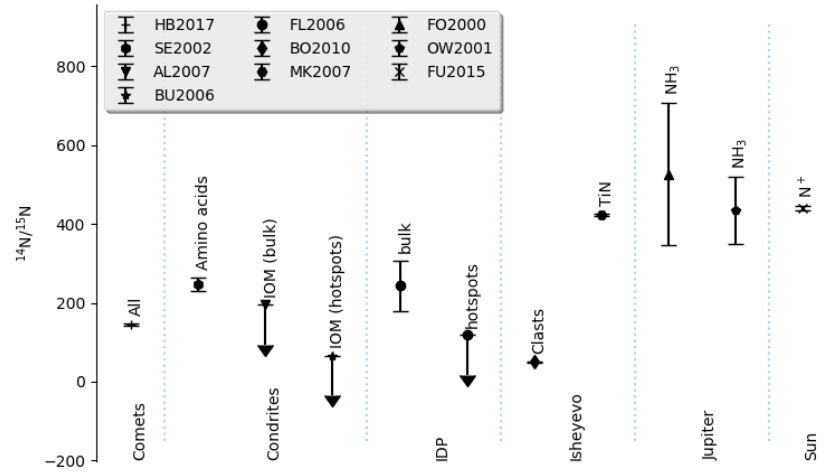


Figure 2.2 – Nitrogen isotopic ratios measured in the Solar system. Different symbols stand for different papers: HB2017 refers to Hily-Blant et al. (2017), BU2006 refers to Busemann et al. (2006), OW2001 refers to Owen et al. (2001), SE2002 refers to Sephton et al. (2002), FL2006 refers to Floss et al. (2006), FU2015 refers to Füri, Chaussidon, and Marty (2015), AL2007 refers to Alexander et al. (2007), MK2007 refers to Meibom et al. (2007), BO2010 refers to Bonal et al. (2010) and FO2000 refers to Fouchet et al. (2000). IDP stands for interplanetary dust particle.

sistent with each other, with the uncertainty weighted average being $^{14}\text{N}/^{15}\text{N} = 275 \pm 16$.

In the dense ISM there are a plethora of measurements. Species in the hydride family, NH_3 , N_2H^+ , presumably chemical descendants of N_2 (Hily-Blant et al., 2010; Hily-Blant et al., 2013a), had their nitrogen isotopic ratio measured directly, while species for the nitrile family, CN, HCN, etc have mostly indirect measurements of their isotopic ratios, with few exceptions (HCN, HNC and CN in B1 by Daniel et al., 2013). The weighted average of the direct measurements yields $^{14}\text{N}/^{15}\text{N} = 251 \pm 12$, a surprisingly low value. This value is probably skewed by the low isotopic ratios measured in the nitriles which can be underestimated due the enormous optical depths of the main isotopologues (Daniel et al., 2013). If we do this weighted average only with molecules in the hydride family, which are less plagued by high optical depth issues we get $^{14}\text{N}/^{15}\text{N} = 340 \pm 16$. This value is very similar to the value measured directly in CN in the protoplanetary disk of TW Hydra of $^{14}\text{N}/^{15}\text{N} = 323 \pm 30$ measured by Hily-Blant et al. (2017). The authors point this similarity as an evidence of this being the current value of the isotopic ratio of nitrogen in the local ISM. Figure 2.4 displays the available measurements of $^{14}\text{N}/^{15}\text{N}$ in the dense ISM.

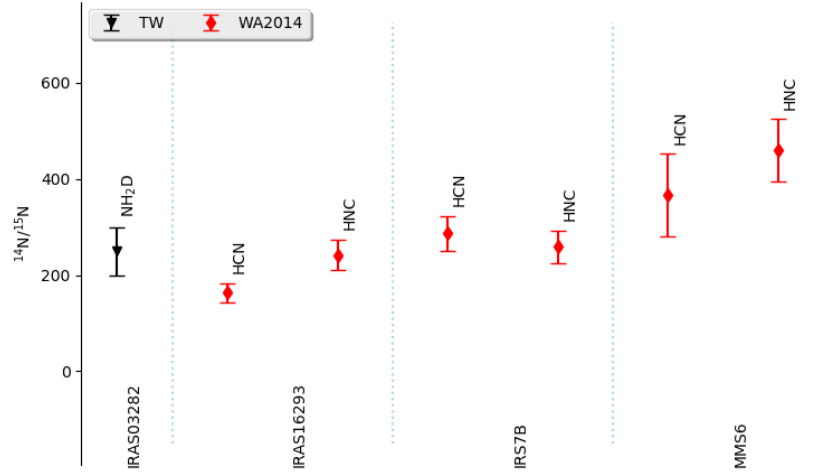


Figure 2.5 – Nitrogen isotopic ratio measured in protostellar envelopes. WA2014 stands for Wampfler et al. (2014), while TW stands for this work.

2.4.3 Protostellar envelopes

To date there has been only one published paper regarding isotopic ratios of nitrogen in the envelopes of protostars, Wampfler et al. (2014). The authors measured the nitrogen isotopic ratio through the double isotopic method (Figure 2.5). Their measurements are based on APEX observations of these protostars. The large beam of APEX at the observed frequencies (24" at 259 GHz and 18" at 345 GHz) suggest that these measurements sample both the protostar and its cold envelope. The weighted average of these measurements give a weighted average $^{14}\text{N}/^{15}\text{N} = 227 \pm 14$. We have obtained a direct measurement of the nitrogen isotopic ratio in the cold envelope of IRAS 03282 + 3035, $\text{NH}_2\text{D}/^{15}\text{NH}_2\text{D} = 250 \pm 50$. This measurement was obtained with the $1_{1,1} \rightarrow 1_{1,0}$ transition of these species.

2.4.4 Protoplanetary disks

In protoplanetary disks isotopic measurements are very difficult due to the minute size of disks (diameters of the order of a few arc seconds). Such measurements became possible with the advent of the Atacama Large Millimetre Array, due to its large collecting area. With ALMA the nitrogen isotopic ratio in HCN has been measured in 5 disks in the Solar neighbourhood through the double isotopologue method, assuming $\text{HCN}/\text{H}^{13}\text{CN} = 70$, and found to be quite low, $^{14}\text{N}/^{15}\text{N} = 111 \pm 19$ (Guzmán et al., 2015; Guzmán et al., 2017; Hily-Blant et al., 2017). The only direct measurement of the isotopic ratio of Nitrogen in disks is $\text{CN}/\text{C}^{15}\text{N}$ in the disk of TW Hya,

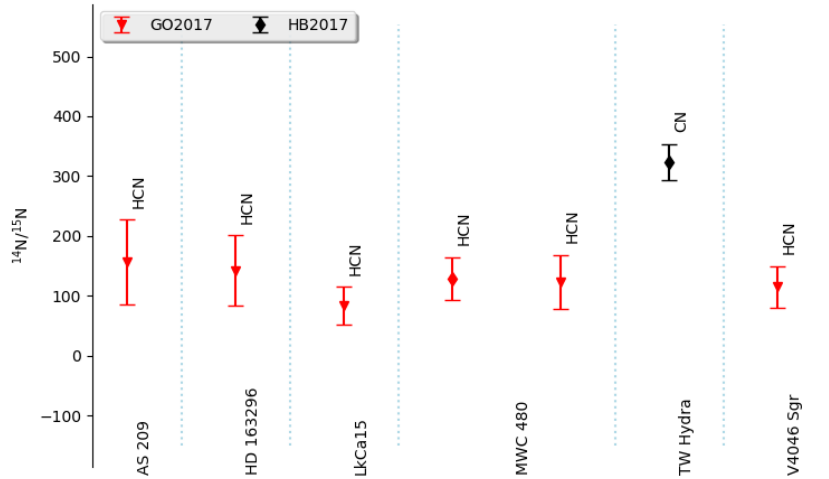


Figure 2.6 – Nitrogen isotopic ratio measured in the nearby protoplanetary disks. Black markers stand for direct measurements, while red markers stand for double isotopologue measurements. Different symbols stand for different papers: GO2017 refers to Guzmán et al. (2017) and HB2017 refers to Hily-Blant et al. (2017).

$^{14}\text{N}/^{15}\text{N} = 323 \pm 30$ (Hily-Blant et al., 2017). All these measurements can be seen in Figure 2.6. This acute difference between the HCN and CN measurements points to the presence of two gaseous reservoirs of nitrogen in protoplanetary disks, one with an isotopic ratio that is one third of the other.

2.4.5 The big picture

With all this measurements there a big picture is emerging. In this big picture we see two reservoirs of nitrogen in protoplanetary disk and two main reservoirs also in the Solar system (Figure 2.7). The isotopic ratios of these reservoirs are not the same in both instances but the ratios between the reservoirs is the same, which is consistent with models of the chemical evolution of the galaxy (Romano and Matteucci, 2003). The question now is to identify how and when these two reservoirs get separated. To do so we need a reliable way of measuring $^{14}\text{N}/^{15}\text{N}$ in the dense ISM, this requires advancements in radiative transfer modelling and has been tackled in this thesis with the direct measurement of the HCN/ HC^{15}N ratio in L1498 (Section 4.2) through the aid of a better understand of the spectroscopy of HCN (Chapter 4) and developments in radiative transfer modelling (Section 3.3.1).

A point where there is little knowledge of nitrogen isotopic ratios is in the vicinity of protostars, with only one work published so far (Wampfler et al., 2014). These measurements have been very diffi-

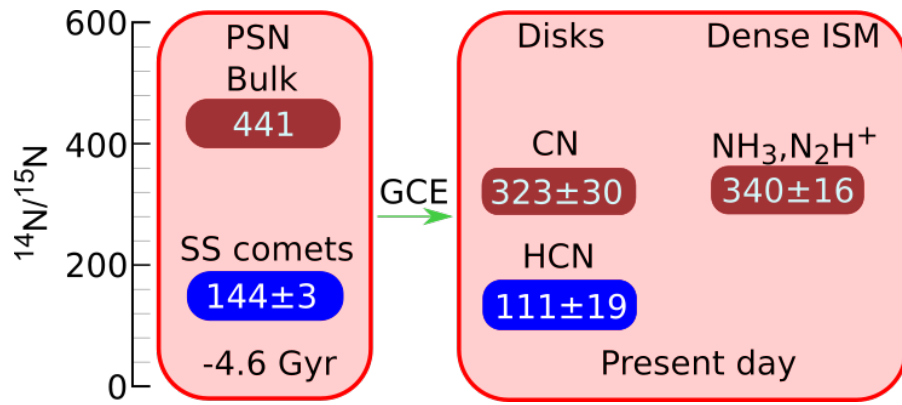


Figure 2.7 – The big picture of the nitrogen isotopic ratio. In the Solar system and in protoplanetary disks two reservoirs have been identified. The difference in isotopic ratios between these two sets of reservoirs are consistent with the evolution of the nitrogen isotopic ratio with time. The remaining question is where and when does the fractionation of the minor reservoir happens.

cult so far, but progress will probably be made with the aid of the ALMA PILS survey (Jørgensen et al., 2016). This unbiased spectral survey will probably provide a few $^{14}\text{N}/^{15}\text{N}$ measurements. In this thesis we attack this front by trying to measure $^{14}\text{N}/^{15}\text{N}$ in the sublimated ices around protostars (Section 6). The $^{14}\text{N}/^{15}\text{N}$ ratio has never been measured in ices, as infrared spectroscopy is not capable of distinguishing isotopologues due to the very broad features seen in absorption, even though the James Webb Space Telescope may be able to change this picture (Boogert, Gerakines, and Whittet, 2015). Ices are very relevant for the measurements of the nitrogen isotopic ratio as isotopic exchanges are known to happen in ices (Faure et al., 2015) and they are also the source of the gaseous material in cometary comae.

This thesis also contributed to the measurement of $^{14}\text{N}/^{15}\text{N}$ in the protoplanetary disks around MWC 480 and TW Hydra (Section 5.2), thus helping in the identification of the two reservoirs of nitrogen in protoplanetary disks.

One of the main objectives of this thesis is to comprehend the rotational emission of HCN in prestellar cores in order to measure its abundance directly without relying on the abundance of any of its isotopologues. To achieve this objective several scientific numerical tools were written.

The first of these pieces is `NSLAB` (Section 3.1). `NSLAB` is a simple code aimed at computing emergent line profiles resulting from the combination of an arbitrary number of homogeneous plane-parallel slabs. `NSLAB` was useful to understand the hyperfine anomalies that manifest themselves in HCN rotational transitions, described in more detail in Chapter 4.

The second piece is called `ALICO` (Section 3.2). `ALICO` is the main machinery behind the complex radiative transfer modelling done in this thesis. Simply put, `ALICO` is a set of wrapper routines around the `1DART` code (Daniel and Cernicharo, 2008) that allows large grids to be executed, potentially in a parallelised fashion. The final piece of software developed during this thesis is called the `MCMC TOOLKIT` (Section 3.3). This toolkit was designed as a way of further simplifying the application of Monte Carlo Markov Chain techniques to astrophysical problems. The application of the `MCMC TOOLKIT` coupled with `ALICO` (Section 3.3.1) is what ultimately allowed us to directly measure the abundance of HCN in L1498 and consequently derive precise isotopic ratios for HCN in L1498 (Section 4.2).

3.1 `NSLAB`

`NSLAB` is a versatile and simple implementation of plane parallel 1 dimensional radiative transfer. The main purpose of `NSLAB` is to build spectra from homogeneous slabs. This endeavour was inspired by earlier works (de Vries and Myers, 2005) demonstrating that simple plane-parallel radiative transfer is able to reproduce multiple characteristics of spectral lines observed in collapsing cores. However, `NSLAB` generalises the 2 slab toy model of de Vries and Myers (2005) to an arbitrary number of slabs. In `NSLAB` each spectral line has 4 parameters: Excitation temperature T_{ex} , line centre opacity τ , central velocity V_0 and a full width at half maximum (FWHM) ΔV . Multiple spectral lines can be computed for each slab provided all slabs have the same number of spectral lines. Light is propagated from a background, usually assumed to be the Cosmic Microwave Background

(CMB), towards the observer. The spectrum, I_ν at slab k is calculated as:

$$I_{\nu,k} = \sum_i^N [J_\nu(T_{\text{ex},i})(1 - e^{-\tau_{\nu,i}})] + I_{\nu,k-1} e^{-\sum_i^N \tau_{\nu,i}} \quad (3.1)$$

where $T_{\text{ex},i}$ stands for the excitation temperature of line i in Kelvin, $\tau_{\nu,i}$ stands for the velocity dependent opacity of line i , and \sum_i^N is the summation over all the N spectral lines. The velocity dependent opacity, τ_ν , is calculated as:

$$\tau_\nu = \tau e^{-\frac{(V-V_0)^2}{2\sigma_V^2}} \quad (3.2)$$

with V being a point along the velocity axis of the spectrum, V_0 the line centre in km/s, and σ_V the velocity dispersion of the line in km/s computed from ΔV as $\sigma_V = \frac{\Delta V}{2\sqrt{2\ln(2)}}$. The remaining term in eq. 3.1 $J_\nu(T_{\text{ex},i})$ stands for:

$$J_\nu(T_{\text{ex},i}) = \frac{h\nu}{k_b} \frac{1}{e^{\frac{h\nu}{k_b T_{\text{ex},i}}} - 1}, \quad (3.3)$$

where ν is the line frequency in Hz, h is the Planck constant and k_b is the Boltzmann constant.

3.1.1 Implementation

N_{SLAB} is implemented as a python executable that makes use of three Python (*Python Language Reference, version 2.7*) libraries, Numpy (Walt, Colbert, and Varoquaux, 2011), Matplotlib (Hunter, 2007) and argparse. The current implementation of N_{SLAB} can be found in Section A.1.1. It consists of 175 lines of code. Its execution time and memory footprint are dominated by the python overheads when there are a small number of channels and slabs (~68 Mb and 1 millisecond). On larger computations the execution time scales linearly with the number of spectral lines, number of channels and slabs while the memory footprint increases linearly with the number of channels only.

The input to N_{SLAB} is done through a file containing the parameter for the lines that will show up in the final spectra. An example of such an input file can be found in Section A.1.2. The output of N_{SLAB} is a ASCII file containing the spectrum in two columns, the velocity axis in km/s and the brightness temperature in K. An example of an output file can be seen in Section A.1.3.

Complementary functionalities of N_{SLAB} are:

1. Command line help.
2. Choice of spectral axis sampling (initial and final values as well as the spectral resolution).

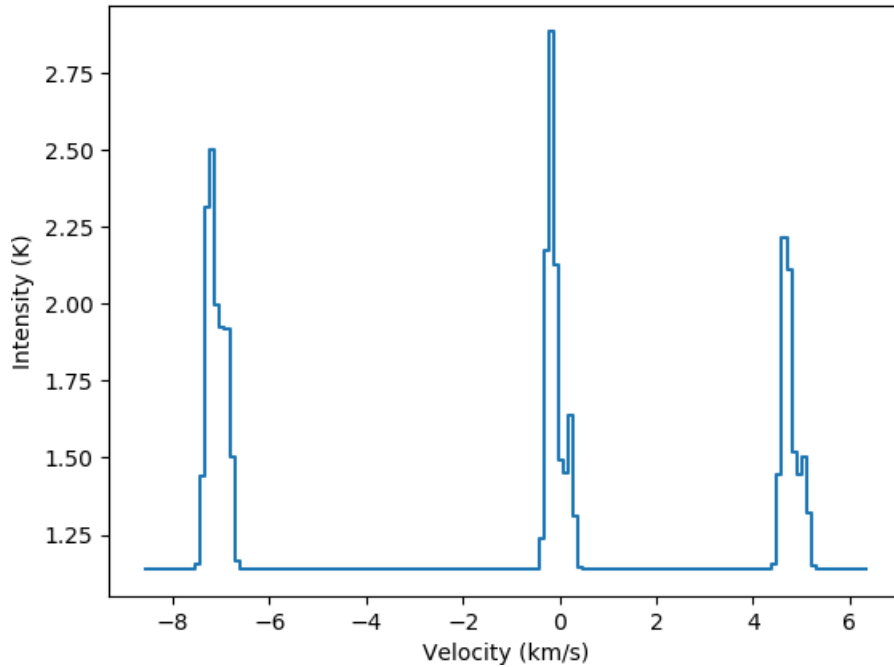


Figure 3.1 – Automatically generated plot by NSLAB from the output file in Section A.1.3 with spectral resolution of 0.1 km/s.

3. The ability to receive a spectrum as background. This can be used as the application of a foreground to a given spectrum.
4. The ability to plot the spectra computed by it.
5. The ability to make plots of the "physical structure" used to make the spectra i.e. T_{ex} , τ , V_0 and ΔV as a function of slab number.

The Command line help can be invoked as shown in Section A.1.4. Figure 3.1 contains the automatically generated plot of the spectrum produced by the usage of the example input file in Section A.1.2. Figure 3.2 contains the automatically generated plot of the input parameters in each line per slab.

3.1.2 Benchmarking

Some tests have been performed to assure that NSLAB propagates the line intensities correctly through the slabs. We first tested whether the intensities are correctly reproduced for different opacities using only 1 slab. The results of this test are displayed in Figure 3.3. Each one of the lines in Figure 3.3 has $T_{\text{ex}} = 3.5$ K and $\Delta V = 0.3$ km/s. The lines are labelled from A to E according to their opacities that go from 10^{-2} to 10^2 in logarithmic steps (see Table 3.1). The comparison with the line intensities expected from eq. 3.1 are displayed in Table 3.1 along with the intensities computed by NSLAB. The line intensities computed by NSLAB are in full accord with what would be expected

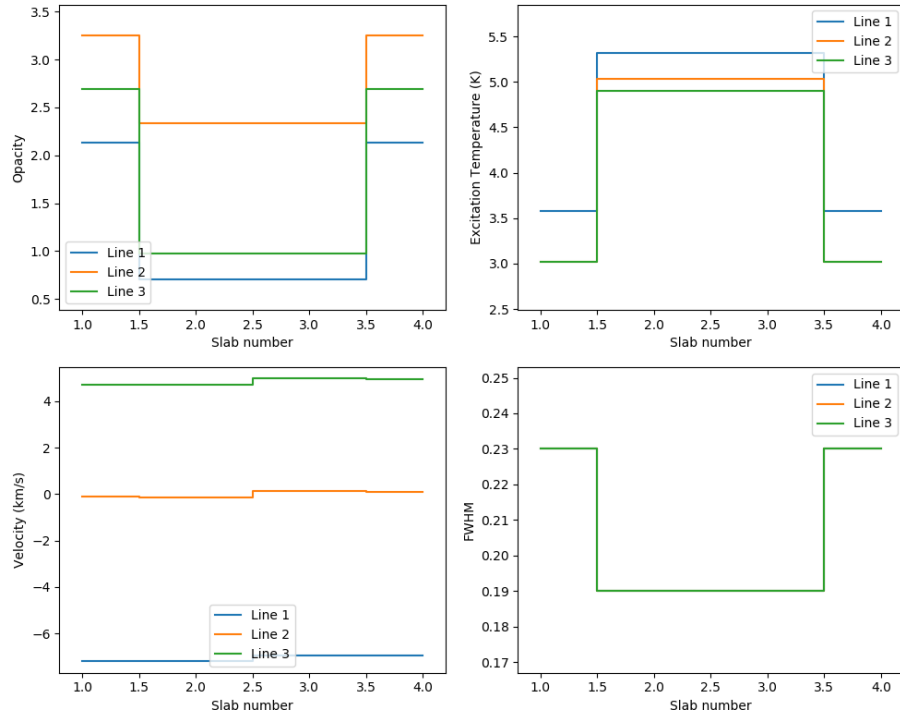


Figure 3.2 – NSLAB parameters as function of the slabs as produced automatically by NSLAB. The input file contains 4 slabs and 3 spectral lines, which are reflected in the x axis and legend respectively.

from eq. 3.1. We also note that the background intensity is well reproduced, along with the line widths. The low opacity lines *A*, *B* and *C* have FWHMs of 0.3 km/s while *D* and *E* have somewhat larger FWHMs due to the saturation caused by their large opacities.

The second test has to do with the propagation of spectral lines through two or more slabs. In this test we have 5 experiments labelled from *F* to *J*. *F* is our single slab reference line, with an excitation temperature of 5 K an opacity of 5, and a FWHM of 0.3 km/s. *G* has the same properties as *F* the difference being that the opacity is divided between two slabs, each with an opacity of 2.5. *H* has two slabs each with the same properties of line *F*. *I* has two slabs with an opacity of 5.0 and a FWHM of 0.3 km/s, the difference between *I* and *H* being the excitation temperatures of each slab. In experiment *I* the first slab has an excitation temperature of 5 K while the second slab has an excitation temperature of 4 K. *J* is just like *I* except that the excitation temperature of the second slab is lower at 2 K. The properties of lines *F* to *J* are listed in Table 3.2 and in Figure 3.4 we can see the results from this second test.

As expected lines *F* and *G* are equal, while line *H* is slightly broader due to saturation. Lines *I* and *J* present self absorption features as would be expected from the fact that the second slab has an excitation temperature below the excitation temperature of the first slab. Line *J*

Table 3.1 – Parameters for the lines in test 1, along with analytically predicted brightness temperatures and NSLAB computed brightness temperatures. Opacities quoted refer to line centre opacities.

Line	T_{ex} (K)	τ	V_0 (km/s)	ΔV (km/s)	Analytical Intensity (K)	Computed Intensity (K)
A	3.5	10^{-2}	-5.0	0.3	1.13	1.13
B	3.5	10^{-1}	-2.5	0.3	1.18	1.18
C	3.5	1	0.0	0.3	1.53	1.53
D	3.5	10	2.5	0.3	1.77	1.77
E	3.5	10^2	5.0	0.3	1.77	1.77

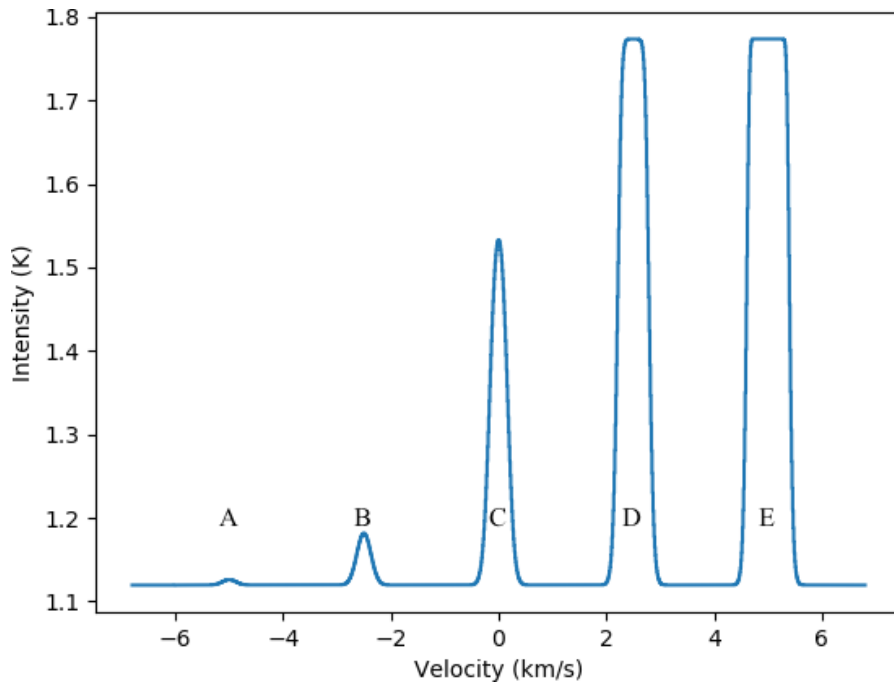


Figure 3.3 – Spectrum computed by NSLAB for a single slab experiment (test 1, see Table 3.1). The labels from A to E denote the different experiments in Table 3.1.

Table 3.2 – Parameters for the lines in test 2. Opacities quoted refer to line centre opacities.

Line	slab 1				slab 2			
	$T_{\text{ex},k=1}$ (K)	$\tau_{k=1}$	$V_{0,k=1}$ (km/s)	$\Delta V_{k=1}$ (km/s)	$T_{\text{ex},k=2}$ (K)	$\tau_{k=2}$	$V_{0,k=2}$ (km/s)	$\Delta V_{k=2}$ (km/s)
<i>F</i>	5.0	5.0	-5.0	0.3				
<i>G</i>	5.0	2.5	-2.5	0.3	5.0	2.5	-2.5	0.3
<i>H</i>	5.0	5.0	0.0	0.3	5.0	5.0	0.0	0.3
<i>I</i>	5.0	5.0	2.5	0.3	4.0	5.0	2.5	0.3
<i>J</i>	5.0	5.0	5.0	0.3	2.0	5.0	5.0	0.3

also presents the interesting aspect of being in absorption against the background, since its excitation temperature of 2 K is smaller than the excitation temperature of the background ($T_{\text{bg}} = 2.73$ K).

The third test consists in testing the propagation of lines through slabs with opposite sign velocities and a gradient in excitation temperature, with the aim of being able to reproduce qualitatively the red-blue asymmetries that are seen in molecular lines. The 5 experiments conducted are labelled from *K* to *O*. Lines *K*, *L* and *M* have the same excitation temperature, 5 K, an opacity of 2, and FWHM, 0.3 km/s in both slabs, but have different line centre velocities. In experiment *K* we have a difference of 0.4 km/s between the two slabs. In experiment *L* this difference is 0.2 km/s and finally in *M* there is no difference in velocity between slabs as it serves as our reference line. In the remaining lines *N* and *O* we have the same properties as in *L* and *K* respectively, except that the second slab has a lower excitation temperature of 3.5 K. The properties of lines *K* to *O* are listed in Table 3.3 and the results of this experiment can be seen in Figure 3.5.

Line *K* presents a double peaked line since the difference in velocity between the slabs, 0.4 km/s is larger than the FWHM of 0.3 km/s. Line *L* on the hand presents the emission of both slabs merged in a single broad line, as would be expected since the velocity difference between both slabs, 0.2 km/s is smaller than the FWHM of the lines ($\Delta V = 0.3$ km/s). In line *M* we recover the expected single peaked Gaussian profile with a FWHM of 0.3 km/s. The remaining lines, *N* and *O* reproduce the so-called red blue asymmetries commonly seen in the interstellar medium emission lines. *N* displays a red shoulder while *O* displays a double peaked profile with the red peak being much less intense than the blue peak.

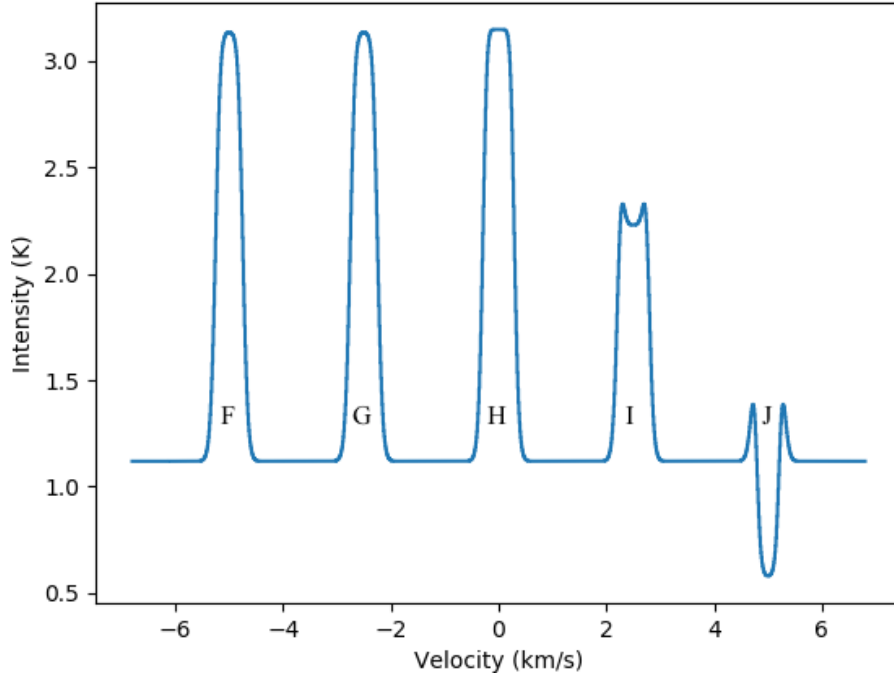


Figure 3.4 – Results of the second benchmarking test of NSLAB, testing the propagation of spectral lines through two slabs. The labels *F* to *J* correspond to the spectral lines described in Table 3.2.

Table 3.3 – Parameters for the lines in test 3. Opacities quoted refer to line centre opacities.

Line	slab 1				slab 2			
	$T_{\text{ex},k=1}$ (K)	$\tau_{k=1}$	$V_{0,k=1}$ (km/s)	$\Delta V_{k=1}$ (km/s)	$T_{\text{ex},k=2}$	$\tau_{k=2}$	$V_{0,k=2}$	$\Delta V_{k=2}$
<i>K</i>	5.0	2.0	-5.2	0.3	5.0	2.0	-4.8	0.3
<i>L</i>	5.0	2.0	-2.6	0.3	5.0	2.0	-2.4	0.3
<i>M</i>	5.0	2.0	0.0	0.3	5.0	2.0	0.0	0.3
<i>N</i>	5.0	2.0	2.4	0.3	3.5	2.0	2.6	0.3
<i>O</i>	5.0	2.0	4.8	0.3	2.5	2.0	5.2	0.3

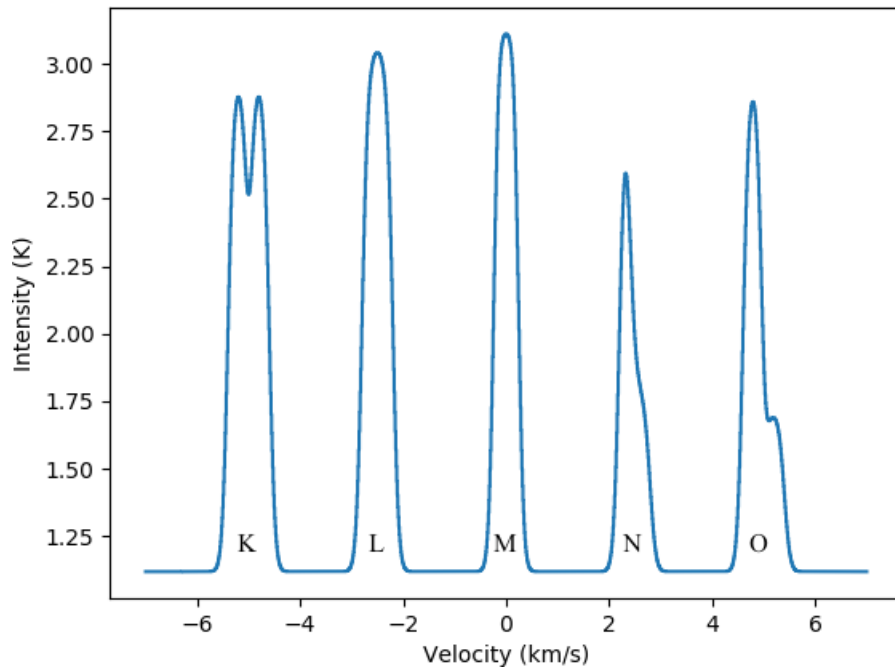


Figure 3.5 – Results of the third benchmarking test of NSLAB, testing the propagation of spectral lines through two slabs with different velocities. The labels K to O correspond to the spectral lines described in Table 3.2.

The tests conducted demonstrate the versatility of NSLAB in computing simple spectra while also demonstrating its numerical accuracy.

3.1.3 Perspectives

Due to its versatility NSLAB can be used in various situations, such as simple radiative transfer or as complement to more complex radiative codes (such as applying a plane parallel foreground to the output of a complex radiative transfer code). Below we give two examples of where NSLAB has been coupled with other codes to produce powerful tools:

- NSLAB + RADEX (van der Tak et al., 2007) - a plane parallel radiative transfer code that does not assume local thermodynamical equilibrium (LTE) and works under the Large Velocity Gradient (LVG) approximation and produces lines profiles.
- (NSLAB + RADEX) MCMC - A way of solving simple non-LTE radiative transfer problems under the 4 slabs approximation (see Section 4.1.3.1) using Markov Chain Monte Carlo sampling.

A future project involving NSLAB is:

- Interactive NSLAB - A graphical interface for NSLAB enabling real-time evaluation of spectra produced by NSLAB.

3.2 ACCELERATED LAMBDA ITERATION CODE, ALICO

The Accelerated Lambda Iteration COde (ALICO) is a set of wrapper routines to control the 1-D radiative transfer code 1DART (Daniel and Cernicharo, 2008). 1DART has been extensively tested (Daniel and Cernicharo, 2008) and has already demonstrated its ability to reproduce the emission of prestellar cores (e.g. Daniel et al., 2013). 1DART is written in FORTRAN90 using the accelerated lambda iteration scheme (Olson, Auer, and Buchler, 1986) to deal with the radiative transfer problem. The development of 1DART is still under way and recently a bug related to the computation of line widths has been fixed. One essential functionality of 1DART for this thesis is its capability of dealing with the overlap of lines of a molecule such as in the case of several molecules with hyperfine structure (HCN, N_2H^+ , HNC, etc). The hyperfine treatment follows Rybicki and Hummer (1992). 1DART is capable of modelling diverse scenarios, based on a radial 1-D model that is given for the code as an input. This model is a 1-D description of the physical structure to be modelled, the following parameters must be given as a function of unitary radius:

1. H_2 number density in cm^{-3} .
2. Kinetic temperature of the gas in Kelvin.
3. Non thermal velocity dispersion of the gas in km/s
4. Molecular abundance relative to H_2 .
5. and optionally the velocity field in km/s.

This physical model may also include a grey body emitting source at $r = 0$, as would be the case for a protostellar envelope.

The physical model along with computational parameters are written in a complex and large input file, an example of such a input file can be found in Section A.2.1.1. The physical model is then used to compute the populations of the molecular levels, along with the excitation temperature and opacities of the radiative transitions for the molecule in question. With these quantities computed for each layer of the model the next step is to compute the emergent spectra through a ray tracing algorithm that includes the convolution with a Gaussian telescope beam of arbitrary size and beam efficiency at different offsets from the centre of the model. Ray tracing is a technique for generating an image by tracing the path of light through the line of sight for various impact parameters. The beam convolution is done by making an weighted average of different impact parameters and is controlled by a separate input file for which an example can be seen in Section A.2.1.2.

3.2.1 Model cloud

Due to the complexity of the inputs needed to operate 1DART and the rigidity of the input files dictated by the complexity of parsing in FORTRAN90 I developed a Python wrapper to operate 1DART for the range of physical conditions seen in prestellar cores. Model cloud does this by setting most numerical parameters of 1DART to default values adequate to the modelling of prestellar cores. The input process is simplified by using a smaller input file that allows for larger flexibility including arbitrary length comments in between parameters. In this input file we can input the physical conditions in a simplified manner:

1. The H₂ density profile is computed from a simple density profile:

$$n(r) = \frac{n_0}{1 + \left(\frac{r}{r_0}\right)^\alpha} + n_{\text{ext}}$$

Therefore the input of the density physical model is simplified to simply to the choice of: n_0 the density at the centre of the model in cm⁻³; r_0 the full width at half maximum of the density profile in unitary radius units; α the exponent of the density profile decay and n_{ext} the number density at $r = \infty$ in cm⁻³. This density profile is based on the number density profile for prestellar cores presented in Tafalla et al. (2004).

2. The kinetic temperature of the gas and the abundance of a molecule can be entered as a step function of radius enabling various possible profiles for these two quantities.
3. The non thermal dispersion of velocities can be given in three ways, as a step function, as a power law and as a smooth arc tangent profile. These three mechanisms enable a very versatile way of describing the non thermal dispersion of velocities.
4. The velocity field of the cloud can be given in 3 ways: as a truncated power law with inner and outer values, as a wedge profile and as a Gaussian profile.
5. An abundance multiplier that can be used to introduce an isotopic ratio.

An example of a Model cloud input file can be found in Section [A.2.2](#).

Apart from the main functionalities that are accessed through the input file some other options are available through the command line interface. These other options are presented in Section [A.2.2.1](#).

The options worth noting are the benchmarking option and the no overlap option. The benchmarking option is used to automatically produce plots of the opacity and excitation temperatures of the transitions included in the calculation along with the populations of all energy levels included in the calculation. The no overlap option permits to speed up calculations in the case when line overlaps are not

important, but also allows us to check whether the line overlap is important for a given model.

3.2.2 ALICO gridding software

With the necessity of running several ALICO models to try and fit the observed spectra came the necessity of a gridding software for ALICO. Such a software was created and implemented in Python 2.7. It consists of a wrapper for `Model cloud` that builds parameter files for `Model cloud` and then calls it multiple times to run the different models. To take advantage of the multiple cores in modern computers this software takes advantage of the multiprocessing module of Python. This module enables the parallelisation of the `Model cloud` calls allowing for the execution of several models at once, being limited by the number of cores available in the host machine, the default number of threads being the number of cores in the machine minus 1.

The input for the gridding software is given in three input files:

1. Source file, a file containing information about the modelled source: density parameters, distance, temperature, size, etc. An example file can be found in Section [A.2.3.1](#).
2. Molecular file, a file containing information about the molecule that will be used by the calculation, including telescope pointings, rotational levels to be included, lines for which to compute the emerging spectra, etc. An example file can be found in Section [A.2.3.2](#).
3. Grid file, a file containing the parameters over which a grid can be made: Abundance, non thermal dispersion profile, Velocity profile and abundance ratio. In this file the parameters over which there will be a grid are listed, An example file can be found in Section [A.2.3.3](#).

As with `Model cloud` A few options are available from the command line interface as is shown in Section [A.2.3.4](#). Most options are related to the control of the execution of the grid, such as the number of cores used by the grid. The benchmarking option performs the same plots as in `Model cloud` and the provided and override options relate to the case in which we have a physical profile to be used, supplanting most options in the source file along with most options in the grid file.

3.2.3 The ALICO model and observation classes

To facilitate the utilisation of ALICO models inside more complex codes, for example Markov Chain Monte Carlo (MCMC) minimisations, a Python class wrapping up `Model cloud` has been imple-

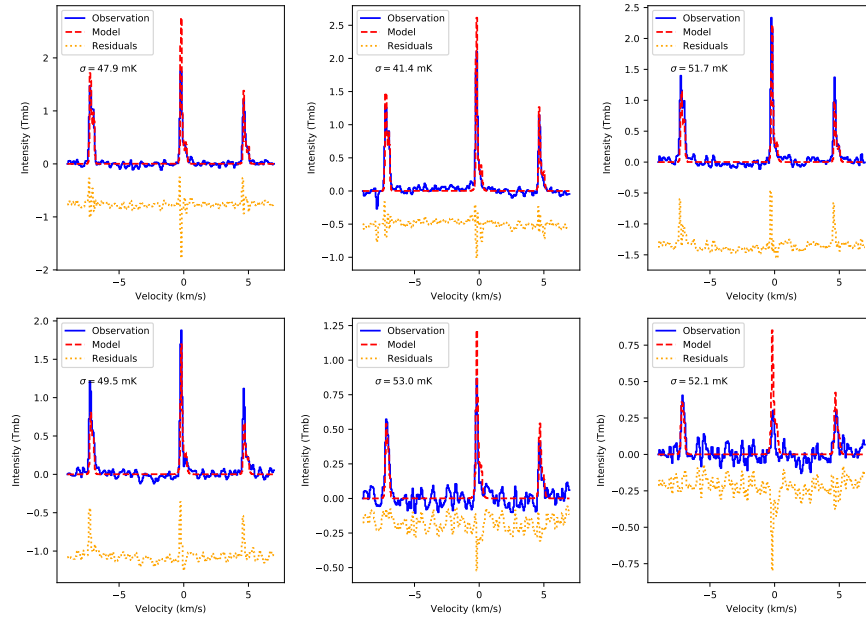


Figure 3.6 – HCN $J = 1 \rightarrow 0$ spectra produced by the model class along with HCN $J = 1 \rightarrow 0$ observations as plotted by the function `plot_with_obs` from the model class (see Section A.2.4.1).

mented. This class wraps up most functionalities of `Model` cloud in an easy to use Python code and is called `model`. It depends on two smaller Python classes that deal with molecular spectroscopic information, which are used to simplify the task of inputting spectroscopic information. Another class of importance is called `observation`, which is used to store spectroscopy observations to be compared to the ALICO models. These two classes work in tandem to make it possible to produce easy to write code with all the desired functionality: running models, comparing models to observations, making plots of models, making plots of the models with the observations, making plots of the observations. In Section A.2.4.3 we see a snippet of code in which all these classes are used to compute a model and then plot it with the observations. Figure 3.6 displays the plot of the HCN $J = 1 \rightarrow 0$ transition produced by the code in Section A.2.4.3. The complete codes for classes `model` and `observation` can be found in Sections A.2.4.1 and A.2.4.2 respectively.

3.2.4 Perspectives

The perspectives for ALICO are:

- Further simplification of the input of the parameters for `Model` cloud which are to be propagated through the dependent software.

- Make the code as portable possible (minimal reconfiguration upon deployment on a new machine).
- Make the code easy to maintain by subdividing it further into modules.
- Optimise 1DART to reduce the overall run time.
- Change the way 1DART deals with collisional coefficients and spectroscopy to allow the usage of LAMDA-type spectroscopic files as input for collisional coefficients.

3.3 MCMC TOOLKIT

The MCMC TOOLKIT is a small Python module intended to wrap the Emcee and Corner Python modules (Foreman-Mackey et al., 2013; Foreman-Mackey, 2016, respectively) in a simple interface while also providing coherent input and output options. Emcee is an MIT licensed pure-Python implementation of Goodman & Weare’s Affine Invariant Markov Chain Monte Carlo (MCMC) Ensemble sampler (Goodman and Weare, 2010). While Corner is a wrapper onto Matplotlib to produce cross-histograms of the space parameter explored by an emcee run. The main objectives of the MCMC TOOLKIT are: easy to use functions for controlling the input to emcee, functions that control the execution of an emcee run providing user friendly conveniences such as progress bars and to produce user friendly results at the end of the process. The present version of the MCMC TOOLKIT can be found in Section A.3.1.

The first objective is already accomplished and easy input is achieved by the functions `read_input_sel` and `read_legend`. The first function, `read_input_sel`, reads an input file and returns 6 arrays along with the number of dimensions of the parameter space. These arrays consist in the initial guesses, priors (inferior and superior), the input parameters that are fixed through the run and two array masks to reconstruct which parameters are given in log form and which are the parameters that are fixed and which are to be fitted. The other function, `read_legend`, reads the input file and returns labels for the parameters that are to be fitted in the run. At first it might look that such an input file would be fairly complex to write, but thanks to Python parsing capabilities is fairly straight forward to write one as can be seen in Section A.3.2. The remaining function related to input is `completepset` which is used to reconstruct the complete set of parameters for the model being run inside the MCMC run.

The second objective of the toolkit is to develop functions that wrap the execution of emcee providing plug and play solutions for parallel execution, user conveniences such as progress bars, and saving the status of the Markov chain in each step, for later reuse in the case of interrupted execution. As of now part of this development is accomplished as the ability of saving a Markov Chain and the ability to

re-initiate the code from it have already been implemented but other functionalities such as controlling the execution of emcee have been implemented in a case by case basis, so no functions controlling the execution of emcee readily available. Examples of parallel execution of emcee are described in Section 3.3.1.

The final objective, provide comprehensible results from a MCMC run, is already accomplished as the functions `plot_walkers` and `run_corner` provide a wealth of plots and also files containing the results with 1σ error bars from the analysis of the Markov chains.

In Figure 3.7 we see an example of a plot of the Markov chains produced by a simple MCMC run trying to fit the parameters of a Gaussian to a mock up observation. This mock up observation was produced by generating a Gaussian curve with peak intensity $A = 50$, centre $X_0 = -4$ and dispersion $\sigma = 15$ and then adding random noise with an RMS of 2.5. Figure 3.8 displays the cross histograms from the fit as plotted by corner through the use of the function `run_corner` from the MCMC TOOLKIT. Figure 3.9 displays the best fit for the example described above along with the mock up observation and the results extracted from the corner plot are listed below as they are output by `run_corner`.

```
#Best fit parameters and their uncertainties for the run:
  example_run
#Burn in: 200
$A$ = 49.8980 -2.3616 +2.4058
$x_0$ = -3.9826 -0.7818 +0.8338
$\sigma$ = 15.0266 -0.8144 +0.8496
```

This MCMC run lasts 23 seconds when using 200 walkers and 400 steps. This kind of simple example is run on a single thread as the overheads of calling Python for multiple threads slow down the execution of the code. In models that take more than a few milliseconds to run it is worth while to invoke multiple threads as the Python overheads become less important.

The MCMC TOOLKIT has been successfully coupled with RADEX to produce RADEX+MCMC. We have used RADEX+MCMC to determine the isotopic ratio of HC_3N in L1544 under the escape probability formalism. An article on this result will be published soon. The current draft can be found in Appendix D.

3.3.1 ALICO MCMC

The main application for which the MCMC TOOLKIT was developed was to enable the usage of Monte Carlo Markov Chain techniques with ALICO. This is an advancement in radiative transfer modelling for our group as it enables the minimisation of the parameters in radiative transfer models in a unbiased way along with having quan-

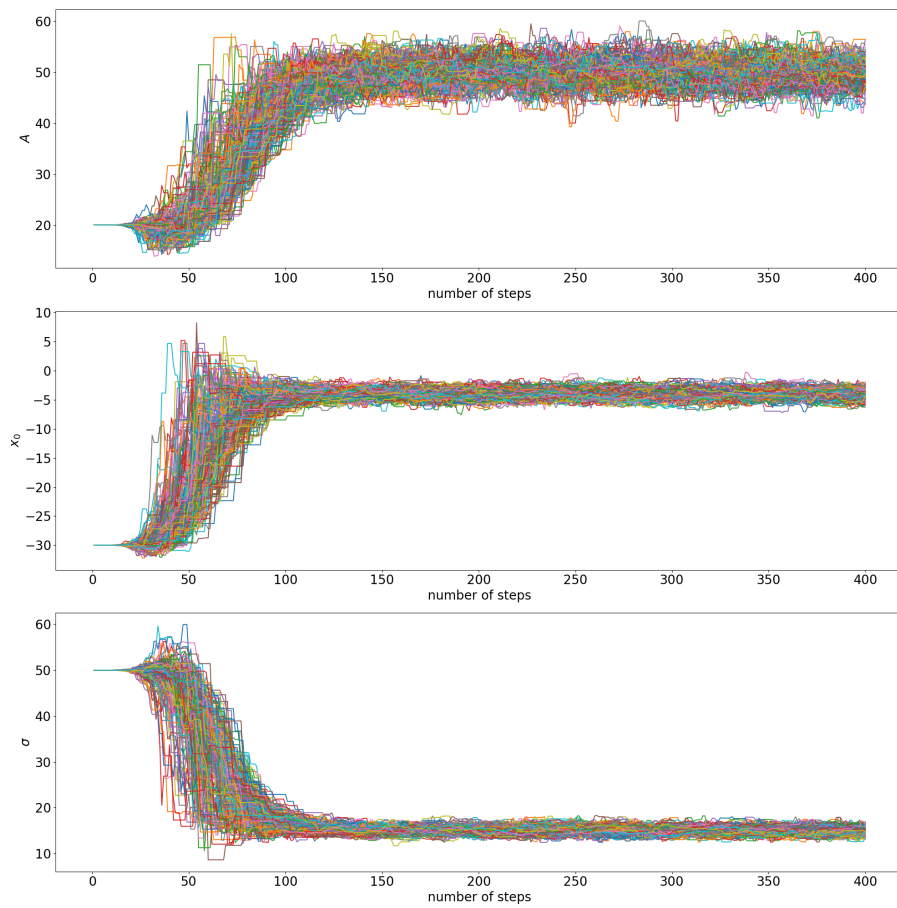


Figure 3.7 – Evolution of the walkers in a Markov chain as a function of the steps taken. For the three parameters displayed it is possible to see that the MCMC walkers rapidly converge to the correct values for the parameters (within ~ 100 steps).

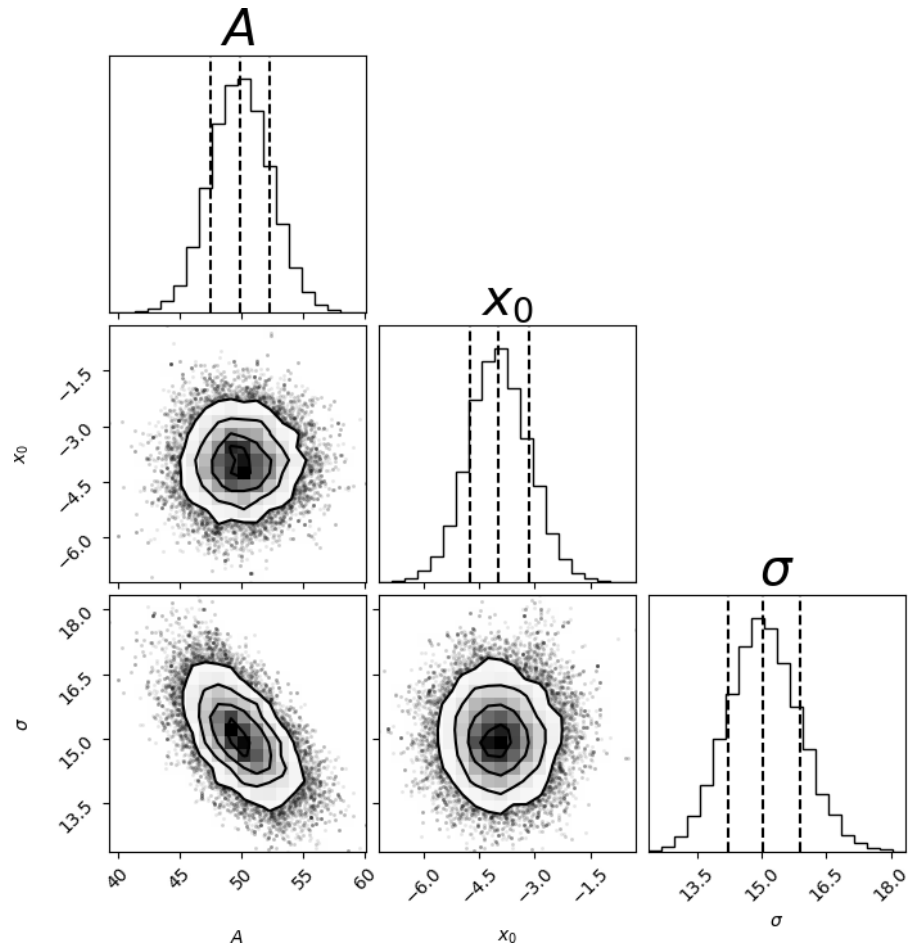


Figure 3.8 – Cross histograms of the parameters for a model Gaussian. A is the peak intensity, X_0 is the Gaussian centre and σ is its dispersion. From this plot we can learn which parameters are not correlated with each other as is the case between the centre of the Gaussian and its amplitude (the cross histogram is circular) and which parameters do present a correlation with each other like the amplitude of the Gaussian and its dispersion (The cross histogram is elliptical and inclined). The dashed vertical lines in the histograms indicate the 0.16, 0.5 and 0.86 fractional quantiles and are used to automatically compute the best fit parameters and their uncertainties.

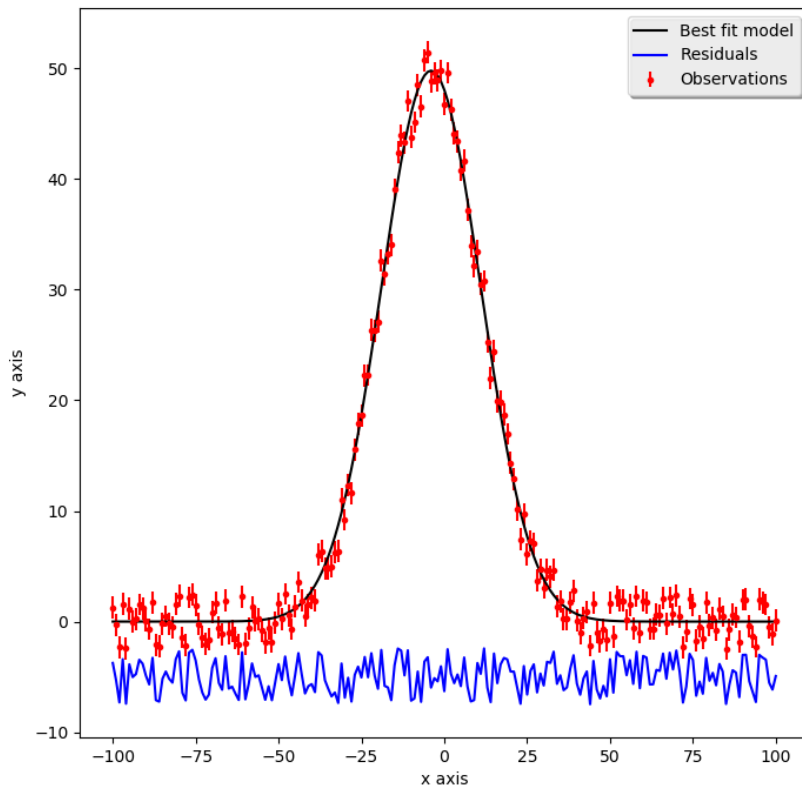


Figure 3.9 – Results of the MCMC fit to a Gaussian with a RMS noise of 2.5. The fit clearly converges and presents a good agreement with the mock up observations.

Table 3.4 – Physical parameters for the time benchmarking of ALICO/iDART.

Parameter	Value
Density	10^5 cm^{-3}
Temperature	10 K
Non thermal dispersion	0.1 km/s
Collapse velocity	0.0 km/s
Radius	10^{18} cm
Number of model layers	10
Number of rotational levels for each molecule	4

tified uncertainties from one MCMC run. The uncertainties derived from a MCMC run are better determined than in χ^2 analysis as they do not depend on the absolute values of the computed χ^2 , since they depend on the likelihood of the observation given a range of models. The main challenge encountered when implementing ALICO MCMC was the computational time that ALICO models require. This computational time depends on the opacity of the transitions in the model and also to the complexity of the spectroscopy of the molecule. For simple linear molecules without hyperfine structure ALICO converges very quickly even for very high opacities, while for molecules with complex spectroscopy the converging time depends on the opacity as it will determine the number of iterations to converge given the effect that transitions may have on each other (Overlaps, collisional and radiative transitions). To prove these statements we have run a set of ALICO models for 4 different molecules with increasing opacities. The 4 molecules chosen are: CO a simple linear molecule with no hyperfine splitting of its rotational spectra; HCN also a simple linear molecule but that present hyperfine splitting in the rotational transitions due to the N atom; N_2H^+ still a linear a molecule but that presents a very complex hyperfine splitting of its rotational transitions due to the presence of 2 N atoms and lastly NH_2D an asymmetrical molecule, the most complex molecule in the test. The physical model used in this test is described in Table 3.4 and the running time as a function of molecular abundance can be seen in Figure 3.10. As expected the CO models are the fastest to run, with each model taking less than a second run. The HCN models on the other hand increase in time with increasing abundance but not as fast as N_2H^+ which is expected as the hyperfine structure of N_2H^+ is more complicated than that of HCN. The models that take the longest to run are the NH_2D ones, which due to its complicated spectroscopy take much longer to run than any of the other molecules.

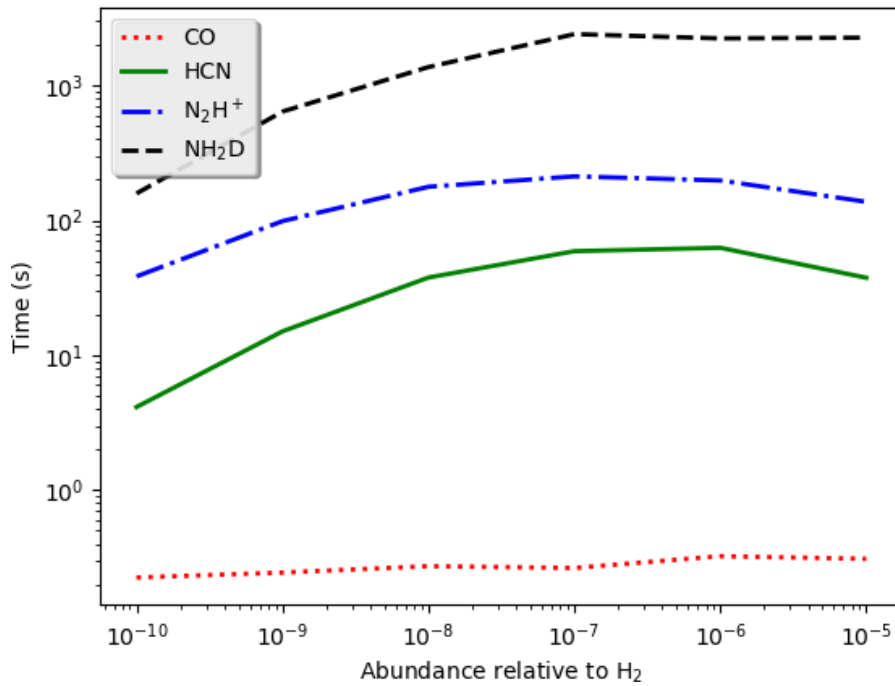


Figure 3.10 – Time for ALICO execution as a function of molecular abundance for CO, HCN, N₂H⁺ and NH₂D.

Due to the long run times of ALICO, the MCMC code had to be parallelised. The first form of parallelisation implementation was with the Python multiprocessing module. This module enables the usage of all processors in a single computer to run a code. In the case of ALICO MCMC this made possible the usage of the code in the IPAG servers (number of threads ~ 40). In this case an ALICO MCMC run would still take upwards of 20 days to convert in our case of interest, modelling the emission of HCN and its isotopologues in L1498. To speedup the code execution time and also be able to add more walkers to the MCMC run the code was then reimplemented with the MPI4PY Python module, which enables the usage of Python codes under the Open MPI (Message Passing Interface) protocol. Open MPI enables a code to be run in heterogeneous clusters of machines thus making the code able to be run in the clusters of CIMENT the high performance computing facility of Université Grenoble Alpes. Access to the CIMENT clusters was granted to us under the ANR project HYDRIDES (P.I. Alexandre Faure). The reimplementing of the code in MPI required some study of the MPI capabilities of the CIMENT clusters, and in the end the best cost benefit compromise was encountered by running the code using 96 processors on the FROGGY machine. FROGGY is a cluster containing 3184 CPUs divided into 190 nodes containing 2 Intel Sandy Bridge EP E5-2670, containing 8 cores. Each node has 64Gb of RAM and is connected to the remaining nodes through an Infiniband FDR network. A typical run takes

Table 3.5 – Summary of the radiative transfer codes developed in this thesis along typical execution times. The execution times have been measured in a 2.2 GHz intel i7 processor, with either 1 or 8 cores, except for ALICO/MCMC which had its execution time measured in FROGGY.

Tool	Geometry	Parallelised	Execution time (s)
N _{SLAB}	Plane-parallel (PP)	No	10^{-3}
RADEX+MCMC	Spherical or PP	Yes	5×10^2
RADEX+N _{SLAB} +MCMC	Plane-parallel	Yes	3×10^3
ALICO	1D spherical	No	$10^0-2 \times 10^3$
ALICO/MCMC	1D spherical	Yes	9×10^5

between one week and 10 days to be completed on FROGGY. Due to scheduling limitations, a FROGGY run has to be broken in execution blacks that last 85 hours, meaning that ALICO/MCMC has to be relaunched every 3 and a half days.

3.3.2 Perspectives

The future of the MCMC TOOLKIT includes further simplifications for the user. The main goal is to require very little input from the user, such as simply designing the function to compute the likelihood of the observations given the model. The ALICO/MCMC project is also under continuous development. The main perspectives for it are: Generalisation of the code, so that it can be used in general 1D radiative transfer models of molecular emission, and generalisation to 2D geometries.

3.4 SUMMARY OF RADIATIVE TRANSFER TOOLS

Several radiative transfer tools have been developed in this thesis. Table 3.5 summarises this tools.

In our quest to obtain direct measurements of the isotopic ratio of nitrogen we came to the conclusion that we needed a reliable measurement of the isotopic ratio of a nitrile in the dense ISM. Previous measurements by Daniel et al. (2013) suggested a tantalising low value ($^{14}\text{N}/^{15}\text{N} \approx 165$), but went shy from taking any conclusions as they had no spatial information on the HCN emission to try to disentangle the optical depth effects. Nitriles are an important chemical group as they are direct descendants of atomic nitrogen (Hily-Blant et al., 2010). The best possible target molecule for such an endeavour is HCN, an abundant linear molecule that presents a resolved hyperfine structure in its lower rotational transitions ($J_{upper} \leq 4$). Measuring the abundance of HCN would also help in other aspects of nitrogen chemistry in the ISM, such as understanding which is the dominant reservoir of nitrogen in the ISM N or N_2 . One such aspect is the HCN/HNC ratio, which is predicted to be of the order of unit by chemical models (Herbst, Terzieva, and Talbi, 2000), and therefore can serve as a useful probe to test the accuracy of chemical networks.

Due to the high opacity of HCN rotational lines (even with hyperfine splitting) the most frequently method to determine HCN column densities is through the rare isotopologue method (Section 2.3.2). The caveat here is that it is not guaranteed that the $^{12}\text{C}/^{13}\text{C}$ ratio in HCN would be the elemental one, with estimates and predictions varying wildly ($^{12}\text{C}/^{13}\text{C}=30-140$ Daniel et al., 2013; Roueff, Loison, and Hickson, 2015). This leads to an uncertainty of a factor of 4 in the determination of HCN column densities derived from the double isotopologue method.

4.1 THE HYPERFINE ANOMALIES OF HCN

To actually accomplish the task of measuring $^{14}\text{N}/^{15}\text{N}$ directly in HCN a complete study of the hyperfine anomalies of the rotational transitions of HCN had to be undertaken. In Section 4.1.1 we start by describing what are the hyperfine anomalies with a focus on the hyperfine spectroscopy of HCN. Section 4.1.2 describes the possible mechanisms behind these anomalies while Section 4.1.3 tests these mechanisms with the aid of a simple toy model. On Section 4.1.3.2 we apply what has been learned on a realistic physical model of L1498 and finally on Section 4.1.4 we present the main conclusions regarding the reproduction of hyperfine anomalies.

4.1.1 What are Hyperfine Anomalies?

The resolved hyperfine structure of HCN is of great help as each hyperfine line has a different opacity enabling hence probing different depths in a dense cloud within a single rotational transition. But all is not perfect as this hyperfine structure usually presents anomalous line ratios (e.g. Walmsley et al., 1982; Sohn et al., 2007). The existence of this anomalous line ratios was noticed for the first time by Kwan and Scoville (1974) and have since then been called hyperfine anomalies. To better understand these hyperfine anomalies a good grasp of the rotational spectroscopy of HCN is needed.

So what are these hyperfine anomalies? Hyperfine anomalies consist in the hyperfine components of a transition having hyperfine ratios that are not compatible with the hypothesis that they share the same excitation temperature. Observed HCN spectra frequently present hyperfine anomalies on two rotational transitions, $J = 1 \rightarrow 0$ and $J = 3 \rightarrow 2$. The most commonly observed anomaly of the $J = 1 \rightarrow 0$ transition observed in prestellar cores is when we have a so-called hyperfine inversion, where a weak hyperfine component outshines a stronger one (Sohn et al., 2007; Loughnane et al., 2012, see also Table B.1). This type of anomaly is usually observed towards dense cores (Walmsley et al., 1982; Sandell, Hoglund, and Kisliakov, 1983; Cernicharo et al., 1984; Sohn et al., 2007). Another commonly observed hyperfine anomaly is when the ratio between the hyperfine components $F = 1 \rightarrow 1$ and $F = 2 \rightarrow 1$ is smaller than what is expected ($F = 1 \rightarrow 1/F = 2 \rightarrow 1 < 0.6$), and is commonly observed in warm regions such as HII regions (Gottlieb et al., 1975; Guilloteau and Baudry, 1981). In Figure 4.1 we have an example of an anomalous HCN $J = 1 \rightarrow 0$ spectrum together with a H^{13}CN $J = 1 \rightarrow 0$ spectrum, a proxy for non anomalous HCN $J = 1 \rightarrow 0$ emission. Figure 4.2 displays the variation of the hyperfine ratios of the $J = 1 \rightarrow 0$ over a selected sample of dense cores.

The other commonly observed hyperfine anomaly of HCN is the one seen in the spectra of the $J = 3 \rightarrow 2$ rotational transition (e.g. Loughnane et al., 2012). In this transition there are 4 partially blended hyperfine components while there are two satellites hyperfine components $F = 2 \rightarrow 2$ and $F = 3 \rightarrow 3$ which are not. These two satellite hyperfine components have the same relative intensities, which means that if when they have the same excitation temperature they display the same intensity. What is observed however, is that the $F = 3 \rightarrow 3$ hyperfine component is several times stronger than $F = 2 \rightarrow 2$ hyperfine component. Figure 4.3 displays an example of an observed HCN $J = 3 \rightarrow 2$ spectrum alongside a synthetic HCN $J = 3 \rightarrow 2$ spectrum representing the relative intensities of each hyperfine component.

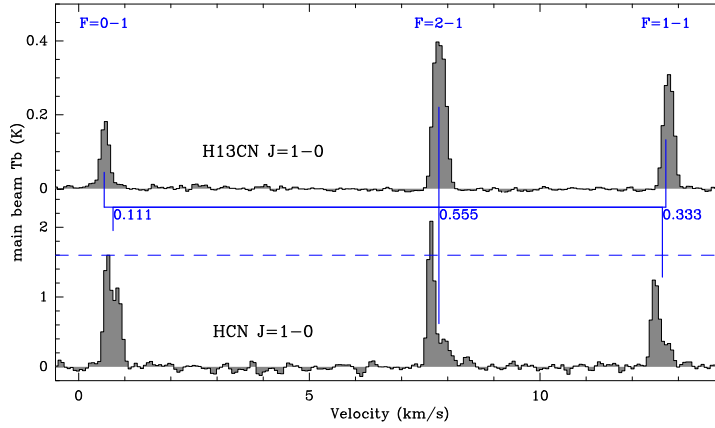


Figure 4.1 – HCN $J = 1 \rightarrow 0$ spectrum presenting hyperfine anomalies (bottom) and $\text{H}^{13}\text{CN } J = 1 \rightarrow 0$ spectrum displaying no hyperfine anomalies (top). Both HCN and H^{13}CN have the same resolved hyperfine structure, therefore the $\text{H}^{13}\text{CN } J = 1 \rightarrow 0$ transition is a proxy for non anomalous HCN $J = 1 \rightarrow 0$. The hyperfine splitting caused by the presence of ^{13}C is not resolved in H^{13}CN . The hyperfine components of the $J = 1 \rightarrow 0$ transition of both HCN and H^{13}CN are labeled with their respective relative intensities. Both spectra were obtained towards the continuum peak of L1498.

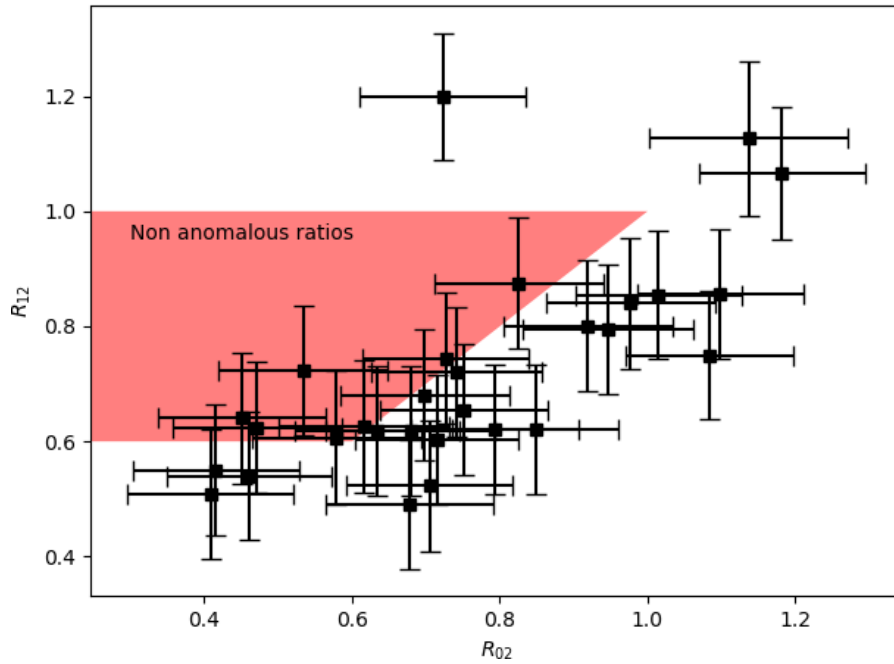


Figure 4.2 – R_{12} vs. R_{02} ($R_{12} = F = 1 \rightarrow 1 / F = 2 \rightarrow 1$, $R_{02} = F = 0 \rightarrow 1 / F = 2 \rightarrow 1$) for several sources in the dense ISM. The red polygon indicates the region where hyperfine ratios are not anomalous. There is only one set of ratios that is completely inconsistent with hyperfine anomalies, that of L234-ES. The hyperfine ratios were extracted from the data in Sohn et al. (2007) and are listed in Table B.1.

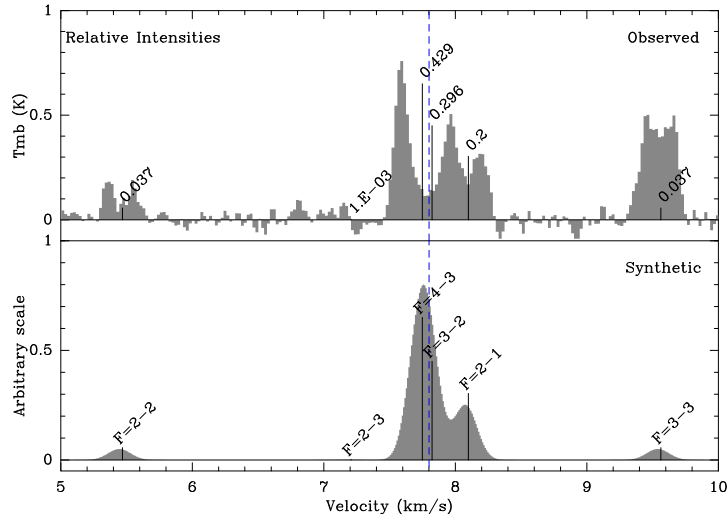


Figure 4.3 – Top panel: Observed HCN $J = 3 \rightarrow 2$ spectrum towards the continuum peak of L1498; Bottom panel: Synthetic HCN $J = 3 \rightarrow 2$ spectrum build by NSLAB (Section 3.1) using the relative intensities of the hyperfine components of the $J = 3 \rightarrow 2$ rotational transition.

4.1.2 Possible mechanisms for the origins of the hyperfine anomalies

To date two mechanisms have been suggested as the cause of these anomalies: overlap of hyperfine components of transitions with $J_{\text{up}} \geq 2$ (Gottlieb et al., 1975; Guilloteau and Baudry, 1981) and self-absorption (e.g. Langer et al., 1978; Walmsley et al., 1982; Cernicharo et al., 1984). Of these two models the only capable of making quantitative predictions was the overlap model. With it Guilloteau and Baudry (1981) and Gonzalez-Alfonso and Cernicharo (1993) were able to constrain the parameter space capable of producing the hyperfine anomalies of the HCN $J = 1 \rightarrow 0$ transition. Even though lacking precise collisional coefficients and accurate physical models Gonzalez-Alfonso and Cernicharo (1993) were able to show that a simplistic 1-D spherical model containing two regions, one of high density and low line width and a foreground with low density but high line width is capable of reproducing the range of observed hyperfine ratios for a series of sources in Taurus.

Despite this early advancement, the problem of the HCN hyperfine anomalies is still not completely solved, despite some renewed interest (Loughnane et al., 2012; Mullins et al., 2016). Loughnane et al. (2012) made a compendium of HCN $J = 1 \rightarrow 0$ and $J = 3 \rightarrow 2$ observations towards star formation regions and argue that the most probable mechanism behind hyperfine anomalies are the overlap between hyperfine components but do not present any quantitative predictions. The second paper, Mullins et al. (2016), uses 3D radiative models to make radiative transfer simulations to reproduce the hy-

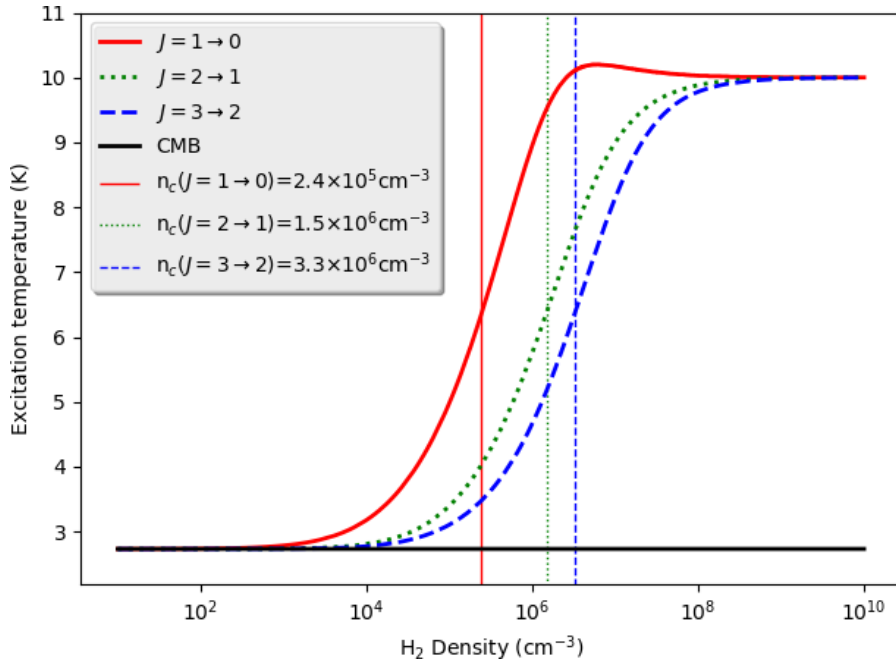


Figure 4.4 – Rotational curves of growth for HCN transitions $J = 1 \rightarrow 0$, $J = 2 \rightarrow 1$ and $J = 3 \rightarrow 2$. These curves of growth were computed with the usage of RADEX for a kinetic temperature $T_k = 10$ K, a HCN column density $N(\text{HCN}) = 10^{14} \text{ cm}^{-2}$ and using the latest hyperfine collisional coefficients for HCN (Lique et al. private communication).

perfine anomalies of the HCN $J = 1 \rightarrow 0$ transition but still failed to accurately reproduce the observed hyperfine ratios and also the line profiles of the HCN $J = 1 \rightarrow 0$ transition towards TMC-1.

4.1.2.1 Rotational spectroscopy of HCN

To understand the physics behind the mechanisms proposed for the hyperfine anomalies we have to delve deep into the spectroscopy of HCN. HCN is a linear molecule with a high dipole moment ($\mu = 2.9852$ D, Ebenstein and Muentner, 1984) with a small spacing between rotational levels making 4 of these levels available to HCN in normal conditions of the dense ISM (the rotational levels of HCN are separated by 8.5 K with $E_{J=1} = 4.25$ K, Ahrens et al., 2002). The first rotational transitions of HCN have high critical densities (Figure 4.4), which indicates that HCN is a tracer of moderate and high density gas ($n_{\text{H}_2} > 10^4 \text{ cm}^{-3}$).

The hyperfine splitting arises due to the presence of the nitrogen atom. The nitrogen atom has a nuclear spin, $I = 1$, which splits the rotational levels into three hyperfine levels. The splitting is represented by the quantum number F , which is the sum of the rotational angular momentum and the spin of the nitrogen atom ($F = J + I$). In

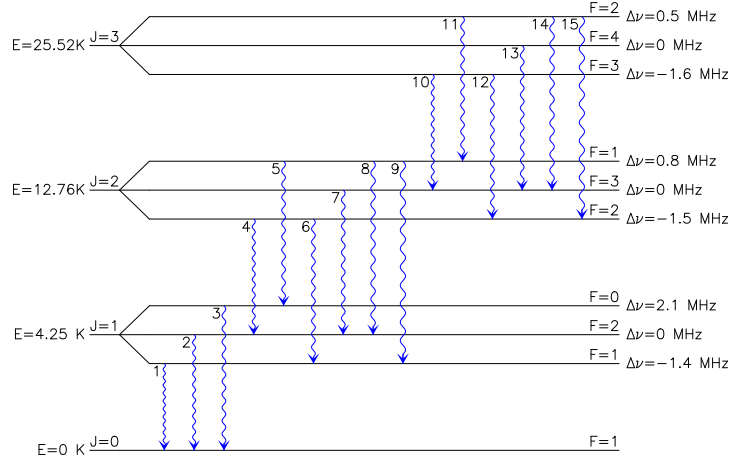


Figure 4.5 – Spectroscopy of HCN for $J = 0, 1, 2, 3$ including allowed radiative transitions between these levels, F denotes the nuclear spin state. Splitting not to scale.

Figure 4.5 we have a representation of the energy levels available for HCN up to $J=3$, including the allowed radiative dipolar transitions between these levels ($\Delta J = \pm 1$ and $\Delta F = 0$ or ± 1). The spectroscopic properties of these transitions are listed in Table 4.1, in which they are labelled from 1 to 15 according to their frequency.

These selection rules allow for 3 hyperfine components on the $J = 1 \rightarrow 0$ transition and 6 hyperfine components on higher rotational transitions. Due to the different properties of the upper and lower levels each hyperfine component of a rotational transition has its own Einstein coefficient (A_{ul} , with u being the upper level and l being the lower level). This, coupled with the different degeneracies of each hyperfine level, translates in each hyperfine component within a rotational transition having a different intensity, even when all hyperfine components have the same excitation temperature. We can take advantage of this phenomenon and define a very useful quantity the Relative Intensity (ρ) of a hyperfine component. The ρ of the hyperfine component x from rotational level J_{up} to rotational level J_{low} is defined as:

$$\rho_x = \frac{A_x g_x}{\sum_i A_i g_i}, \quad (4.1)$$

where A_j is the Einstein coefficient for transition j , g_j is the degeneracy of the upper level of transition j and $\sum_i A_i g_i$ is the sum of the intensities of the N hyperfine components within the rotational transition $J = J_{up} \rightarrow J_{low}$.

The relative intensity comes in hand as it helps us identify whether the populations within a rotational level of a transitions are in thermal equilibrium. If all hyperfine components of a rotational transition

Table 4.1 – Spectroscopic properties of the hyperfine components of the HCN $J = 1 \rightarrow 0$, $J = 2 \rightarrow 1$ and $J = 3 \rightarrow 2$ rotational transitions. Transitions are numbered according to increasing frequency.

Number	Upper J F	Lower J' F'	Frequency (MHz)	A_{ul} (s^{-1})	g_{up}	Relative Intensity
1	1 1	0 1	88630.414	2.41×10^{-5}	3	0.333
2	1 2	0 1	88631.848	2.41×10^{-5}	5	0.555
3	1 0	0 1	88633.936	2.41×10^{-5}	1	0.111
4	2 2	1 2	177259.677	5.78×10^{-5}	5	0.083
5	2 1	1 0	177259.923	1.28×10^{-4}	3	0.111
6	2 2	1 1	177261.111	1.73×10^{-4}	5	0.250
7	2 3	1 2	177261.223	2.31×10^{-4}	7	0.467
8	2 1	1 2	177262.011	6.42×10^{-6}	3	0.006
9	2 1	1 1	177263.445	9.63×10^{-5}	3	0.083
10	3 3	2 3	265884.888	9.28×10^{-5}	7	0.037
11	3 2	2 1	265886.188	7.02×10^{-4}	5	0.200
12	3 3	2 2	265886.434	7.43×10^{-4}	7	0.296
13	3 4	2 3	265886.501	8.36×10^{-4}	9	0.429
14	3 2	2 3	265886.976	3.71×10^{-6}	5	0.001
15	3 2	2 2	265888.522	1.30×10^{-4}	5	0.037

have a single excitation temperature (T_{ex}), the integrated intensity ratio between any two hyperfine component will vary from the ratio between their ρ and 1. To understand this phenomenon let's compute the line ratios between two hyperfine components of a single rotational transition, x and y , with relative intensities ρ_x and ρ_y respectively:

$$\frac{I_x}{I_y} = \frac{J_\nu(T_{\text{ex}})(1 - e^{-\rho_x\tau})}{J_\nu(T_{\text{ex}})(1 - e^{-\rho_y\tau})} \quad (4.2)$$

where I_x and I_y are the background subtracted integrated intensities of x and y respectively, T_{ex} is the excitation temperature of both hyperfine components, τ is the total opacity of the rotational transition and J_ν is calculated as in eq. 3.3. Since both hyperfine components have the same excitation temperature this can be further simplified to:

$$\frac{I_x}{I_y} = \frac{1 - e^{-\rho_x\tau}}{1 - e^{-\rho_y\tau}}. \quad (4.3)$$

In the optically thin case, i.e. when $\tau \ll 1$ we can make the approximation:

$$1 - e^{-\tau} \approx \tau, \quad (4.4)$$

and therefore the intensity ratio in eq. 4.3 reduces to:

$$\frac{I_x}{I_y} = \frac{\rho_x}{\rho_y}, \quad (4.5)$$

thus in the optically thin case the intensity ratio of two hyperfine components is the ratio of their relative intensities.

Now in the optically thick case, i.e. when $\tau \gg 1$ we can make the approximation:

$$1 - e^{-\tau} \approx 1 \quad (4.6)$$

therefore eq. 4.3 reduces to:

$$\frac{I_x}{I_y} = 1 \quad (4.7)$$

In the moderately thick case the hyperfine ratios fall in between these two values. This leads to a method to derive opacities from hyperfine ratios under the assumption that all hyperfine components have a single excitation temperature. Under this assumption eq. 4.2 can be solved numerically for τ . This method has been implemented in the CLASS software in the so called HFS routine (*GILDAS software*).

4.1.2.2 Self-absorption

The self-absorption mechanism was first proposed by Langer et al. (1978) to explain the anomalous $J = 1 \rightarrow 0$ emission of HCO^+ that is observed towards a few sources in Taurus. These anomalies consist in the $J = 1 \rightarrow 0$ transition of H^{13}CO^+ being stronger than that of HCO^+ . For example towards a position in TMC 1, they observed that the H^{13}CO^+ $J = 1 \rightarrow 0$ emission was 2 times stronger than HCO^+ $J = 1 \rightarrow 0$ emission ($T_A^*(\text{HCO}^+) \sim 450$ mK and $T_A^*(\text{H}^{13}\text{CO}^+) \sim 900$ mK). Another example is L134N where they observed HCO^+ $J = 1 \rightarrow 0$ emission to be about 1.5 times stronger than the $J = 1 \rightarrow 0$ emission of H^{13}CO^+ but at a different velocity ($T_A^*(\text{H}^{13}\text{CO}^+) \sim 550$ mK, $V(\text{H}^{13}\text{CO}^+) \sim 2.3$ km/s and $T_A^*(\text{HCO}^+) \sim 850$ mK, $V(\text{HCO}^+) \sim 3.5$ km/s).

These phenomena can be explained by assuming that a molecular cloud can be divided in two regions: a collisionally excited core and a non-collisionally excited envelope. Emission occurs in the excited core from collisionally excited molecules. The emission of HCO^+ in the core is stronger than that of H^{13}CO^+ due to its abundance being approximately 70 times larger (assuming $^{12}\text{C}/^{13}\text{C} = 70$), but it will not be 70 times as strong due to the effects of line saturation caused by the high opacity of HCO^+ . The emission from the core has to traverse the non excited envelope and therefore suffers absorption in it. The opacity in the envelope is proportional to the abundances of the isotopologues, leading to $\tau_{\text{HCO}^+} \gg 1$ and $\tau_{\text{H}^{13}\text{CO}^+} \sim 1$ since $X_{\text{HCO}^+} \gg X_{\text{H}^{13}\text{CO}^+}$. Due to the much larger optical depth of HCO^+ its emission is severely absorbed when compared to the H^{13}CO^+ emission therefore explaining how the emission of an under abundant isotopologue can be comparable to or even stronger than the emission of the main isotopologue. For HCN what would be expected in a similar situation is that transitions 1 and 2 would be more absorbed in the envelope than transition 3, due to their larger optical depths, generating the hyperfine anomalies (Walmsley et al., 1982). Since HCN spectra are usually self absorbed towards prestellar cores this mechanism may help to explain the observed HCN $J = 1 \rightarrow 0$ hyperfine anomalies.

4.1.2.3 Radiative trapping caused by the overlap of hyperfine components

The radiative trapping mechanism was first proposed by Gottlieb et al. (1975) and was improved by Guilloteau and Baudry (1981) who argued that overlaps in the $J = 2 \rightarrow 1$ transition would favour the $F = 2 \rightarrow 1$ hyperfine component of the $J = 1 \rightarrow 0$ over the other hyperfine components and that this effect would be dependent on the column density of HCN. This can be understood when we look into the details of HCN rotational spectroscopy.

The HCN $J = 2 \rightarrow 1$ transition has 2 main overlapping transitions, transitions #6 and #7 ($F = 2 \rightarrow 1$ and $F = 3 \rightarrow 2$ respectively, from here onwards transitions will be referred to by the numbering in Table 4.1), which are separated by 0.19 km/s which is very similar to the thermal FWHM of HCN at 10 K (~ 0.19 km/s). Since these two transitions overlap they exchange photons and if the optical depth is high enough some photons may become trapped between them. Transition #7 has a larger optical depth than transition #6 due to its higher Einstein coefficient and upper level degeneracy ($g_6 A_6 = 8.65 \times 10^{-4} \text{ s}^{-1}$ and $g_7 A_7 = 1.62 \times 10^{-3} \text{ s}^{-1}$). This higher optical depth makes the $J, F = 1, 2$ intercept more photons from transition #6 through the red wing of transition #7 than $J, F = 1, 1$ intercepts from transition #7 through the blue wing of transition #6. This leads to a population imbalance at $J = 2$, $J, F = 2, 3$ effectively steals population from $J, F = 2, 2$.

The de-excitation of these two levels proceeds mainly through the emission of radiation as their Einstein coefficients are approximately two orders of magnitude larger than their collisional de-excitation rates (for a density of 10^5 cm^{-3} and a temperature of 10 K, see Figures 4.6 and 4.7). This means that the population imbalance produced in the $J = 2$ level is propagated to the $J = 1$ level, through transitions #6 and #7, and to a lesser degree #4 ($F = 2 \rightarrow 2$). The end result is that $J, F = 1, 2$ is pumped at the expense of $J, F = 1, 1$, increasing the excitation temperature of transition #2 while lowering the excitation of transition #1 ($F = 2 \rightarrow 1$ and $F = 1 \rightarrow 1$ respectively).

The schematics of this process are shown in Figure 4.8. With this mechanism alone we can reproduce hyperfine inversions using a oversimplified model obtaining qualitatively similar results to Guilloteau and Baudry (1981) (see Figure 4.9). The differences in hyperfine ratios obtained here and those obtained by Guilloteau and Baudry (1981) may be explained by the fact that Guilloteau and Baudry (1981) used a set of approximated collisional rates, and a simplified radiative transfer model, just a modification of the escape probability formalism.

Of crucial importance to this mechanism is the amount of photons transferred from $J, F = 2, 2$ to $J, F = 2, 3$. This amount will depend on how much transitions 6 and 7 overlap, thus making the velocity field and non-thermal broadening essential for the reproduction of the phenomenon. This has been demonstrated by Gonzalez-Alfonso and Cernicharo (1993) who were able to reproduce a range of observed integrated intensity ratios with radiative transfer simulations of various velocity fields and non thermal broadenings. They obtained values for R_{12} in the range 0.4-1.2 and R_{02} ($F = 0 \rightarrow 1 / F = 2 \rightarrow 1$) in the range 0.3-2 for a range of physical conditions.

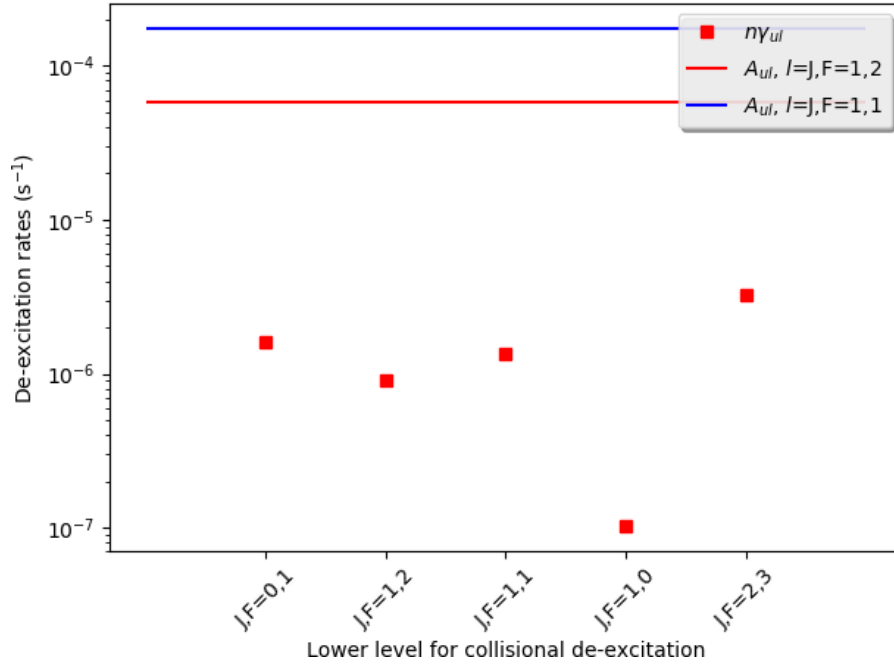


Figure 4.6 – Collisional and radiative de-excitation rates for HCN $J, F = 2, 2$ at a temperature of 10 K and a density of 10^5 cm^{-3} .

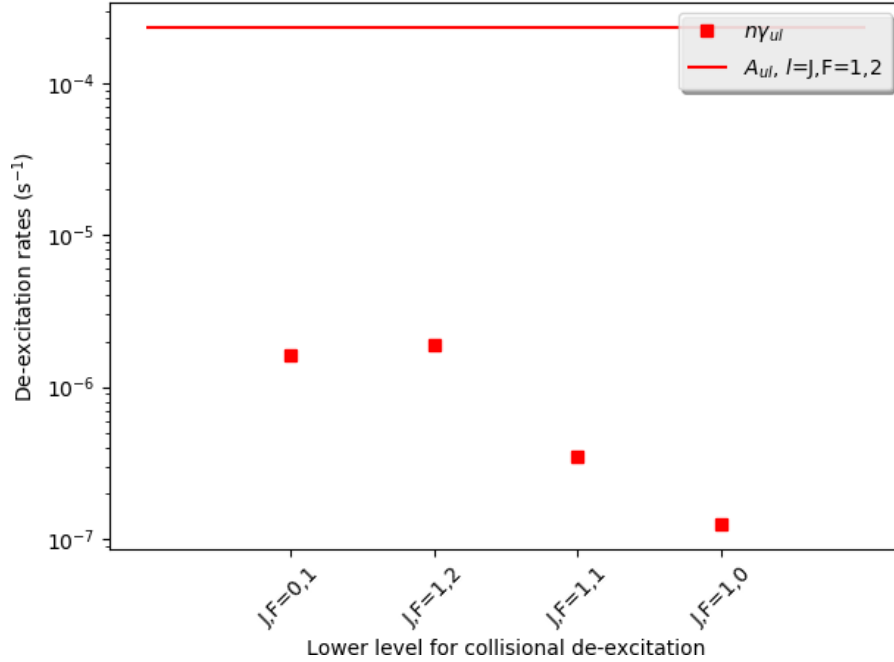


Figure 4.7 – Collisional and radiative de-excitation rates for HCN $J, F = 2, 3$ at a temperature of 10 K and a density of 10^5 cm^{-3} .

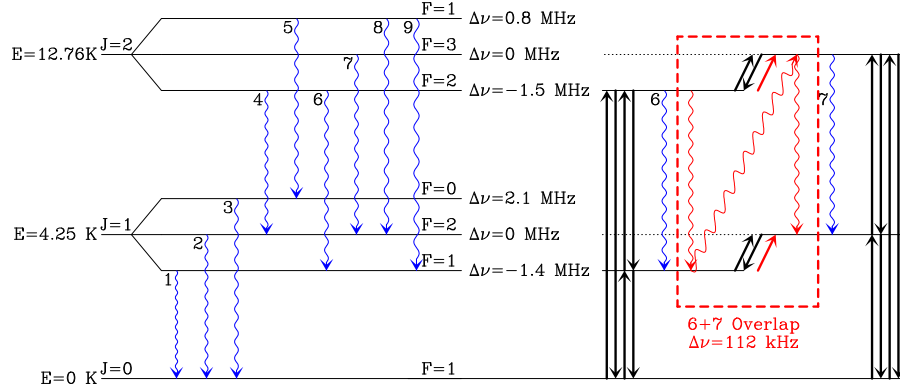


Figure 4.8 – Left: Schematic representation of the spectroscopy of HCN for $J \leq 2$. Right: Schematic description of the radiative trapping mechanism. The transition labels follow the scheme in Table 4.1. Solid black arrows represent the allowed collisional transitions, Sinusoidal blue lines represent the allowed radiative transitions and the red sinusoidal lines represent the effects of the overlap between transitions #6 and #7. The red arrows indicate the net flux of population.

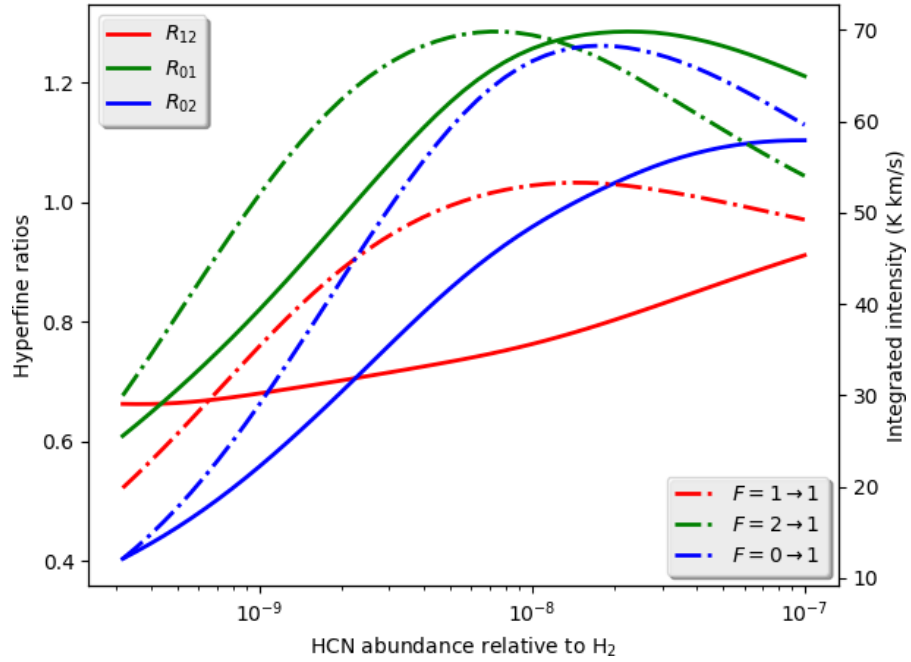


Figure 4.9 – Evolution of the HCN $J = 1 \rightarrow 0$ hyperfine ratios as a function of HCN abundance for a simplified model with $n_{\text{H}_2} = 10^5 \text{ cm}^{-3}$, $T_{\text{kin}} = 10 \text{ K}$ and a non thermal dispersion of velocities, $\sigma = 0.05 \text{ km/s}$. Hyperfine ratios computed with ALICO.

4.1.3 Testing the possible mechanisms

To fully understand the hyperfine anomalies seen in HCN spectra it is necessary to test the two mechanisms described before. To do so we have used NSLAB (Section 3.1) to construct a simple 4 slabs toy model (Section 4.1.3.1). This toy model was then used to test if the self-absorption mechanism alone can reproduce the HCN $J = 1 \rightarrow 0$ hyperfine anomalies, i.e. when all hyperfine components have the same excitation temperature or if different excitation temperatures are required. Lastly we take a look on the ability of the hyperfine overlap mechanism to generate hyperfine anomalies using ALICO (Section 4.1.3.2). Our tests with ALICO benefit from the latest *ab initio* HCN hyperfine rotational coefficients (Lique et al. in preparation). The collisional rates of Lique et al. (in preparation) for HCN-H₂ have been computed using a full quantum time-independent scattering method. The so-called "close-coupling" method was combined with the potential energy surface (PES) computed by Denis-Alpizar et al. (2013) at the explicitly correlated coupled-cluster with single, double, and perturbative triple excitations [CCSD(T)-F12a] level of theory. The accuracy of this PES was checked by comparing the measured rovibrational spectra of the HCN-H₂ complex with bound states calculations. Excellent agreement was found, with differences between observed and calculated transition frequencies lower than 0.5%, suggesting that the PES can be used with confidence to compute collisional rate coefficients. The rotational rate coefficients are described in Hernández Vera et al. (2017) where data are provided for the lowest 26 rotational levels and temperatures in the range 5 – 500 K for both para- and ortho-H₂ as colliders. Hyperfine collisional rates were obtained by Lique et al. (in preparation) using the so-called almost exact "recoupling" method for the lowest 25 hyperfine levels and temperatures in the range 5 – 30 K for para-H₂.

4.1.3.1 Four slabs Toy model

Our toy model is designed to be a simple way to test the possible hypothesis for the origin of the hyperfine anomalies. With it we can run several hundred of models with different excitation conditions to check which outcome those conditions would have on the hyperfine ratios. This toy model was inspired by the two layer model from de Vries and Myers (2005), and it does the same type of simplified radiative transfer calculations by using NSLAB albeit with 4 slabs instead of 2 (Section 3.1). For the specific case of understanding HCN $J = 1 \rightarrow 0$ hyperfine anomalies we adopted a toy model with 4 slabs: two central slabs, henceforth A slabs, with moderate to high excitation ($T_{\text{ex,A}} = 4 - 10$ K), narrow lines (FWHM = 0.15 km/s) and opposing velocities ($V = \pm 0.05$ km/s); and two envelope slabs, henceforth B slabs, with low excitation ($T_{\text{ex,B}} = 3$ K), broader lines (FWHM

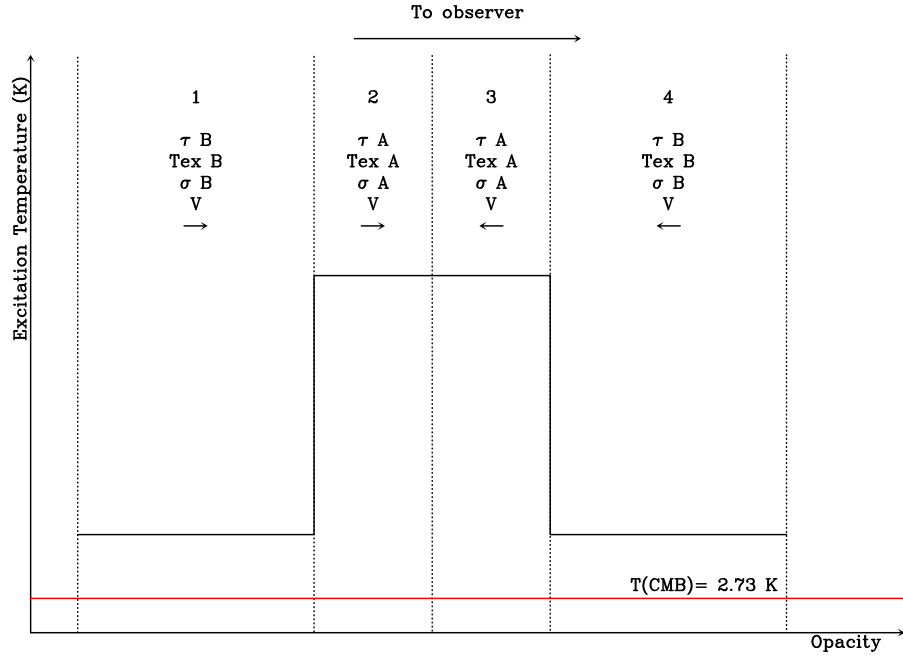


Figure 4.10 – Schematic description of the toy model. Slabs are numbered according to Table 4.2.

Table 4.2 – Parameters of the toy model. Slabs are numbered from the background to the observer.

Slab	Excitation Temperature(K)	Opacity	FWHM (km/s)	Velocity (km/s)
1	3	τ_B	0.35	0.05
2	4-10	τ_A	0.15	0.05
3	4-10	τ_A	0.15	-0.05
4	3	τ_B	0.35	-0.05

= 0.35 km/s) and also with opposing velocities ($V = \pm 0.05$ km/s). The total opacity was divided into τ_A and τ_B , with $\tau_B = 2\tau_A$. This ratio, albeit arbitrary, has little impact on the following conclusions as long as $\tau_B > \tau_A$, which is supported by the more complex models run with ALICO. The toy model is a simple implementation of the scenario proposed for the self-absorption mechanism, and represents the kind of excitation structure used by Gonzalez-Alfonso and Cernicharo (1993) in their Monte-Carlo radiative transfer models. The schematics of this toy model can be seen in Figure 4.10 and the parameters of its four slabs are given in Table 4.2.

In our toy model the brightness temperature (T_b) from a slab k is described by eq. 3.1. If we propagate this equation through all 4 slabs for one transition x we get:

$$T_b^x = J_\nu(T_{ex,B}^x)(1 - e^{-\tau_{v,B}^x} + e^{-2\tau_{v,B}^x} - e^{-3\tau_{v,B}^x}) + J_\nu(T_{ex,A}^x)(e^{-\tau_{v,B}^x} - e^{-2\tau_{v,B}^x}) + J_\nu(T_{CMB})e^{-3\tau_{v,B}^x} \quad (4.8)$$

where the x superscript refers to the one transition mentioned before, τ_A does not appear here as this equation was simplified by substituting τ_A for $0.5\tau_B$. This equation will be the base of the following discussions on the hyperfine ratios and will be used to compute hyperfine ratios in various situations.

Single Excitation Temperature

To test the hypothesis of self-absorption as the main mechanism for the $J = 1 \rightarrow 0$ hyperfine anomalies we have ran a grid of toy models. In this grid, henceforth G1, we varied two parameters, the excitation temperature of the A slabs and the total opacity. The excitation temperature of the B slabs was kept constant at 3 K while the excitation temperature of the A slabs was varied from 4 K to 10 K in steps of 1 K. The total opacity was varied from 0.1 to 100 in logarithmic steps. For the treatment of the hyperfine structure of the $J = 1 \rightarrow 0$ we assumed that all hyperfine components of the $J = 1 \rightarrow 0$ transition had the same excitation temperature within a given slab. The opacity of each hyperfine component in a given slab is the total opacity in the slab multiplied by the relative intensity of the hyperfine component. The hyperfine line intensity ratio is then computed from the background subtracted integrated intensity of each hyperfine component. The variation of the 3 hyperfine ratios with opacity in G1 can be seen in Figure 4.11.

We also note that the different excitation temperatures in the A slabs produce exactly the same hyperfine ratios as a function of opacity and thus appear as a single curve for each hyperfine ratio. This can be understood with the aid of two limiting cases: the optically thin case and the optically thick case. In the optically thin case, $\tau \ll 1$, thus we can simplify eq. 4.8 to:

$$\Delta T_b^x \approx \frac{3\tau_{v,B}^x(J_\nu(T_{ex,B}^x) + J_\nu(T_{ex,A}^x))}{2} \quad (4.9)$$

and hence the hyperfine ratios can be written as:

$$R_{xy} \approx \frac{\tau_{v,B}^x(J_\nu(T_{ex,B}^x) + J_\nu(T_{ex,A}^x))}{\tau_{v,B}^y(J_\nu(T_{ex,B}^y) + J_\nu(T_{ex,A}^y))} \quad (4.10)$$

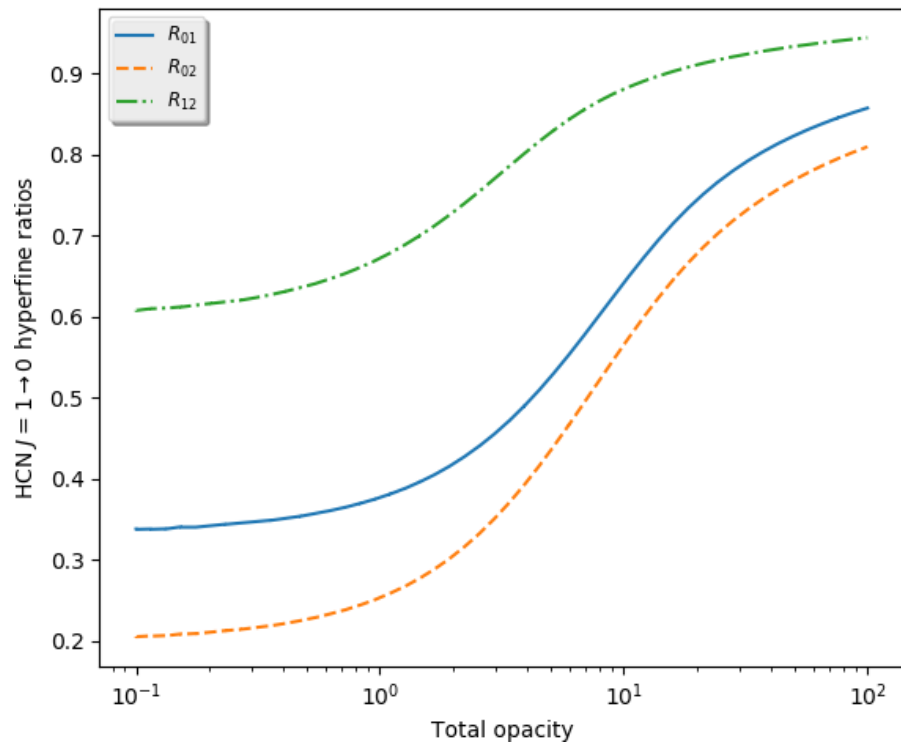


Figure 4.11 – HCN hyperfine ratios as a function of total opacity for grid G1. The non anomalous optically thin values for R_{02} , R_{01} and R_{12} are 0.2, 0.333, and 0.6 respectively.

where x and y stand for any pair of hyperfine transitions. Since $T_{\text{ex},A}$ is equal for all hyperfine components and $T_{\text{ex},B}$ is always equal to 3 K, the hyperfine ratios reduce to:

$$R_{xy} = \frac{\rho^x \tau_{v,B}}{\rho^y \tau_{v,B}}, \quad (4.11)$$

since:

$$\tau_{v,B}^x = \rho^x \tau_{v,B} \quad (4.12)$$

and thus the ratio of hyperfine components is reduced to the ratio between their ρ ($R_{01} = 1/3$, $R_{02} = 1/5$ and $R_{12} = 3/5$).

In the opposite case, when $\tau \gg 1$, we can simplify eq. 4.8, at the line centre, to:

$$\Delta T_b^x = J_v(T_{\text{ex},B}^x) \quad (4.13)$$

which might lead us to conclude that hyperfine ratios would always be 1 in the optically thick case, independent of the excitation temperature in the A slabs. This is not true since at the line wings we might still get some contribution from the A slabs, due to the difference in line width between A and B slabs. This contribution from the A slabs might produce double peaked profiles, but since the excitation temperatures for all hyperfine components at the A slabs are always the same in G1 we still get all hyperfine ratios equal to 1 when $\tau \gg 1$. All this hyperfine ratios remain in their expected interval therefore there are no hyperfine anomalies being produced.

HF anomalies reproduced with different excitation temperatures within the HCN $J = 1 \rightarrow 0$ triplet

The main effect of the overlap mechanism in the $J = 1 \rightarrow 0$ transition is to move population from the $J, F = 1, 1$ level to $J, F = 1, 2$. This phenomenon can be simulated by increasing the excitation temperature of the $F = 2 \rightarrow 1$ transition in expense of the excitation temperature of the $F = 1 \rightarrow 1$ transition while leaving the excitation temperature of the $F = 0 \rightarrow 1$ transition unchanged. With that in mind we have ran a second grid of toy models, henceforth G2, with a parameter space equal to that of G1, the only difference being in the excitation temperatures in the A slabs. In G2 the excitation temperature of the $F = 0 \rightarrow 1$ hyperfine components in the A slabs was left unchanged from G1 while the excitation temperatures of the $F = 1 \rightarrow 1$ and $F = 2 \rightarrow 1$ transitions were assumed to be 0.8 and 1.2 times that of the $F = 0 \rightarrow 1$ respectively. The hyperfine ratios computed from the toy models in G2 can be seen in Figure 4.12.

As we can see from Figure 4.12 each set of excitation temperatures produces a different hyperfine ratio curve as a function of opacity in G2. In the optically thin case, $\tau \ll 1$, it is a consequence of the

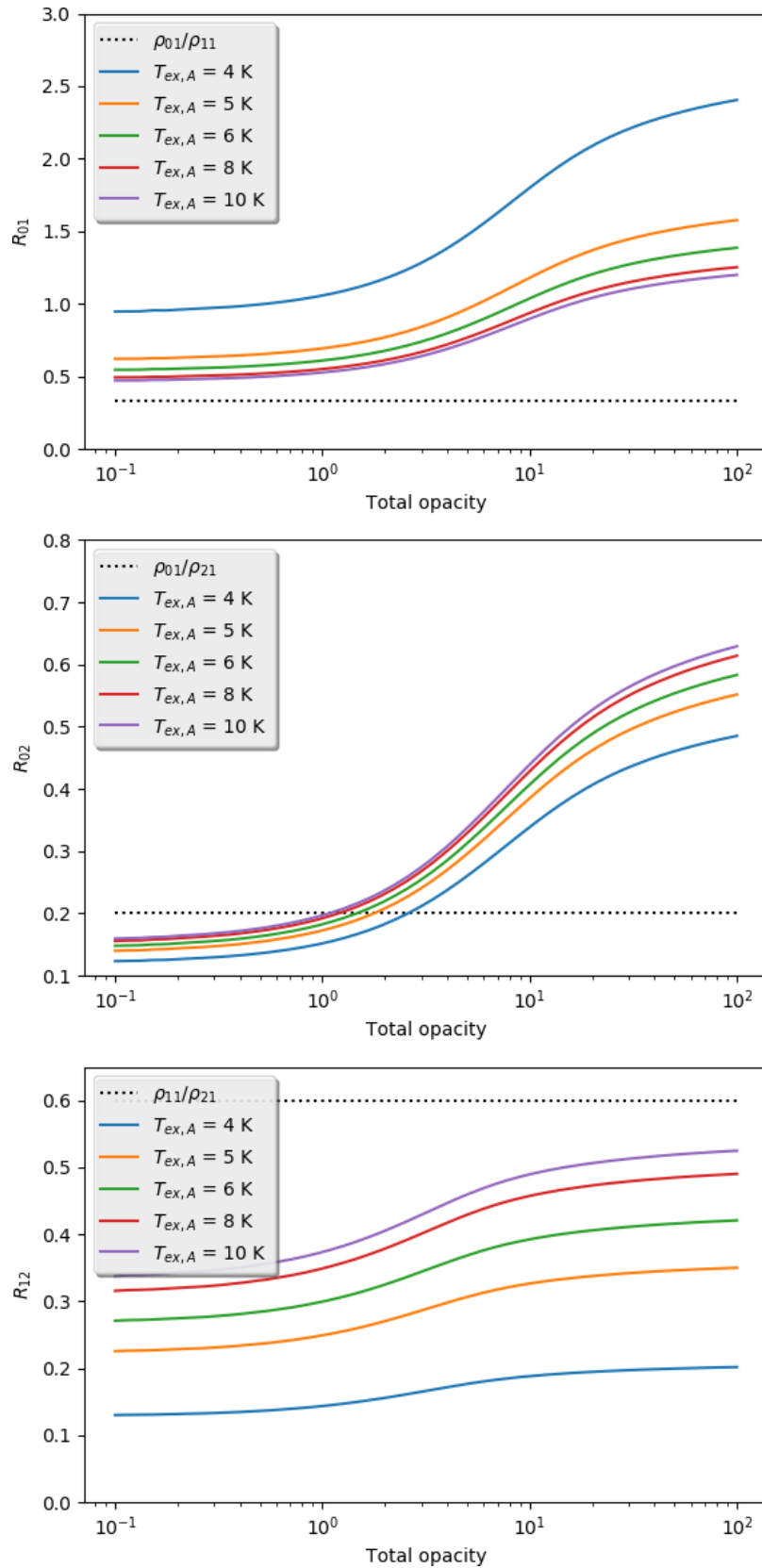


Figure 4.12 – HCN hyperfine ratios as a function of total opacity in the envelope for grid G2. Here $T_{ex,A}^{21} = 1.2T_{ex,A}^{01}$ and $T_{ex,A}^{11} = 0.8T_{ex,A}^{01}$ mimicking an excitation temperature imbalance such as what would be expected from the hyperfine overlap mechanism. The non anomalous optically thin values for R_{02} , R_{01} and R_{12} are 0.2, 0.333, and 0.6 respectively.

$T_{\text{ex},A}^x$ dependence of eq. 4.10. Whereas in the optically thick case the line intensity ratios are biased towards the wings of the lines, thus also depending on $T_{\text{ex},A}^x$. The take home message of G2 is that by introducing a small imbalance in excitation temperatures it is possible to produce HCN $J = 1 \rightarrow 0$ hyperfine anomalies, with $R_{01} = 0.5-2.8$, $R_{02} = 0.1-0.8$ and $R_{12} = 0.1-0.6$.

Interestingly if we compute the hyperfine ratios without the presence of the B slabs, the hyperfine ratios evolve differently with opacity. The range of hyperfine ratios is the same, but the hyperfine ratios increase at slower pace with the total opacity Figure 4.13.

The main conclusions that can be draw from the analysis of our toy model grids are:

- G1 results shows that self-absorption alone cannot reproduce the observed HCN hyperfine anomalies as the hyperfine ratios do not deviate from their expected ranges.
- G2 demonstrates that a small imbalance in excitation temperatures, such as the imbalance created by the hyperfine overlap mechanism, can reproduce anomalous hyperfine ratios.
- G2 also demonstrates that self-absorption is however needed for a complete understanding of the problem as it changes the dependency of the hyperfine ratios with opacity.

4.1.3.2 Tests with ALICO

Effects of the hyperfine overlap

To test whether the hyperfine overlap is behind the excitation temperature imbalance needed to recreate the hyperfine anomalies we need a tool more powerful than NSLAB. For that we resorted to ALICO (Section 3.2). As previously explained, ALICO is capable of dealing with hyperfine overlaps and can even turn on and off the treatment of this phenomenon. To be able to accurately treat HCN excitation the latest *ab initio* hyperfine collisional coefficients for HCN have been included in ALICO(Lique et al. private communication). To test the effect of the overlaps on the excitation temperatures of the $J = 1 \rightarrow 0$ hyperfine components two models with the same parameters have been run (see Table 4.3), one with the overlaps being taken into account, the other ignoring hyperfine overlaps. In Table 4.4 we can see the effect that hyperfine overlap has on the excitation temperatures of the $J = 1 \rightarrow 0$ hyperfine components. In this section we use the notation established in Table 4.1 for the hyperfine components of the rotational transitions of HCN.

As shown in Table 4.4, hyperfine overlaps have a large impact on the excitation temperature of transitions #1 and #2 while barely changing anything for transition #3. The effect is also in the direction that was expected, transition #1 drops in excitation temperature by 1.2 K while transition #2 increases in excitation temperature by

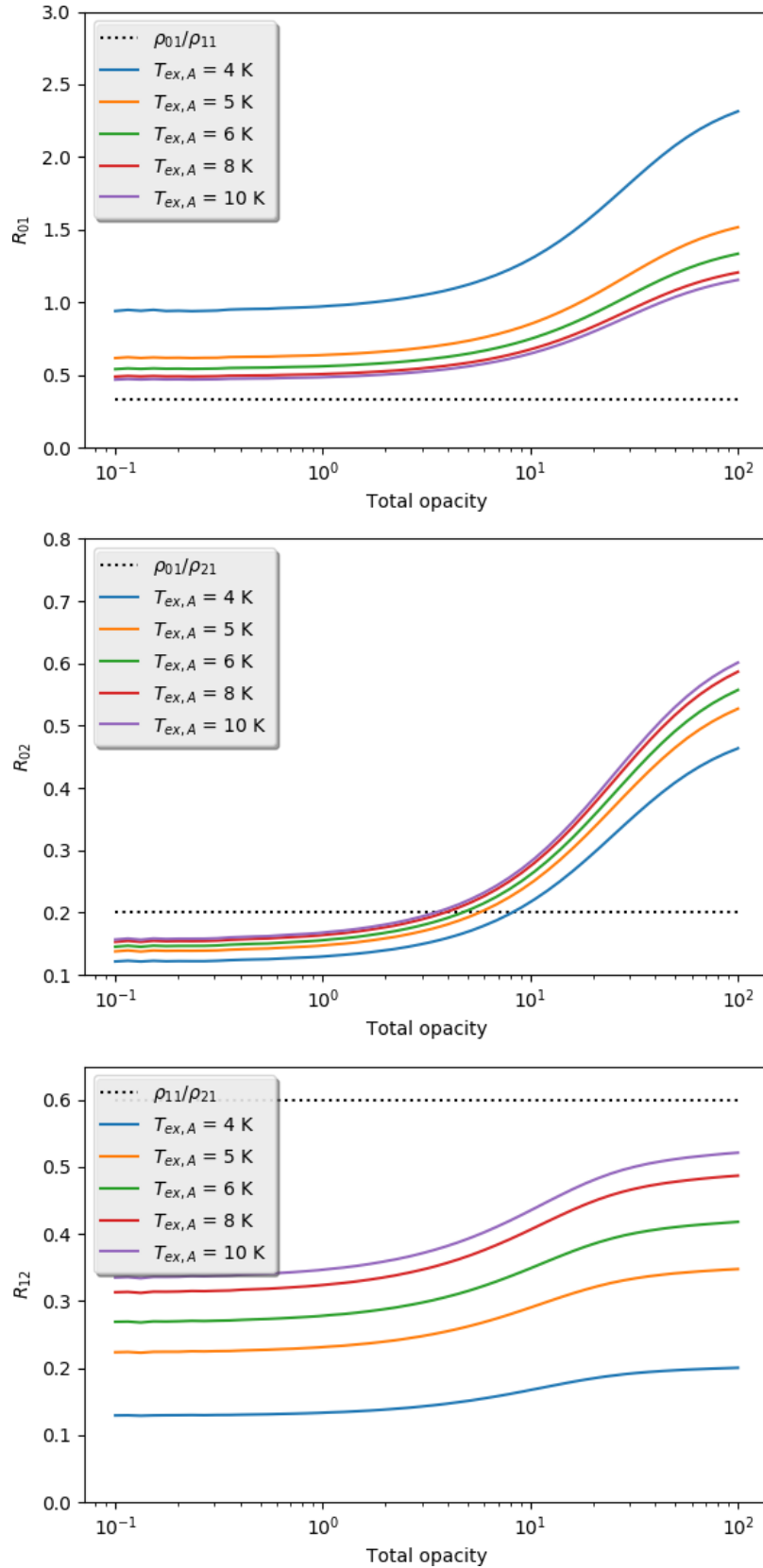


Figure 4.13 – HCN hyperfine ratios as a function of total opacity in the envelope for grid G2, with B slabs suppressed. Here $T_{ex,A}^{21} = 1.2T_{ex,A}^{01}$ and $T_{ex,A}^{11} = 0.8T_{ex,A}^{01}$ mimicking an excitation temperature imbalance such as what would be expected from the hyperfine overlap mechanism. The non anomalous optically thin values for R_{02} , R_{01} and R_{12} are 0.2, 0.333, and 0.6 respectively.

Table 4.3 – default

Parameter	Value
$n(\text{H}_2)$	10^5 cm^{-3}
σ	0.1 km/s
$T_{\text{kin.}}$	10 K

Table 4.4 – Excitation temperatures for the hyperfine components of the $J = 1 \rightarrow 0$ and $J = 3 \rightarrow 2$ transitions of HCN for two different models: a model where the hyperfine overlaps have been taken into account, and another where hyperfine overlaps have not been taken into account.

Rotational transition	Hyperfine component	Overlap Off $T_{\text{ex}}(\text{K})$	overlap On $T_{\text{ex}}(\text{K})$
$J = 1 \rightarrow 0$	$F = 1 \rightarrow 1$	10.0	8.8
	$F = 2 \rightarrow 1$	10.9	11.4
	$F = 0 \rightarrow 1$	9.6	9.3
$J = 3 \rightarrow 2$	$F = 3 \rightarrow 3$	6.4	7.3
	$F = 2 \rightarrow 1$	6.1	7.6
	$F = 3 \rightarrow 2$	6.8	7.9
	$F = 4 \rightarrow 3$	8.4	7.9
	$F = 2 \rightarrow 3$	5.2	5.9
	$F = 2 \rightarrow 2$	5.5	6.3

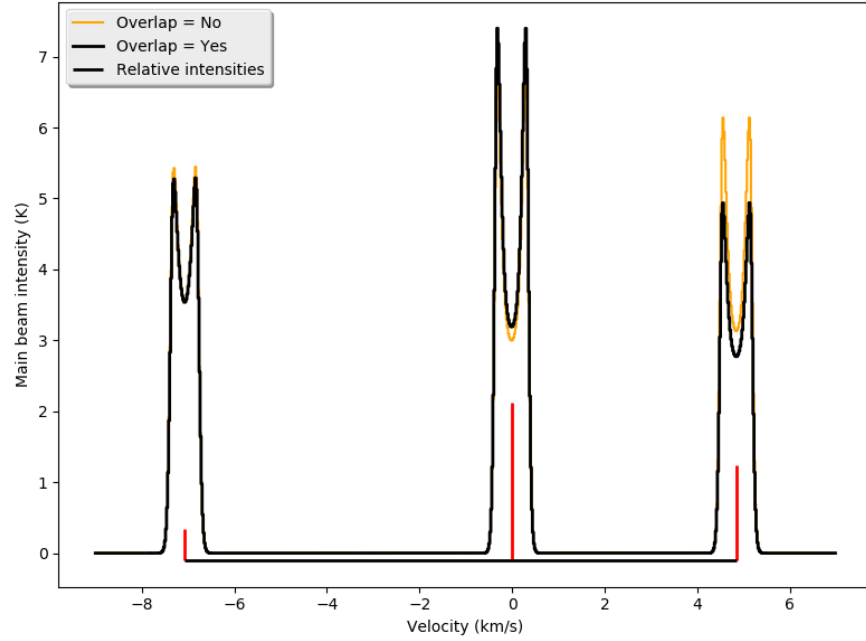


Figure 4.14 – Comparison between the emergent spectra for the $J = 1 \rightarrow 0$ transition of HCN produced by ALICO with (black) and without (orange) hyperfine overlap taken into account.

~ 0.5 K. The resulting spectra can be seen in Figure 4.14 where we see that the model taking into account the hyperfine overlap is capable of producing HCN $J = 1 \rightarrow 0$ hyperfine anomalies while the model without hyperfine overlap is not.

Analysing the excitation temperatures of the HCN $J = 3 \rightarrow 2$ transition we see that the hyperfine overlap changes the excitation temperature of all hyperfine components (see Table 4.4). All hyperfine components except for transition #13 increase in excitation temperature, while this transition suffers a small loss of excitation temperature (0.5 K). For the hyperfine anomalies the most interesting increase is that to transition #15, which increases by almost 1 K. Unsurprisingly this increase to the excitation temperature of transition #15 makes it several times stronger than transition #10, thus reproducing what is usually observed (see Figure 4.15).

Understanding hyperfine ratios using a realistic source model

With the knowledge that the hyperfine overlap is behind the hyperfine anomalies we know that the hyperfine ratios of HCN depend on the optical depth of the transitions with $J_{\text{up}} > 1$, and on the line width of the HCN lines (the line width will determine how much the hyperfine components do overlap). Therefore we need to study the space parameter of 5 physical quantities to reproduce the hyperfine anomalies of HCN:

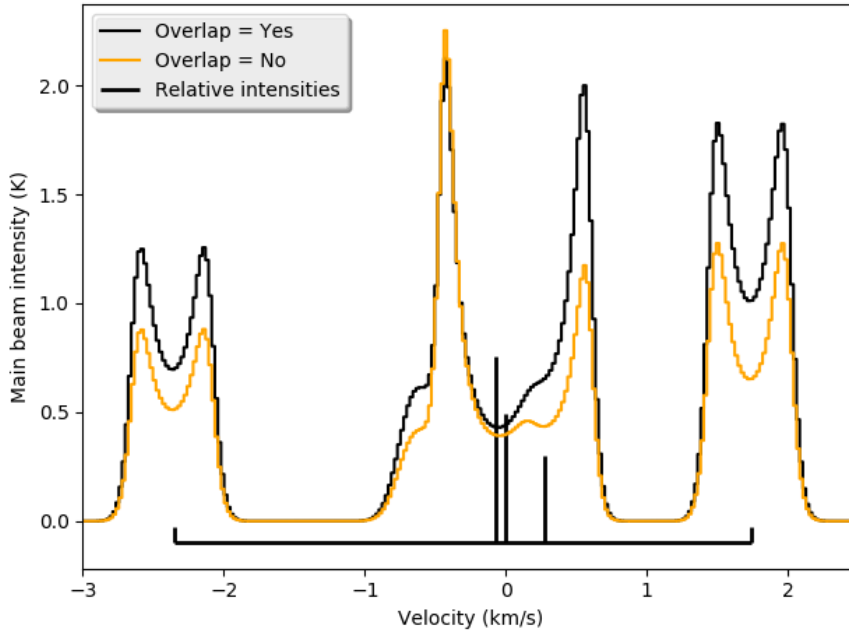


Figure 4.15 – Same as Figure 4.14 for HCN $J = 3 \rightarrow 2$.

- The abundance of HCN;
- The density of the medium;
- The kinetic temperature;
- The non thermal velocity dispersion;
- The velocity field.

The abundance of HCN coupled with the density of the medium and the size of the source will give us the total HCN column density, which limits the total amount of material that can be excited to $J \geq 2$. The density has another important task, as it along with the kinetic temperature controls the collisional excitations of HCN, dictating the relative populations of the rotational levels of HCN which determine the total optical depth for each rotational transition. The amount of actual overlap between hyperfine components depends on the line widths of the lines and also on the difference in line centre velocities between the different layers of the model. The line width is controlled by two factors, the kinetic temperature and the non thermal velocity dispersion. Therefore in order to correctly reproduce the line profiles of HCN we need to take into account all these physical quantities.

For a case of study we use the prestellar core L1498. This core has been studied with great detail (e.g. Tafalla et al., 2002; Tafalla et al., 2004; Tafalla et al., 2006; Padovani et al., 2011) and its density profile was established from the analysis of a 1.25 mm map (Tafalla et al., 2004). This prestellar core has been studied in much detail in this thesis and a revised physical structure was obtained, which will be discussed in great detail in Section 4.2. For the sake of simplicity,

here we adopt the physical model described in Tafalla et al. (2004), with the adoption of an extra parameter to account for the envelope of a prestellar core as in Gonzalez-Alfonso and Cernicharo (1993), accordingly, the H_2 number density (n_{H_2}) is:

$$n_{\text{H}_2}(r) = \frac{n_0}{1 + \left(\frac{r}{r_0}\right)^\alpha} + n_{\text{ext}} \quad (4.14)$$

where n_0 is the central density, r is the radius, r_0 is the half width at half maximum of the density profile, α is the exponent of the density profile decay and n_{ext} is the H_2 number density at $r = \infty$. For the kinetic temperature we adopt a constant kinetic temperature, $T_{\text{kin}} = 10$ K, based on NH_3 temperature measurements by Tafalla et al. (2004). For the collapse velocity profile, $V(r)$, we chose a gaussian profile of the form:

$$V(r) = V_c e^{-\frac{(r-r_V)^2}{2(\Delta r_V)^2}} \quad (4.15)$$

where V_c is the maximal collapse velocity, r_V is the radius at which the maximal collapse velocity occurs, and Δr_V is the dispersion of the gaussian profile. This profile was chosen to mimic the kind of collapse profile expected to take place in prestellar cores (Foster and Chevalier, 1993; Lesaffre et al., 2005), and which has seen similar implementations being used to model HCN line profile in prestellar cores (Lee et al., 2007; Seo et al., 2011; Seo, Hong, and Shirley, 2013). The abundance of HCN was assumed constant with radius for the sake of simplicity. And finally the non thermal velocity dispersion profile, $\sigma(r)$, was assumed to be of the form:

$$\sigma(r) = \sigma_0 + \frac{\sigma_{\text{ext}} - \sigma_0}{2} \left[1 + \tanh \left(\frac{r - r_j}{\Delta r_j} \right) \right] \quad (4.16)$$

where σ_0 is the non thermal velocity dispersion at $r = 0$, σ_{ext} is the non thermal velocity dispersion at $r = \infty$, r_j is the radius at which occurs the transition between σ_0 and σ_{ext} with Δr_j being its characteristic width. This non thermal velocity dispersion profile was chosen to conciliate the thermally dominated line widths seen towards the centre of the core (FWHM ~ 0.2 km/s) with the non thermal line widths seen in the vicinity of the core (FWHM ~ 0.6 km/s, appendix B of Tafalla et al., 2006).

The main objective here is not to accurately reproduce the line profiles of the HCN observation, it is to comprehend on which scale the parameters involved influence the HCN hyperfine anomalies in a realistic situation. For that we have chosen reference values for the physical parameters described in eqs. 4.14, 4.15 and 4.16 that are capable of generating hyperfine anomalies in both the $J = 1 \rightarrow 0$ and $J = 3 \rightarrow 2$ transition albeit not exactly like the observations. This much more nuanced job is taken in Section 4.2. The actual values taken for the parameters can be seen in Table 4.5 with the plots of the non constant

Table 4.5 – Values for the parameters in the reference model. Some of the parameters were chosen from an already published value.

Parameter	Value	Reference
n_0	$9.4 \times 10^4 \text{ cm}^{-3}$	Tafalla et al. (2004)
n_{ext}	$5 \times 10^2 \text{ cm}^{-3}$	
r_0	75''	Tafalla et al. (2004)
α	-3.5	Tafalla et al. (2004)
T_{kin}	10 K	Tafalla et al. (2004)
σ_0	0.05 km/s	
σ_{ext}	0.25 km/s	Tafalla et al. (2006)
r_j	336''	
Δr_j	62.4''	
$X(\text{HCN})$	$6 \times 10^{-9} \text{ rt H}_2$	
V_c	-0.25 km/s	Foster and Chevalier (1993)
r_V	288''	
Δr_V	48''	

parameters displayed in Figure 4.16 and the output spectra compared to the observations of L1498 towards the continuum peak displayed in Figure 4.17.

The first parameter for which the variation of the hyperfine ratios was checked was the non thermal velocity dispersion profile. Since the line overlap mechanism for the hyperfine anomalies depends crucially on the line widths a series of models was run with ALICO(Section 3.2.2) with different values for σ_0 , σ_{ext} , r_j and Δr_j to see their individual influence on the hyperfine ratios. The dependencies of the hyperfine ratios with the non thermal velocity profile can be seen in Figure 4.18. For the sake of comparison the expected statistical hyperfine ratios are given in Table 4.6.

As expected the value of σ_0 and σ_{ext} have rather dramatic effects on the hyperfine ratios. For very small values of σ_0 , $\sigma_0 < 0.05 \text{ km/s}$, the hyperfine ratios with transition #1 diverge as the radiative trapping between transitions 6 and 7 is so intense that leads transition #1 to appear in absorption against the CMB. For values larger than 0.05 km/s the hyperfine ratios vary smoothly with σ_0 , with larger values producing less anomalous spectra. The tendency is inverted for σ_{ext} which produces divergent ratios for $\sigma_{\text{ext}} > 0.25 \text{ kms}$. This can be understood from the effect of σ_{ext} in the self-absorption, if σ_{ext} is too big the opacity per velocity interval is smaller and therefore the anomalous emission can scape the core without being further reprocessed in the envelope.

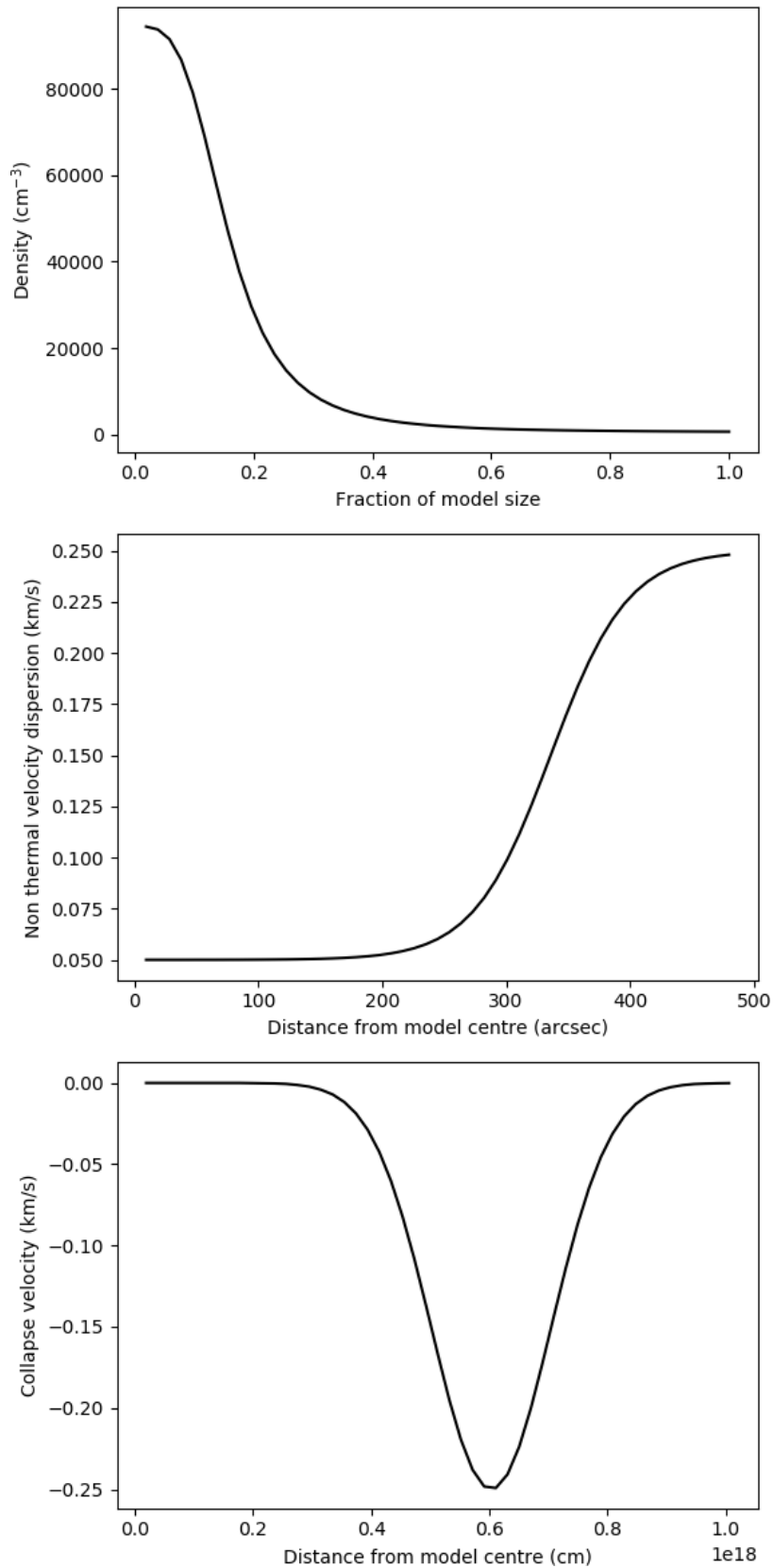


Figure 4.16 – Profile for the physical quantities in the reference model. Top: H_2 number density as a function of the fraction of the model size. Middle: Non thermal velocity dispersion as a function of the projected distance from the model centre in arc seconds. Bottom: Collapse velocity profile as a function of the distance from the model centre in cm.

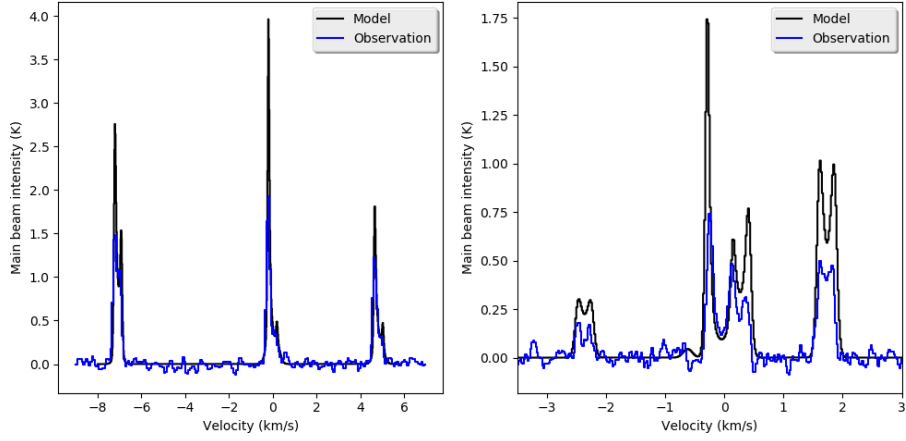


Figure 4.17 – Spectra produced by ALICO towards the model centre along with HCN observations towards the continuum peak of L1498. Left: $J = 1 \rightarrow 0$ spectra; Right: $J = 3 \rightarrow 2$ spectra.

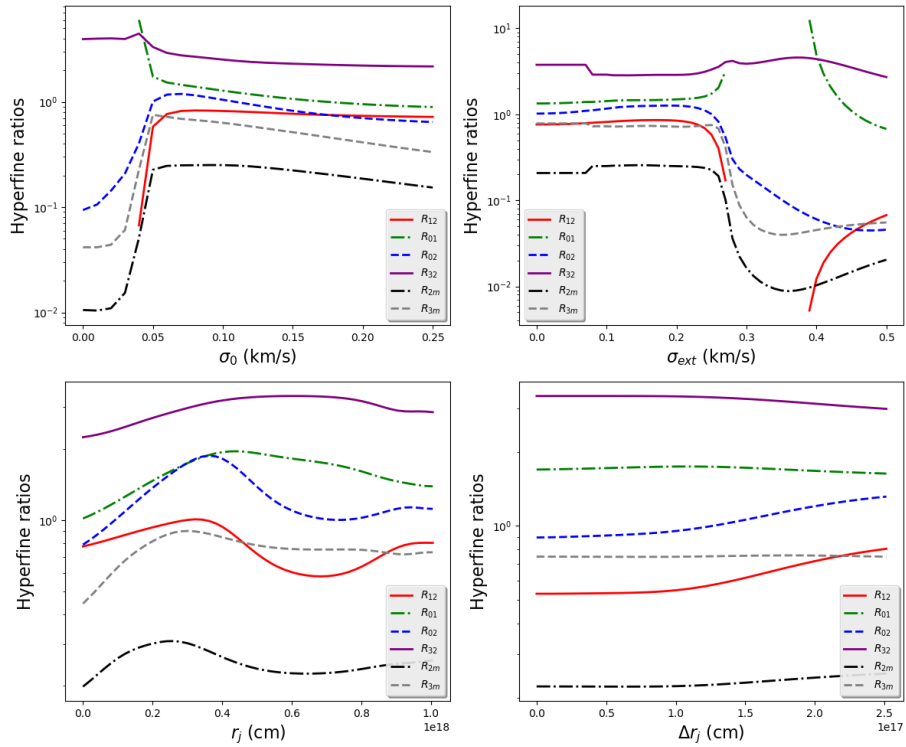


Figure 4.18 – Dependency of the hyperfine ratios on the non thermal velocity dispersion profile parameters. Top left: Hyperfine ratios as a function of σ_0 ; Top Right: Hyperfine ratios as a function of σ_{ext} ; Bottom left: Hyperfine ratios as a function of r_j ; Bottom right: Hyperfine ratios as a function of Δr_j .

Table 4.6 – Expected hyperfine ratios for HCN $J = 1 \rightarrow 0$ and $J = 3 \rightarrow 2$. Hyperfine transitions numbered according to the notation in Table 4.1.

Abbreviation	Hyperfine components	Rotational transition	statistical value
R_{12}	#1/#2	$J = 1 \rightarrow 0$	0.6
R_{01}	#3/#1	$J = 1 \rightarrow 0$	1/3
R_{02}	#3/#2	$J = 1 \rightarrow 0$	0.2
R_{32}	#10/#15	$J = 3 \rightarrow 2$	1
R_{2m}	#10/(#11+#12+#13+#14)	$J = 3 \rightarrow 2$	0.04
R_{3m}	#15/(#11+#12+#13+#14)	$J = 3 \rightarrow 2$	0.04

The effects of r_j are also related to the opacity per velocity interval. When r_j is small the line width is very large in the centre of the core and therefore photons can easily escape through transitions 6 and 7 and therefore there are only small anomalies. As r_j increases the hyperfine ratios increase up to $r_j = 2-3 \times 10^{17}$ cm where they start to diminish with r_j as self absorption from the envelope starts to become important in the reprocessing of the hyperfine ratios. The effects of Δr_j on the other hand are small and deserve no further comment.

The following parameter to be studied was the collapse velocity profile. As with the non thermal velocity dispersion profile a series of models were run with varying values for the parameters of the collapse velocity profile. The hyperfine ratios as a function of the collapse velocity parameters can be found in Figure 4.19.

V_c appears to have little impact on the hyperfine ratios of the $J = 3 \rightarrow 2$ transition. This can be explained by the fact that in the reference model the collapse occurs far from the centre of the model where the population in levels $J = 2$ and $J = 3$ is minimal and therefore the collapse has no effect on the $J = 3 \rightarrow 2$ transition. For the $J = 1 \rightarrow 0$ transition there is a tendency of increasing hyperfine ratios with increasing collapse velocity that can be explained by the influence of red-blue asymmetries in the hyperfine ratios of this transition.

The hyperfine ratios as a function of r_V confirm the previous conclusions drawn for the $J = 3 \rightarrow 2$ transition as the hyperfine ratios of this transition do not change for $r_V > 4 \times 10^{17}$ cm. For the $J = 1 \rightarrow 0$ transition the position of the collapse produces minimal yet perceptible variations of the hyperfine ratios.

Lastly the variations of the hyperfine ratios with ΔV are more pronounced as this is the value that dictates the rate at which the line centre velocities vary, profoundly affecting the red blue asymmetries. The ratio between the two transitions that do not show red blue asym-

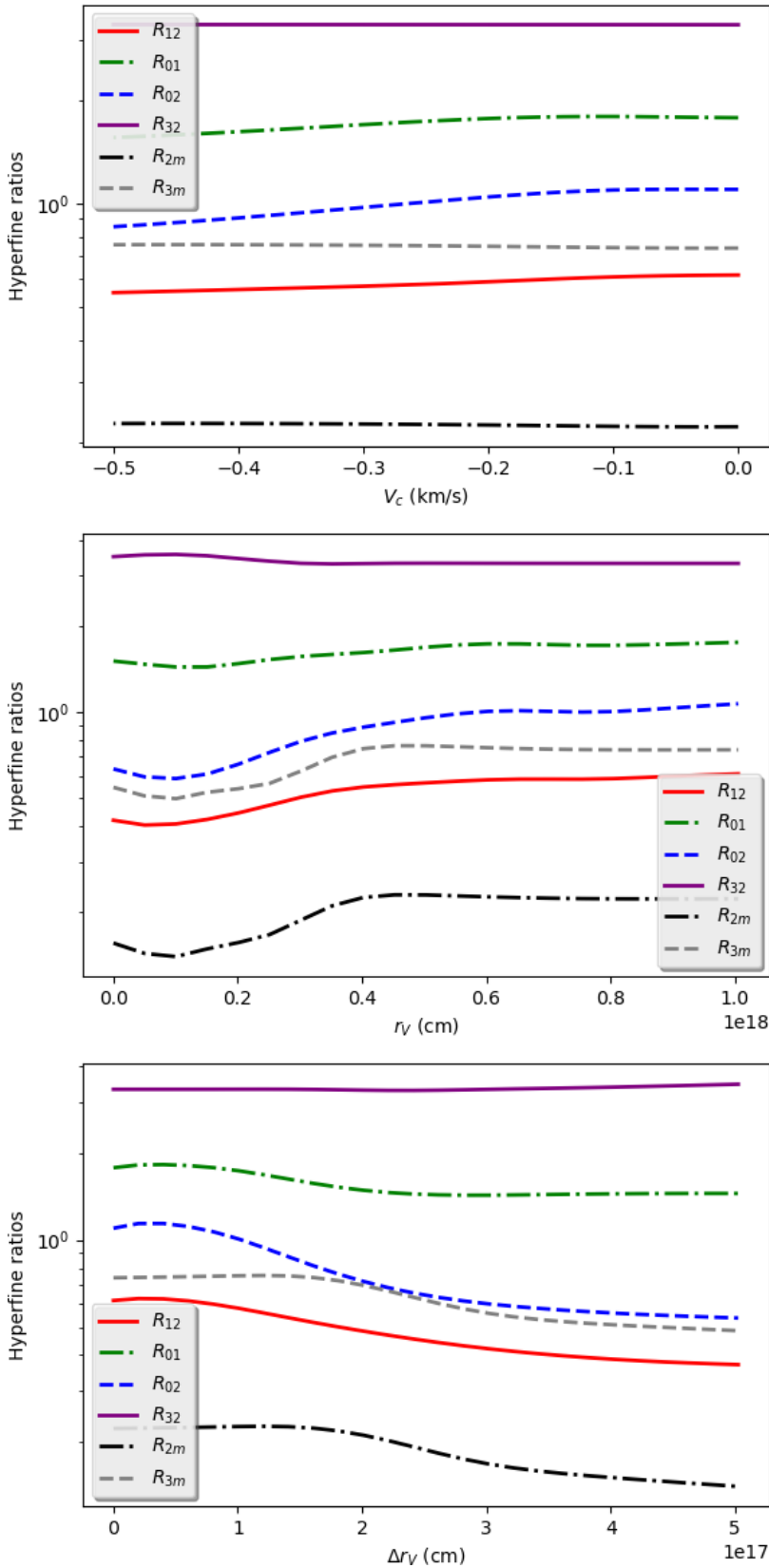


Figure 4.19 – Dependency of the hyperfine ratios on the collapse velocity profile parameters. Top: Hyperfine ratios as a function of the maximal collapse velocity V_c ; Middle: Hyperfine ratios as a function of r_V ; Bottom: Hyperfine ratios as a function of Δr_V .

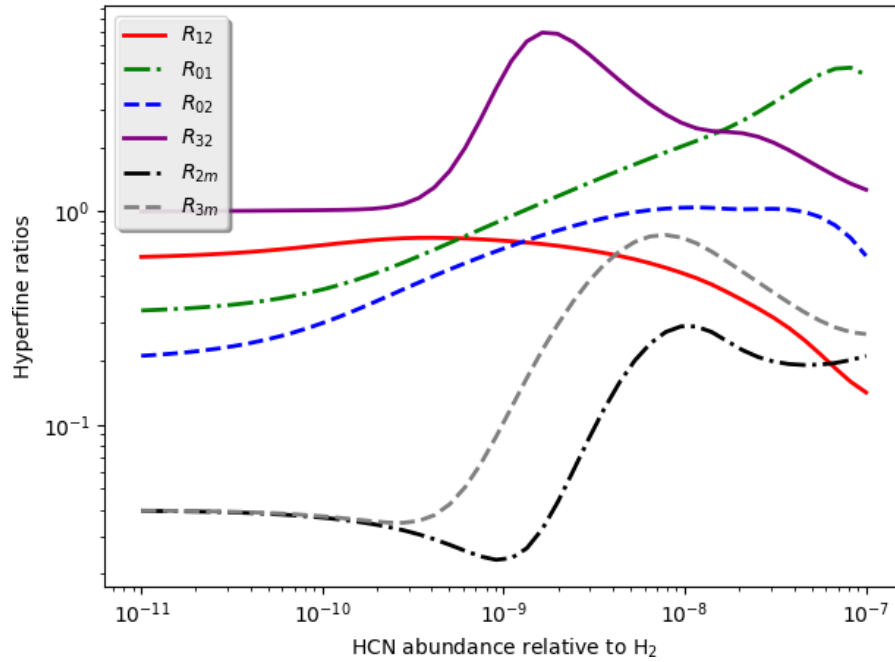


Figure 4.20 – Hyperfine ratios as a function of the abundance of HCN.

metries (transitions 10 and 15) remains constant while all other ratios vary. For the $J = 1 \rightarrow 0$ transition the ratio that is less affected is R_{01} , which involves the two less optically thick transitions of the $J = 1 \rightarrow 0$ which are less prone to red blue asymmetries, specially transition #3.

The last series of models run are intended to test whether the hyperfine ratios are sensitive to the abundance of HCN. This is of crucial importance as it tells us if it is possible to actually probe HCN column densities. If no variation is seen the hyperfine ratios are useless as a probe to the column density of HCN. What is actually found is that the hyperfine ratios do indeed depend on HCN abundances. Thus it is possible to measure the HCN column densities thanks to the sensitivity of the hyperfine ratios to the abundance of HCN (Figure 4.20).

Indeed the abundance of HCN is the parameter with the largest impact on the hyperfine ratios, with some of the hyperfine ratios (R_{01} and R_{3m}) varying by 1 order of magnitude. Yet this variation is small considering that the abundance of HCN, and hence its column density, varies by 4 orders of magnitude for a variation of slightly more than 1 order of magnitude in the ratio with the largest variation ($R_{01}=0.3-5$).

4.1.4 Conclusions

The main phenomenon behind the hyperfine anomalies is the overlap of hyperfine components. The effect of this hyperfine overlap on the level populations is mediated by the line widths of the core and its envelope, and the degree of self-absorption and red-blue asymmetries generated by the collapse profile. Due to all of these dependencies, measuring the abundance of HCN becomes a highly complicated job dependant on a large array of parameters requiring a thorough exploration of a gigantic parameter space. Therefore it is of fundamental importance to have a coherent set of observations containing several spatial offsets and multiple rotational transitions. The spatial offsets are of utmost importance as they are able to probe some of the variations in the values of the physical parameters of the cloud. Multiple transitions are also required as the new set of hyperfine ratios probes new environments. In the case of L1498, the HCN $J = 3 \rightarrow 2$ transition traces a region that sees no collapse while the $J = 1 \rightarrow 0$ transition probes the collapsing region displaying huge red-blue asymmetries. Finally our complete study of the abundance of HCN in L1498 can be found in Section 4.2 where we explain how the problem of exploring the huge parameter space is solved by the usage of ALICO/MCMC (Section 3.3.1).

4.2 HCN AND ITS ISOTOPOLOGUES IN L1498

The knowledge acquired about the hyperfine anomalies meant that to accurately measure the abundance of HCN in L1498 we need a very precise physical model, combined with high signal to noise ratio spectral observations (Section 4.2.1). The first step to obtain such a model is having an accurate description of the density profile. The density profile was obtained by doing multi-wavelength fits to publicly available Herschel SPIRE continuum data of L1498, along with a legacy continuum 1.25 mm map (Section 4.2.4). In any case we decided to use two simpler methods to derive the HCN/¹⁴N/¹⁵N ratio in L1498 before conducting the full experiment with ALICO/MCMC. First we measured the HCN/¹⁴N/¹⁵N ratio indirectly from the LTE computation of the column densities of H¹³CN and HC¹⁵N through the double isotopologue method (Section 4.2.2). Next we used NSLABcoupled with RADEX to fit the spectra to models that compute the emerging spectra under the Large Velocity Gradient (LVG) approximation (Section 4.2.3). And finally we use ALICO/MCMC to derive the abundances of HCN and its isotopologues directly (Section 4.2.5).

4.2.1 Observations

The observational data used in this project consists of spectral data on HCN and its isotopologues obtained at the IRAM 30m telescope, along with continuum data from the Herschel satellite and a legacy 1.25 mm map obtained at the IRAM 30m telescope (Tafalla et al., 2002).

4.2.1.1 Spectral observations

The spectral data were obtained in 4 observational missions to the IRAM 30m telescope. The HCN $J = 1 \rightarrow 0$ observations were obtained in missions 0031-11 and 008-16. With the data on 008-16 mission consisting on the further away offsets The H^{13}CN and HC^{15}N data were obtained on mission 007-16. Lastly the HCN $J = 3 \rightarrow 2$ data were obtained on mission 105-16. A list of the approved proposals submitted during this thesis can be found in Table C.1.

4.2.1.2 Continuum observations

The 1.25 mm map was obtained from Tafalla M., private communication. The Herschel SPIRE maps were downloaded from the Herschel science archive (*The Herschel Science Archive*). These maps are part of the Gould Belt Survey (André et al., 2010). The maps were processed by the Herschel SPIRE standard pipeline, version v14.1.0, to level 3, to make a complete mosaic of the Taurus molecular cloud complex. From this complete maps of the Taurus molecular cloud complex we extracted square maps covering 1 square degree centred at L1498.

To determine the RMS noise of the continuum maps we have done Gaussian fits to the histogram of intensities of the continuum maps. In the case of the 1250 μm map this fit was accomplished with a single Gaussian curve (Figure 4.21), the RMS noise of this map was assumed to be the dispersion of this Gaussian. For the Herschel SPIRE maps we selected a region of the maps showing the minimal possible emission. But even on this we see a source of noise beyond that of simple photon noise; this is noise caused by the variability of diffuse far infrared emission. Therefore the fits to the intensities histograms were done with two Gaussians, one that measures the photon RMS noise, and the other for the background noise. The total RMS noise was assumed to be the quadratic sum of the dispersion of these two Gaussians. These fits can be seen in Figure 4.22. One other particularity of the Herschel SPIRE maps is that they have an intensity offset from zero that was added by the data reduction pipeline to account for the difference in flux to the Planck satellite maps of the region. In Table 4.7 we see the final RMS noise of the continuum maps along with the intensity offsets added to the Herschel SPIRE images.

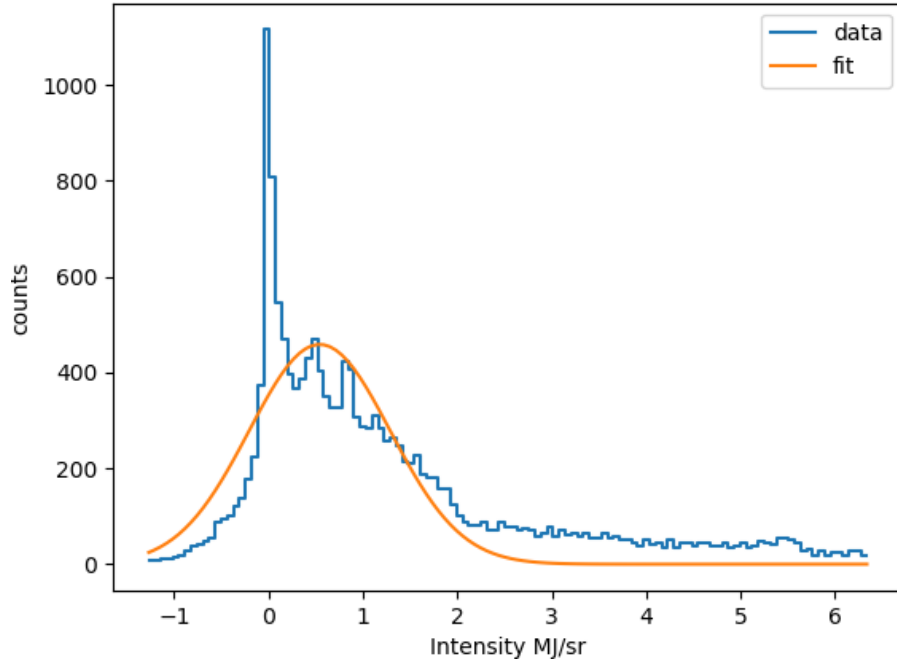


Figure 4.21 – Histogram of intensities for the 1250 μm MAMBO map along with the best Gaussian fit to it.

Table 4.7 – RMS noise and intensity offsets applied to the continuum maps, along with the Half Power at Beam Width of the observations.

Wavelength (μm)	Offset (MJy/sr)	RMS (MJy/sr)	HPBW ($''$)
250	+34.3	4.1	17.6
350	+21.4	2.2	23.9
500	+9.4	1.0	35.2
1250	-	0.6	11

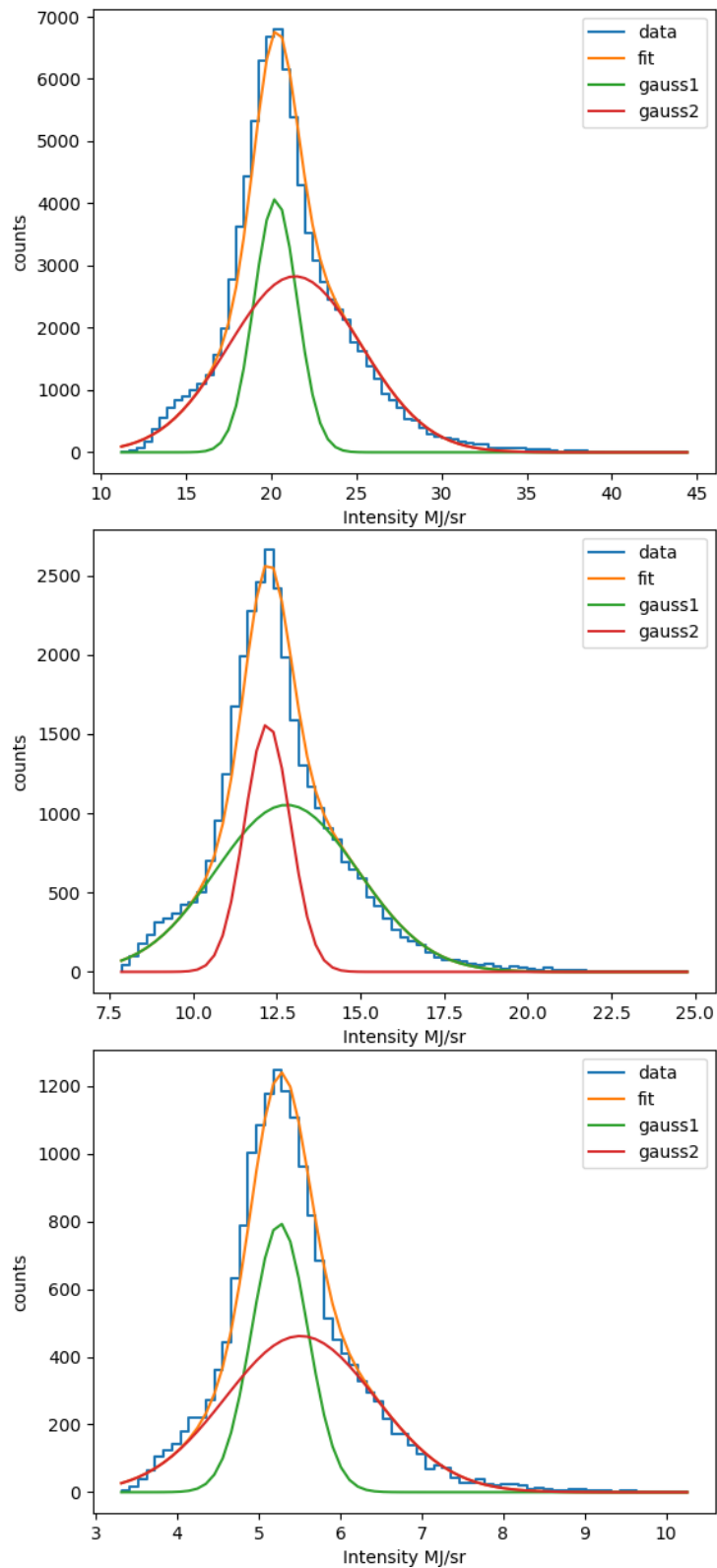


Figure 4.22 – Top panel: histogram of intensities for the 250 μm Herschel SPIRE low signal region map along with the best 2 Gaussian fit to it. Middle panel: histogram of intensities for the 350 μm Herschel SPIRE low signal region map along with the best 2 Gaussian fit to it. bottom panel: histogram of intensities for the 500 μm Herschel SPIRE low signal region map along with the best 2 Gaussian fit to it.

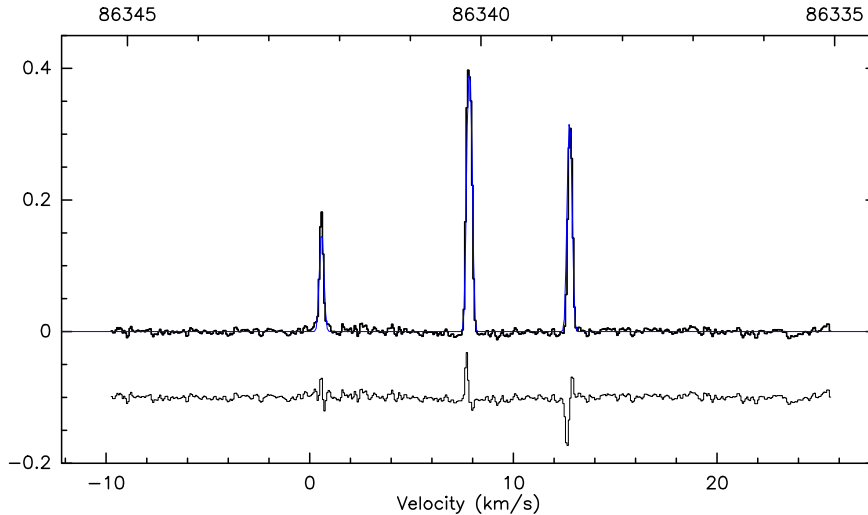


Figure 4.23 – The CLASS HFS fit (blue) to the $\text{H}^{13}\text{CN } J = 1 \rightarrow 0$ transition towards the continuum peak of L1498 (thick black) along with the residuals of this fit (thin black lines). The vertical axis is in the main beam temperature scale in K.

4.2.2 $\text{HCN}/\text{HC}^{15}\text{N}$ under the single excitation temperature hypothesis

The first method we used to determine the $\text{HCN}/\text{HC}^{15}\text{N}$ ratio was the double isotopologue method using the LTE derived column densities of H^{13}CN and HC^{15}N . The column density of H^{13}CN was computed by first deriving its opacity with CLASS HFS method (*GILDAS software*, Figure 4.23). This method uses eq. 4.3 to compute the total opacity of transition under the assumption that all of its hyperfine components have the same excitation temperature. With this method we get a total opacity for the $\text{H}^{13}\text{CN } J = 1 \rightarrow 0$ transition of 3.71. We then use this opacity to compute the excitation temperature of the hyperfine components for which we obtain $T_{\text{ex}} = 3.3$ K. This excitation temperature is then assumed to be the same for the $\text{HC}^{15}\text{N } J = 1 \rightarrow 0$ transition so that we can compute its opacity. Finally from the these opacities and excitation temperatures we compute the column density of HC^{15}N and H^{13}CN . The results of this method can be found in Table 4.8 These result indicates that if HCN is not fractionated in carbon its nitrogen isotopic ratio is very high, meaning that HCN is very poor in ^{15}N .

4.2.3 Measuring the isotopic ratio of HCN with the escape probability formalism

The second method used to derive the isotopic ratios in HCN was to use NSLAB and RADEX to compute spectra based on a simple plane

Table 4.8 – H^{13}CN and HC^{15}N column densities along with the $\text{HCN}/\text{H}^{13}\text{CN}$ ratio compute for different values of $^{12}\text{C}/^{13}\text{C}$.

$N(\text{H}^{13}\text{CN})$ (cm^{-2})	$N(\text{HC}^{15}\text{N})$ (cm^{-2})	$\frac{\text{H}^{13}\text{CN}}{\text{HC}^{15}\text{N}}$	$\frac{\text{HCN}}{\text{HC}^{15}\text{N}}$ $^{12}\text{C}/^{13}\text{C}=45$	$\frac{\text{HCN}}{\text{HC}^{15}\text{N}}$ $^{12}\text{C}/^{13}\text{C}=68$	$\frac{\text{HCN}}{\text{HC}^{15}\text{N}}$ $^{12}\text{C}/^{13}\text{C}=90$
2.3×10^{12}	2.8×10^{11}	8.2	370	559	740

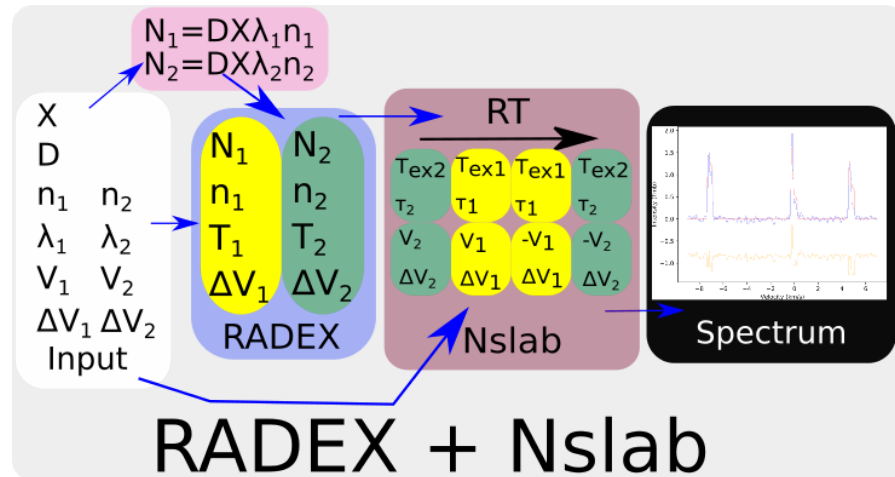


Figure 4.24 – Schematics of the inner workings of the RADEX+Nslab LVG model.

parallel source model. This simple model consists of 4 slabs, just like the toy model of Section 4.1.3, in which the last two slabs are mirror images of the first two. The model has a fixed total size D , which for L1498 was chosen to be 0.5 pc. All slabs have the same abundance for all isotopologues. The other parameters are given per pair of mirror slabs:

- λ the Fractional size of the slab, which can vary from 0 to 1.
- H_2 density in the slab.
- Kinetic temperature in the slab.
- FWHM at the slab.
- Velocity of the slab relative to the observer.

The density, Kinetic temperature and FWHM are used to compute excitation temperatures and opacities with RADEX for all the slabs. These excitation temperatures and opacities along with FWHM and the slab velocity are then plugged into Nslab to produce an output spectrum that can then be compared to the observations. Figure 4.24 displays a scheme of how such emergent spectra are computed in this type of model.

Table 4.9 – Best fit results to the observations of HCN and its isotopologues by RADEX+N_{SLAB} MCMC. We also present the fixed parameters used in the fit.

Parameter	Value	Unit	Fixed
Diameter	0.5	pc	yes
T_K	10	K	yes
X_{HCN}	$1.0 \pm 0.1 \times 10^{-8}$	relative to H_2	no
$X_{H^{13}CN}$	$2.8 \pm 0.5 \times 10^{-10}$	relative to H_2	no
$X_{HC^{15}N}$	$3.4 \pm 0.8 \times 10^{-11}$	relative to H_2	no
$n_1(H_2)$	$3.3 \pm 0.5 \times 10^4$	cm^{-3}	no
λ_1	0.39 ± 0.06		no
V_1	0.0	km/s	yes
FWHM ₁	0.2	km/s	yes
$n_2(H_2)$	10^3	cm^{-3}	no
λ_2	0.60 ± 0.06		no
V_2	0.15	km/s	yes
FWHM ₂	0.625	km/s	yes

For L1498 we performed the fit with some of this parameters fixed. We know from the $HC^{15}N$ observations that the FWHM at the central slabs is ~ 0.2 km/s, while from Tafalla et al. (2006) we know that the FWHM at the envelope is 0.625 km/s. The temperature was fixed to 10 K in all slabs in accordance to the NH_3 temperature measurements (Tafalla et al., 2004). For the collapse velocity we chose a value that is 0.0 km/s on the inner slabs as no collapse signatures are seen in the HCN $J = 3 \rightarrow 2$ observations, and 0.15 km/s in the outer slabs since we know that there is collapse thanks to the collapse signatures in the HCN $J = 1 \rightarrow 0$ observations. This is in qualitative agreement with what is expected for the collapse of prestellar cores (Foster and Chevalier, 1993; Lesaffre et al., 2005). The last parameter that was fixed was the external density, which was set to 10^3 cm^{-3} , as the degeneracy between its value and the fractional of the envelope slabs did not allow for it to be fitted. This comes from the fact that this layer does not contribute to the emission only to absorption therefore what is constrained is its column density not its density, which creates a degeneracy between the external density and the size of the envelope. The best fit results can be seen in Table 4.9, and the best fit spectra can be seen in Figures 4.25 to 4.28.

As can be seen in Figure 4.26 the fit does not converge for the HCN $J = 3 \rightarrow 2$ transition but does indeed present a good fit for the $H^{13}CN$ and $HC^{15}N \ J = 1 \rightarrow 0$ transitions. The HCN $J = 1 \rightarrow 0$ lies some-

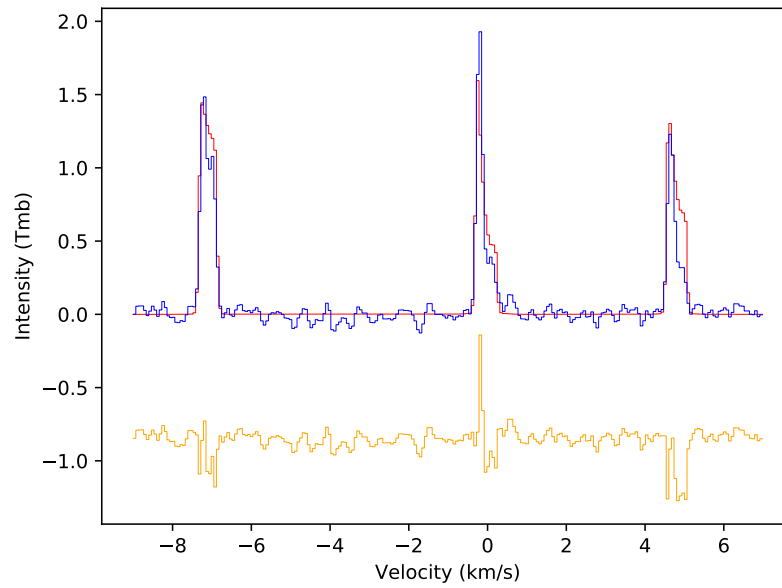


Figure 4.25 – HCN $J = 1 \rightarrow 0$ observations towards the continuum peak of L1498 (blue) along with the best fit from RADEX+NslabMCMC (red) and the residuals of this fit (orange).

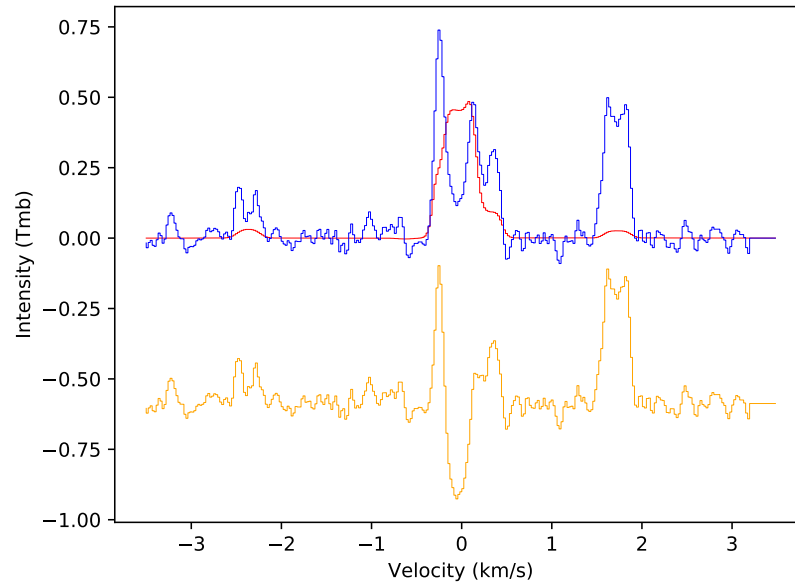


Figure 4.26 – HCN $J = 3 \rightarrow 2$ observations towards the continuum peak of L1498 (blue) along with the best fit from RADEX+NslabMCMC (red) and the residuals of this fit (orange). Notice the very poor quality of the fit caused by the inability of RADEX to process hyperfine overlaps.

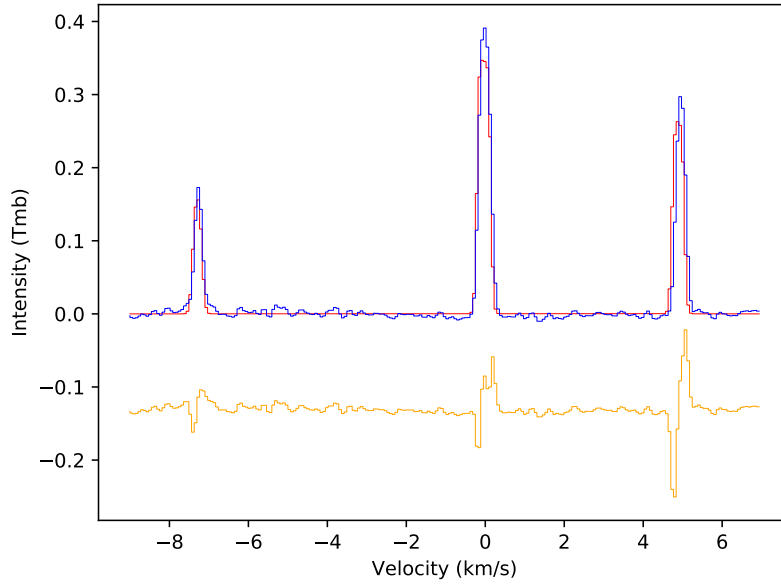


Figure 4.27 – $\text{H}^{13}\text{CN } J = 1 \rightarrow 0$ observations towards the continuum peak of L1498 (blue) along with the best fit from RADEX+NslabMCMC (red) and the residuals of this fit (orange).

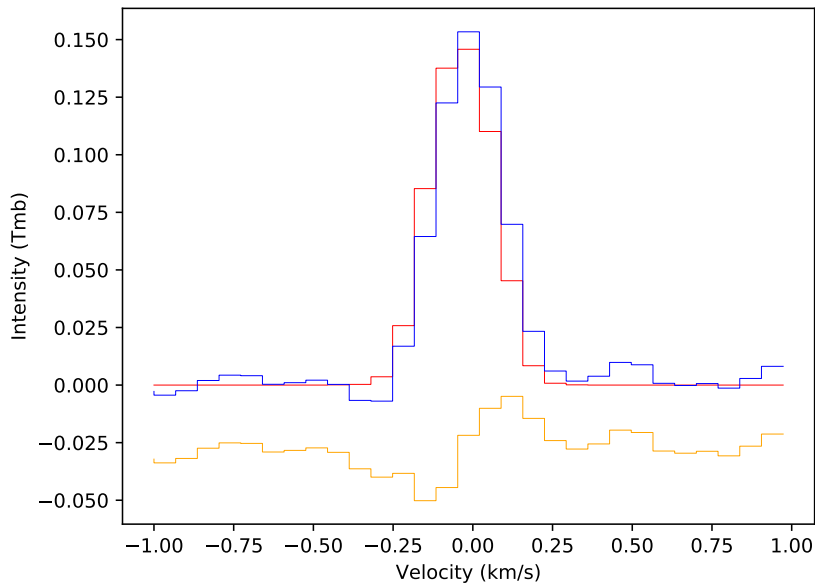


Figure 4.28 – $\text{HC}^{15}\text{N } J = 1 \rightarrow 0$ observations towards the continuum peak of L1498 (blue) along with the best fit from RADEX+NslabMCMC (red) and the residuals of this fit (orange).

Table 4.10 – Column densities for HCN and its isotopologues and the isotopic ratios between this isotopologues and HCN as computed from the results of the MCMC fit with RADEX+N_{SLAB}.

Isotopologue	Column density ($\times 10^{12} \text{ cm}^{-2}$)	Isotopic ratio
HCN	114 ± 32	
H^{13}CN	3.2 ± 1.1	36 ± 7
HC^{15}N	0.39 ± 0.16	295 ± 75

where in between with the main characteristics of the line profiles being represented. The $F = 0 \rightarrow 1$ and $F = 1 \rightarrow 1$ hyperfine components do even display the hyperfine inversion, but their red wings are over produced. On the other hand the $F = 2 \rightarrow 1$ component is under reproduced but its red wing is well reproduced.

The inability to reproduce the HCN $J = 3 \rightarrow 2$ spectra and to fully reproduce the intensities of the hyperfine components of the HCN $J = 1 \rightarrow 0$ transition is expected. RADEX does not treat hyperfine overlaps and thus the effects of hyperfine overlaps are not seen in the resulting spectra. From the best fit values we computed the column densities of the three isotopologues and the corresponding isotopic ratios, these can be seen in Table 4.10.

4.2.4 Density profile of L1498

The density profile parameters for L1498 presented in Tafalla et al. (2004) were obtained from a fit to only 1 continuum wavelength assuming a constant temperature for the dust. Thanks to the availability of Herschel SPIRE continuum maps we are now able to obtain more reliable density profiles. These new profiles are more reliable because multiple wavelengths lets us disentangle the effects of column density and temperature on the dust emission. Variations on the dust temperature will vary the intensity of the dust emission, but also the intensity ratio between different wavelengths while a column density variation will vary the intensity but not the ratio between the different wavelengths.

To fit the dust emission and derive parameters for our density profile we have created a simple 1D radiative transfer model of the continuum dust emission, and fitted it to a radial cut of the continuum observations using the MCMC TOOLKIT. This radial cut was chosen based on the offsets for which we have better signal to noise ratio spectral observations Figure 4.29.

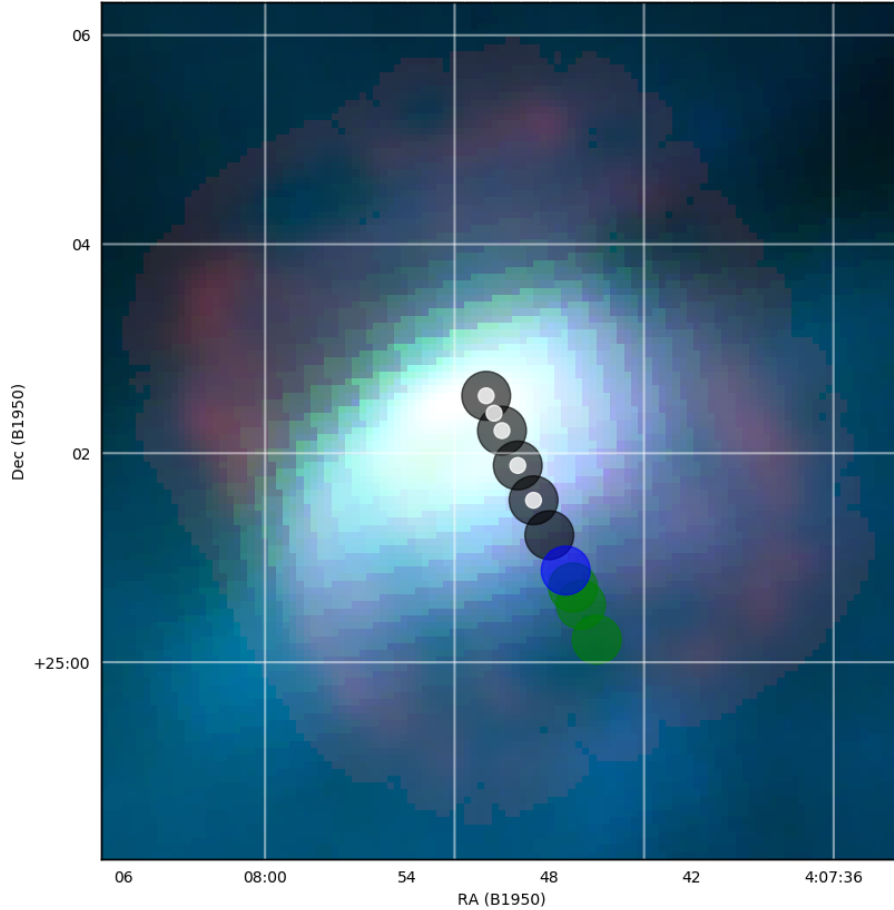


Figure 4.29 – Color composite map of L1498. 1.25 mm is Red, 500 μm is green and 250 μm is blue. Black circles indicate where the $J = 1 \rightarrow 0$ of all HCN isotopologues was observed, green circles indicate the positions that were only observed in HCN $J = 1 \rightarrow 0$, the blue circle indicates the position that was observed only on HCN and H^{13}CN $J = 1 \rightarrow 0$ and the white circles indicate the positions where HCN $J = 3 \rightarrow 2$ was observed. The sizes of the circles indicate the HPBW of the IRAM-30m telescope at the observed frequencies, 28'' for the $J = 1 \rightarrow 0$ transitions and 9'' for the HCN $J = 3 \rightarrow 2$ transition.

In our continuum emission model the dust emission of L1498 is assumed to be optically thin, so that it can be modelled as the sum of the emission of small cells in the line of sight which have an H_2 column density $n(r) \times \Delta l$, with Δl being the length of the cell in the line of sight, and $n(r)$ being the density at the centre of the cell, which is at a distance r from the center of the model. Under this assumption the continuum dust emission, $I_{\nu, \text{dust}}$, can be computed as:

$$I_{\nu, \text{dust}} = \sum^N \kappa_{\nu} B_{\nu}(T_{\text{dust}}(r)) n(r) \times \Delta l, \quad (4.17)$$

where \sum^N is the summation over the N cells in the line of sight, $B_{\nu}(T_{\text{dust}}(r))$ is the emission of a blackbody of temperature $T_{\text{dust}}(r)$ at frequency ν , and κ_{ν} is the mass absorption coefficient in cm^2/g at frequency ν .

To account for the wavelength dependency of the mass absorption coefficient we adopted the simple formula:

$$\kappa_{\nu} = \kappa_{\nu_0} \left(\frac{\nu}{\nu_0} \right)^{\beta}, \quad (4.18)$$

where β is the power law index for the dust opacity law and κ_{ν_0} is the dust absorption coefficient at frequency ν_0 . To fit the continuum maps κ_0 was set to $0.06 \times 10^{-2} \text{ cm}^2/\text{g}$ for $\nu_0 = 1.2 \text{ THz}$ ($250 \mu\text{m}$, Juvela et al., 2015). The value of β depends on the grain size distribution which can vary from source to source, therefore it is left to be fitted.

The density profile was chosen to be of the same form as in Tafalla et al. (2004), being that of eq. 4.14 minus the n_{ext} term. n_{ext} was dropped as the non homogeneity of the environment around L1498 shows up the in radial profiles of the herchel SPIRE maps at off-sets larger than 200 arc seconds (Figure 4.30). This non homogeneity makes it impossible to get a correct fit to n_{ext} .

As a first approximation we chose a constant dust temperature with model radius as in Tafalla et al., 2004. Under such an assumption the fit to the continuum emission does converge, but the resulting fit is less than optimal. The derived value for β is 2.2 which means that the mass absorption coefficient at $1250 \mu\text{m}$ is only $1.7 \times 10^{-3} \text{ cm}^{-2}\text{g}^{-1}$. With this low mass absorption coefficient the single dust temperature models underestimate the flux at $1250 \mu\text{m}$ by almost a factor of 2 (Figure 4.31). This is not the only problem as the radial profile of the emission at the Herschel SPIRE wavelengths is also not reproduced (Figure 4.32). Another problem is that the derived density profile has a very small plateau that is comparable to the beam size of the Herschel SPIRE images ($r_0 = 22''$) and its radial decay is too shallow ($\alpha = 1.2$). These parameters are outside the range expected for prestellar cores (Larson, 1969; Foster and Chevalier, 1993; Lesaffre et al., 2005). Another point where the derived profile is deficient is its central density which is too high ($n_0 = 1.8 \times 10^5 \text{ cm}^{-3}$) to be in agreement with

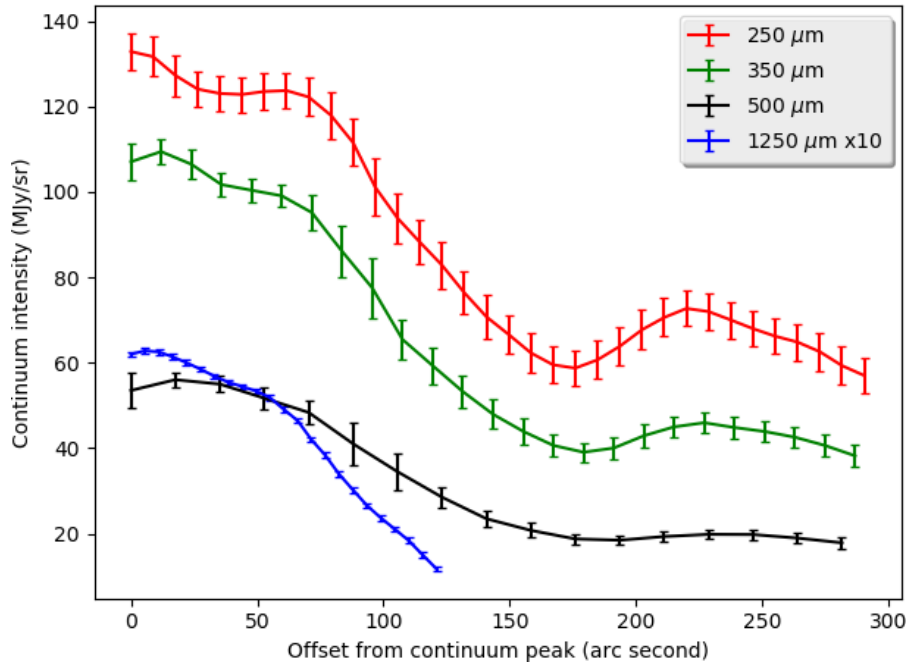


Figure 4.30 – Radial profile of the continuum emission along the SW axis of L1498. The offsets refer to the continuum peak of L1498 at $\alpha=4:10:52.2$, $\delta=25:10:20$ (J2000). The $1250 \mu\text{m}$ emission was multiplied by 10 so that it could be displayed on the same linear scale as the other continuum wavelengths. Notice the bump in emission at an offset of 220 arc seconds.

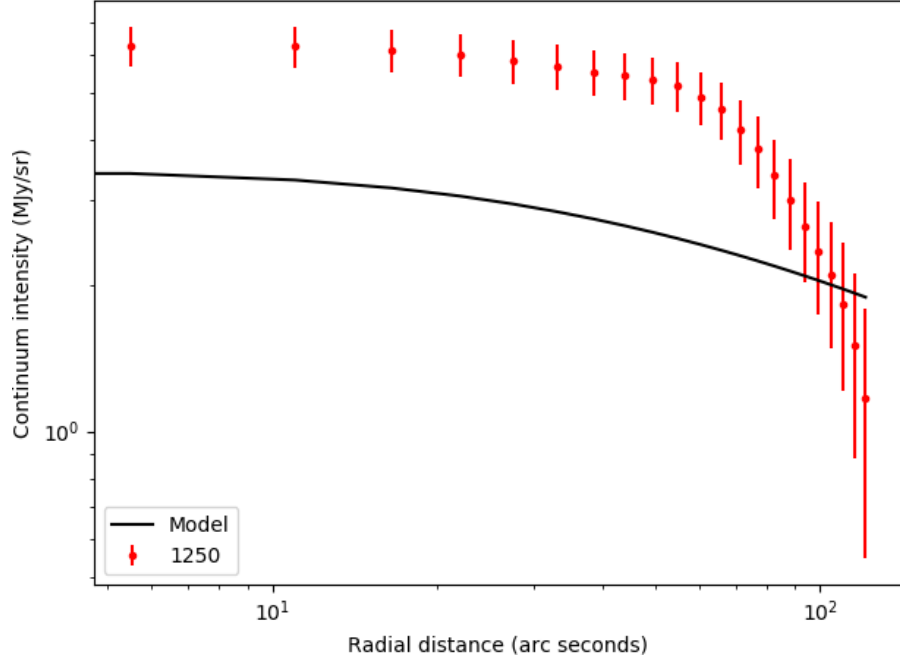


Figure 4.31 – Single dust temperature fit to the continuum emission at $1250\ \mu\text{m}$. Here we can see that the single dust temperature fit underestimates the emission at $1250\ \mu\text{m}$ by a factor of ~ 2 .

the emission of HCN $J = 3 \rightarrow 2$ which is highly sensitive to the central density and is best fit by a central density of $\sim 10^5\ \text{cm}^{-3}$.

Due to the failure of the single dust temperature model we decided to try a more realistic dust temperature profile. Due to the increased exposure to interstellar UV photons, dust grains in the more diffuse parts of molecular clouds are therefore warmer than grains in the denser parts (Zucconi, Walmsley, and Galli, 2001; Makiwa et al., 2016; Hocuk et al., 2017). To conciliate this two different temperature regimes we have adopted a dust temperature profile of the form:

$$T_{\text{dust}}(r) = T_0 + \frac{T_{\text{ext}} - T_0}{2} \left[1 + \tanh \left(\frac{r - r_{\text{tjump}}}{\Delta r_{\text{tjump}}} \right) \right] \quad (4.19)$$

where T_0 is the dust temperature at the centre of the model, T_{ext} is the dust temperature at $r = \infty$, the transition from the cold regime to the warmer regime is centred at radius r_{tjump} and has a characteristic width Δr_{tjump} .

This difference in temperature raised the concern that maybe the outer regions would dominate the dust emission thus making us incapable to probe the column density of L1498 towards its centre. This concern was abated when we computed the emission of the model as a function of radius and demonstrate that the emission is dominated by the emission of the cold and dense centre of the core Figure 4.33.

The final results for the continuum fit are shown in Table 4.11, and the results of the fit compared to the observations can be seen in Fig-

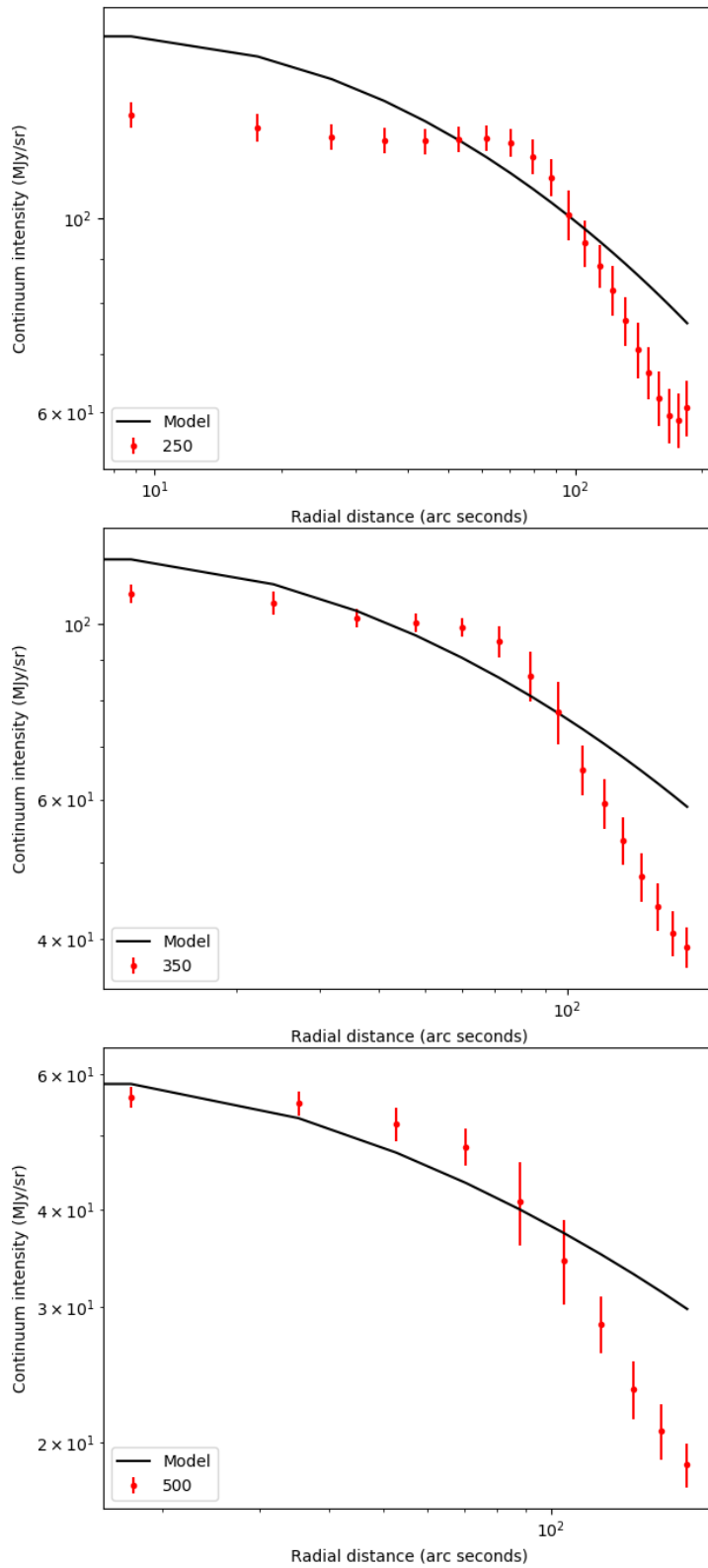


Figure 4.32 – Top panel: Single dust temperature fit to the continuum emission at 250 μm . Middle panel: Single dust temperature fit to the continuum emission at 350 μm . Bottom panel: Single dust temperature fit to the continuum emission at 500 μm . Here we can see that the best fit with a single dust temperature falls short of accurately reproducing the dust emission profiles at the Herschel SPIRE wavelengths.

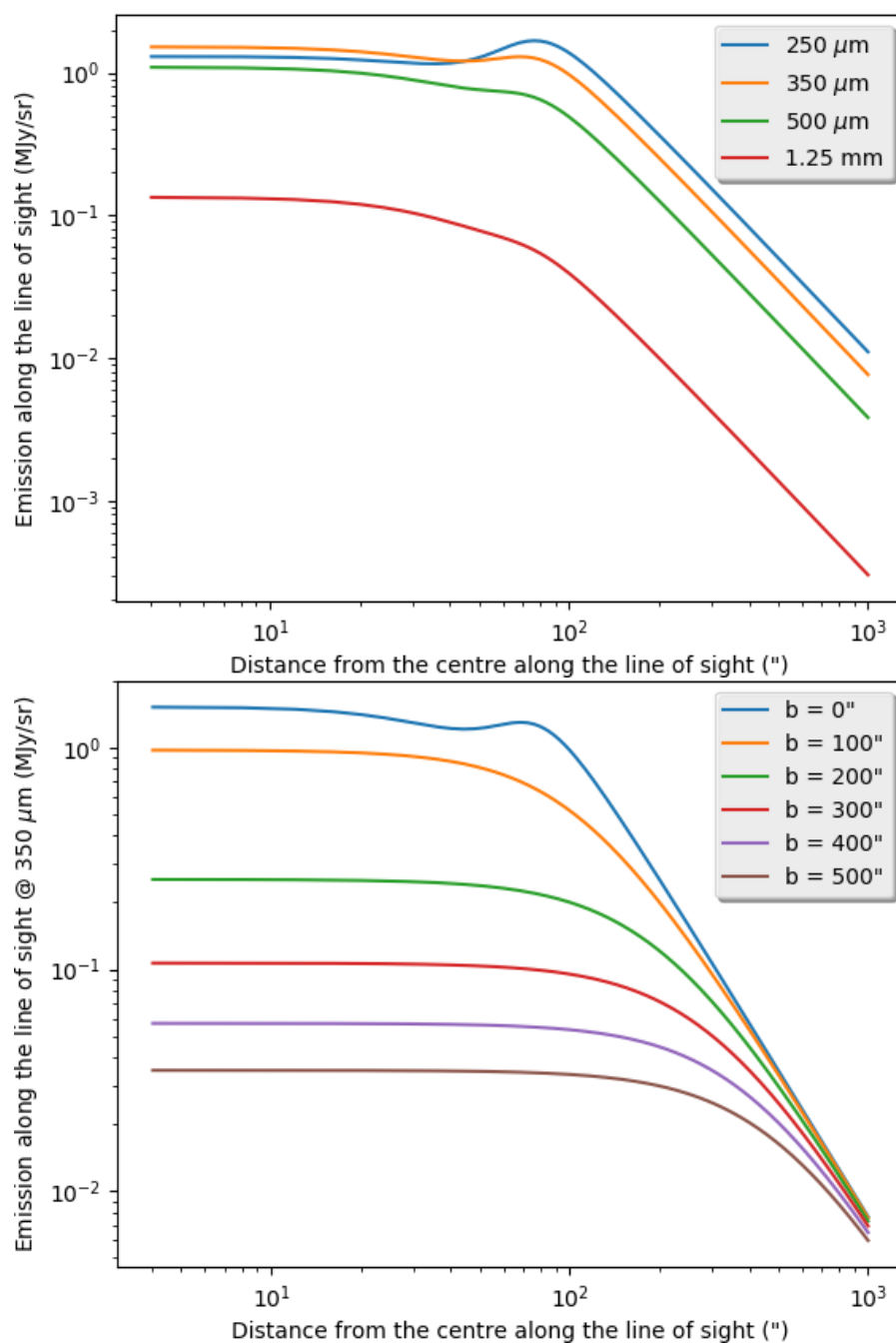


Figure 4.33 – Top panel: Dust emission at 4 different wavelengths as a function of distance along the line of sight towards the centre of the model. Bottom panel: Dust emission at 350 μm as a function of distance along the line of sight for different impact parameters, b . It is possible to see that the emission at small impact parameters is approximately two orders of magnitude more intense than the emission with larger impact parameters.

Table 4.11 – Best fit parameters for our continuum dust emission model.

Parameter	Value	Unit
$\log(n_0)$	$1.00 \pm 0.16 \times 10^5$	cm^{-3}
r_0	47 ± 5	arcsecond
α	2.2 ± 0.1	
T_0	9.8 ± 0.5	K
T_{ext}	14.6 ± 0.3	K
r_{tjump}	61 ± 3	arcsecond
Δr_{tjump}	26^{+10}_{-7}	arcsecond
β	1.56 ± 0.04	

ures 4.34 and 4.35. The resulting density and temperature profiles are shown in Figure 4.36. The cross histogram plot shown in Figure 4.37 demonstrates that all parameters of the fit have converged properly and therefore that the fit is satisfactory.

Our continuum fit differs significantly from the values obtained by Tafalla et al. (2004) for r_0 and α ($r_0=47''$ instead of $75''$, $\alpha = 2.2$ instead of 3.5), while the central density obtained here is consistent with Tafalla et al. (2004), $n_0 = 1 \times 10^5 \pm 0.15 \times 10^5 \text{ cm}^{-3}$ versus $0.94 \times 10^5 \text{ cm}^{-3}$. The discrepancy in r_0 and α can be explained by the fact that Tafalla et al. (2004) had only the $1250 \mu\text{m}$ map, which displays a large emission plateau and a sharp decay. Tafalla et al. (2004) also assumed that the dust temperature is constant at 10 K which works fine for single wavelength fits but fails when more wavelengths are added. Under this assumption the column density at larger radii has to be kept large to account for the intensity plateau seen in the radial profiles (Figure 4.30). While under the assumption that the dust temperature increases with increasing radius the decrease in column density is compensated by a increase in dust temperature sustaining the emission plateau.

In our fit $\beta=1.56 \pm 0.04$, this value is consistent with the expected range for prestellar cores (1.6-2.4, e.g. Makiwa et al., 2016). This value is much lower than the value measured by Chacón-Tanarro et al. (2017) in L1544 ($\beta = 2.3$), this discrepancy may arise from the fact that they fitted β with a fixed temperature profile, while here we fit both the temperature profile and β simultaneously. Another important difference is that they also fit $\kappa_{250\mu\text{m}}$ and find a value that is $\sim 3 - 4$ times the value we have adopted from Juvela et al. (2015). Thus β in Chacón-Tanarro et al. (2017) has to be larger than β derived here in order to compensate for the flux at 1.2 and 2 mm that they used to derive β and $\kappa_{250\mu\text{m}}$. If we pluck the values from Chacón-Tanarro et al. (2017)

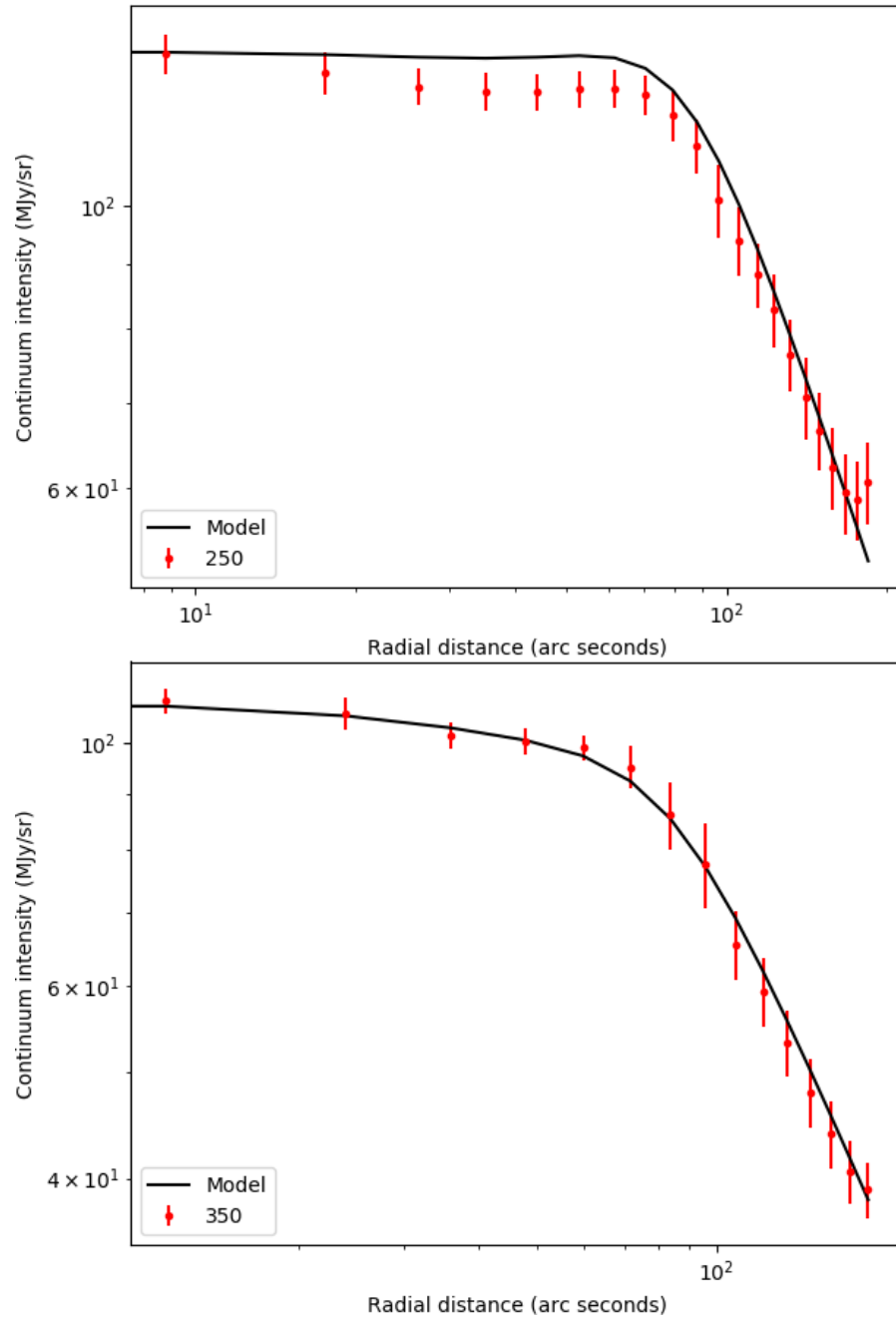


Figure 4.34 – Top panel: best fit continuum dust emission model along with the Herschel SPIRE observations at $250 \mu\text{m}$. Bottom panel: best fit continuum dust emission model along with the Herschel SPIRE observations at $350 \mu\text{m}$.

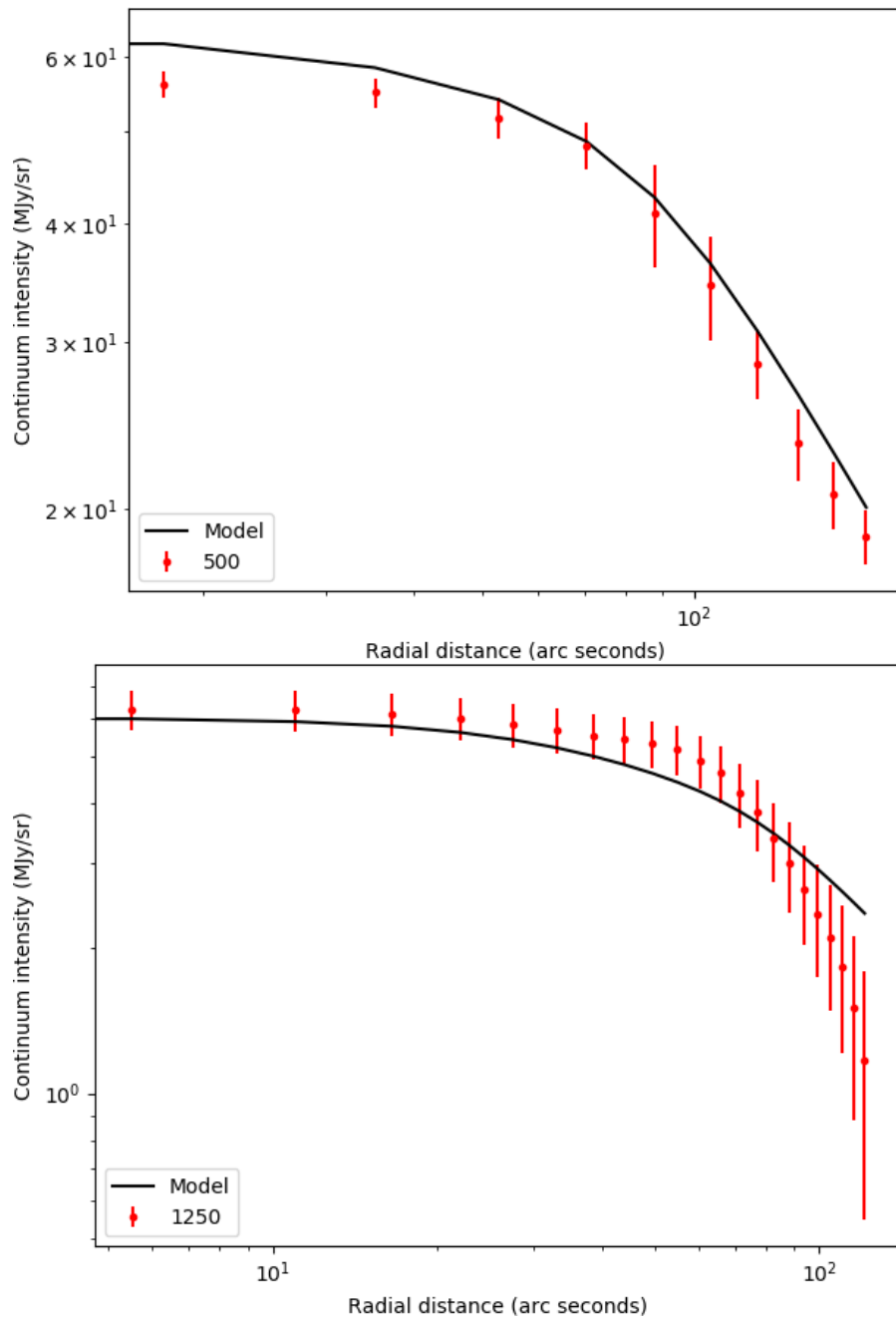


Figure 4.35 – Top panel: best fit continuum dust emission model along with the Herschel SPIRE observations at 500 μm . Bottom panel: best fit continuum dust emission model along with MAMBO observations at 1250 μm .

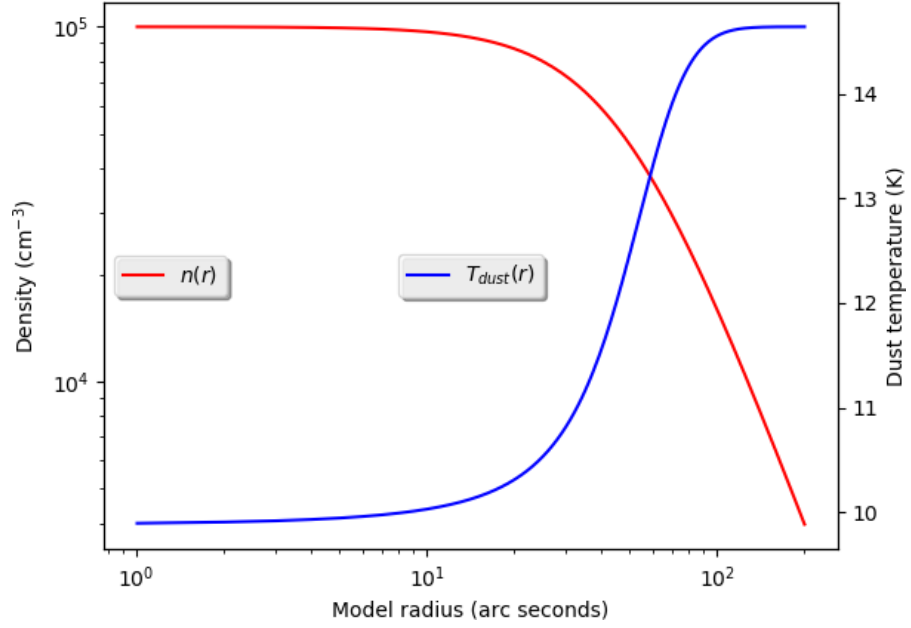


Figure 4.36 – Density and dust temperature profiles for the best fit dust continuum emission profile.

into eq. 4.18 we obtain $\kappa_{1.25\text{mm}} = 4.9 \times 10^{-3} \text{ cm}^{-2}\text{g}^{-1}$, if we do the same but with our values we also obtain $\kappa_{1.25\text{mm}} = 4.9 \times 10^{-3} \text{ cm}^{-2}\text{g}^{-1}$ which means that both values are in fact consistent with each other at $1250 \mu\text{m}$.

One interesting thing to note about Figure 4.37 is the presence of multiple correlations and anti-correlations between the fit parameters. The anti-correlation between n_0 and r_0 can be understood from the fact that an increase in any of them increases the dust column density and thus the emission, so as one parameter increases the other has to decrease to preserve the observed emission. The positive correlation between r_0 and α is related to the slope of the emission profile decay. Larger values of r_0 have to be coupled with larger values of α to preserve the slope seen on the radial profiles.

The positive correlations between r_0 and α on one side and r_{tjump} and Δr_{tjump} on the other are related to the slope of the emission profile. When r_0 is larger, α also increases, therefore the dust temperature jump has to be further from the centre as well as wider to compensate the increase in flux at $r \sim r_0$, and decrease in flux for $r > r_0$. The anti-correlations between n_0 and r_{tjump} , and T_0 and r_{tjump} come from the fact that a decrease in r_{tjump} increases the flux at short radii which has to be offset by either a decrease of T_0 or n_0 to conserve the flux.

The anti-correlation between n_0 and T_0 comes from the fact that the emission is proportional to the column density of dust and the dust temperature, albeit through B_ν . The anti-correlations between β and the two dust temperatures (T_0 and T_{ext}) come from the fact that β has

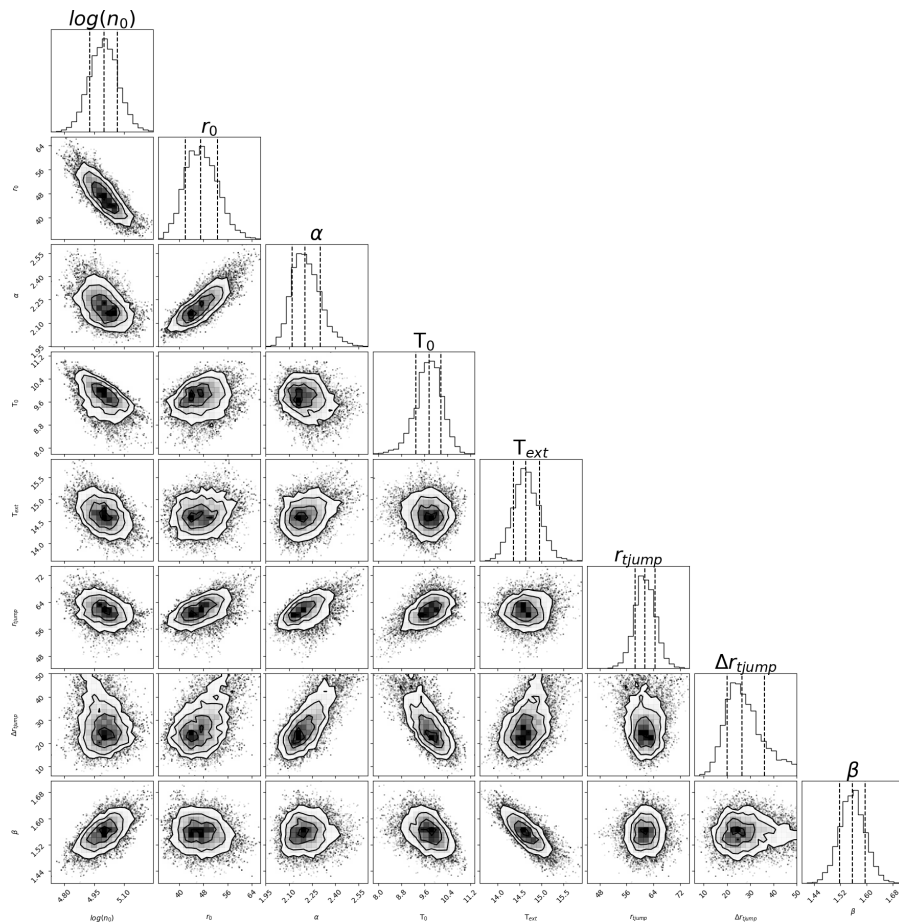


Figure 4.37 – Cross histograms for the parameters in the continuum fit.

an impact on the relative fluxes between the different wavelengths, with large values of β favouring short wavelengths, which is the opposite effect of the temperature. Thus to maintain the same ratio between the fluxes at different wavelengths a decrease in β has to be offset by an increase in either T_0 at small radii or T_{ext} at large radii. The remaining correlation, that between β and n_0 comes from the fact that an increase in column density requires a decrease in dust temperature to maintain the same emission, and therefore with a decrease in dust temperature β has to increase to maintain constant the flux ratio between the different continuum wavelengths.

4.2.5 ALICO/MCMC fitting of HCN, H^{13}CN and HC^{15}N spectra

As demonstrated in Section 4.1.3.2 a complex source model is needed to accurately reproduce the hyperfine anomalies of HCN. For this reason we have chosen to use the parametric functions described therein to model the variations of the density, velocity and non thermal broadening of L1498. The sole difference is the HCN abundance profile. Here we choose a simple step function to test the possibility of depletion of HCN towards the centre of the core as proposed by Padovani et al. (2011). The abundance profile of the HCN isotopologues was taken to be a multiple of the HCN abundance profile under the assumption that HCN is co-spatial with its isotopologues.

We have chosen to fit all spectral lines simultaneously as different lines provide probes for different aspects of the source model. The H^{13}CN and HC^{15}N $J = 1 \rightarrow 0$ emission is expected to be close to be optically thin, therefore these species are the best probes for the presence of a depletion hole as well as the non thermal velocity dispersion at the core centre (σ_0). The HCN $J = 1 \rightarrow 0$ emission is extremely optically thick as demonstrated by the self-absorption features seen in its spectra, therefore this spectral line is expected to probe the external most parts of the core. The probing of the external part of the core is essential to the determination of the collapse velocity profile and non thermal velocity dispersion profile as those show significant variation only at large radii. Finally the HCN $J = 3 \rightarrow 2$ emission is sensitive to the abundance of HCN as its two satellite hyperfine components ($F = 2 \rightarrow 2$ and $F = 3 \rightarrow 3$) are expected to be at most moderately optically thick and their hyperfine ratio is one of the most sensitive to changes in the abundance of HCN (Figure 4.20).

In the end the MCMC fit to the spectra with ALICO/MCMC has 12 free parameters:

1. σ_0 , the non thermal velocity dispersion at $r = 0$, in km/s.
2. σ_{ext} , the non thermal velocity dispersion at $r = \infty$, in km/s.
3. r_j , the position where the transition between σ_0 and σ_{ext} occurs, in normalised radial units.

4. Δr_j , the characteristic width of the transition between σ_0 and σ_{ext} occurs, in normalised radial units.
5. V_c , the peak collapse velocity, in km/s.
6. r_V , the position where the peak collapse velocity occurs, in normalised radial units.
7. Δr_V , the dispersion of the collapse velocity profile, in normalised radial units.
8. $X_0(\text{HCN})$, the abundance of HCN at $r = 0$ up to r_{X_1} , abundance relative to H_2 .
9. r_{X_1} , the radius at which the abundance of HCN changes from $X_0(\text{HCN})$ to $X_1(\text{HCN})$, in normalised radial units.
10. $X_1(\text{HCN})$, the abundance of HCN radii larger than r_{X_1} , abundance relative to H_2 .
11. $X(\text{HCN})/X(\text{H}^{13}\text{CN})$, the abundance ratio between HCN and H^{13}CN .
12. $X(\text{HCN})/X(\text{HC}^{15}\text{N})$, the abundance ratio between HCN and HC^{15}N .

The best fitting values as of the writing of this manuscript can be found in Table 4.12. The best fit models are displayed along with the observations in Figures 4.38 to 4.41.

These results contradict the results of Padovani et al. (2011) who suggested that there is a depletion hole for HCN in L1498 with a size of 8×10^{16} cm where the abundance of HCN drops by several orders of magnitude. The small drop in abundance towards the centre can be explained by the fact that towards the central position the large beam of the IRAM-30M telescope for the $J = 1 \rightarrow 0$ transitions (HPBW $\sim 28''$) also samples the emission from the compacted side of the core towards the northwest, thus decreasing the average column density inside the beam. In fact other studies regarding the abundance of HCN in prestellar cores have found no evidence of HCN depletion. Sohn et al. (2004) mapped HCN $J = 1 \rightarrow 0$ towards six prestellar cores and found that the intensity of the $F = 0 \rightarrow 1$ component correlated strongly with the intensity of N_2H^+ suggesting that HCN does not suffer depletion. In accordance to that Lee et al. (2007) found that the abundance of HCN relative to H_2 in L694 – 2 appears to be constant at 7×10^{-9} and in L1157 it shows a tendency to increase inwards, from 1.7 to 3.5×10^{-9} . Recently Spezzano et al. (2017) did a map of the H^{13}CN $J = 1 \rightarrow 0$ emission towards the very dense prestellar core L1544 (central density $\sim 1 \times 10^7 \text{ cm}^{-3}$, Keto and Caselli, 2010), in this map it is clearly seen that HCN does not deplete from the gas phase even in the most dense parts of prestellar cores.

The HCN abundance obtained from ALICO/MCMC translates into a column density of $1.25 \times 10^{14} \text{ cm}^{-3}$, this value is slightly larger than the value obtained with RADEX+NSLAB and this difference can

Table 4.12 – Best fit values for the ALICO/MCMC fit to the emission of HCN and its isotopologues in L1498.

Parameter	Value	Unit	Fixed
n_0	$1.00 \pm 0.16 \times 10^5$	cm^{-3}	yes
n_{ext}	5×10^2	cm^{-3}	yes
r_0	47 ± 5	arc second	yes
α	2.2 ± 0.1		yes
T_{kin}	10	K	yes
σ_0	$0.046^{+0.033}_{-0.002}$	km/s	no
σ_{ext}	0.25 ± 0.08	km/s	no
r_j	320 ± 14	arc second	no
Δr_j	78 ± 14	arc second	no
V_c	-0.26 ± 0.02	km/s	no
r_V	290 ± 8	arc second	no
Δr_V	55 ± 8	arc second	no
$X_0(\text{HCN})$	$2.6 \pm 0.2 \times 10^{-9}$	relative to H_2	no
r_{X_1}	33 ± 8	arc second	no
$X_1(\text{HCN})$	$6.1 \pm 0.4 \times 10^{-9}$	relative to H_2	no
$X(\text{HCN})/X(\text{H}^{13}\text{CN})$	45 ± 3		no
$X(\text{HCN})/X(\text{HC}^{15}\text{N})$	338 ± 28		no

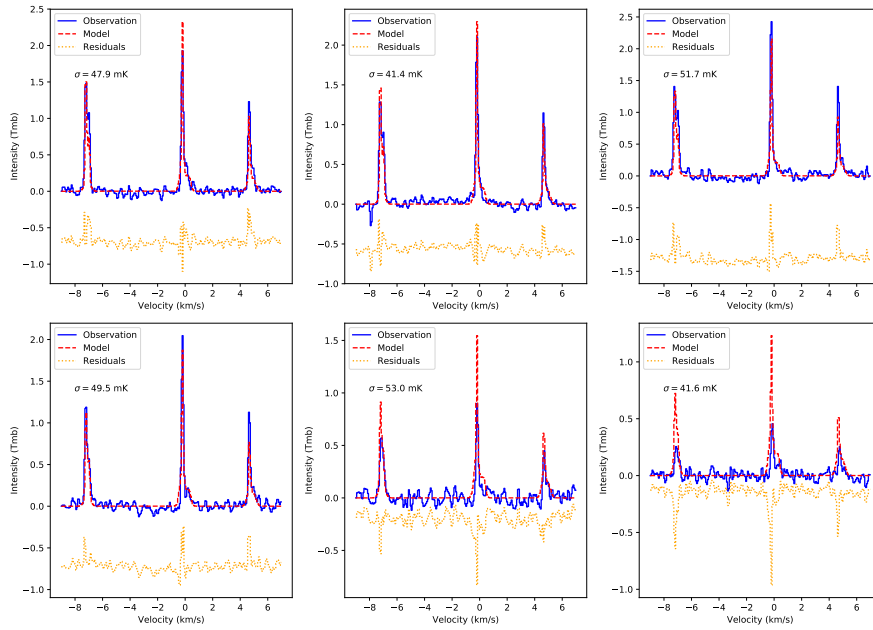


Figure 4.38 – Best fit HCN $J = 1 \rightarrow 0$ (red) spectra along the HCN $J = 1 \rightarrow 0$ observations (blue) and the residuals of the fit (orange) for different offsets from the continuum peak of L1498: top left (0,0)"', top centre: (-10,-20)"', top right (-20,40)"', bottom left (-30,-60)"', bottom centre: (-50,-100)"', bottom right (-60,-120)"'

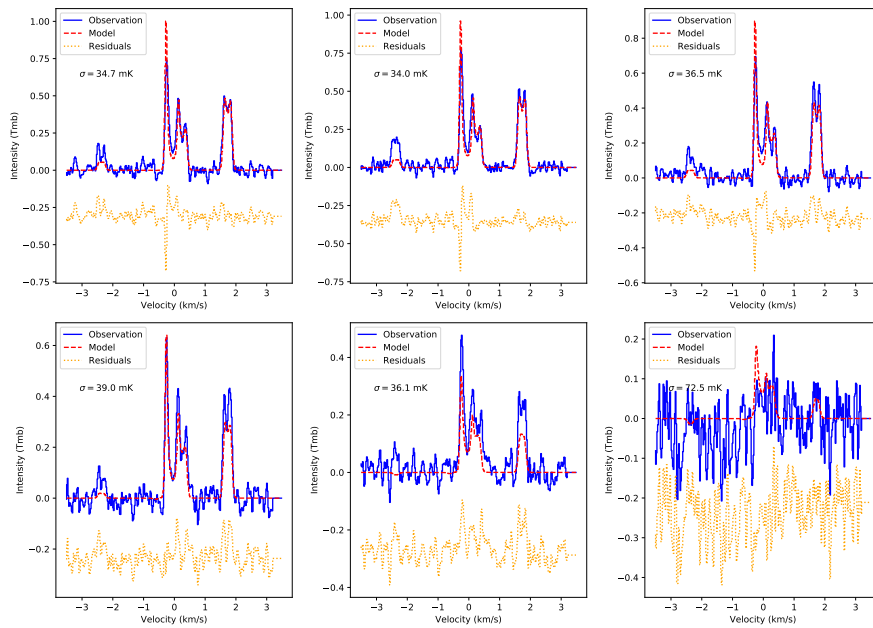


Figure 4.39 – Best fit HCN $J = 3 \rightarrow 2$ (red) spectra along the HCN $J = 3 \rightarrow 2$ observations (blue) and the residuals of the fit (orange) for different offsets from the continuum peak of L1498: top left (0,0)"', top centre: (-5,-10)"', top right (-10,-20)"', bottom left (-20,-40)"', bottom centre: (-30,-60)"', bottom right (-40,-80)"'

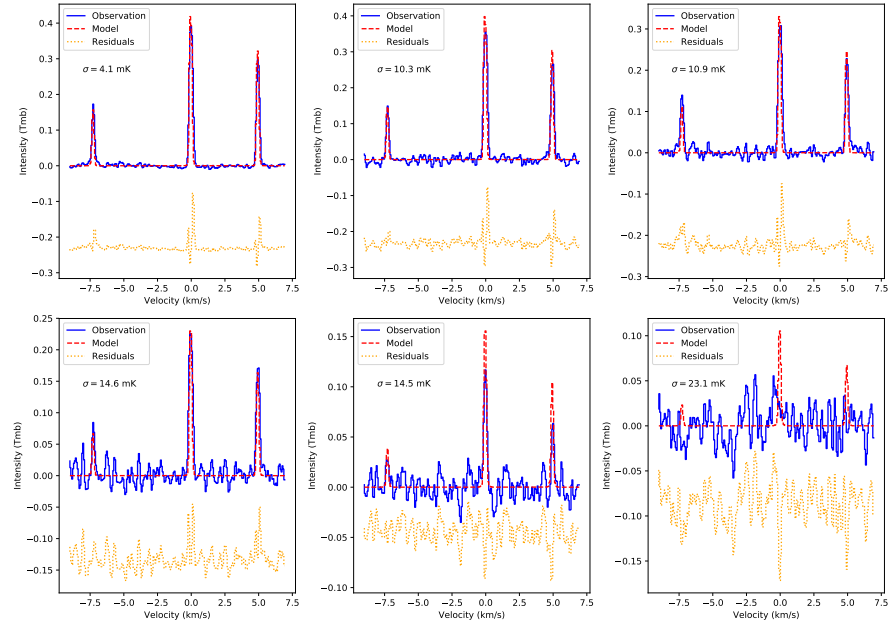


Figure 4.40 – Best fit $\text{H}^{13}\text{CN } J = 1 \rightarrow 0$ (red) spectra along the $\text{H}^{13}\text{CN } J = 1 \rightarrow 0$ observations (blue) and the residuals of the fit (orange) for different offsets from the continuum peak of L1498: top left (0,0)'' , top centre: (-10,-20)'' , top right (-20,-40)'' , bottom left (-30,-60)'' , bottom centre: (-50,-100)'' , bottom right (-60,-120)'' .

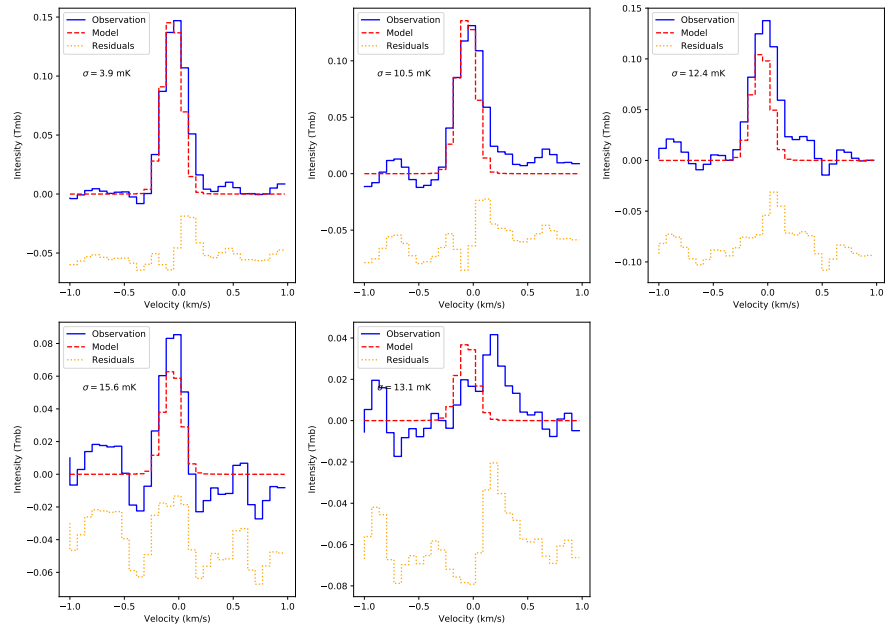


Figure 4.41 – Best fit $\text{HC}^{15}\text{N } J = 1 \rightarrow 0$ (red) spectra along the $\text{HC}^{15}\text{N } J = 1 \rightarrow 0$ observations (blue) and the residuals of the fit (orange) for different offsets from the continuum peak of L1498: top left (0,0)'' , top centre: (-10,-20)'' , top right (-20,-40)'' , bottom left (-30,-60)'' , bottom centre: (-50,-100)'' .

be understood by the fact that LVG analysis tend to underestimate the column density of optically tracers such as HCN. Nevertheless the isotopic ratios obtained with ALICO/MCMC are consistent within one sigma with the isotopic ratios obtained with RADEX+N_{SLAB}. This confirms that RADEX+N_{SLAB} can be used as a inexpensive first guess generator for the more expensive ALICO/MCMC runs. One other interesting point is that the LTE derived HCN/HC¹⁵N ratio is also consistent with the ALICO/MCMC ratio as long as we assumed that HCN is fractionated in carbon with $^{12}\text{C}/^{13}\text{C} = 45$, which is the value we find for the $^{12}\text{C}/^{13}\text{C}$ ratio in HCN with ALICO/MCMC.

4.2.6 *Article on HCN/HC¹⁵N in L1498*

The work done on the isotopic ratio of nitrogen in L1498 is soon to be submitted to a peer reviewed journal. The current status of the draft is included in the following pages.

The abundance of HCN and its isotopologues in L1498

V. S. Magalhães¹, P. Hily-Blant^{1,2}, A. Faure¹, and F. Lique^{2,3}

¹ Institut de Planétologie et d'Astrophysique de Grenoble, Université Grenoble Alpes, 414 Rue de la Piscine, Grenoble CEDEX 9
e-mail: victor.de-souza-magalhaes@univ-grenoble-alpes.fr

² Institut Universitaire de France

³ Université du Havre

⁴ Arcetri

ABSTRACT

tbid

Key words. ISM: clouds – stars: formation – ISM: individual objects L1498

1. Introduction

The link between the chemical composition of the protosolar nebula and of the interstellar medium (ISM) may be more direct than previously thought. Recent work on the comet 67P/Churyumov-Gerasimenko done with data obtained by the ROSINA instrument on the ESA/ROSETTA spacecraft shows that the presence and abundance of O₂ and S₂ on the coma of this comet are consistent with a prestellar origin for these molecules within cometary ices (Bieler et al. 2015; Calmonte et al. 2016). The origin of the materials seen in comets is indeed particularly relevant as comets are thought to be pristine records of the protosolar nebula (PSN) (Bockelée-Morvan et al. 2015). Two scenarios are possible: one in which the interstellar grain structure and composition is only marginally altered during comet formation. In this scenario, O₂ and S₂ would be produced by radiolysis of H₂O and H₂S, respectively, during the prestellar phase (Taquet et al. 2016; Mousis et al. 2016a, 2017). In the other scenario, the icy components rearrange themselves in clathrates during comet formation, thus trapping gases from the PSN inside the grains (Mousis et al. 2016a,b). In contrast with the first scenario, some mixing is thus expected place between the ice and the gas phases during comet formation.

One possible clue to decide which is the best scenario lies in the isotopic ratio of nitrogen in comets. The nitrogen isotopic ratio in solar system comets is basically uniform, $^{14}\text{N}/^{15}\text{N} \approx 144$, and independent of the molecular carrier (NH₂, CN, HCN) and comet family (Mumma & Charnley 2011; Shinnaka et al. 2016; Hily-Blant et al. 2017a). Yet this ratio is three times lower than that of the bulk in the PSN, $^{14}\text{N}/^{15}\text{N} = 441$ (Marty et al. 2011), a sharp difference which raises questions regarding the formation of comets. Such discrepancy also tells us that there were at least two distinct reservoirs of nitrogen in the PSN when comets formed, a primary one, sampled by the Sun and Jupiter, and a ¹⁵N-rich, secondary one, sampled by the comets. These two reservoirs may have an interstellar origin or the secondary reservoir may have been created *in situ* during the comet formation stage. Interestingly, the comparison of the CN/C¹⁵N and HCN/HC¹⁵N ratios measured in several close-by protoplanetary disks has revealed that two reservoirs —the bulk with an elemental ratio 323 ± 30 , and a fractionated reservoir with a ratio

111 ± 19 — are present in these PSN analogues with precisely the same 3:1 ratio as in the primitive solar system (Hily-Blant et al. 2017a).

To explore the pre-solar origin of these two reservoirs, it is necessary to measure the isotopic ratio of nitrogen at different stages of the star formation process. In the prestellar stage, isotopic ratios from nitrogen hydrides —NH₃ and NH₂D, N₂H⁺— which are presumably chemical descendants of N₂ (Hily-Blant et al. 2010, 2013a), have been measured directly yielding a weighted average of 336 ± 16 (Hily-Blant et al. 2017a), hence compatible with the elemental ratio of 323 ± 30 . On the other hand, species in the nitriles family —CN, HCN, and HNC— likely chemical descendants of atomic nitrogen (Hily-Blant et al. 2010, 2013a) present a big challenge for direct measurement of their isotopic ratios as the opacity of the main isotopologue is too great for an accurate measurement of their column densities in the dense ISM. In some instances, the hyperfine splitting of the rotational lines provide optically thin transitions, as in CN, which may be used to infer the total column density, hence allowing direct measurements (Adande & Ziurys 2012). However, departures of the hyperfine intensity ratios from single excitation temperature predictions are often met in cold cores which trouble the process (Guilloteau & Baudry 1981; Walmsley et al. 1982; Adande & Ziurys 2012). A common work-around is the double isotopologue method, in which the main isotopologue is replaced by its less abundant ¹³C-isotopologue, (Ikeda et al. 2002; Hily-Blant et al. 2013b,a), as in the case of HCN, for which the nitrogen isotopic ratio derives from

$$\frac{\text{HCN}}{\text{HC}^{15}\text{N}} = \frac{^{12}\text{C}}{^{13}\text{C}} \times \frac{\text{H}^{13}\text{CN}}{\text{HC}^{15}\text{N}} \quad (1)$$

where it is assumed that HCN/H¹³CN is equal to the elemental carbon isotopic ratio. A usual value for the latter in the present-day solar neighbourhood is $^{12}\text{C}/^{13}\text{C}=70$ (Milam et al. 2005). Nevertheless, chemical models suggest that the carbon isotopic ratio in nitriles may be far from the elemental one (Roueff et al. 2015), namely, the HCN/H¹³CN ratio in dense and cold cores is predicted in the range from 90 to 140. Therefore isotopic ratios in the dense ISM based on the double isotopologue method should be regarded with a grain of salt.

Table 1. Summary of the line observations. The reference position is $(\alpha, \delta)_{J2000} = 04:10:52.2, +25:10:20$.

Line	Rest. Freq. MHz	δv km s ⁻¹	T_{rec} K	T_{sys} K	rms mK [Tmb]	Program
HCN(1-0)	88631.6022	0.066		115	50	031-11
		0.066		100	20	008-16
HCN(3-2)	265886.4339	0.022		170	36	105-16
H ¹³ CN(1-0)	86339.9214	0.068		90	10	007-16
HC ¹⁵ N(1-0)	86054.9664	0.068		90	10	007-16

In some instances, however, the ¹²C/¹³C ratio can be measured in the carrier of interest. Taniguchi & Saito (2017) measured the isotopic ratio of nitrogen in HC₃N and HC₅N in the cyanopolyne peak of TMC-1 (see Hily-Blant et al. 2017b, for a review). The HC₅N/HC₃N abundance ratio was measured both indirectly and directly, leading to ratios ¹⁴N/¹⁵N = 323 ± 80 and ¹⁴N/¹⁵N = 344 ± 53 respectively. The isotopic ratio of nitrogen in HC₅N is thus in harmony with the elemental ratio of 323±30 (Hily-Blant et al. 2017a). For HC₃N, the indirect and direct methods also agree within 1σ, and the derived average value is 264±40. This ratio is only marginally compatible with the local ISM, suggesting a secondary reservoir of nitrogen in the ISM. For the double isotopologue method, the values of ¹²C/¹³C were measured for all carbon atoms in either HC₃N or HC₅N (Taniguchi et al. 2016), making the determination more robust than would be otherwise expected.

The chief objective of the present work is the direct measurement of the nitrogen isotopic ratio in a nitrile (HCN) in a prestellar core, L1498 located at a distance of 140 pc, at the South-West end of the Taurus-Auriga complex. To achieve our aims, we use the emission of the $J = 1 \rightarrow 0$ and $J = 3 \rightarrow 2$ rotational transitions of HCN and the $J = 1 \rightarrow 0$ transition of H¹³CN and HC¹⁵N, along a cut through L1498. The synthetic spectra were generated using our Accelerated Lambda Iteration COde, ALICO, a python wrapping over the 1Dart code (Daniel & Cernicharo 2008). ALICO handles line overlaps, including hyperfine transitions, which is fundamental for the reproduction of the HCN spectra from cold cores (Gottlieb et al. 1975; Guilloteau & Baudry 1981; Gonzalez-Alfonso & Cernicharo 1993). In the process, a physical model of the source (density, dust temperature) is required, which is obtained by fitting the Herschel/SPIRE and IRAM30m/MAMBO continuum maps at 250, 350, 500, and 1250 μm simultaneously.

2. Observations

Our observations can be divided in two datasets: spectra of HCN and its isotopologues, used to infer the abundances of HCN and its isotopologues; and a set of continuum maps used to derive the radial density profile of L1498.

2.1. HCN and its isotopologues

All our observations of HCN and its isotopologues were obtained at the IRAM-30m telescope, albeit in different runs (see Table 1 for a summary). All spectra have been reduced and analyzed using the IRAM GILDAS/CLASS software. Bandpass calibration was measured every 15 min using the standard three-steps method implemented at IRAM-30m. The typical receiver and system temperatures are 100 and 170 K at 89 and 266 GHz respectively. The obtained rms (main-beam temperature scale) are 10 mK for the H¹³CN and HC¹⁵N(1-0), 20 to 50 mK for

HCN(1-0), and 36 mK for HCN(3-2). Pointing and focus were checked regularly on a one to two hours basis, leading to a pointing accuracy of typically 1-2'' at all frequencies. Finally, residual bandpass effects were removed by subtraction of low-order polynomials (up to degree 3). Table 1 summarizes the observation setups and performances. Spectra were brought into a main-beam temperature scale using tabulated beam efficiencies appropriate at the time of observations. Figures ?? and ?? show the final set of spectra.

2.2. Continuum

We retrieved the Herschel/SPIRE maps at 250, 350 and 500 μm, from the Gould Belt Survey (André et al. 2010) available from the Herschel public archive. We retrieved Level 3 data which were calibrated following the standard *extended source* procedure of pipeline SPG v14.1.0. In the process, an offset was added to the images to comply with ESA/Planck absolute intensities. The continuum map at 1.25 mm was obtained at IRAM-30m telescope with the MAMBO 37-channels bolometer array (Tafalla et al. 2002). The continuum maps (in MJy/sr) can be seen in Fig. 1. For the Herschel maps, the statistical noise was computed as the quadratic sum of the calibration noise (as estimated by the pipeline and taken from the file header) and the contribution from the spatially varying contribution from cirrus-like emission, showing up in histograms of the intensity as a broad, low-level, Gaussian. Indeed, two-Gaussian fits to these histograms recover well the calibration uncertainty. At 1250 μm, the noise was estimated in a similar fashion although a single Gaussian was sufficient. The final noise are 4.1, 2.2, 1.0, and 0.6 MJy/sr at 250, 350, 500, and 1250 μm respectively.

3. Physical model of L1498 from the dust emission

The line radiative transfer calculations of the lines of HCN and its isotopologues towards L1498 compute the populations at the hyperfine level, in spherical geometry, assuming density, temperature, and velocity profiles, as well as a profile of the velocity dispersion. The number of free parameters can become outrageously large in such simulations, but in principle all these parameters could be minimized—at least after adopting some simple parametrization for each—using the various transitions at the several locations along the cut. Nevertheless, we have used maps of the dust-dominated continuum emission towards L1498 (Fig. 1) to obtain independent constraints on the density profile which is critical to the calculation of the molecular excitation. The present analysis encompasses and extends beyond earlier works (Tafalla et al. 2006), by considering the dust emission at four wavelengths, which allow us to derive constraints on the density and dust temperature profiles. In the process, the spectral index is also measured, and found in very good agreement

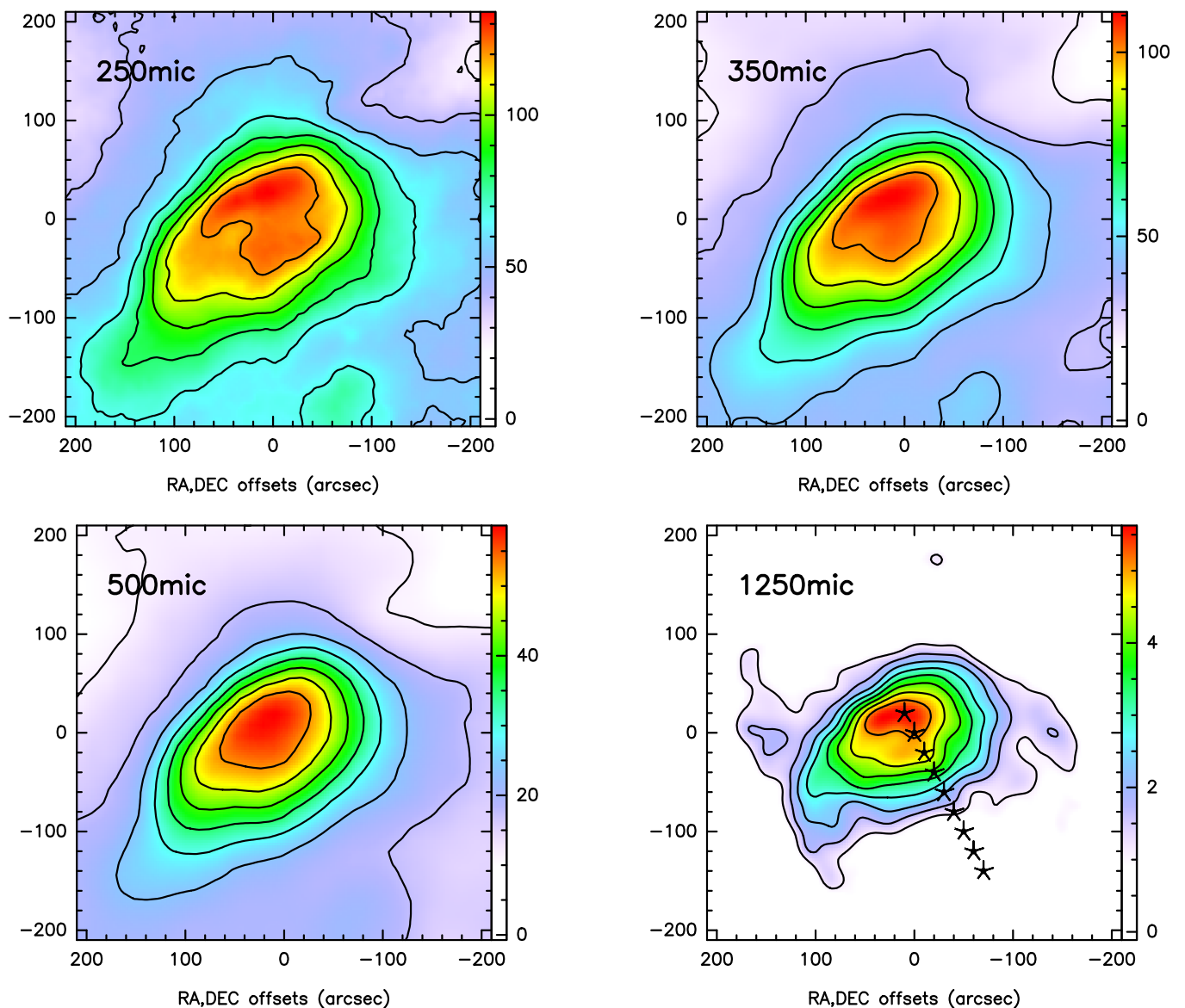


Fig. 1. Herschel/SPIRE and IRAM30m/MAMBO maps of the continuum emission (in MJy/sr) at 250, 350, 500, and 1250 μm . The HPBW are 18, 24, 35, and 11'' respectively. Contours are evenly spaced between 20 to 90% of the maximum intensity. The reference position is $(\alpha, \delta)_{J2000} = 04:10:52.2, +25:10:20$.

with comprehensive studies. We here review the basic model and assumptions used in the analysis of the dust emission maps.

3.1. Dust emission

From Kirchoff's law, the emissivity of the dust is directly related to the absorption coefficient, noted κ_ν (in $\text{cm}^2 \text{g}^{-1}$) at frequency ν , which we hereafter express by gram of dust and gas, assuming a standard gas-to-dust mass ratio of 1%. The modeling of the dust emission then follows a standard approach (Bergin & Tafalla 2007) in which the optically thin dust emission is treated as a graybody radiation

$$I_\nu = 2 \int \kappa_\nu n_{\text{H}_2}(x) \mu_{\text{H}_2} m_{\text{H}} B_\nu [T_{\text{d}}(x)] dx \quad (2)$$

where the integral extends over the line of sight. In our notation, m_{H} is the mass of one hydrogen atom, $\mu_{\text{H}_2} = 2.8$ is the mean molecular weight per H_2 molecule, assuming 10% of Helium atoms with respect to total hydrogen nuclei. $B_\nu(T_{\text{d}})$ is the

emission of a blackbody at temperature T_{d} and frequency ν . Note that in our formulation, κ_ν is assumed homogeneous, but the dust temperature is allowed to vary along the line of sight.

The frequency dependence of the dust absorption coefficient is described by a power-law

$$\kappa_\nu = \kappa_{250} (\lambda/250 \mu\text{m})^{-\beta} \quad (3)$$

This parametrization appears to hold reasonably well at the sub-mm to mm wavelengths of concern in our analysis, although the value of κ_0 and of the spectral index β are known to vary with the temperature and composition of the dust particles (Juvella et al. 2015a; Demyk et al. 2017). With such a parametrization of κ_ν , β primarily constrains the long wavelength, Rayleigh-Jeans, domain of the emission where $B_\nu \propto \nu^{2+\beta}$. On the other hand, the value of κ_0 fixes the dust column density but not the shape of the SED. Typical values of β that are appropriate for dense gas are in the range 1.5–3, with $\beta = 2$ being a commonly adopted value which describes the asymptotic behaviour of κ_ν at long wavelength. Comprehensive multiwavelengths analysis of dust

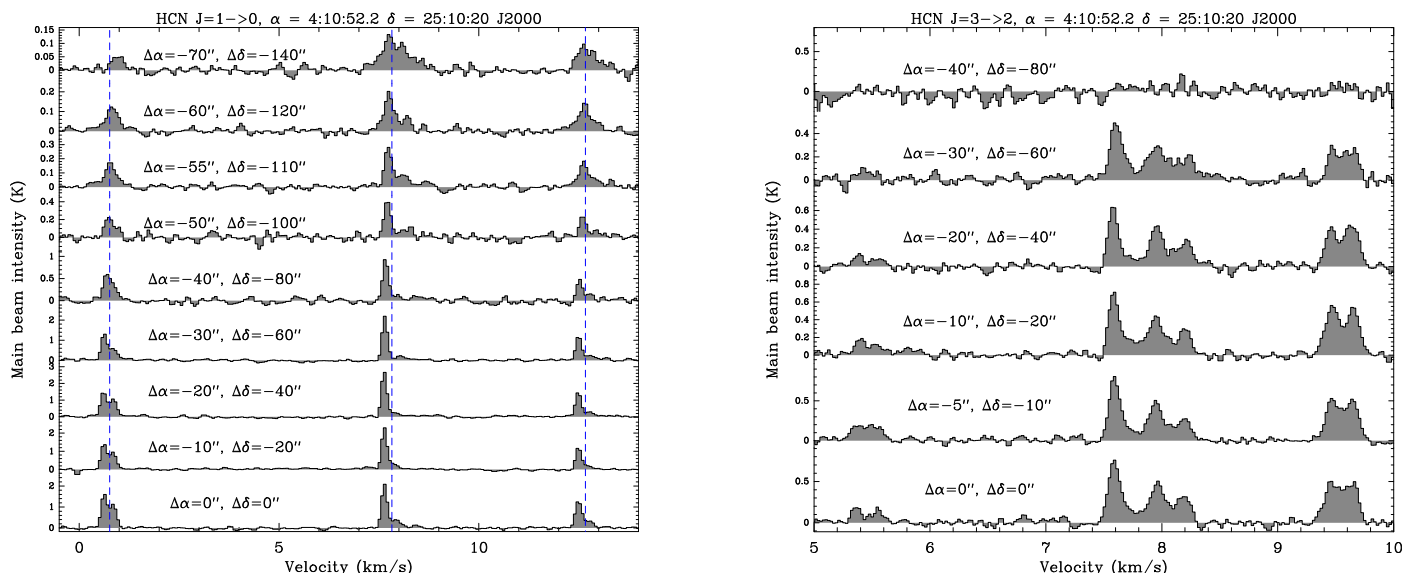


Fig. 2. HCN $J = 1 \rightarrow 0$ (left) and $J = 3 \rightarrow 2$ (right) spectra at several positions towards L1498 (RA-DEC offsets from the continuum peak position are in seconds of arc). The systemic velocity for each of the hyperfine components is indicated (dashed blue lines).

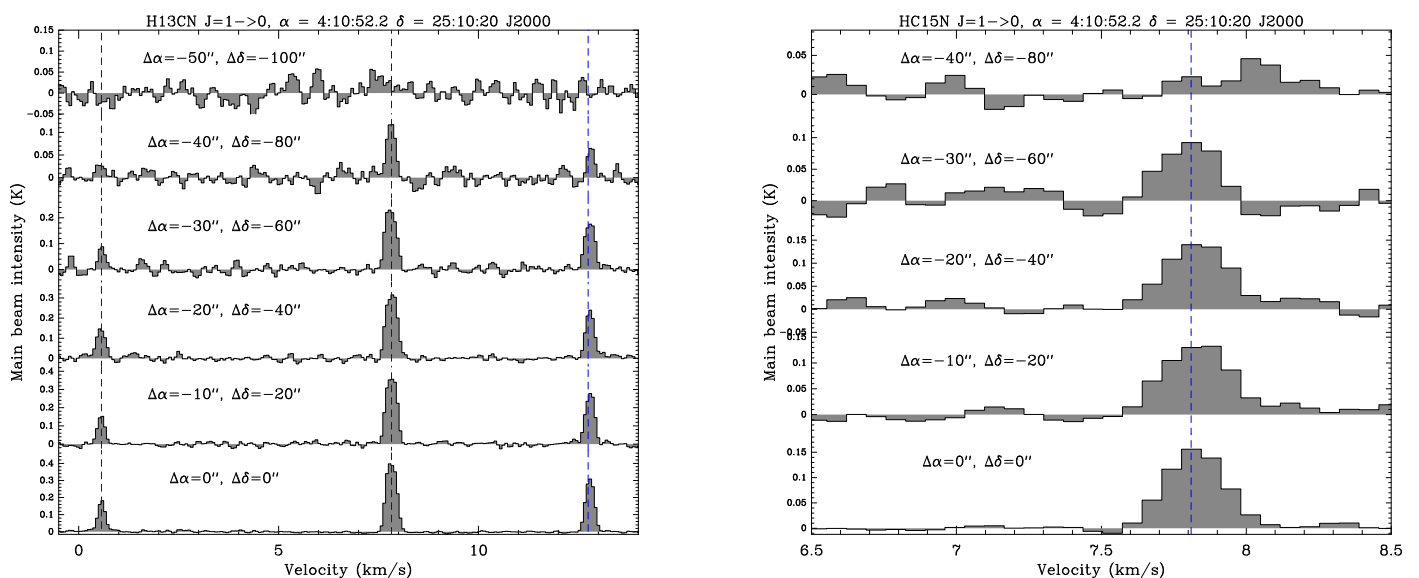


Fig. 3. Same as Fig. 2 for the $J = 1 \rightarrow 0$ transition of H^{13}CN (left) and HC^{15}N (right).

emission from cold, starless, cores find $\beta \approx 1.9 \pm 0.3$ for dust temperatures $\approx 16 \pm 2$ K (Juvella et al. 2015a, Fig. 27).

In our analysis, κ_{ν} is assumed homogeneous throughout the core and we adopted $\kappa_{250} = 0.1 \text{ cm}^2 \text{ g}^{-1}$, which appears well suited to our study of a dense starless core (see Table 2). The spectral index β was also assumed uniform, but was let as a free parameter in the minimization process.

3.2. Density profile

The density profile was parameterized in a form that describes an inner plateau of constant density surrounded by a power-law envelope (Bacmann et al. 2000; Tafalla et al. 2002):

$$n_{\text{H}_2}(r) = \frac{n_0}{1 + (r/r_0)^\alpha} \quad (4)$$

where $n_{\text{H}_2}(r)$ is the H_2 number density at radius r . The plateau has a radius r_0 and a constant H_2 density n_0 , while the density in the envelope decreases as $r^{-\alpha}$. This type of profile is well

sued to describe starless cores in which the pressure gradient evolves on timescales longer than the sound crossing-time, such that these cores evolve quasi-statically towards collapse, well before the formation of the first hydrostatic core (Larson 1969; Lesaffre et al. 2005). As will be described later, L1498 is precisely in such a state. Indeed, this profile was adopted in previous studies of the chemical structure of L1498 (Tafalla et al. 2006). This density profile eventually merges with the ambient medium with typical H_2 density 500 cm^{-3} (Hily-Blant & Falgarone 2007; Lippok et al. 2016). However, with the typical values of r_0 and n_0 that describe L1498, such a density is obtained at large radii (beyond $200''$) and need not be considered in our dust emission fitting (see Fig. 4).

3.3. Dust temperature profile

The gas in a prestellar core such as L1498 with relatively small central density ($\approx 10^5 \text{ cm}^{-3}$) is, to a good approximation, con-

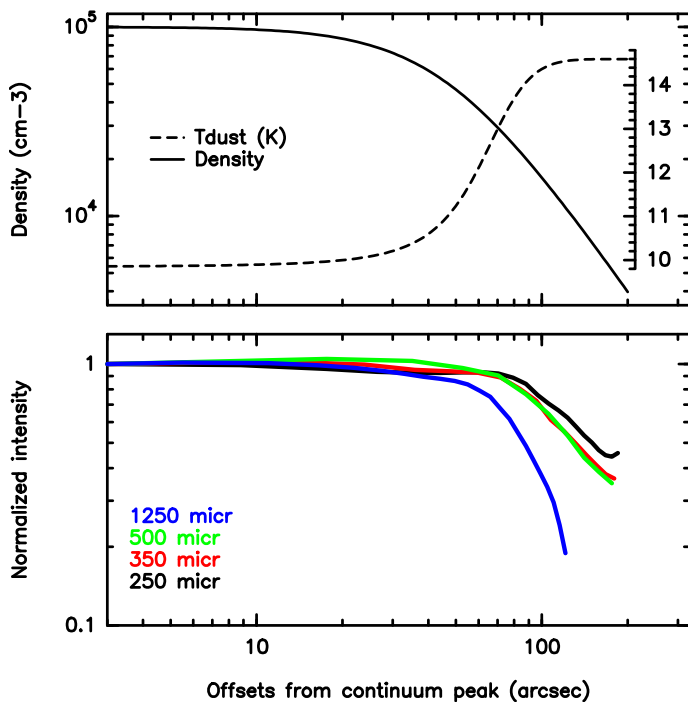


Fig. 4. The physical structure adopted for the continuum map fitting. Top panel: the density and dust temperature (inset scale) profiles. Bottom panel: normalized continuum intensity at 250, 350, 500, and 1250 μm along the HCN cut (see Fig. 1).

Table 2. Compilation of values of the mass absorption coefficient κ_ν (in $\text{cm}^2 \text{g}^{-1}$, expressed per gram of gas and dust) used in dense core studies. The values assume $\beta = 2$ (see Eq. 3). Numbers in parentheses are powers of ten.

250 μm	350 μm	500 μm	1250 μm	Reference
0.10	5.1(-2)	2.5(-2)	4.0(-3)	(1)
0.125	6.4(-2)	3.1(-2)	5.0(-3)	(2)
0.14	7.1(-2)	3.5(-2)	5.6(-3)	(3)
0.09	4.6(-2)	2.2(-2)	3.6(-3)	(4) [†]
0.05	2.6(-2)	1.3(-2)	2.0(-3)	(5) [‡]
0.10	5.2(-2)	2.6(-2)	4.0(-3)	(5) [‡]
0.2 \pm 0.1	1.0(-1)	5.0(-2)	8.0(-3)	(6)
0.2 \pm 0.1	9.2(-2)	4.1(-2)	4.9(-3)	(6) [§]
0.06	3.1(-2)	2.5(-2)	2.4(-3)	This work

References: (1) Hildebrand (1983) (2) Tafalla et al. (2004) (3) Roy et al. (2014) (4) Juvela et al. (2015b) (5) Demyk et al. (2017) (6) Chacón-Tanarro et al. (2017). *Notes:* [†] Using their relation $\tau(250) = 2.16 \times 10^{-25} N_{\text{H}} \text{cm}^2 / \text{H}$ and assuming 10% of He atoms with respect to hydrogen nuclei. [‡] Values are from their model calculations (their Table 1); values from the synthesized samples, which are probably more emissive than interstellar dust grains, are larger by factors of 4 to 10. [§] Using $\beta = 2.3$ as obtained from their study of the dust emission at 1.2 and 2 mm.

stant and close to 10 K as long as CO cooling is sufficient (Zucconi et al. 2001; Tafalla et al. 2006). In the inner parts where the density is large, collisions become efficient in thermalizing the gas and the dust to temperatures close to and below 10 K (Makiwa et al. 2016). However the dust temperature is known to increase outwards from typically below 10 K to approximately 15 K or more (Lippok et al. 2016; Bracco et al. 2017). Indeed,

our attempts to fit simultaneously the dust emission at the four wavelengths with a constant dust temperature did not converge. To allow for a radial increase, we have adopted a simple radial profile of the form

$$T_d(r) = T_{\text{in}} + \frac{T_{\text{out}} - T_{\text{in}}}{2} \left(1 + \tanh \frac{r - r_d}{\Delta r_d} \right) \quad (5)$$

which describes a continuous increase from T_{in} to T_{out} , at a radius r_d and over a characteristic scale Δr_d . In the following, T_{in} , T_{out} , r_d , and Δr_d are considered free parameters. Having a non-uniform dust temperature but uniform spectral index β may seem contradictory, as variations of β with T_d have been reported in starless cores (Juvela et al. 2015a). Yet, our study is focused towards the determination of the density profile in view of an accurate measurement of the abundances of HCN and isotopologues. We therefore decided to keep the number of free parameters as low as possible. Moreover, the variations of β with T_d still remain elusive (Bracco et al. 2017).

3.4. Results

With the above assumptions on the dust emissivity and on the adopted density and dust temperature profiles, we performed a minimization calculation using a MCMC approach to explore the 8-dimension parameter space. The fitting of the graybody emission was calculated in a spherical geometry, by integrating along lines of sight at offsets evenly spaced along the South-West cut from the continuum peak, where line integrations have been performed (see Fig. 1 and the bottom panel of Fig. 4). Our calculation is thus similar to those of Roy et al. (2014); Bracco et al. (2017). However, we did not attempt to compute the derivative of the intensity to obtain $n_{\text{H}_2} B_\nu$, but instead adopted a forward approach in which the various parameters (density, temperature, β) are free to vary within pre-defined intervals (with uniform probability) and the emergent intensity was computed assuming optically thin dust emission. A typical minimization takes 30 minutes.

The best fit parameters are summarized in Table 3, while the probability distribution for the parameters can be seen in Fig. A.1. The corresponding best fit models are compared to the observed radial intensity profiles in Fig. 5.

Our results may be compared with the core properties obtained in previous studies (Tafalla et al. 2004). The main difference is the slope of the density profile in the envelope, which we find significantly shallower, with $\alpha = 2.2$. Our value is closer to what would be expected from theoretical considerations of spheres experiencing gravitational collapse, either isothermal or not, which predict that the envelope density profile of such cores tend towards an exponent of 2 (Larson 1969; Lesaffre et al. 2005). Previous studies, based solely on the 1.3 mm map, suggested significantly steeper profiles ($\alpha = 3.5$). However, the 1.3 mm emission best traces the cold dust emission from the innermost regions of the core rather than the warmer envelope, hence emitting at smaller wavelength. In addition, compared to Herschel/SPIRE, the dual-beam observing mode used with the IRAM30m/MAMBO instrument makes it less sensitive to the extended, shallow, regions. The decrease of α towards the theoretical value of 2 is therefore expected from both observational and theoretical considerations.

The other parameters of the density profile are close to those from the analysis of Tafalla et al.. The plateau in our study is smaller, $r_0 = 47''$ instead of $75''$, can be explained by the fact we used a non-uniform dust temperature. Indeed, attempts with

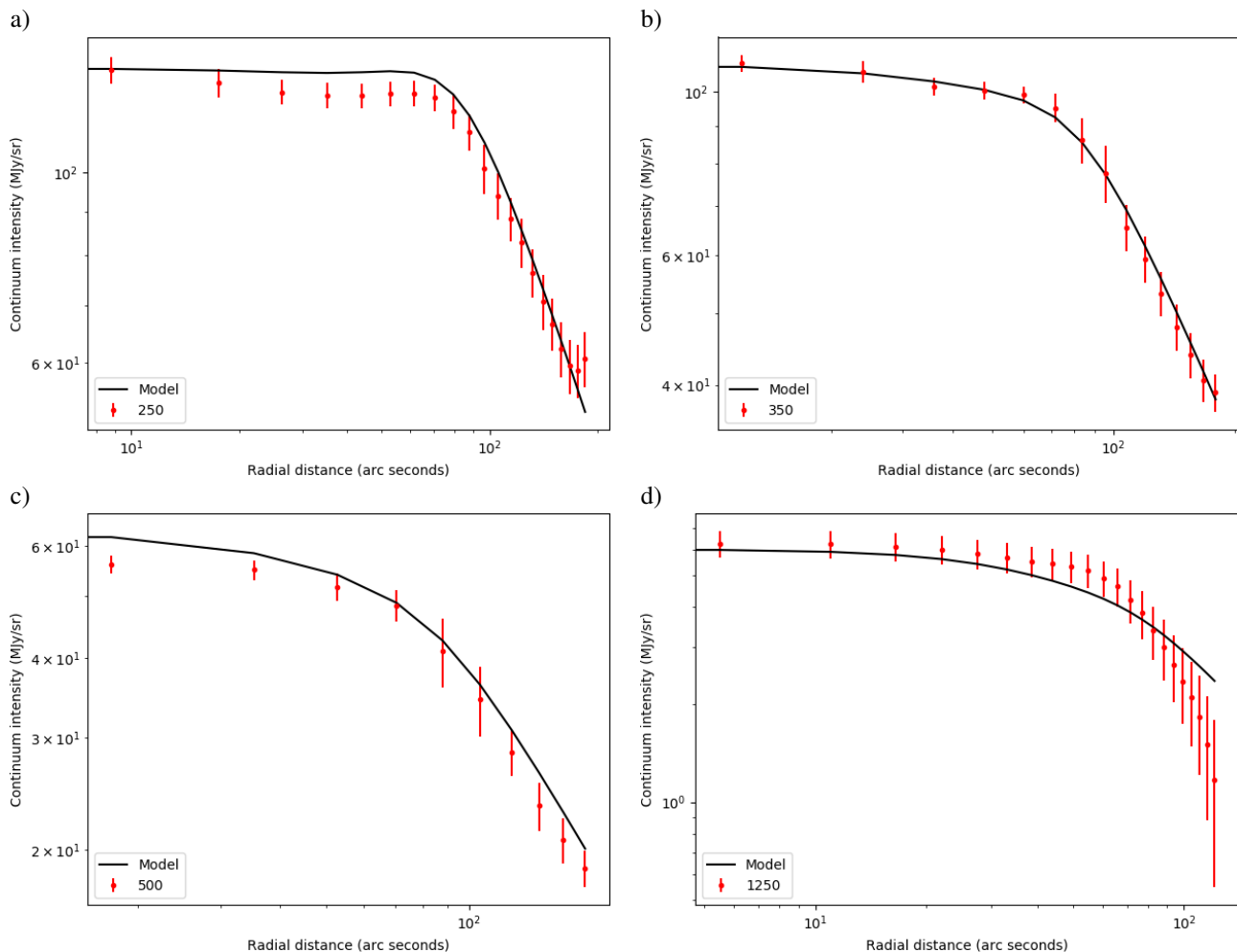


Fig. 5. Continuum fit results along with the radial profiles for the continuum emission. a) The emission at $250 \mu\text{m}$, b) the emission at $350 \mu\text{m}$, c) the emission at $500 \mu\text{m}$ and d) the emission at 1.25 mm . The black lines represent the emission computed from the best fit model, while the red dots represent the average continuum intensity inside the elliptical rings described in Section 3, the error bars displayed are the quadratic sum of the mean RMS noise for each map and the standard deviation of all the pixels within each ring UPDATE.

a uniform temperature, although not satisfactory, give a plateau size of $65''$. What happens is that a large plateau is needed to compensate for the lower temperature in the envelope than in our non-uniform temperature profile.

The spectral index we obtain is $\beta=1.6$. This low value is still within the expected range of 1.6 to 2.4 for prestellar cores (Makiwa et al. 2016), but is significantly lower than the value of 2.3 ± 0.4 measured in a more evolved core, L1544 (Chacón-Tanarro et al. 2017). In a comprehensive analysis of the 1.2 and 2 mm dust emission from prestellar to protostellar cores, a broad range of β was obtained, with a trend towards a decrease with evolutionary stage (Bracco et al. 2017). This may be indicative of variations of the dust size distribution and/or composition, although degeneracy with variations of the mass absorption coefficient can be excluded. Interestingly, low values encompassing $\beta = 1.6$ are found in one of the prestellar core (Miz-2). We also note that low values of β may be associated with dust temperatures above 10 K, in agreement with what we obtain in L1498. Indeed, dust temperatures in L1544 are found to be lower than 10 K throughout, a difference with L1498 which may be attributed to the tenfold lower density in the latter core.

4. Line radiative transfer of HCN and isotopologues

The physical model of the source obtained from the analysis of the dust emission maps is now used to model the emission of HCN and its isotopologues. The aim is to reproduce the spectra observed along a southwest cut from the continuum peak. Our model shares similarities with the previous study of Lee et al. (2007) who computed the HCN(1-0) spectra emerging from a gently contracting starless core, with properties similar to L1498. Indeed, our physical setup (density and velocity profile) is very similar to theirs. However, the isotopologues and HCN(3-2) bring additional, and very sensitive, constraints.

5. Line radiative transfer model

One important aspect that we need to include in our radiative transfer model of L1498 is the presence of a foreground layer of material that is seen towards L1498 (Tafalla et al. 2006), Section ?? explains how we treat this foreground and how it is applied to the models. Furthermore, except for the kinetic temperature of the gas which we assume to be a constant of 10 K through the prestellar core, based on ammonia temperature measurements from Tafalla et al. (2004), all other inputs for the radiative trans-

Table 3. The L1498 source model (density, dust properties, velocity field and line broadening) from the MCMC minimization. Note that $50'' \approx 0.04$ pc at 140 pc. Quoted are the median values, while the uncertainties are the 16% and 86% quantiles.

Component	Parameter	Value	Unit
Dust	n_0	$1.00 \pm 0.16 \times 10^5$	cm^{-3}
	r_0	47 ± 6	arcsec
	α	2.2 ± 0.1	
	T_{in}	9.8 ± 0.5	K
	T_{out}	14.6 ± 0.3	K
	r_d	61 ± 3	arcsec
	Δr_d	26_{-7}^{+10}	arcsec
	β	1.56 ± 0.04	
Gas	n_{ext}	500	cm^{-3}
	T_{kin}	10	K
	V_c	-0.26 ± 0.02	km s^{-1}
	r_V	290 ± 8	arcsec
	Δr_V	55 ± 8	arcsec
	σ_0	0.046 ± 0.03	km s^{-1}
	σ_{ext}	0.25 ± 0.08	km s^{-1}
	r_j	320 ± 14	arcsec
	Δr_j	78 ± 14	arcsec
	X(HCN)	$6.1 \pm 0.4 \times 10^{-9}$	
	X(HCN)/X(H ¹³ CN)	45 ± 3	
	X(HCN)/X(HC ¹⁵ N)	338 ± 28	

fer models were chosen to be a smooth function of the model radius, and are described in the following sections. For Sections 5.2 and 5.3 we use a reference model whose parameters can be found in Table ??, varying only the parameters relative to the collapse velocity profile and non thermal broadening profile respectively.

5.1. Density profile

For our H₂ radial density profile we have adopted the parametrization of Eq. 4 to which a constant external density n_{ext} was added which represents the density in the ambient molecular cloud.

To determine the values of the parameters governing our density profile we have fitted the continuum emission of L1498 with a continuum emission model. The description of how this fit was done can be found in Section 3

5.2. Collapse velocity Profile

For the collapse velocity profile we chose an approximation of the profile described in Lesaffre et al. (2005) for a prestellar core. We assumed the following mathematical description for such a profile:

$$V(r) = V_c e^{-\frac{(r-r_V)^2}{2\Delta r_V^2}}, \quad (6)$$

with V_c the maximum collapse velocity, r_V the radius at which the collapse is equal to V_c and Δr_V the dispersion of the collapse velocity profile. The choice of such a profile is corroborated by the absence of dynamical signatures, such as red blue asymmetries on HCN $J = 3 \rightarrow 2$ spectra, while these effects are present in the HCN $J = 1 \rightarrow 0$ spectra. In Figure 6 we can see examples of spectra produced by ALICO with different collapse

velocity profiles, and how these different profiles affect the HCN $J = 1 \rightarrow 0$ and $J = 3 \rightarrow 2$ transitions.

In models with no collapse velocity it can be seen that the HCN $J = 3 \rightarrow 2$ line profiles are fairly well reproduced with minimal residuals whilst the HCN $J = 1 \rightarrow 0$ line profiles are not reproduced at all with each hyperfine component displaying 2 peaks, leading to very important residuals. On the other hand models with a constant collapse velocity fail to reproduce the features of HCN $J = 3 \rightarrow 2$ line profiles by introducing red blue asymmetries in the strong satellite hyperfine component at 1.8 km/s and making the strongest peak 2 times stronger than it should be, all of this while the HCN $J = 1 \rightarrow 0$ synthetic spectra display the red-blue asymmetry seen in the observations even though the intensities are exaggerated by a factor of 2 in the central hyperfine component at 0 km/s, which can be compensated by different abundances and density profiles. Lastly models following the profile described in equation 6 can reproduce the features of both HCN $J = 3 \rightarrow 2$ and HCN $J = 1 \rightarrow 0$ line profiles with minimal residuals, as long as reasonable values for r_V and Δr_V are chosen.

5.3. Non-Thermal dispersion profile

The line width of the $J = 1 \rightarrow 0$ transition of HC¹⁵N at L1498 is very narrow (full width at half maximum, FWHM = 0.2 km/s). This indicates that the turbulence inside this core is very small, as if we assume $T_{\text{kin}} = 10$ K, the non thermal velocity dispersion seen in the HC¹⁵N $J = 1 \rightarrow 0$ transition is ~ 0.05 km/s. This is very different from the situation seen in the surrounding Taurus molecular cloud, which has very broad line widths for the material surrounding L1498 (FWHM ~ 0.63 km/s, Tafalla et al. 2006). To conciliate this very discrepant line widths we have adopted a smooth radial profile for the non thermal velocity dispersion:

$$\sigma_{\text{nth}}(r) = \sigma_0 + \frac{\sigma_{\text{ext}} - \sigma_0}{\pi} \left[\frac{\pi}{2} + \arctan\left(\frac{r - r_j}{\Delta r_j}\right) \right], \quad (7)$$

where σ_0 is the non thermal velocity dispersion at the centre of the core and σ_{ext} is the non thermal velocity dispersion in the ambient cloud. The transition from the low dispersion to the high dispersion regime is centred at a radius r_j , with a characteristic width Δr_j .

In panels a) and d) of figure 7 we can see that a constant σ_{nth} cannot reproduce well the observed $J = 1 \rightarrow 0$ and $J = 3 \rightarrow 2$ line profiles. The $J = 3 \rightarrow 2$ hyperfine components are under produced while the $J = 1 \rightarrow 0$ hyperfine components have incorrect line profiles: a big self-absorption dip at $V = 0$ km/s and the line ratios between the hyperfine components are not anomalous, i.e. the line ratios between the hyperfine components are within the expected ratios ($1/5 \geq F = 0 \rightarrow 1/F = 2 \rightarrow 1 \leq 1$ and $3/5 \geq F = 1 \rightarrow 1/F = 2 \rightarrow 1 \leq 1$). On the other hand a linear expression for σ_{nth} is also not capable of reproducing the line profiles. The $J = 3 \rightarrow 2$ hyperfine components are slightly under produced, while the $J = 1 \rightarrow 0$ hyperfine components are severely under produced and the line ratios between the hyperfine components is even more anomalous than the observed ones (panels b) and e)). While finally in panels c) and f) we have a good reproduction of the profiles of both transitions, by using the profile described in eq. 7.

The big differences seen between the different types of σ_{nth} profiles can be understood if we take into account the overlap of hyperfine components that happens in HCN rotational

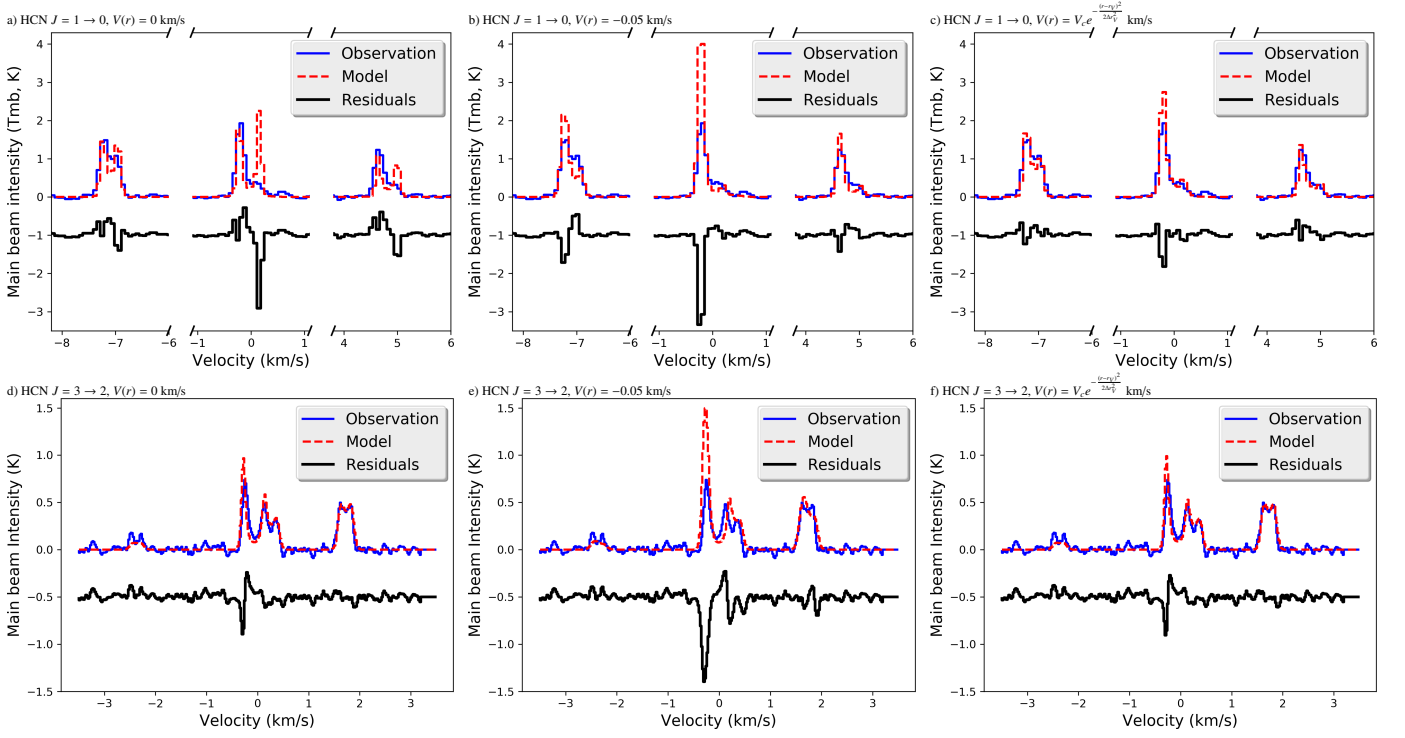


Fig. 6. Line profiles of the $J = 1 \rightarrow 0$ (panels a), b) and c)) and $J = 3 \rightarrow 2$ (panels d), e) and f)) computed by ALICO for different collapse velocity profiles. No collapse velocity (panels a) and d)), constant collapse velocity (panels b) and f)) and the profile described in eq. 6 (panels c) and f))

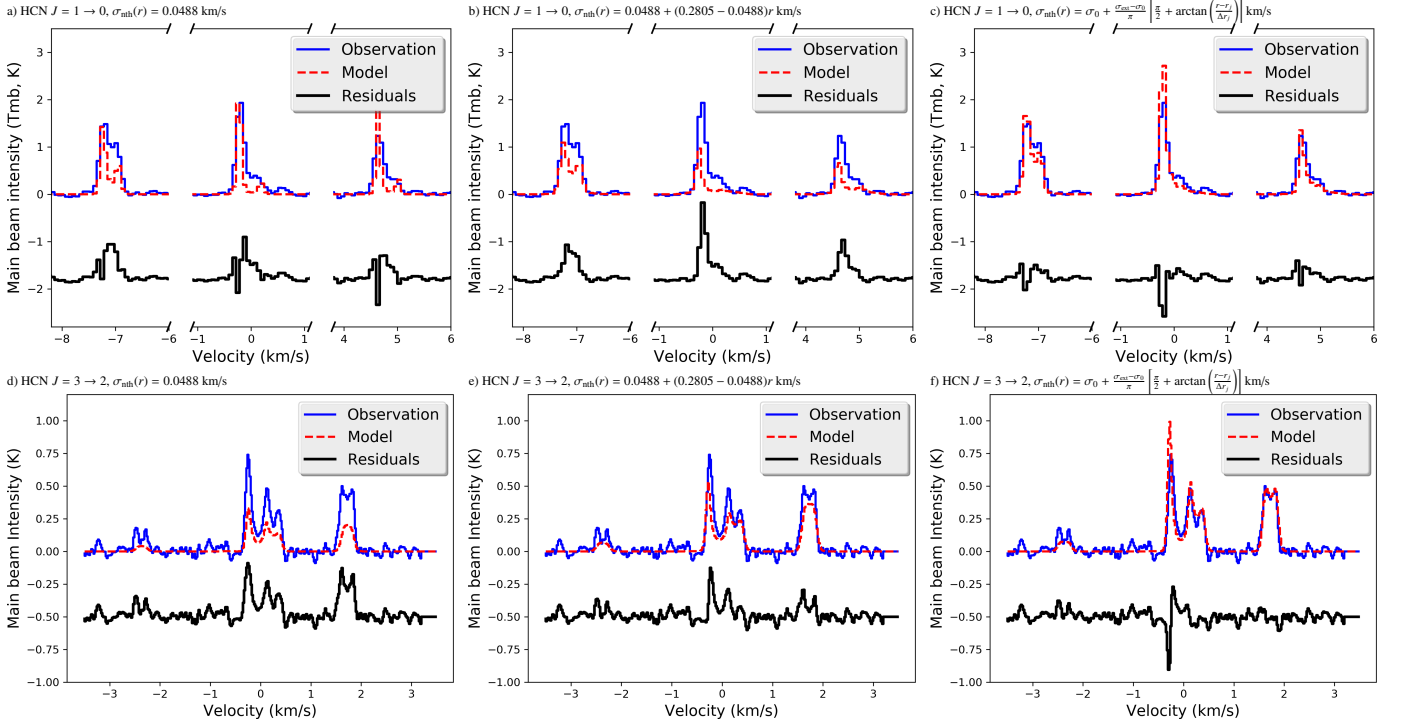


Fig. 7. Line profiles of the $J = 1 \rightarrow 0$ (panels a), b) and c)) and $J = 3 \rightarrow 2$ (panels d), e) and f)) computed by ALICO for different non thermal broadening profiles. constant σ_{nth} (panels a) and d)), linear σ_{nth} (panels b) and f)) and the profile described in eq. 7 (panels c) and f))

transitions with $J_{\text{upper}} > 1$ (Gottlieb et al. 1975; Guilloteau & Baudry 1981; Gonzalez-Alfonso & Cernicharo 1993). Due to the small line widths seen in L1498 (FWHM ~ 0.2 km/s) under a constant and small σ_{nth} there is very little overlap between hyperfine components. In this case the excitation temperatures of the hyperfine components of the $J = 1 \rightarrow 0$ transition follow

the expected trend, the very optically thick $F = 2 \rightarrow 1$ component ($\tau \sim 72$) is thermalized at the center of the model, with the excitation temperature decreasing in the outer layers, the other hyperfine components are less thick, ($\tau \sim 14$ and $\tau \sim 43$ for $F = 0 \rightarrow 1$ and $F = 1 \rightarrow 1$ respectively, and therefore further from thermalization (Figure 8 panels b) and c)). In this scenario

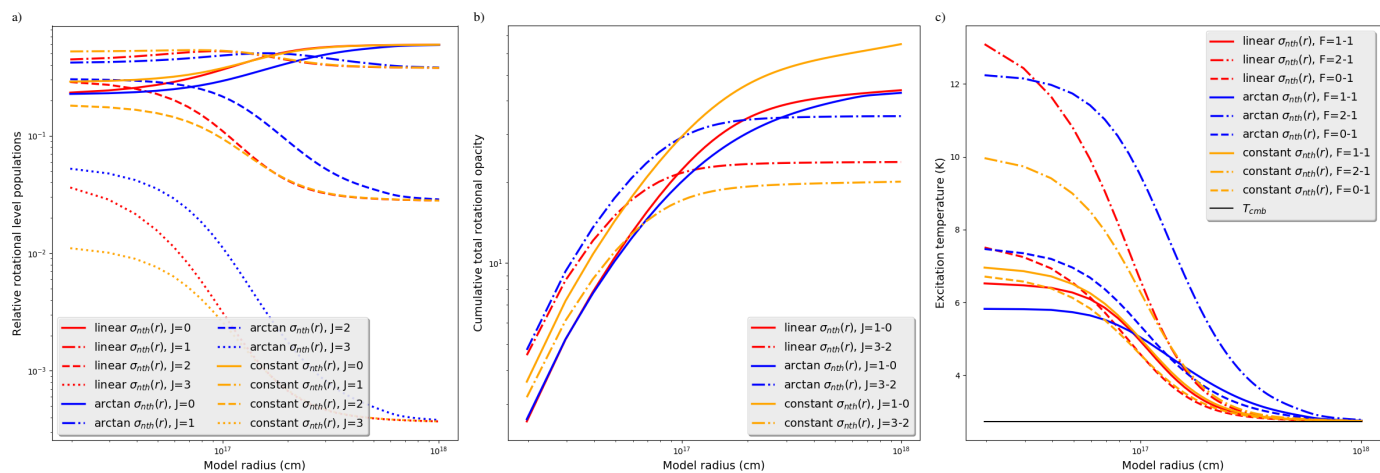


Fig. 8. Relative rotational level populations (panel a)), cumulative total rotational opacities (panel b)) and excitation temperature for the hyperfine components of the $J = 1 \rightarrow 0$ transition for the different kinds of σ_{nth} profiles described in Figure 7. Blue lines correspond to the profile in eq. 7, red lines to a linear function for σ_{nth} profile and the orange lines correspond to constant σ_{nth} .

there is no extra pumping of population to $J = 2$ and $J = 3$ levels due to the radiative trapping caused by the hyperfine overlap, thus making the $J = 3 \rightarrow 2$ excitation temperature low (average $J = 3 \rightarrow 2$ $T_{\text{ex}} \sim 3.6$ K) which in turn under produce the line emission.

Now in the case of a linear increase of σ_{nth} with radius we see that there is some radiative pumping of $J = 2$ and $J = 3$ caused by the hyperfine component overlap, leading to $J = 2$ and $J = 3$ being more populated here than in the case of constant σ_{nth} (Figure 8 panel a)). This creates an excitation temperature imbalance in the $J = 1 \rightarrow 0$ transition at small radii, the $F = 2 \rightarrow 1$ component becomes suprathermal while the $F = 1 \rightarrow 1$ has an excitation temperature smaller than $F = 0 \rightarrow 1$. Yet due to the fact that σ_{nth} keeps increasing at a certain point photons can scape easily in transitions $J = 2 \rightarrow 1$ and $J = 3 \rightarrow 2$ leading to a fast depopulation of this levels, leading to a fast drop of the excitation temperature of the $F = 2 \rightarrow 1$ component which due to its high opacity ($\tau \sim 48$, Figure 8 panel b)) becomes heavily self-absorbed thus explaining the extreme hyperfine anomalies seen in panel b) of Figure 7.

The σ_{nth} profile described in eq. 7 solves the problems presented by the other two profiles in a simple way. The small increase in the non-thermal broadening with radii at small radii allows for the pumping of the $J = 2$ and $J = 3$ levels to proceed to larger radii, creating the observed $J = 1 \rightarrow 0$ hyperfine anomalies and keeping the $J = 3 \rightarrow 2$ excitation high enough to account for the observed intensities (average $J = 3 \rightarrow 2$ $T_{\text{ex}} \sim 4.7$ K).

6. Fitting of the line profiles of HCN and its isotopologues.

Acknowledgements. We thank Marco Padovani for providing us with unpublished IRAM30m spectra (program 031-11). VM is supported by a PhD grant from the XXXX (brazilian agency). PHB acknowledges the *Institut Universitaire de France* for financial support. This research has made use of data from the Herschel Gould Belt survey (HGBS) project (<http://gouldbelt-herschel cea.fr>). The HGBS is a Herschel Key Programme jointly carried out by SPIRE Specialist Astronomy Group 3 (SAG 3), scientists of several institutes in the PACS Consortium (CEA Saclay, INAF-IFSI Rome and INAF-Arcetri, KU Leuven, MPIA Heidelberg), and scientists of the Herschel Science Center (HSC).

7. Discussion

outside in collapse mention sohn et al 2007 with the fact that they discovered hcn traces more collapse than other molecules, probable reason: HCN traces the outside in collapse while N2H+ traces only inner collapse. due to the diff in optical depth and excitation.

8. conclusions

References

- Adande, G. R. & Ziurys, L. M. 2012, ApJ, 744, 194
André, P., Men'shchikov, A., Bontemps, S., et al. 2010, A&A, 518, L102
Bacmann, A., André, P., Puget, J.-L., et al. 2000, A&A, 361, 555
Bergin, E. A. & Tafalla, M. 2007, ARA&A, 45, 339
Bieler, A., Altwegg, K., Balsiger, H., et al. 2015, Nature, 526, 678
Bockelée-Morvan, D., Calmonte, U., Charnley, S., et al. 2015, Space Sci. Rev., 197, 47
Bracco, A., Palmeirim, P., André, P., et al. 2017, A&A, 604, A52
Calmonte, U., Altwegg, K., Balsiger, H., et al. 2016, MNRAS, 462, S253
Chacón-Tanarro, A., Caselli, P., Bizzocchi, L., et al. 2017, ArXiv e-prints [arXiv:1707.00005]
Daniel, F. & Cernicharo, J. 2008, A&A, 488, 1237
Demyk, K., Meny, C., Lu, X.-H., et al. 2017, A&A, 600, A123
Gonzalez-Alfonso, E. & Cernicharo, J. 1993, A&A, 279, 506
Gottlieb, C. A., Lada, C. J., Gottlieb, E. W., Lilley, A. E., & Litvak, M. M. 1975, ApJ, 202, 655
Guilloteau, S. & Baudry, A. 1981, A&A, 97, 213
Hildebrand, R. H. 1983, QJRAS, 24, 267
Hily-Blant, P., Bonal, L., Faure, A., & Quirico, E. 2013a, Icarus, 223, 582
Hily-Blant, P. & Falgarone, E. 2007, A&A, 469, 173
Hily-Blant, P., Magalhaes, V., Kastner, J., et al. 2017a, A&A, 603, L6
Hily-Blant, P., Pineau des Forêts, G., Faure, A., Le Gal, R., & Padovani, M. 2013b, A&A, 557, A65
Hily-Blant, P., Vastel, C., Faure, A., & Pineau des Forêts, G. 2017b, MNRAS
Hily-Blant, P., Walmsley, M., Pineau Des Forêts, G., & Flower, D. 2010, A&A, 513, A41
Ikeda, M., Hirota, T., & Yamamoto, S. 2002, ApJ, 575, 250
Juvela, M., Demyk, K., Doi, Y., et al. 2015a, A&A, 584, A94
Juvela, M., Ristorcelli, I., Marshall, D. J., et al. 2015b, A&A, 584, A93
Larson, R. B. 1969, MNRAS, 145, 271
Lee, S. H., Park, Y.-S., Sohn, J., Lee, C. W., & Lee, H. M. 2007, ApJ, 660, 1326
Lesaffre, P., Belloche, A., Chièze, J.-P., & André, P. 2005, A&A, 443, 961
Lippok, N., Launhardt, R., Henning, T., et al. 2016, A&A, 592, A61
Liszt, H. & Lucas, R. 2001, A&A, 370, 576
Makiwa, G., Naylor, D. A., van der Wiel, M. H. D., et al. 2016, MNRAS, 458, 2150
Marty, B., Chaussidon, M., Wiens, R. C., Jurewicz, A. J. G., & Burnett, D. S. 2011, Science, 332, 1533
Milam, S. N., Savage, C., Brewster, M. A., Ziurys, L. M., & Wyckoff, S. 2005, ApJ, 634, 1126

- Mousis, O., Lunine, J. I., Luspáy-Kuti, A., et al. 2016a, ApJ, 819, L33
Mousis, O., Özgürel, O., Lunine, J. I., et al. 2017, ApJ, 835, 134
Mousis, O., Ronnet, T., Brugger, B., et al. 2016b, ApJ, 823, L41
Mumma, M. J. & Charnley, S. B. 2011, ARA&A, 49, 471
Roueff, E., Loison, J. C., & Hickson, K. M. 2015, A&A, 576, A99
Roy, A., André, P., Palmeirim, P., et al. 2014, A&A, 562, A138
Shinnaka, Y., Kawakita, H., Jehin, E., et al. 2016, MNRAS, 462, S195
Tafalla, M., Myers, P. C., Caselli, P., & Walmsley, C. M. 2004, A&A, 416, 191
Tafalla, M., Myers, P. C., Caselli, P., Walmsley, C. M., & Comito, C. 2002, ApJ, 569, 815
Tafalla, M., Santiago-García, J., Myers, P. C., et al. 2006, A&A, 455, 577
Taniguchi, K., Ozeki, H., Saito, M., et al. 2016, ApJ, 817, 147
Taniguchi, K. & Saito, M. 2017, PASJ, 69, L7
Taquet, V., Furuya, K., Walsh, C., & van Dishoeck, E. F. 2016, MNRAS, 462, S99
van der Tak, F. F. S., Black, J. H., Schöier, F. L., Jansen, D. J., & van Dishoeck, E. F. 2007, A&A, 468, 627
Walmsley, C. M., Churchwell, E., Nash, A., & Fitzpatrick, E. 1982, ApJ, 258, L75
Zucconi, A., Walmsley, C. M., & Galli, D. 2001, A&A, 376, 650

Appendix A: Dust emission fitting

Appendix A.1: Correlations between the fitting parameters

One interesting thing to note about Figure A.1 is the presence of correlations and anti-correlations between some of the fit parameters. The loose anti-correlation between n_0 and r_0 can be understood from the fact that an increase in any of them increases the dust column density and thus the emission, so as one parameter increases the other has to decrease to preserve the observed emission. The positive correlation of n_{ext} and α comes from the fact that there is a need for some minimal emission at larger radii, so as α increases, decreasing the line of sight column density at larger radii, n_{ext} has to increase to preserve it. Not surprisingly the tight anti-correlation of n_{ext} and T_{ext} comes from this same necessity, as T_{ext} is decreased n_{ext} has to be increased to maintain the emission and vice versa. On the other hand the positive correlation between r_0 and α is related to the slope of the emission profile decay. Larger values of r_0 have to be coupled with larger values of α to preserve the slope seen on the radial profiles.

The anti-correlation between T_0 and T_{ext} can be explained from the fact that the emission increases with both temperatures through the term $B_\nu(T_{\text{dust}}(r))$ in equation 2, therefore if T_0 is increased T_{ext} has to be decreased to conserve the flux. The anti-correlation between n_0 and T_0 also comes from the fact that the emission increases with T_0 while also being proportional to n_0 through equation 4, thus if T_0 is increased n_0 has to be decreased to conserve flux. The constraints leading to the correlation between r_0 and T_{ext} come from the emission at large offsets from the source, where it is dominated by n_{ext} and T_{ext} , but also having a contribution from the tail of the term dependent on r_0 in equation 4, so if flux is to be conserved an increase in r_0 has to be offset by a decrease in T_{ext} . The correlations between T_0 and r_0 and T_0 and n_{ext} arise from the anti-correlation between T_0 and T_{ext} acts upon T_{ext} which due to its anti-correlations with n_{ext} and r_0 make in turn r_0 and n_{ext} correlated to T_0 . The loose positive correlation of n_{ext} and r_0 may arise from the fact that both n_{ext} and r_0 present correlations with T_0 and anti-correlations with T_{ext} , thus they are forced to vary together by the strength of these correlations.

The anti-correlations between β and the temperatures (T_0 and T_{ext}) come from the fact that β has an impact on the relative fluxes between the different wavelengths, with large values of beta favoring short wavelengths, which is the opposite effect of the temperature. Thus to maintain the same ratio between the fluxes at different wavelengths a decrease in β has to be offset by an increase in either T_0 or T_{ext} . The remaining correlations, that between β and the density parameters (n_0 , n_{ext} and r_0) come from the fact that an increase in column density requires a decrease in the dust temperature to maintain the same emission, and therefore with a decrease in dust temperature β has to increase to maintain the flux ratio between the different continuum wavelengths.

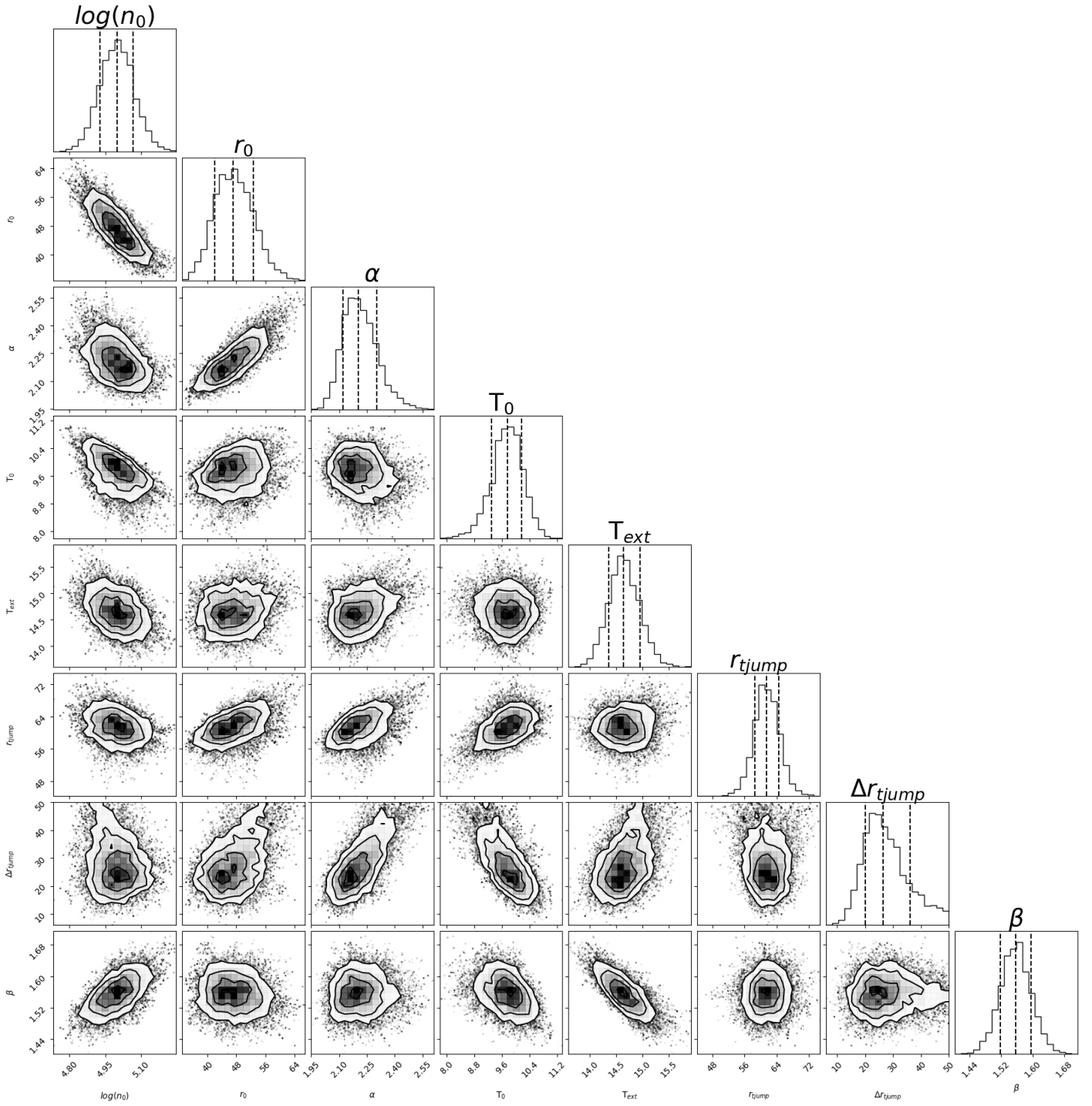


Fig. A.1. Probability density distribution for the parameters in the continuum MCMC fit, along with the scatter plots between each possible pair of probability density distributions. It is clearly visible from the scatter plots that several parameters are correlated.

THE $^{14}\text{N}/^{15}\text{N}$ RATIO IN PROTOSOLAR NEBULA ANALOGS

5.1 INTERFEROMETRIC OBSERVATIONS

The region immediately adjacent to a protostar, the warm circumstellar material in an embedded protostar or the protoplanetary disk around a T Tauri or Herbig A star, is the analog to the protosolar nebula. These regions have sizes of the order of a few hundred astronomical units. Even in the case of the closest known protoplanetary disk, the disk around TW Hya which is at 59 ± 1 pc as recently measured by the ESA/Gaia satellite, such sizes require spatial resolutions of the order of $1''$ to be resolved. Single-dish observations at high frequencies may achieve a spatial resolution of the order of a few arc seconds ($7.4''$ at 340 GHz at the IRAM-30m telescope). Yet this is not enough to accurately resolve these regions. The solution is to use interferometers.

Radio interferometers work by correlating the electric field measured by pairs of antennas. Each pair of antenna defines a baseline, whose projection on the sky corresponds to a given spatial scale in the brightness distribution on the sky. Each sample is called a *visibility*. The visibility is what a radio interferometer actually measures: it is one component of the Fourier transform of the sky brightness distribution. The best way to gauge the quality of the sampled visibilities is to look at the so-called uv coverage of an interferometric observation (Figure 5.1). The uv coverage is a graphical representation of the sampling of the spatial frequencies sampled by the baselines of an interferometer. The name uv comes from the coordinates in the Fourier plane which are usually noted u and v .

The Fourier transform of the uv coverage is the so-called dirty beam. The dirty beam is the interferometer's sensitivity to a point source in the sky. Which is to say that a point source in the sky appears in an interferometric image as a dirty beam which is scaled by the flux of the point source.

To visualise interferometric data in a more familiar way, the visibilities are Fourier-transformed to obtain a representation of the sky plane that is called a dirty image (Figure 5.2). To accurately reproduce the sky brightness distribution it is necessary to sample as many spatial frequencies as possible. The dirty image—so-called because the plane of the sky is convolved with the dirty beam—generally contains artifacts. Actually, the Fourier transform of the visibilities is only possible if the phase of the visibilities is known. In the optical domain

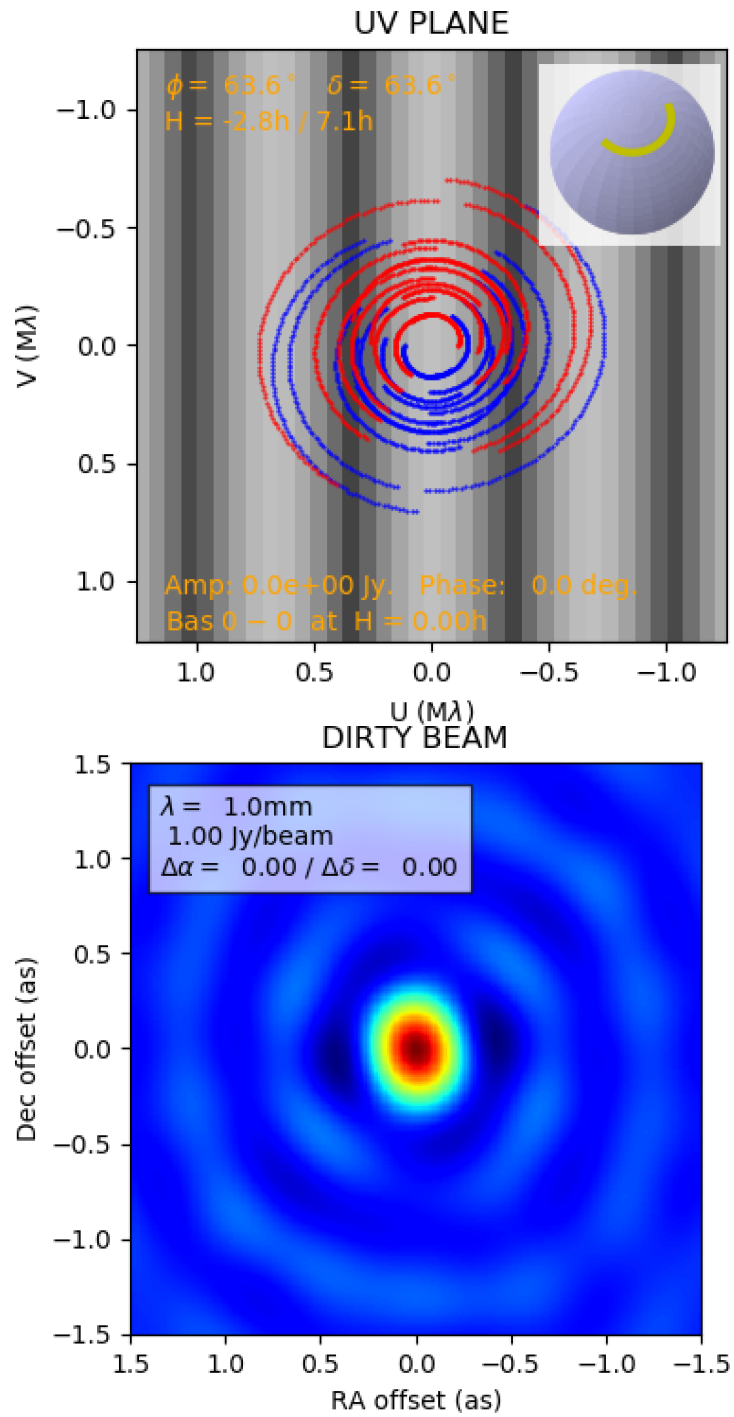


Figure 5.1 – uv coverage of an artificial interferometer (top panel) and the resulting dirty beam obtained from the Fourier transform of the uv coverage. Notice the side lobes produced in the dirty beam by the blanks in uv coverage. Images produced with *APSYN-SIM* (Marti-Vidal, 2017).

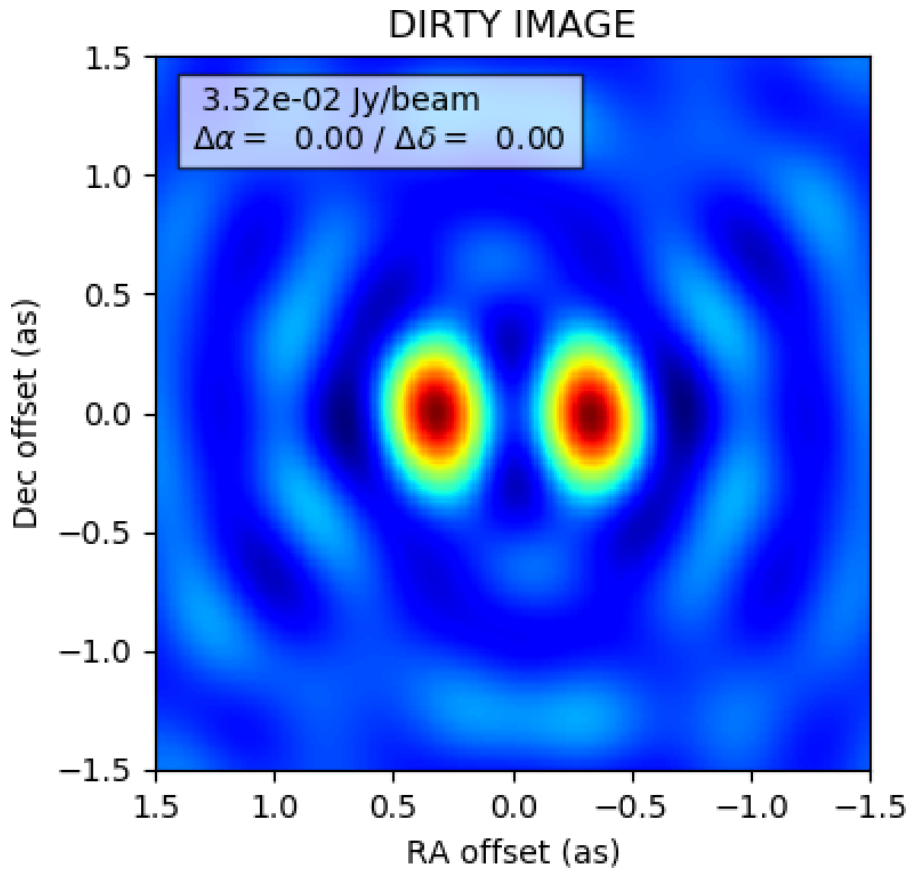


Figure 5.2 – Dirty image produced by the synthetic observation of two point sources with the uv coverage in Figure 5.1. Image produced with *APSYNSIM* (Marti-Vidal, 2017).

this information is lost, and therefore a source geometrical model has to be assumed in order to produce an image. In the radio domain the signal correlators are capable of keeping track of the phase of a visibility, thus no geometrical source model is required to reconstruct a dirty image reducing the systematic errors in the analysis of the data.

To reduce the number of artifacts seen in an interferometric image a process called cleaning is applied to the dirty images to create an image that is as free as possible from artifacts. The CLEAN algorithm for cleaning the dirty image is an iterative procedure, introduced by Högbom (1974) which can be summarised as follows:

1. Normalise the dirty beam to a fraction of the intensity of the maximum intensity in the dirty image;
2. Subtract the normalised dirty beam from the dirty image at the location of maximum intensity.
3. Find the point of maximum intensity in the new dirty image, this may or may not be the same point as before, and repeat the first two steps;

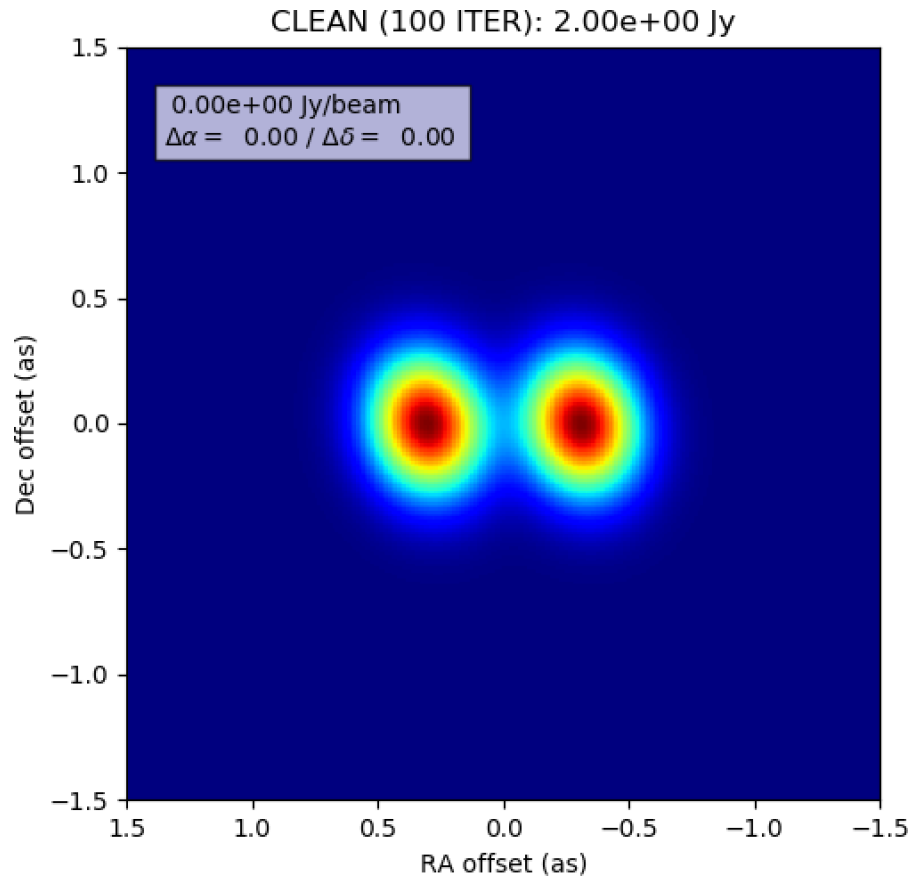


Figure 5.3 – Results of CLEAN when applied to the dirty image in Figure 5.2. Image produced with *APSYNSIM* (Marti-Vidal, 2017).

4. Continue the process iteratively until the maximum intensity in the dirty image is comparable to the noise.
5. Produce a final "cleaned" image by returning all the components removed in the previous stages in the form of "clean beams" with appropriate positions and amplitudes. The clean beams are typically chosen to be Gaussian with similar widths to the central response of the dirty beam.

Figure 5.3 shows the effects of CLEAN in the dirty image shown in Figure 5.2.

5.1.1 Self-calibration

The process of interferometric calibration—amplitude, frequency, and phase—is certainly the most crucial part of the data processing. It involves various calibration sources and procedures. Due to its complexity the final calibrated data set may still present significant spread in phase and amplitude with time. To improve the phase and amplitude calibration, the idea behind so-called 'self-calibration' is

to use the structure of the source itself that is generated during the cleaning process. It is thus an iterative procedure. Indeed, the cleaning process creates so-called *clean components* which are the iteratively dirty-beam-subtracted images.

These clean components can then be Fourier-transformed to produce a model set of visibilities. The phase and amplitude of the model visibilities can be compared to the observed visibilities to obtain a best fit solution to correct the observed visibilities. The corrected observed visibilities are then imaged and cleaned producing a new set of clean components that can be used to further improve the model visibilities. This process is done iteratively until the differences between two consecutive steps becomes lower than some threshold, or if it decreases the image quality.

The principal requirement for this method to work is that the observed visibilities have sufficient signal-to-noise ratio (snr), generally 50 or more, to allow a good fitting of the phases and amplitudes to the model visibilities. This is usually not possible with spectral lines which have too small an snr, due to their small frequency width. This is normally circumvented by observing the continuum in parallel to spectral line observations. Continuum data usually have much better snr than spectral data sets. Moreover, because continuum observations are usually observed in parallel to the spectral ones, they are similarly affected by phase and amplitude drifts. In practice, self-calibration is thus performed using the solutions obtained by the cleaning of the continuum. Figure 5.4 displays the effects of self-calibration to continuum observations of TW Hya.

5.2 DIRECT EVIDENCE OF MULTIPLE RESERVOIRS OF VOLATILE NITROGEN IN A PROTOSOLAR NEBULA ANALOGUE

The last link on the star formation process before a complete solar system is the protoplanetary disk stage. With that in mind we have set to investigate the isotopic ratio of Nitrogen in the closest protoplanetary disk to Earth, TW Hydra. A proposal was submitted by Pierre Hily-Blant for ALMA cycle 2 with the intention of directly measuring the CN/C¹⁵N ratio in this disk. The proposal was granted time under the ALMA project 2013.1.00196.S.

The TW Hya observations were carried out in three epochs and the data was delivered in July 2015. The data was calibrated and concatenated by me at the IRAM headquarters in Grenoble. Following the concatenation the data was self-calibrated by me with the aid of a self-calibration script (Chunhua Qi private communication). The self-calibration process took two rounds of phase self-calibration and one round of amplitude self-calibration. This lead to a three fold increase of the signal noise ratio of the continuum and its effects can be seen in Figure 5.4. All the data reduction was conducted

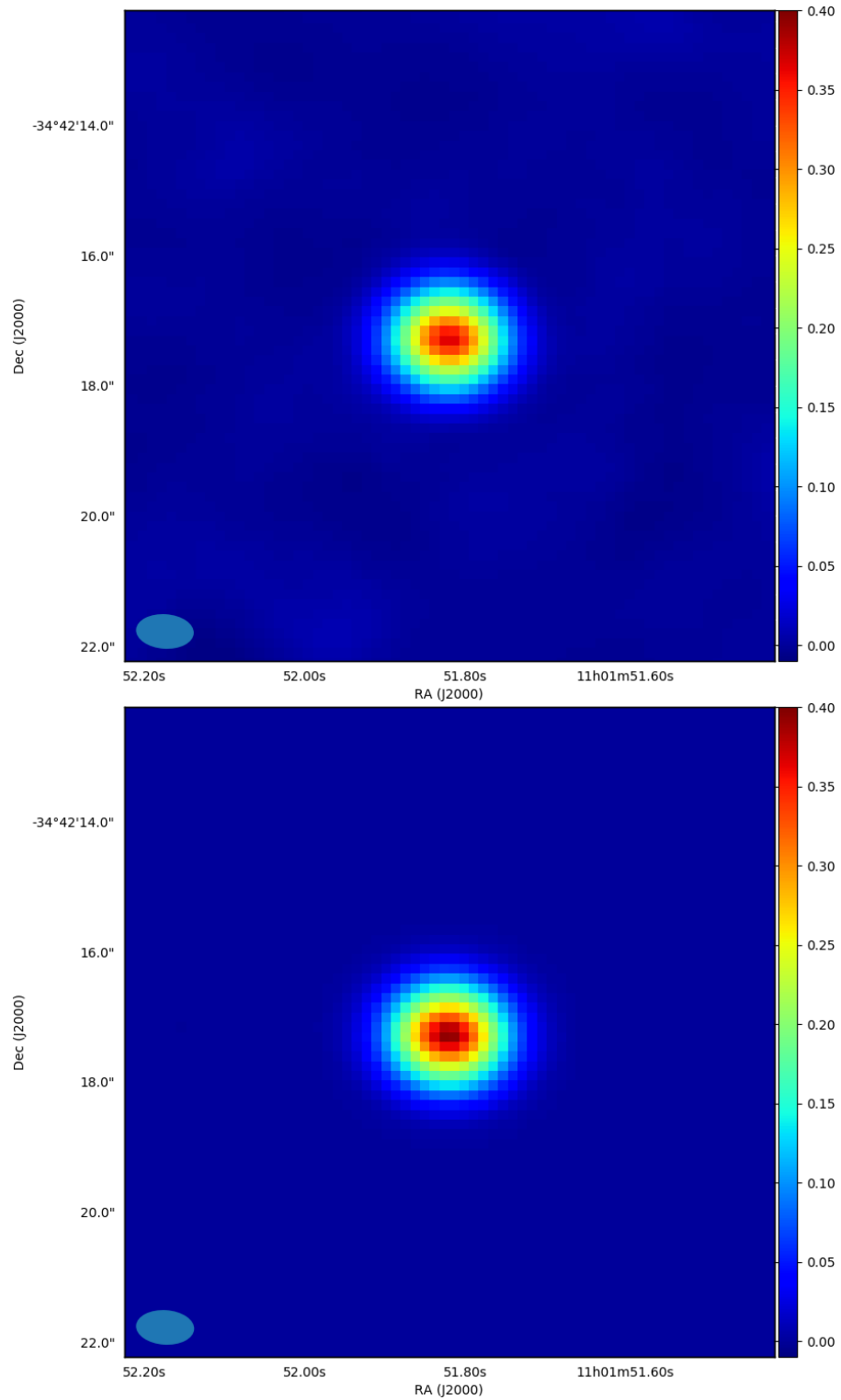


Figure 5.4 – Continuum emission of TW Hya at 340 GHz before and after self-calibration (top and bottom panels respectively). Notice the reduction of residuals and the increase in flux after self-calibration. Maps in Jy/beam.

in CASA (*The Common Astronomy Software Applications package*), under version 4.2.2. All the visibilities were then converted from the CASA format to the GILDAS\mapping UV table format (*GILDAS software*). In GILDAS\mapping the visibilities of the optically thin hyperfine components of CN were integrated in frequency to obtain integrated intensity UV tables of these lines. The same was done to the visibilities of C¹⁵N.

The MWC 480 data we used to derive the H¹³CN/HC¹⁵N ratio were retrieved from the ALMA science archive since they are already open to public access. Similarly to the TW Hydra CN data, these data were calibrated and self-calibrated by me using CASA version 4.2.2. The strong continuum of MWC 480 allowed for a 5 fold increase in the signal to noise ratio during self-calibration. The self-calibration took two rounds of phase self-calibration iterations and one round of amplitude self-calibration. After the self-calibration the data was exported to the GILDAS mapping UV table format. In GILDAS\mapping these UV tables were integrated in frequency to provide integrated intensity UV tables for the subsequent analysis.

The analysis of the UV plane data led to the derivation of 10% uncertainty isotopic ratio for CN in TW Hya. The detailed steps of this analysis are described in the appendixes of Hily-Blant et al. (2017). Hily-Blant et al. (2017) is presented in its integral form in the following pages as it is one of the main results of this thesis.

LETTER TO THE EDITOR

Direct evidence of multiple reservoirs of volatile nitrogen in a protosolar nebula analogue

P. Hily-Blant^{1,2}, V. Magalhaes², J. Kastner^{2,3}, A. Faure², T. Forveille², and C. Qi⁴

¹ Institut Universitaire de France, 75231 Paris Cedex 05, France

² Université Grenoble Alpes, CNRS, IPAG, 38000 Grenoble, France
e-mail: pierre.hily-blant@univ-grenoble-alpes.fr

³ Chester F. Carlson Center for Imaging Science, School of Physics & Astronomy, and Laboratory for Multiwavelength Astrophysics, Rochester Institute of Technology, 54 Lomb Memorial Drive, Rochester, NY 14623, USA

⁴ Harvard-Smithsonian Center for Astrophysics, 60 Garden Street, Cambridge, MA 02138, USA

Received 30 January 2017 / Accepted 23 June 2017

ABSTRACT

Isotopic ratios are keys to understanding the origin and early evolution of the solar system in the context of Galactic nucleosynthesis. The large range of measured $^{14}\text{N}/^{15}\text{N}$ isotopic ratios in the solar system reflects distinct reservoirs of nitrogen whose origins remain to be determined. We have directly measured a $\text{C}^{14}\text{N}/\text{C}^{15}\text{N}$ abundance ratio of 323 ± 30 in the disk orbiting the nearby young star TW Hya. This value, which is in good agreement with nitrogen isotopic ratios measured for prestellar cores, likely reflects the primary present-day reservoir of nitrogen in the solar neighbourhood. These results support models invoking novae as primary ^{15}N sources as well as outward migration of the Sun over its lifetime, and suggest that comets sampled a secondary, ^{15}N -rich reservoir during solar system formation.

Key words. astrochemistry – ISM: abundances – galaxies: abundances – Galaxy: evolution – comets: general

1. Introduction

Understanding the formation of the solar system is a prerequisite to a comprehensive theory of our origins, while providing essential clues for the birth of planetary systems in general. Early solar system bodies, such as comets and asteroids, provide a detailed view of the composition of the protosolar nebula (PSN) 4.6 billion years ago (Mumma & Charnley 2011; Bockelée-Morvan et al. 2015). The physical and chemical conditions prevailing in the PSN were set up in the collapsing proto-Sun, which were themselves products of the conversion, over a few million years, of diffuse and mostly atomic interstellar gas into a dense, gravitationally unstable, molecular prestellar core (Ceccarelli et al. 2014). A key question from both astrophysical and planetary science perspectives is to know to what extent the reservoirs of volatiles (namely, gas and ice) in planetary systems are of interstellar nature or if chemistry was reset in the PSN at the epoch of planet formation.

Isotopic ratios are a powerful tool to evince the chemical heritage preserved during this secular evolution. For example, the large D/H ratio in terrestrial water may indicate that it likely encoded the interstellar history of the solar system (Cleeves et al. 2014). In contrast, the origin of nitrogen, the most reactive and abundant heavy nuclei, together with carbon and oxygen, has not been elucidated for two main reasons: i) the elemental $^{14}\text{N}/^{15}\text{N}$ isotopic ratio of nitrogen in the present-day solar neighbourhood (which we denote \mathcal{R}_\odot) is poorly constrained; and ii) the primary repository of nitrogen in star and planet forming regions is unknown, such that chemical model predictions are highly uncertain. Constraints on the origin of nitrogen in the PSN derive from laboratory and in situ analysis

of primordial solar system materials (Rubin et al. 2015), and from observations of solar-type star-forming regions in the solar neighbourhood within a few 100 pc (Hily-Blant et al. 2013a). The primary reservoir of nitrogen in the PSN had a $^{14}\text{N}/^{15}\text{N}$ ratio $\mathcal{R}_\odot = 441$ as measured in Jupiter's atmosphere and in the solar wind (Füri & Marty 2015) but values as low as 50 are observed today in some primitive cosmomaterials (Bonal et al. 2010). Comets, observed in CN, HCN, and NH_2 , show a strikingly uniform ratio of ≈ 140 regardless of their orbital parameters (Mumma & Charnley 2011; Shinnaka et al. 2016, and Fig. A.1), suggesting that they recorded a secondary nitrogen reservoir or that the main reservoir of nitrogen has not yet been seen in comets.

A central question is to establish whether the different reservoirs of nitrogen that are observed today in the solar system were inherited from the interstellar phase, or if they result from fractionation processes within the PSN or in parent bodies (Hily-Blant et al. 2013a; Füri & Marty 2015). A first step in addressing this issue would be to demonstrate the existence of multiple reservoirs in protoplanetary disks, which serve as analogues for the PSN. This is a primary objective of the present work.

The origin of nitrogen in the solar system is actually a problem in both space and time, as it involves the comparison of the composition of the PSN, formed at some location in the Galaxy 4.6 billion years ago, to that of present-day star-forming regions at a galactocentric radius $r_G \approx 8.5$ kpc. One key point is the chemical homogeneity of the local interstellar medium (LISM) within ~ 1 kpc (Sofia & Meyer 2001), which makes nearby protoplanetary disks representative of planetary formation at $r_G \approx 8.5$ kpc. Qualitatively, the elemental $^{14}\text{N}/^{15}\text{N}$

in the Galaxy is expected to decrease with time, and to increase with increasing galactocentric radius, as a result of stellar nucleosynthesis (Audouze et al. 1975; Matteucci 2012). Nevertheless, predictions of Galactic chemical evolution (GCE) models can vary significantly depending on the specific assumptions concerning the nuclear processes leading to ^{15}N , the Galactic star formation history, and the initial mass function of newly born stars (Romano & Matteucci 2003; Minchev et al. 2013). Moreover, the birthplace of the Sun remains poorly known (Martínez-Barbosa et al. 2015). Measuring \mathcal{R}_0 would provide the reference value needed to establish the heretofore missing link between the PSN and present-day planet-forming disks orbiting young stars. The value of \mathcal{R}_0 is the other aim of the present study.

However, measuring \mathcal{R}_0 is challenging because the primary reservoir of nitrogen in cores, protostars, and protoplanetary disks – presumably N or N_2 (or perhaps icy ammonia in the densest parts) – cannot be observed directly. Therefore, \mathcal{R}_0 must be inferred from trace species (e.g. HCN, NH_3 , etc.) usually with the aid of chemical models (Le Gal et al. 2014; Roueff et al. 2015). Moreover, radiation from ^{15}N isotopologues is intrinsically weaker than from the main isotopologue by typically two orders of magnitude thus requiring excellent sensitivity.

It is well established that evolved protoplanetary disks are bright CN line sources (Guilloteau et al. 2013) and that, even for the strongest CN sources among disks, some hyperfine transitions of CN are optically thin (Kastner et al. 2015; Punzi et al. 2015). This species hence potentially affords a direct means to infer N isotope ratios in disks, without the need to resort to assumptions concerning secondary elemental isotopic ratios or line optical depths.

2. Observations

With this as motivation, we have undertaken ALMA observations of the $\text{C}^{14}\text{N}(3-2)$ and $\text{C}^{15}\text{N}(3-2)$ rotational emission at 340 and 330 GHz respectively (see Table A.1) from the molecule-rich disk orbiting TW Hya, a nearby ($d = 59.5(9)$ pc¹), nearly pole-on T Tauri star and disk system that displays exceptionally bright, narrow CN line emission (Kastner et al. 2015; Teague et al. 2016).

Observations of TW Hya were performed in December 2014 and April 2015, using the Atacama Large Millimeter/submillimeter Array (ALMA) interferometer (proposal 2013.1.00196.S). The Fourier plane was sampled by 47 antennas, covering baselines from 15 to 343 m. The CN and C^{15}N rotational lines $N = 3-2$ were observed simultaneously with a channel spacing of 61 kHz (or 0.107 km s^{-1} effective velocity resolution at 340 GHz). The rest frequency for the $\text{C}^{15}\text{N}(3-2)$ hyperfine transitions were taken from the CDMS spectroscopic catalogue (Müller et al. 2005), with 1σ uncertainties of 90 kHz. The CDMS frequencies for the CN(3–2) set of hf lines have much reduced uncertainties of a few 10 kHz only. Flux calibration was performed using Callisto as an absolute reference, while bandpass and phase calibrations were obtained by observing the J1256-0547 and J1037-2934 QSOs respectively. After a first round of calibration using the CASA software (version 4.2.2), the phase calibration was improved using a self-calibration procedure based on the continuum, line-free, emission, from large bandwidth observations performed in parallel to the spectral line observations. The self-calibrated output was then applied to both CN and C^{15}N . Cross-calibration uncertainties were mitigated by

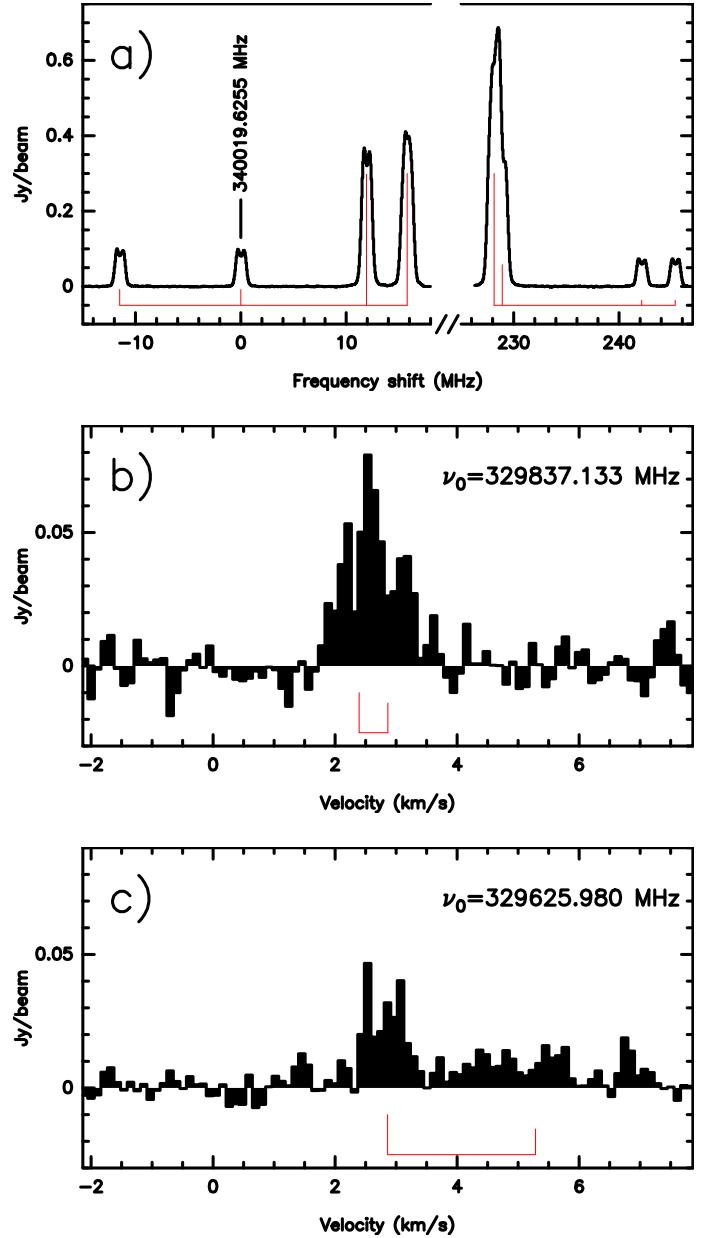


Fig. 1. Spectra, averaged within the dashed circle in Fig. 2, of the entire C^{14}N a) and of the two sets of hyperfine lines of C^{15}N b) and c). The hyperfine splitting and relative strengths of the hf components are indicated below the spectra.

the simultaneous observation of the two isotopologues, while the small (3%) difference in lines frequency ensures nearly identical Fourier plane coverages, continuum emission, and absolute intensity calibration. The calibrated data were then exported to the GILDAS² package format for imaging and analysis.

The CN hyperfine (hf) transitions are well resolved and detected with a high signal-to-noise ratio (S/N) (see Figs. 1 and 2). Specifically, our CN detections include four hf lines with relative intensities 0.054 and 0.027 (see Table A.1). Of the four hf components of the $\text{C}^{15}\text{N}(N = 3-2)$ rotational transition included in our frequency setups, three were successfully detected and are optically thin, while the weakest was only tentatively detected (see panels b and c of Fig. 1).

¹ Here and elsewhere, 1σ uncertainties are given within brackets in units of the last digit.

² <http://www.iram.fr/IRAMFR/GILDAS>

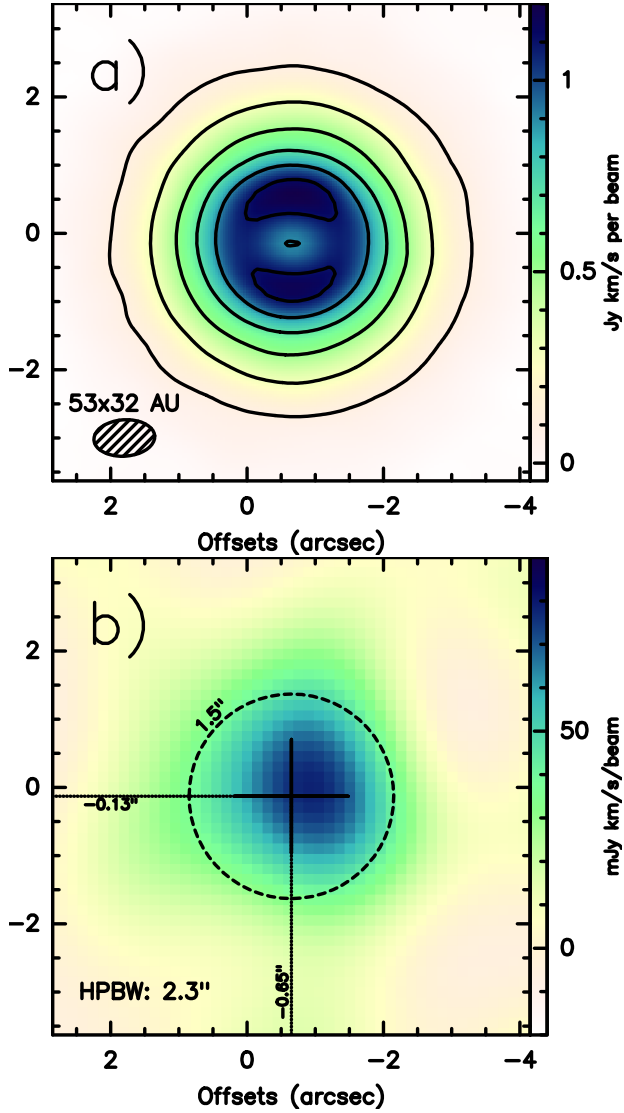


Fig. 2. Integrated intensity maps towards TW Hya with ALMA. **a)** $C^{14}N$ emission summed over the four weakest hyperfine components. **b)** $C^{15}N$ from 329835.5 to 329838.5 MHz, with spatial resolution degraded to $2.3''$. The phase center is at $11^{\text{h}}01^{\text{m}}51.875^{\text{s}}$, $-34^{\circ}42'17.16''$ (J2000).

To produce the images shown in Fig. 2, deconvolution was performed using the Högbom algorithm as implemented in the GILDAS/MAPPING software. The clean beam at 340 GHz was $0.90'' \times 0.53''$ and with a position angle of 86° , and the final sensitivity is between 1.8 and 3.6 mJy/beam/channel. The continuum peak and integrated flux at 340.0465 GHz are 378.0(3) mJy/beam and 1.426(2) Jy respectively, in agreement with observations at nearby frequencies (Qi et al. 2013; Nomura et al. 2016). To increase the S/N of the $C^{15}N$, robust weighting was applied providing good compromise between beam size and secondary lobes level. The synthesized beamwidth is $2.3''$, and the sensitivity was between 5.3 to 6.4 mJy/beam/channel.

The CN map shows a ring structure of deconvolved inner and outer half-maximum radii of roughly 15 and 70 AU respectively, as derived from a very simple model (Figs. 2 and 3), consistent with previous studies based on molecular and continuum emissions (Qi et al. 2013; Teague et al. 2016; Nomura et al. 2016). The very high S/N channel maps of the optically thin CN hyperfine transitions at 340.020 and 340.265 GHz are shown in

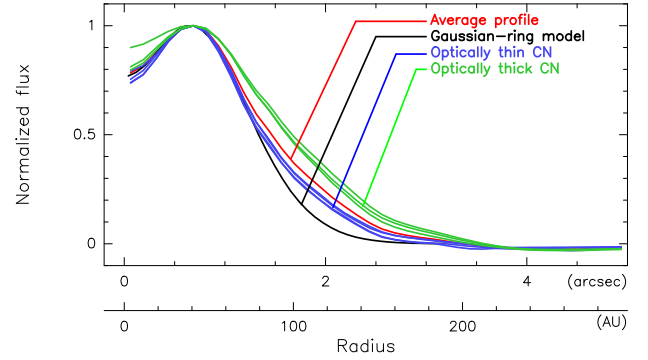


Fig. 3. Azimuthally averaged radial profiles of the integrated flux for the 7 hyperfine (hf) components of $C^{14}N$, four of which are optically thin, the remaining three being optically thick (Fig. 2). The average of the 7 hf components is shown in red. The black line shows the result of a sharp inner-ring model plus Gaussian decrease outwards, convolved by the synthesized beam. The unconvolved ring has a radius of $0.7''$ or 42 AU, and a full-width at half-maximum of 54 AU (at a distance of 59.5 ± 0.9 pc).

Fig. A.2, illustrating both the well-known kinematic pattern of Keplerian disks and the ring-like emission pattern.

3. The CN/ $C^{15}N$ abundance ratio in TW Hya

The disk-averaged CN/ $C^{15}N$ abundance ratio was derived from the integrated visibilities of optically thin hf components of each isotopologue. The chosen CN hf transition at 340.020 GHz is readily shown to be optically thin by considering the total opacity of the CN line, which is of order 4–5 (Kastner et al. 2014), and recognizing that this hf line carries 5.4% of the total intensity. The low optical depth is confirmed by hyperfine analysis of the ALMA spectra and by the identical lineshapes of the disk-averaged spectra of the 4 weakest hf transitions with relative intensities 2.7 and 5.4% (see Fig. C.1 and Appendix C for details). Because $C^{15}N$ is typically a hundred times (or more) less abundant than CN, its detected hf lines are also optically thin. The visibilities of the CN hf line and of the overlapping $C^{15}N$ hf transitions at 329.837 GHz were integrated over a 2 km s^{-1} velocity interval, to optimize S/N, and tapered before fitting in the uv plane by a two-dimensional Gaussian distribution. In doing so, the geometrical parameters were indeed obtained from the high S/N CN map, and then applied to the $C^{15}N$ visibilities letting the $C^{15}N$ integrated flux as the unique free parameter.

The derived integrated flux ratio was translated into a column density ratio by assuming a single excitation temperature for both isotopologues. This assumption is strongly supported by the common excitation temperature of $\approx 20\text{--}25$ K for the CN(3–2) (see Appendix C) and CN(2–1) transitions (Teague et al. 2016). Thermalization is most likely ensured by the high density regions responsible for the CN emission, as inferred from the low kinetic temperatures traced by the narrow CN lines (see Appendix C).

After propagating the various sources of uncertainty, the disk-averaged CN/ $C^{15}N$ abundance ratio is

$$\mathcal{R}_{\text{CN}} = 323(30). \quad (1)$$

4. Two isotopic reservoirs of nitrogen in disks

This direct determination of the CN isotopic ratio in TW Hya can be compared to the indirectly measured ratio in HCN in the nearby ($d = 140$ pc) protoplanetary disk orbiting MWC 480.

Table 1. Results of the uv -plane analysis (see the text for details) using visibilities within a uv radius of 60 m.

	Center position		$FWHM$ (")		Area arcsec ²	Flux [§] Jy km s ⁻¹
	δRA (")	δDec (")	major	minor		
CN	-0.65(1)	-0.13(1)	2.55(2)	2.54(2)	7.33(8)	2.02(2)
C ¹⁵ N [†]	-0.65(0)	-0.13(0)	2.55(0)	2.54(0)	7.33(0)	0.166(13)
C ¹⁵ N [‡]	-0.71(11)	-0.05(12)	2.46(35)	2.13(33)	5.93(126)	0.150(20)

Notes. The center of the 2D-Gaussian is given with respect to the phase center position at RA, Dec coordinates 11^h01^m51.875^s, 34°42'17.16" (J2000). Number in brackets are uncertainties in units of the last digit. ^(§) Fluxes integrated over the CN(3 7/2 5/2 → 2 5/2 5/2) and the two C¹⁵N(3 7/2 → 2 5/2) transitions. The quoted uncertainty does not include the calibration uncertainty (3%). ^(†) uv -fit results with fixed, circular, Gaussian disk taken from the CN fit. ^(‡) uv -fit results without imposing the size of the Gaussian disk.

We have applied the same uv plane analysis described above to archival H¹³CN and HC¹⁵N data for MWC 480 (Guzmán et al. 2015), obtaining

$$H^{13}CN/HC^{15}N = 1.88(34) \quad (2)$$

which improves on, but is consistent with, the 2.8(1.4) value formerly derived. The improvement over the previous analysis is most likely due to our fitting approach which involves fewer free parameters by assuming identical disk properties for both isotopologues. Indeed, our ratio for the MWC 480 disk also agrees well with recent re-analysis of the data (Guzmán et al. 2017).

Assuming that the abundance ratio HCN/H¹³CN is equal to the elemental ¹²C/¹³C isotopic ratio, and adopting 68(15) for the latter (Milam et al. 2005), we obtain an isotopic ratio of nitrogen in HCN in MWC 480 of

$$\mathcal{R}_{HCN} = 128(36). \quad (3)$$

The chemical composition of the solar neighbourhood being homogeneous (Sofia & Meyer 2001), it follows that the elemental, hence primary, reservoir of nitrogen in both TW Hya and MWC 480 should have the same isotopic ratio. Consequently, the distinct ratios in CN and HCN demonstrate that, in addition to the elemental reservoir, at least one of these two disks contains another reservoir of nitrogen, which is fractionated and ¹⁵N-rich. Although the HCN/H¹³CN in disks is not known, the foregoing conclusion would hold true unless this ratio was larger than 132. In the context of prestellar cores, such high ratios have been predicted by recent chemical models (Roueff et al. 2015), but are inconsistent with observations which lead to a ratio of 30 (Daniel et al. 2013). Combined with GCE models predicting that the enrichment in ¹⁵N through stellar nucleosynthesis over the last 4.6 billion years implies $\mathcal{R}_0 > 232$ (Romano & Matteucci 2003), our result demonstrates that HCN in MWC 480, and in the disks studied in Guzmán et al. (2017), traces a heavily fractionated, hence secondary, reservoir of nitrogen.

From our study, it appears that CN and HCN in disks are not tracing the same reservoirs and therefore that the detected CN is not a photodissociation product of HCN. This would imply that CN emission is not dominated by the upper, UV-exposed, disk layer, as is usually assumed (Teague et al. 2016). In contrast, CN emission from cold and UV-shielded regions seems to be favoured. This is further supported by the narrow CN linewidths which constrain the kinetic temperature to be lower than 20–25 K within the CN ring and beyond (see Appendix C). Observations of both CN and HCN at high spatial resolution in a sample of disks spanning a range of viewing geometries, coupled with comprehensive radiative transfer models, are required to fully address the question of the specific origin of the CN emission in disks.

5. The ¹⁴N/¹⁵N isotopic ratio in the present-day ISM

In the following, we provide arguments that the CN/C¹⁵N abundance ratio we have directly measured in the disk orbiting TW Hya is in fact also a measurement of the elemental ¹⁴N/¹⁵N isotopic ratio in the present-day LISM.

The CN abundance measured in the TW Hya disk ratio agrees very well with the average ratio in NH₃ of 321(36) towards Barnard 1, and in N₂H⁺ of 365(135) towards L1689E. Although ratios up to ~1000 have been obtained using N₂H⁺ (Bizzocchi et al. 2013), the weighted average of direct measurements performed in prestellar cores is 336(16) (see Table D.1) and is in very good agreement with our CN ratio in TW Hya. If one adopts the predictions from selective photodissociation disk models (Heays et al. 2014), CN in TW Hya would be enriched in ¹⁵N by ~80% with respect to the elemental reservoir. The elemental ratio in TW Hya, and hence in the LISM, would be $\mathcal{R}_0 \approx 600$, thus larger than in the PSN 4.6 Gyr ago, at odds with galactic evolution chemical model predictions. This would require ammonia and diazalinium (N₂H⁺) in dense cores to be similarly enriched by 80%, in sharp disagreement with predictions of chemical fractionation models (Hily-Blant et al. 2013b; Roueff et al. 2015; see Appendix D). This suggests that the efficiency of selective photodissociation may be much lower in TW Hya.

Given the concomitant ratios in TW Hya and in prestellar cores, a more likely interpretation is that CN, NH₃, and N₂H⁺, are tracing a single reservoir of nitrogen. Furthermore, this reservoir would be the primary one, therefore reflecting the elemental isotopic ratio in the present-day solar neighbourhood. This scenario is in good agreement with the HCN/HC¹⁵N and CN/C¹⁵N ratios in the diffuse LISM (see Fig. 4 and Table D.1). Ratios derived from CN lines in the ultraviolet (UV) show a large scatter, with ratios as high as 452(107), but yield an average ratio of 274(18) – although not compatible with one lower limit at 312. Absorption spectroscopy using the (1–0) rotational line of HCN in translucent clouds ($A_V = 1–4$ mag, Glück et al. 2017) yield a similar average of 276(34) (Lucas & Liszt 1998). In these clouds, CN is efficiently produced by photodissociation of HCN, and both species most likely originate from a single reservoir of nitrogen, presumably in atomic form (Boger & Sternberg 2005). Chemical mass fractionation is inefficient in these clouds ($T_k > 15–30$ K), but selective photodissociation is predicted to enhance ¹⁵N by 10% in CN and HCN (Heays et al. 2014). The low ratios in diffuse clouds would thus correspond to an elemental ratio of 304(37), in agreement with, although at the lower end of, the CN ratio we have measured in TW Hya.

The conclusion that CN in TW Hya traces the primary reservoir of nitrogen also is in accord with predictions from galactic models. According to purely dynamical models,

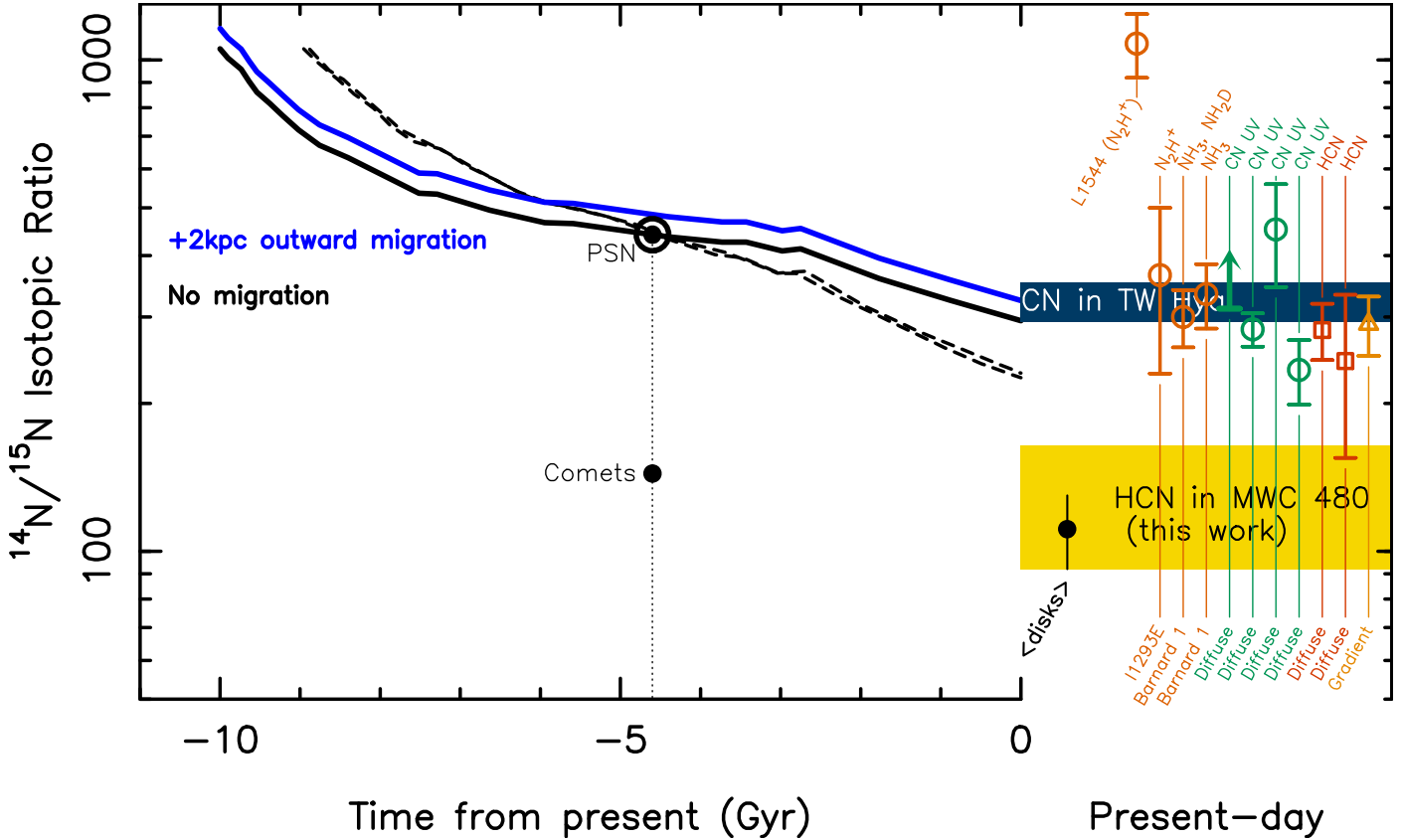


Fig. 4. Present-day nitrogen isotopic ratio in the solar neighbourhood compared to Galactic Chemical Evolution models predictions. Shaded areas: ALMA measurements of the CN/C¹⁵N and HCN/H¹⁵N ratios in TW Hya and MWC 480 respectively. Symbols: directly measured ratios (i.e. not using double-isotopic ratios) in the present-day solar neighbourhood at $r_G = 8.5(10)$ kpc (references are provided in Table D.1). Black curves: GCE model predictions Romano & Matteucci (2003) scaled to a PSN ratio of $\mathcal{R}_\odot = 441$, with ¹⁵N as a primary (full line, their model 2) or secondary product (dashed lines, their models 3s and 3n). Blue curve: GCE model 2 including a 2 kpc outward Sun migration (see the text for details). The weighted average isotopic ratios in comets of 144(3) (see also Fig. A.1) and of 111(19), from H¹³CN/H¹⁵N observations in 5 disks (Guzmán et al. 2017), are also indicated.

the Sun most likely did not migrate from its birthplace (Martínez-Barbosa et al. 2015), and the proposed current ratio $\mathcal{R}_0 = 323(30)$ would indicate a ¹⁵N-enrichment by up to 38(13)% above \mathcal{R}_\odot over the last 4.6 Gyr. This agrees, although marginally, with GCE calculations including ¹⁵N synthesis through novae outbursts (Fig. 4), and especially with models treating ¹⁵N as a primary product (Romano & Matteucci 2003). The agreement is much better with dynamical GCE models which instead predict that the Sun migrated outward by 0.3 to 3.6 kpc (Minchev et al. 2013). Indeed, applying the present-day galactic gradient $d\mathcal{R}/dR = 22.1 \text{ kpc}^{-1}$ (Adande & Ziurys 2012) to the Milky Way at 4.6 Gyr in the past, our CN/C¹⁵N ratio would correspond to an outward migration of the Sun by ~ 2 kpc from its birth location, within the range predicted by dynamical GCE models. It is worth noting that, in addition to provide an explanation for the anomalously high solar metallicity with respect to young, local, B-type stars (Nieva & Przybilla 2012), the outward migration hypothesis would also bring the ¹²C/¹³C elemental isotopic ratio from GCE models (Romano & Matteucci 2003; Milam et al. 2005) into a better agreement with the PSN value of ≈ 90 .

6. The origin of nitrogen in the solar system

Our inference that a fractionated reservoir of nitrogen is present at the time of comet formation in PSN analogues sheds new light

on the history of nitrogen in the solar system. The presence of such a fractionated nitrogen reservoir in the primitive solar system would indicate that parent body evolution is not required to explain the average cometary ratio of 144(3) (see Fig. A.1). A more likely explanation is that atomic nitrogen, from which HCN presumably derives (Hily-Blant et al. 2013a), is a secondary repository of nitrogen at the PSN stage, supporting the usual assumption that N₂ constitutes the primary reservoir (Schwarz & Bergin 2014; Füri & Marty 2015). In this interpretation, the isotopic ratio of 140 in NH₃ in comets (Shinnaka et al. 2016) could indicate that cometary ammonia was primarily formed by hydrogenation of atomic nitrogen in CO-rich interstellar ices (Fedoseev et al. 2015). In addition, the ring-like distribution of CN in TW Hya, which encompasses the giant planet and Kuiper-belt regions, suggests that the primary reservoir was present in the comet-forming zone. Yet, the uniform isotopic ratio of 144 in all comets and the low N₂/CO abundance ratio in comets Halley and 67P/C-G (Rubin et al. 2015) strongly suggest that the primary reservoir was lost, or not captured, by comets, although the underlying mechanism remains an open question. An alternative would be that the bulk of nitrogen in comets has still escaped detection. It is also striking that the ratio of the CN- and HCN-derived nitrogen isotopic ratios in disks, 323:111 (≈ 2.9), are in the same proportion as the mean PSN ratio, 441:144 (≈ 3.1), as measured in the Sun and comets. This further suggests that the fractionation processes building

the two isotopic reservoirs of nitrogen, evinced in present-day PSN analogues, were equally active in the PSN, or in the prestellar core where it formed, 4.6 Gyr ago.

A picture emerges in which dinitrogen was the primary reservoir of nitrogen in the PSN, with an isotopic ratio of 441, whereas atomic N formed a secondary reservoir characterized by $\mathcal{R} \approx 140$. Earth's atmosphere appears intermediate ($\mathcal{R} = 272$), which could reflect a mixture of the two reservoirs of volatile nitrogen, or a third reservoir in its own right (Füri & Marty 2015). The remarkably uniform ratio in comets (see Fig. A.1) suggests that both reservoirs were homogeneously distributed in the PSN. Disentangling the origin of the fractionated reservoir, between processes in the PSN and an interstellar origin, as suggested by the HCN isotopic ratios in prestellar cores (Hily-Blant et al. 2013a), requires high-sensitivity maps of the isotopic ratio in cores and especially of disks spanning a broad range of physical conditions. However, the small scatter of the HCN/HC¹⁵N ratios indirectly measured towards a sample of disks (Guzmán et al. 2017) spanning a broad range of ages and masses – hence likely representing a range of dust size distributions and UV radiation fields – argues in favour of a prestellar origin. Moreover, HCN/HC¹⁵N isotopic ratios as low as 140 were indirectly obtained in prestellar cores (Hily-Blant et al. 2013a). Nevertheless, direct measurements of HCN/HC¹⁵N in prestellar cores remain the missing clue to put the interstellar origin of the fractionated reservoir on a firmer ground. If the scenario presented here holds, we would predict that the HCN/HC¹⁵N ratio in prestellar cores should indeed be lower than the cometary ratio of 144, and closer to the average ratio in disks of 111(19), as a result of galactic chemical evolution.

7. Conclusions

Measurements of nitrogen isotopic ratios are keys to understanding the origin and evolution of the solar system in the context of Galactic nucleosynthesis. The large range of measured ¹⁴N/¹⁵N isotopic ratios in solar system bodies, from ≈ 440 in the Sun and Jupiter to ≈ 140 in comets, may reflect the presence of distinct reservoirs of nitrogen that have recorded interstellar initial conditions, chemical fractionation processes in the PSN, and/or secular elemental abundance evolution over the past 4.6 billion years. In this paper, we have presented the first direct measurement of the volatile C¹⁴N/C¹⁵N isotopic ratio within a protoplanetary disk. The ratio of 323(30), obtained with the ALMA interferometer, is in good agreement with the ratio measured for prestellar cores. The CN/C¹⁵N abundance ratio in the TW Hya disk therefore likely reflects a non-fractionated reservoir of nitrogen that is representative of the present-day elemental ratio of nitrogen in the solar neighbourhood. The comparison with the indirectly derived HCN/HC¹⁵N ratio in other disks demonstrate that disks at the comet formation stage already contain a heavily fractionated reservoir. The measurement of the HCN/HC¹⁵N ratio in TW Hya would provide a striking confirmation of this finding. On a broader perspective, our results support galactic chemical evolution models invoking novae outbursts as primary ¹⁴N sources as well as significant outward migration of the Sun over its lifetime, and furthermore suggest that, whereas the Sun and Jupiter incorporated mass from the PSN's main nitrogen reservoir, solar system comets recorded a secondary, fractionated reservoir of nitrogen.

Acknowledgements. P.H.B. acknowledges the Institut Universitaire de France for financial support. P.H.B. also thanks L. Bonal, N. Prantzos, and E. Quirico for fruitful discussions. The authors wish to thank the referee for a careful reading and for useful comments which improved the clarity of the paper.

This paper makes use of the CDMS catalogue, the CASA and IRAM/GILDAS softwares, and of ALMA data. ALMA is a partnership of ESO (representing its member states), NSF (USA) and NINS (Japan), together with NRC (Canada), NSC and ASIAA (Taiwan), and KASI (Republic of Korea), in cooperation with the Republic of Chile. The Joint ALMA Observatory is operated by ESO, AUI/NRAO and NAOJ. This work has made use of data from the European Space Agency (ESA) mission *Gaia* (<https://www.cosmos.esa.int/gaia>), processed by the *Gaia* Data Processing and Analysis Consortium (DPAC, <https://www.cosmos.esa.int/web/gaia/dpac/consortium>). Funding for the DPAC has been provided by national institutions, in particular the institutions participating in the *Gaia* Multilateral Agreement.

References

- Adande, G. R., & Ziurys, L. M. 2012, *ApJ*, 744, 194
 Audouze, J., Lequeux, J., & Vigroux, L. 1975, *A&A*, 43, 71
 Bizzocchi, L., Caselli, P., Leonardo, E., & Dore, L. 2013, *A&A*, 555, A109
 Bockelée-Morvan, D., Calmonte, U., Charnley, S., et al. 2015, *Space Sci. Rev.*, 197, 47
 Boger, G. I., & Sternberg, A. 2005, *ApJ*, 632, 302
 Bonal, L., Huss, G. R., Krot, A. N., et al. 2010, *Geochim. Cosmochim. Acta*, 74, 6590
 Bottinelli, S., Boogert, A. C. A., Bouwman, J., et al. 2010, *ApJ*, 718, 1100
 Ceccarelli, C., Caselli, P., Bockelée-Morvan, D., et al. 2014, *Protostars and Planets VI*, 859
 Charnley, S. B., & Rodgers, S. D. 2002, *ApJ*, 569, L133
 Cleeves, L. I., Bergin, E. A., Alexander, C. M. O., et al. 2014, *Science*, 345, 1590
 Daniel, F., Gérin, M., Roueff, E., et al. 2013, *A&A*, 560, A3
 Daniel, F., Faure, A., Pagani, L., et al. 2016, *A&A*, 592, A45
 Fedoseev, G., Ioppolo, S., Zhao, D., Lamberts, T., & Linnartz, H. 2015, *MNRAS*, 446, 439
 Füri, E., & Marty, B. 2015, *Nature Geosci.*, 8, 515
 Glück, C. B., Stutzki, J., Röllig, M., Chambers, E., & Risacher, C. 2017, *A&A*, 600, A94
 Guilloteau, S., Di Folco, E., Dutrey, A., et al. 2013, *A&A*, 549, A92
 Guilloteau, S., Reboussin, L., Dutrey, A., et al. 2016, *A&A*, 592, A124
 Guzmán, V. V., Öberg, K. I., Loomis, R., & Qi, C. 2015, *ApJ*, 814, 53
 Guzmán, V. V., Öberg, K. I., Huang, J., Loomis, R., & Qi, C. 2017, *ApJ*, 836, 30
 Heays, A. N., Visser, R., Gredel, R., et al. 2014, *A&A*, 562, A61
 Henning, T., & Semenov, D. 2013, *Chem. Rev.*, 113, 9016
 Hily-Blant, P., Bonal, L., Faure, A., & Quirico, E. 2013a, *Icarus*, 223, 582
 Hily-Blant, P., Pineau des Forêts, G., Faure, A., Le Gal, R., & Padovani, M. 2013b, *A&A*, 557, A65
 Jehin, E., Manfroid, J., Hutsemékers, D., Arpigny, C., & Zucconi, J.-M. 2009, *Earth Moon and Planets*, 105, 167
 Kastner, J. H., Hily-Blant, P., Rodriguez, D. R., Punzi, K., & Forveille, T. 2014, *ApJ*, 793, 55
 Kastner, J. H., Qi, C., Gorti, U., et al. 2015, *ApJ*, 806, 75
 Le Gal, R., Hily-Blant, P., Faure, A., et al. 2014, *A&A*, 562, A83
 Lis, D. C., Wooten, A., Gerin, M., & Roueff, E. 2010, *ApJ*, 710, L49
 Lucas, R., & Liszt, H. 1998, *A&A*, 337, 246
 Martínez-Barbosa, C. A., Brown, A. G. A., & Portegies Zwart, S. 2015, *MNRAS*, 446, 823
 Matteucci, F. 2012, *Chemical Evolution of Galaxies* (Springer-Verlag)
 Milam, S. N., Savage, C., Brewster, M. A., Ziurys, L. M., & Wyckoff, S. 2005, *ApJ*, 634, 1126
 Minchev, I., Chiappini, C., & Martig, M. 2013, *A&A*, 558, A9
 Müller, H. S. P., Thorwirth, S., Roth, D. A., & Winnewisser, G. 2001, *A&A*, 370, L49
 Müller, H. S. P., Schlöder, F., Stutzki, J., & Winnewisser, G. 2005, *J. Molec. Struct.*, 742, 215
 Mumma, M. J., & Charnley, S. B. 2011, *ARA&A*, 49, 471
 Nieva, M.-F., & Przybilla, N. 2012, *A&A*, 539, A143
 Nomura, H., Tsukagoshi, T., Kawabe, R., et al. 2016, *ApJ*, 819, L7
 Punzi, K. M., Hily-Blant, P., Kastner, J. H., Sacco, G. G., & Forveille, T. 2015, *ApJ*, 805, 147
 Qi, C., Öberg, K. I., Wilner, D. J., et al. 2013, *Science*, 341, 630
 Ritchey, A. M., Federman, S. R., & Lambert, D. L. 2015, *ApJ*, 804, L3
 Romano, D., & Matteucci, F. 2003, *MNRAS*, 342, 185
 Roueff, E., Loison, J. C., & Hickson, K. M. 2015, *A&A*, 576, A99
 Rubin, M., Altwegg, K., Balsiger, H., et al. 2015, *Science*, 348, 232
 Schwarz, K. R., & Bergin, E. A. 2014, *ApJ*, 797, 113
 Shinnaka, Y., Kawakita, H., Jehin, E., et al. 2016, *MNRAS*, 462, S195
 Sofia, U. J., & Meyer, D. M. 2001, *ApJ*, 554, L221
 Teague, R., Guilloteau, S., Semenov, D., et al. 2016, *A&A*, 592, A49
 Terzieva, R., & Herbst, E. 2000, *MNRAS*, 317, 563
 van der Tak, F. F. S., Black, J. H., Schöier, F. L., Jansen, D. J., & van Dishoeck, E. F. 2007, *A&A*, 468, 627

Appendix A: Supplementary materials

Table A.1. Spectroscopic properties and relative intensities (R.I.) of the hyperfine CN and C¹⁵N ($NJF \rightarrow N'J'F'$) transitions.

Species	Group	NJF^{\S}	$N'J'F'$	Rest frequency (MHz)	A_{ul}^{\dagger} (s ⁻¹)	g_u^{\ddagger}	R.I. ^{\#}
CN	b	3 5/2 5/2	2 3/2 5/2	340008.13	6.197×10^{-5}	6	0.054
		3 5/2 3/2	2 3/2 3/2	340019.63	9.270×10^{-5}	4	0.054
		3 5/2 7/2	2 3/2 5/2	340031.55	3.845×10^{-4}	8	0.445
		3 5/2 3/2	2 3/2 1/2	340035.41	2.887×10^{-4}	4	0.167
		3 5/2 5/2	2 3/2 3/2	340035.41	3.231×10^{-4}	6	0.281
	a	3 7/2 7/2	2 5/2 5/2	340247.77	3.797×10^{-4}	8	0.307
		3 7/2 9/2	2 5/2 7/2	340247.77	4.131×10^{-4}	10	0.417
		3 7/2 5/2	2 5/2 3/2	340248.54	3.674×10^{-4}	6	0.222
		3 7/2 5/2	2 5/2 5/2	340261.77	4.479×10^{-5}	6	0.027
		3 7/2 7/2	2 5/2 7/2	340264.95	3.350×10^{-5}	8	0.027
C ¹⁵ N	3 5/2 2	2 3/2 1	329623.32	3.155×10^{-4}	5	0.159	
	3 5/2 3	2 3/2 2	329625.98	3.508×10^{-4}	7	0.247	
	3 7/2 3	2 5/2 2	329837.13	3.583×10^{-4}	7	0.253	
	3 7/2 4	2 5/2 3	329837.65	3.764×10^{-4}	9	0.341	

Notes. ^(§) Quantum numbers: N is the rotational angular momentum, $J = N + 1/2$ describes the electronic spin coupling, and $F = J + I$ describes the nuclear spin coupling ($I = 1$ for ¹⁴N, and $1/2$ for ¹⁵N). ^(†) Einstein coefficient for spontaneous radiative decay. ^(‡) Upper level degeneracy (including fine and hyperfine splitting). ^(#) Normalized to a total of unity per fine structure group.

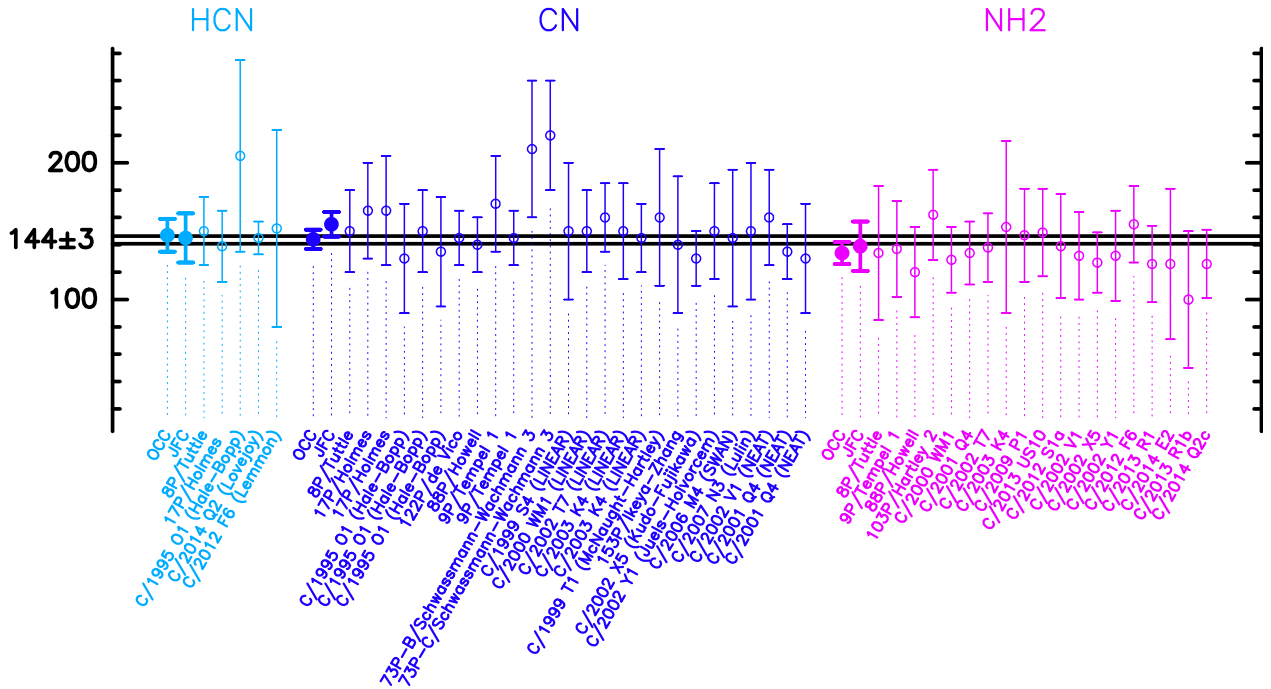


Fig. A.1. Compilation of all isotopic ratios in comets. The observed carrier is indicated above each measurement. Although it is clear that NH₂ is a photodissociation product of ammonia in the coma, the origin of CN is less certain. Data were taken from Jehin et al. (2009) and Bockelée-Morvan et al. (2015). The weighted average ratio is 144(3). For each carrier, the average ratios for Jupiter Family Comets (JFC) and Oort Cloud Comets (OCC), are indicated, where the distinction between JFC and OCC was based only on the periodicity of the comets being respectively lower and higher than 200 yr (Shinnaka et al. 2016).

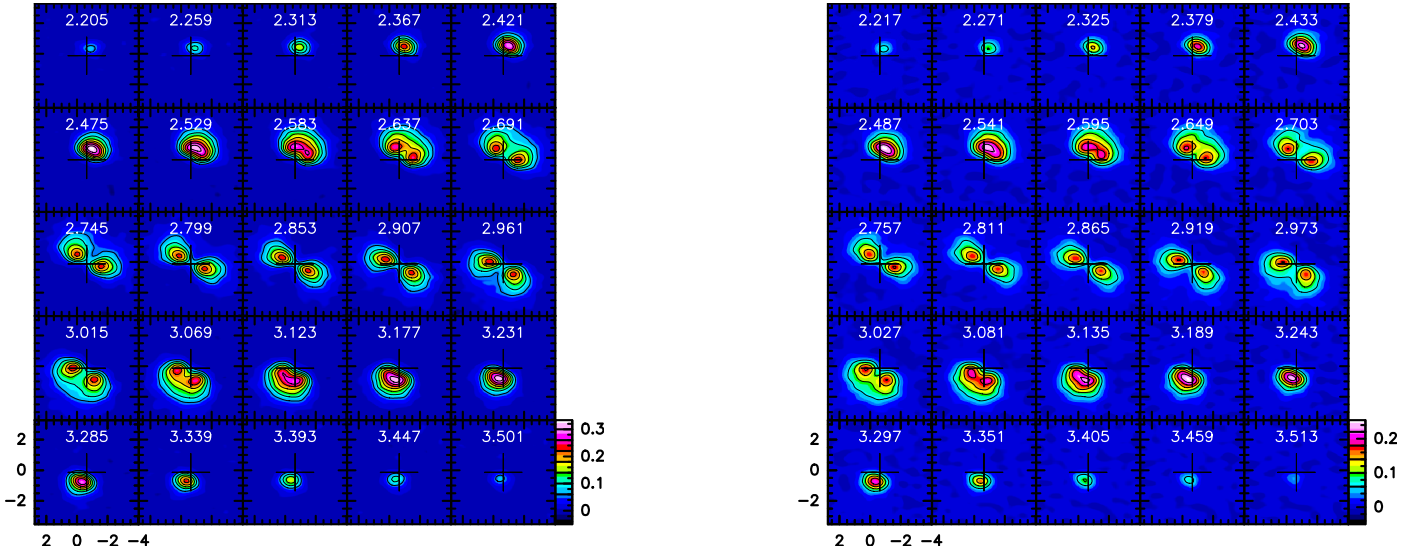


Fig. A.2. Channel maps (in Jy/beam) of the optically thin hyperfine lines of CN at 340.020 GHz (*left*) and 340.265 GHz (*right*). The LSR velocity is indicated (in km s^{-1}) in each panel. Offsets are in arcsec, with respect to the phase center. The half-power beamwidth is $0.89'' \times 0.53''$.

Appendix B: *uv*-plane analysis

The integrated visibilities of CN and C^{15}N were fitted with two-dimensional Gaussian while applying a cutoff radius (equivalent to smoothing in the direct plane), from 60 to 120 m. In particular, with cutoffs smaller than 100 m, the central hole is smeared out and the Gaussian-disk model is mechanically appropriate. The fitting was performed using the `UV_FIT` task of the GILDAS/MAPPING software. The 6 free parameters of the CN fit are the center, major and minor axis, the position angle of the Gaussian disk, and the total flux. The geometrical parameters of the CN disk are applied to the C^{15}N visibilities thus leaving the flux as the only one free parameter. The results depend very marginally on the cutoff radius, although the residuals of the CN fits obviously show an increasing contribution from the central hole as the spatial resolution improves. The results of the fitting procedure for a cutoff *uv* radius of 60 m are shown in Fig. C.2 and summarized in Table 1.

To validate the procedure, we also performed a Gaussian fit to the C^{15}N visibilities while letting all parameters as free, leading to geometrical parameters which agree with the CN fit to within 1σ or less (see Table 1). To estimate the contribution of the geometrical assumptions to the final uncertainties of the fluxes and flux ratio, we performed a series of *uv* minimizations, in which the same (either elliptical or circular) Gaussian shape was imposed to both CN and C^{15}N , with the center and size parameters randomly and independently chosen within 2σ around the previous CN fit result. The resulting fluxes and flux ratios vary by typically 0.1σ , showing that the uncertainty is dominated by the 10% statistical fluctuations of the C^{15}N visibilities.

Of the above assumptions, the co-spatial distribution of CN and C^{15}N is likely the most difficult to firmly assess, as it ideally rests on self-consistent physico-chemical models of disks, in a time-dependent fashion to properly take into account the complex interplay between physical and chemical processes acting on comparable timescales. Moreover, radiative transfer effects can lead to different distribution-to-emission relation even for co-spatial species. However, having optically thin lines in hand greatly alleviates such issues. Still, even if the main production and destruction pathways of isotopologues are the same,

specific reactions may proceed at different rates, giving rise to fractionation. The co-spatial assumption is therefore species- and environment-dependent. In the case of CN in TW Hya, the potential fractionation processes are chemical reactions and selective photodissociation. Chemical fractionation is most likely negligible for CN, because of inefficient fractionation reactions (Roueff et al. 2015) and/or because freeze-out is damping out gas-phase processes (Heays et al. 2014). Selective photodissociation could be a radially variable process, since it is driven by UV photons while being expectedly sensitive to the dust size distribution, two properties which depend on the distance to the central protostar and height above the midplane. The outcome of both effects is far from straightforward, and could even cancel each other, with for example dust growth at large radii compensating for geometrical dilution of the UV photons from the central protostar (if dominating the UV flux). We note that the maps in Fig. 2 suggest that the C^{15}N integrated intensity is shifted North-West with respect to the CN map. However, we stress that these maps require deconvolving the visibilities which always introduces artifacts, especially when the S/N is not high, as is the case for C^{15}N , and no strong effort (apart from using robust weighting) was made to try and improve its deconvolution. Indeed, the C^{15}N map was not used in this work.

Appendix C: Excitation of CN and C^{15}N

One key feature of our derivation of the CN/ C^{15}N abundance ratio is the detection, with high S/N, of the two weakest hyperfine transitions of CN, at 340.262 and 340.265 GHz, thus providing direct access to its total column density with no requirement for radiative transfer calculations. Being able to measure the CN/ C^{15}N abundance ratio directly from the main isotopologue also improves significantly over previous observations in prestellar cores using the $\text{C}^{13}\text{N}/\text{C}^{15}\text{N}$ double isotopic ratio (Hily-Blant et al. 2013b).

We estimated the optical depth of the hf components of the CN rotational transitions by extracting deconvolved CN spectra at different locations across the disk (see Fig. C.3). In what follows, the hf lines of the fine structure group at rest frequencies

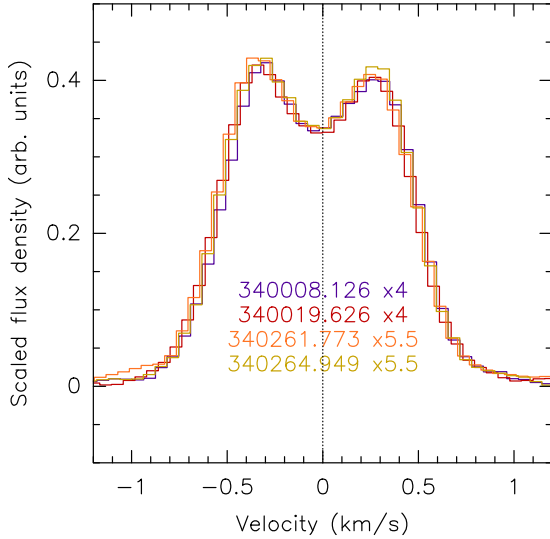


Fig. C.1. Disk-averaged four weakest hf transitions of CN(3-2) (see Table A.1) are superimposed after being scaled by their theoretical relative intensities.

around 340.3 GHz are labelled as *a*, while *b* refers to those around 340.0 GHz (see Table A.1). At each position, each group of hf lines was fitted simultaneously, using the HFS fitting procedure (Hily-Blant et al. 2013a) of the GILDAS/CLASS software. In doing so, the fluxes were brought into the specific-intensity scale by applying a 44 mJy/K conversion factor. The fitting algorithm assumes that the excitation temperature is equal for all hf lines within each group (see below). The results are shown in Fig. C.3. Towards the central parts of the disk, where Keplerian smearing increases, the minimization becomes poorer than towards the external parts where the lines are very well fitted. Fitting each fine structure set of lines provides a consistency check of the results.

The derived total opacity is ≈ 3.4 – 5.4 for groups *a* and *b* lines, confirming previous studies (Kastner et al. 2014). The weakest hf CN lines, in group *a*, which carry 2.7% of the total intensity (see Table 1), is thus less than 0.15, well into the optically thin regime. Figure C.1 shows a comparison of the disk-averaged spectra of the four weakest hf transitions of CN scaled by their relative intensities. The very good match of the spectral profiles indicates that they are all optically thin, as no opacity broadening can be noticed although the relative intensities vary from 2.7 to 5.4%. The detected $C^{15}N$ hf lines can safely be assumed optically thin. This is further supported by the observed relative strengths of these two hf lines (see Fig. 1).

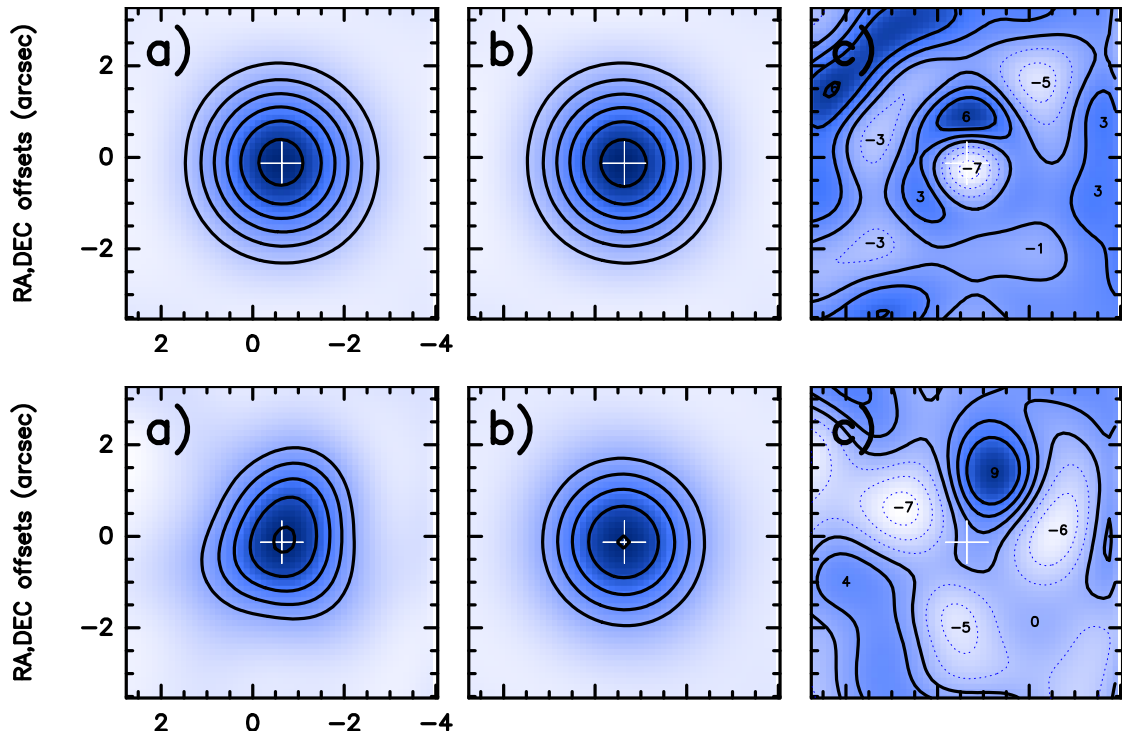


Fig. C.2. Results of the *uv*-plane analysis (see the text for details) for $C^{14}N$ (top) and $C^{15}N$ (bottom). On each row, panels **a**) and **b**) show the dirty image and the fitted Gaussian disk (Jy/beam), and panel **e**) shows the residuals (in mJy/beam). For $C^{14}N$, contours in panels **a**) and **b**) are 0.1 to 0.7 by 0.1 Jy/beam, and for $C^{15}N$ from 0.02 to 0.07 by 0.01 Jy/beam. Values of local extrema are indicated in the residuals. The $C^{15}N$ fit assumes the Gaussian disk from $C^{14}N$. The results are summarized in Table 1.

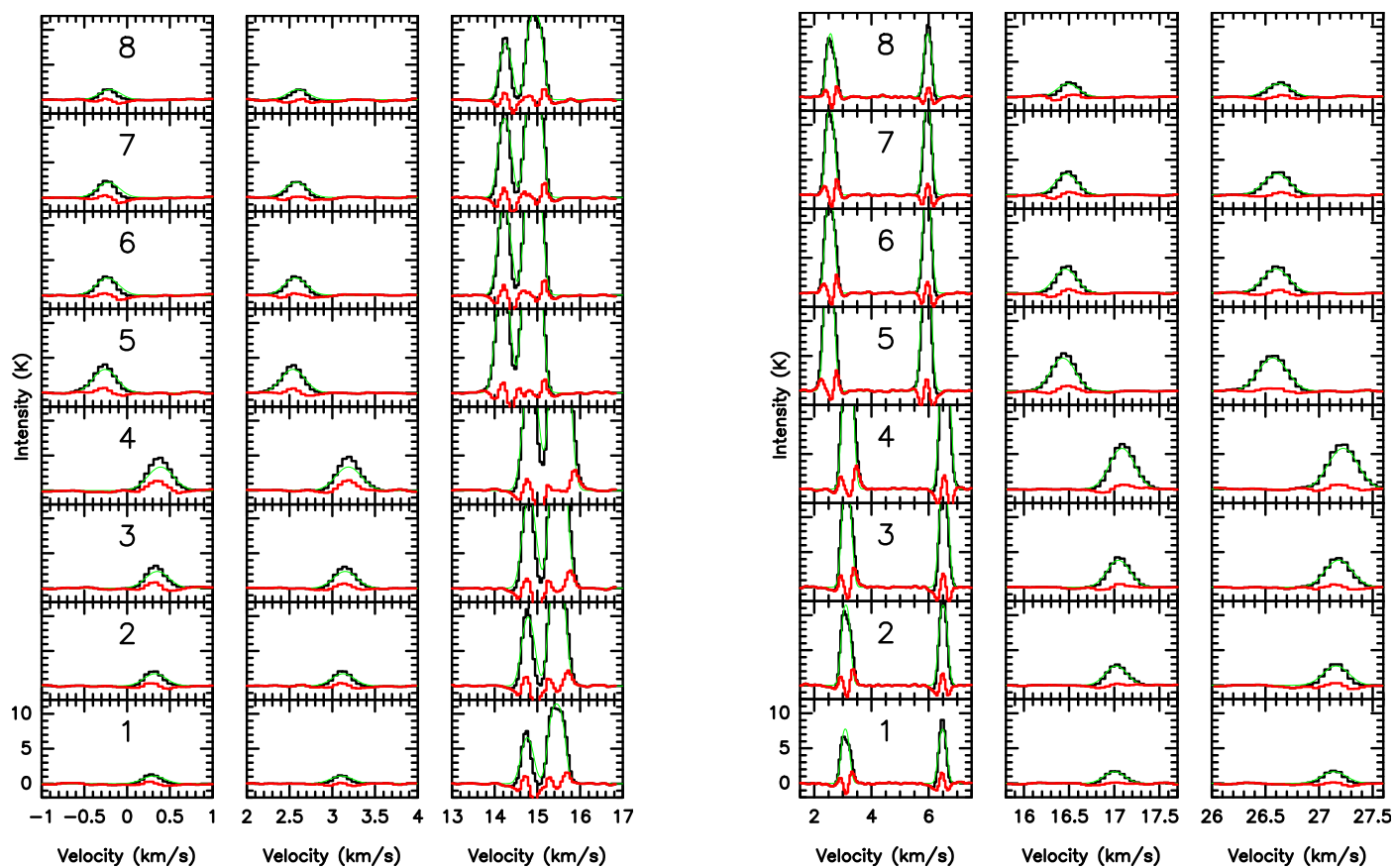
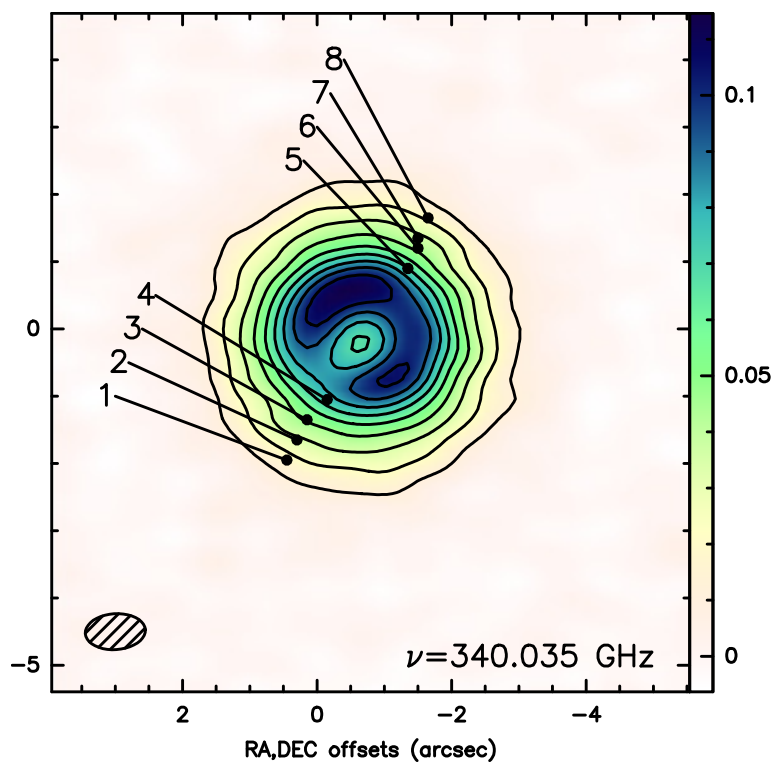


Fig. C.3. Spectra of the hf lines of CN (*a* group, *left*; *b* group *right*) at different locations in the disk (*top panel*; integrated emission, in Jy/beam). Fits and their residuals to hyperfine structure (see Appendix C for details) are shown for each hf transition (green and red, resp.). Only reduced velocity intervals centered on the hf lines are shown.

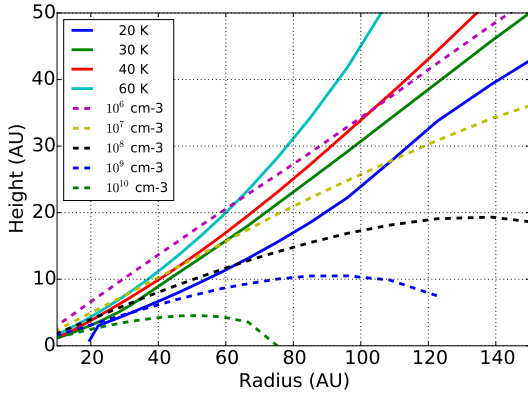


Fig. C.4. Locus of constant kinetic temperature (in K) and total number density (in cm^{-3}) from the physical TW Hya model of (Qi et al. 2013).

For optically thin lines, going from line intensity ratios to abundance ratios only requires the spectroscopic properties and excitation of each line to be taken into account, based on the usual relation between the total column density and the integrated opacity:

$$N_{\text{tot}} = \frac{8\pi\nu^3}{A_{ul}g_u c^3} \frac{e^{E_l/kT_{\text{ex}}}}{1 - e^{-(E_u - E_l)/kT_{\text{ex}}}} Q(T_{\text{ex}}) \int \tau_{\nu} dv = f(ul, T_{\text{ex}}) \int \tau_{\nu} dv, \quad (\text{C.1})$$

where T_{ex} is the excitation temperature of the $u \rightarrow l$ hyperfine transition characterized by its Einstein coefficient A_{ul} and upper level degeneracy g_u (see Table A.1). The partition function Q is also a function of the excitation temperature, and is calculated through a linear interpolation across the tabulated values from the CDMS catalogue (Müller et al. 2001). Accordingly, the CN/ C^{15}N column density ratio is proportional to the ratio of the integrated opacity scaled by a species-dependent prefactor $f(ul, T_{\text{ex}})$ which depends upon the excitation temperature of each transition. In the following, we demonstrate that a single excitation temperature can be adopted for both sets of optically thin hyperfine lines of CN and C^{15}N . We also estimated the uncertainty associated to this assumption.

On general terms, the excitation state of each molecule results from the competition between radiative and collisional processes, which may vary significantly within the disk as the density and kinetic temperature depend on the radius R and height Z above the midplane (see Fig. C.4). However, it must be emphasized that our measurement of the isotopic ratio does not require absolute determinations of the column densities of each isotopologue. Instead, it is important to guarantee that the single excitation temperature assumption holds.

We examined in more details the assumption that all hf lines are characterized by a single excitation temperature. This is supported by the relatively small total opacity of each group of hf lines. Moreover, the excitation temperature of the CN rotational transition, as obtained from the HFS fits, are 17–27 K for both fine structure groups (see Table C.1). In our analysis, spectra labelled 4 and 5 in Fig. C.3, for which the fits are the poorest because the main hf transitions overlap, have the highest opacities (total τ of 6.1). At any given location, the opacity of each group are consistent to better than 15%. The excitation temperatures are also in very good agreement with the 25 K value of the CN(2-1) lines at 100 AU (Teague et al. 2016). This provides a very strong indication that the CN(2-1) and (3-2)

lines are thermalized, or very close to be so. The derived excitation temperatures are higher than in our single-dish study, confirming the suggestion that the beam dilution was not properly taken into account (Guilloteau et al. 2016). The corresponding total CN column density is $\approx 10^{14} \text{ cm}^{-2}$, although we stress that a robust determination of the CN column density should await for a self-consistent modelling of the CN(2-1) and CN(3-2) lines observed with ALMA.

The single excitation temperature assumption is further substantiated by the FWHM of the CN lines which indicate that the emission originates from regions with high density. At any location, the FWHM measured through Gaussian fitting to each hf component, is due to the combined effects of Keplerian motion and non-thermal (e.g. turbulence) plus thermal broadenings, and therefore provides an upper limit on the kinetic temperature through $\sigma_v = \text{FWHM}/2.35 \geq (2kT_k/\mu)^{1/2}$, with $\mu = 26 \text{ amu}$ for the CN molecule. The maps of the FWHM of the group a hf transitions (see Table A.1) are shown in Fig. C.5. The associated upper limit on the kinetic temperature assuming purely thermal broadening are also indicated. The quoted FWHMs have not been deconvolved from the autocorrelator transfer function. The Keplerian smearing associated to the 7° disk inclination was also not subtracted, so that the upper limits on T_k are conservative ones. The FWHMs of the optically thin hf lines at 340.008 and 340.020 GHz correspond to kinetic temperature lower than 20–25 K within the CN-ring (i.e. with convolved radii $\leq 90 \text{ AU}$, see Fig. 3). These upper limits further decrease at larger radii, reaching $T_k \leq 15 \text{ K}$ beyond 120 AU.

Based on a model of the physical structure of the TW Hya disk (Qi et al. 2013), the 20–25 K upper limit corresponds to a lower limit on the density of a few 10^7 cm^{-3} for radii comprised in the range 60 to 120 AU. The non-equilibrium statistical populations of the CN and C^{15}N hyperfine levels were calculated under the escape probability formalism using the RADEX code (van der Tak et al. 2007) and collision rates coefficients, for CN and C^{15}N , at the hyperfine level (Hily-Blant et al. 2013b). At several radii from 60 to 120 AU, level populations were computed as a function of height above the disk midplane for physical conditions appropriate to the TW Hya disk. Figure C.6 shows the results at $R = 60$ and 85 AU, which correspond to upper limits on T_k of ≈ 25 and 20 K respectively. At each density and kinetic temperature, a range of CN column densities from 10^{12} to 10^{15} cm^{-2} was explored while that of C^{15}N was a factor 300 or 441 lower. The value of the isotopic ratio was not found to change the following results. At heights such that $T_k < 20\text{--}25 \text{ K}$, the excitation temperature of the 340.020 CN line and the 329.837 C^{15}N line are equal to better than 3%. At higher kinetic temperatures, the density decreases and both transitions start to deviate from thermalization, although very moderately. The present excitation study includes locations well within the CN ring (Fig. 3), and is thus representative of the excitation of the bulk of the CN emission. In addition to provide strong support to the single excitation temperature assumption, our analysis suggests that the CN emission does not originate in the upper, warm, layer. Yet, 2D radiative transfer calculations are required to demonstrate this claim.

At each radius and height with $T_k < 20 \text{ K}$, the prefactors in Eq. (C.1) were finally computed, leading to a prefactor ratio of

$$f_{14}/f_{15} = 26.5(8). \quad (\text{C.2})$$

The uncertainty in Eq. (1), including all aforementioned contributions, is finally dominated by the statistical uncertainties on

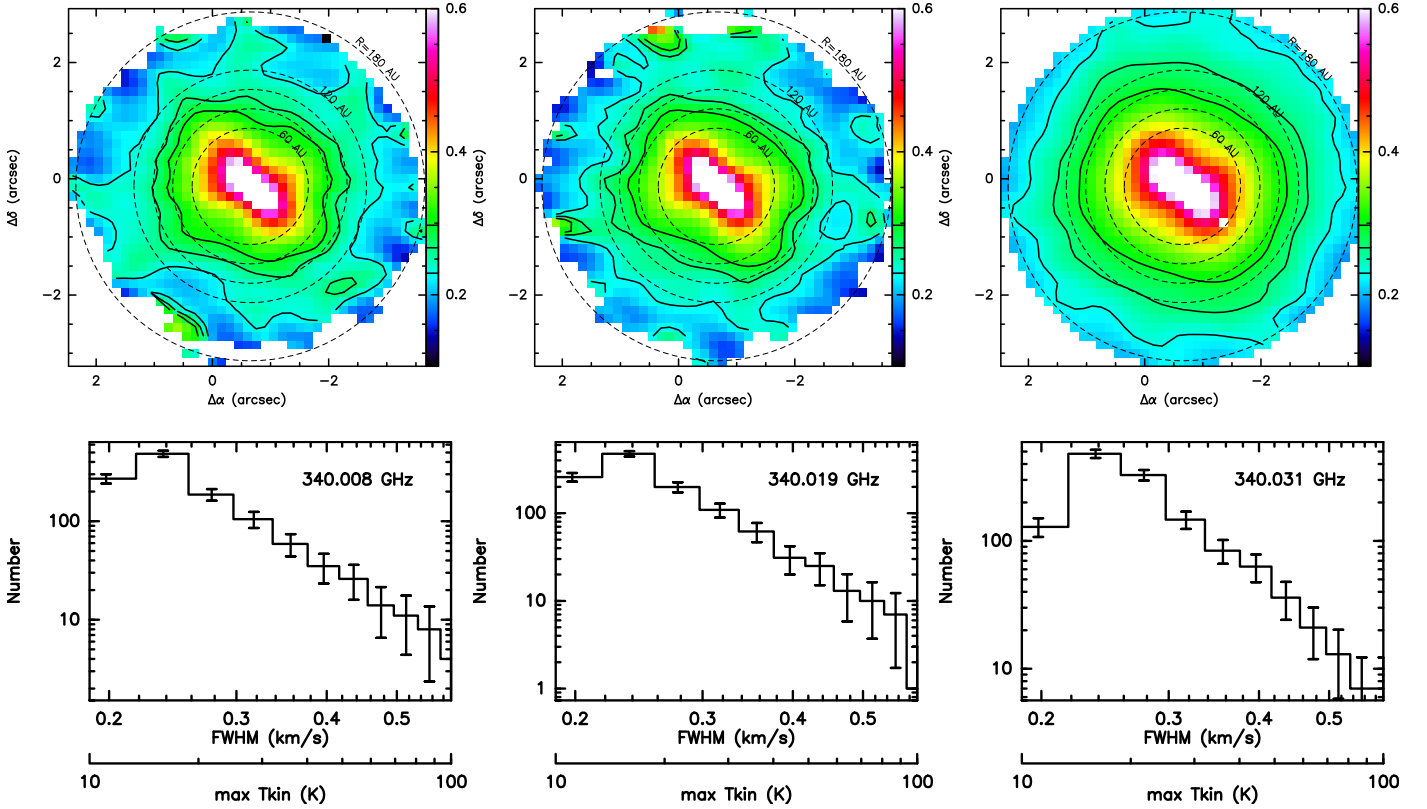


Fig. C.5. Maps (*top*) and histograms (*bottom*) of the raw FWHM (in km s^{-1}) of three CN hf lines obtained from Gaussian fits to each spectrum. Only spectra with an area S/N larger than seven were kept. The contours (*top panels*) show the locus of constant kinetic temperature (15, 20, 25 K) adopting $\text{FWHM}/2.35 = (2kT_k/\mu)^{1/2}$. The distance to the source is 59.5 pc and the effective velocity resolution is 107 m/s.

Table C.1. Results of the HFS fits (total opacity, and excitation temperature), for groups *a* and *b*, at each location (see Fig. C.3).

#	<i>R</i> (AU)	τ_a	$T_{\text{ex}, a}$ (K)	τ_b	$T_{\text{ex}, b}$ (K)
1	126.2	3.4	20	3.4	17
2	106.3	4.2	24	4.3	21
3	86.5	4.8	27	4.9	24
4 [†]	62.0	5.4	32	6.2	28
5 [†]	74.4	6.1	29	5.0	27
6	94.2	5.4	25	4.3	23
7	101.8	5.1	24	4.1	22
8	121.8	4.5	20	3.2	19

Notes. ^(†) Main hf components overlap.

the C^{15}N visibilities:

$$\frac{\delta R}{R} = \left[\left(\frac{\delta(f_{14}/f_{15})}{f_{14}/f_{15}} \right)^2 + \left(\frac{\delta S_{14}}{S_{14}} \right)^2 + \left(\frac{\delta S_{15}}{S_{15}} \right)^2 \right]^{1/2} = 10\%. \quad (\text{C.3})$$

Appendix D: Fractionation in cores and disks

Here, we examine further the possibility that the consistency between the isotopic ratio in CN in TW Hya on the one hand, and in ammonia and diazenilium in prestellar cores on the other hand, represent the elemental ratio rather than the result of fractionation processes. Since the elemental ratio is the same in these objects, the potential fractionation processes would have to be

equally efficient although under significantly different disk- and core-like physical conditions. Indeed, disks have much larger density and are exposed to higher UV fields compared to prestellar cores, which are exposed to a higher flux of ionizing cosmic-rays than disks (Henning & Semenov 2013; Cleeves et al. 2014). Hence, fractionation processes in disks and cores, if efficient, are likely of a different nature, respectively selective photodissociation or chemical mass fractionation.

Chemical fractionation through gas-phase reactions is a temperature-driven process, and for nitrogen, it is expected to become efficient at temperatures significantly lower than 30 K (Terzieva & Herbst 2000). At large density ($>10^7 \text{ cm}^{-3}$), for example, close to the disk midplane where considerable freeze-out of gas-phase species takes place, species-dependent depletion may strongly enhance fractionation (Charnley & Rodgers 2002), although the resulting amount of ammonia in ices is outrageously large with respect to observations of interstellar ices (Bottinelli et al. 2010) and even comets (Mumma & Charnley 2011). At the lower densities typical of prestellar cores ($\sim 10^4 \text{ cm}^{-3}$), the fractionation level may reach 25% on short timescales, and $\sim 10\%$ at steady-state (Terzieva & Herbst 2000; Hily-Blant et al. 2013b; Roueff et al. 2015). Regardless the discrepancies between chemical model predictions in prestellar cores, ammonia and diazenilium are consistently found to be marginally affected by fractionation. Selective photodissociation is also negligible in such environments where the amount of internally-generated UV photons is not sufficient to promote N_2 over N^{15}N (Heays et al. 2014). Altogether, this strongly suggests that NH_3 and N_2H^+ species are tracing the elemental ratio. Nevertheless, measuring their isotopic ratios is not as direct as for CN in TW Hya, because radiative transfer effects can not be

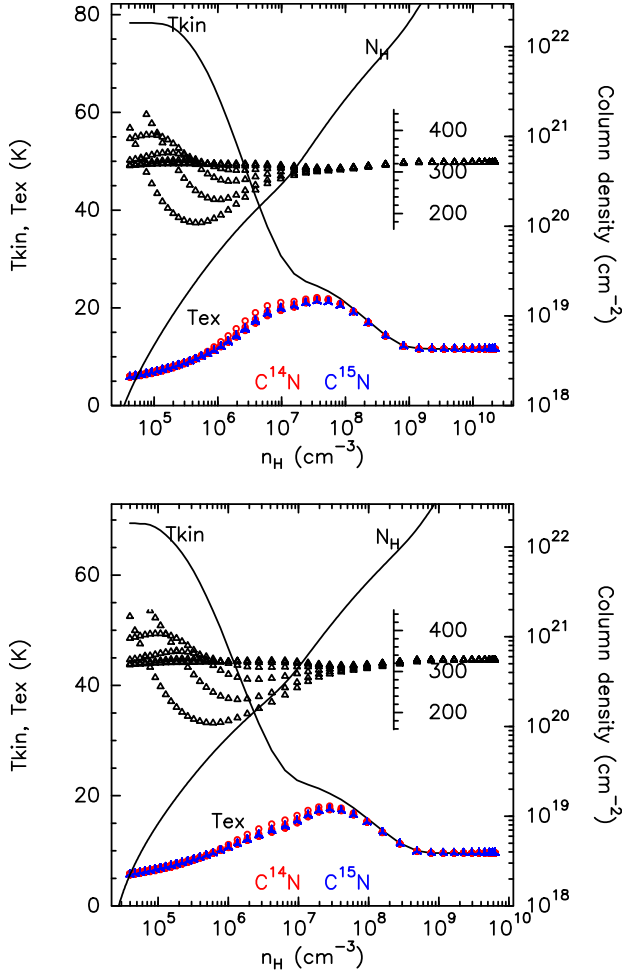


Fig. C.6. Physical structure and excitation temperatures of $\text{CN}(\nu = 340.265 \text{ GHz})$ and C^{15}N , within the CN-ring, at radii of $R = 60$ (*top*) and 85 AU (*bottom*). The total proton number density and kinetic temperature profiles are taken from (Qi et al. 2013). The corresponding cumulative column density, increasing towards the midplane, is also shown (right scale). The excitation temperatures T_{ex} of the CN and C^{15}N hyperfine components (star triangles and open circles, resp.) considered in our uv -plane analysis (see Sects. A.2 and A.3) were obtained in the escape probability formalism using the RADEX code (van der Tak et al. 2007), and adopting a FWHM of 0.25 km s^{-1} . For each density and temperature, a range of CN total column densities were adopted, from 10^{12} to 10^{15} cm^{-2} , with C^{15}N being 300 times less abundant. Also shown is the CN/ C^{15}N isotopic ratio (open triangles, inset scale) obtained by use of Eq. (C.1) when adopting the CN and C^{15}N excitation temperatures from the non-LTE calculations.

neglected and spatial information, which is critical to disentangle between line excitation and abundance gradients, is usually

lacking due to the intrinsic weakness of the ^{15}N isotopologues (Bizzocchi et al. 2013). On the other hand, the total column density of ammonia often relies on assumptions regarding its ortho-to-para ratio (Lis et al. 2010).

In contrast, models of UV-irradiated disks predict significant enrichment of CN and HCN in ^{15}N , at heights of 20 to 40 AU above the midplane at $R = 105 \text{ AU}$, with CN/ C^{15}N column density ratio reaching 250 relative to an elemental ratio of 441 (Heays et al. 2014). A simple scaling indicates that the $\mathcal{R}_{\text{CN}} = 323$ in TW Hya would require an elemental ratio of $\mathcal{R}_0 = 575$. However, such a high elemental ratio would disagree with GCE models which predict an enrichment in ^{15}N with time, hence a present-day elemental ratio lower than $\mathcal{R}_0 = 441$ (or lower than ≈ 500 in the outward Sun migration hypothesis). This high value of \mathcal{R}_0 would also require gas-phase NH_3 and N_2H^+ to be significantly ($\sim 65\text{--}95\%$) fractionated in prestellar cores envelopes, at odds with model predictions (Terzieva & Herbst 2000; Hily-Blant et al. 2013b; Roueff et al. 2015). Last, such a high elemental ratio would also imply that CN and HCN are also strongly enriched in ^{15}N in diffuse molecular clouds, in which the ratios in these species are as low as 250 (see Table D.1), while the same model predicts instead a depletion of $\approx 10\%$ at most at visual extinction below 2 mag.

It appears more likely that the efficiency of N_2 selective photodissociation has been overestimated in disk models. Indeed, we note that these models predict CN and HCN column density ratios of 250 and 90 respectively, which are a factor of 1.3–1.4 smaller than the ratios observed in TW Hya and MWC 480. Yet, selective photodissociation is primarily sensitive to UV propagation and hence to the radial and vertical profiles of density and dust size distribution and, probably to a lesser extent, to the kinetic temperature and the ionization fraction of the gas. To explain the observed CN and HCN ratios with these models and $\mathcal{R}_0 = 441$ would thus require to reduce the efficiency of selective photodissociation by $\approx 30\%$. However, this would, in turn, imply that ammonia ($\mathcal{R} = 321$) is significantly enriched in ^{15}N in prestellar cores (40%), a possibility that models of fractionation in prestellar cores consistently rule out. It appears that contradicting consequences are obtained when assuming that the isotopic ratio observed in disks and cores derive from a present-day elemental ratio of 441, even when allowing for uncertainties on disk and prestellar core fractionation models. Nevertheless, a definitive proof that selective photodissociation has been overestimated in published disk models requires thorough exploration of the wide parameter-space of models selective photodissociation in disks is timely, with particular attention drawn on the impact of the dust size distribution and mass of the central protostar.

Table D.1. Direct measurements of the $^{14}\text{N}/^{15}\text{N}$ isotopic ratio in the local ISM (at a distance d to the Sun), derived from direct $X^{14}\text{N}/X^{15}\text{N}$ abundance ratios using various molecular carriers and techniques.

Carrier	Environment	Source	Gal. coord.	d (pc)	$^{14}\text{N}/^{15}\text{N}$	Reference
HCN	Diffuse	B0415+379 [†]	161.7, -8.8	<1000	244(89)	Lucas & Liszt (1998)
HCN	Diffuse	B0415+379 [†]	161.7, -8.8	<1000	282(37)	Lucas & Liszt (1998)
CN	Diffuse	HD 73882	260.2, 0.64	<1000	234(35)	Ritchey et al. (2015)
CN	Diffuse	HD 154368	350.0, 3.22	<1000	452(107)	Ritchey et al. (2015)
CN	Diffuse	HD 169454	17.5, -0.67	<1000	283(22)	Ritchey et al. (2015)
CN	Diffuse	HD 210121	56.9, -44.5	<1000	>312	Ritchey et al. (2015)
NH ₃	Prestellar	Barnard 1	159.2, -20.1	235	334(17)	Lis et al. (2010)
NH ₃	Prestellar	Barnard 1	159.2, -20.1	235	307(50)	Daniel et al. (2013)
NH ₂ D	Prestellar	Barnard 1	159.2, -20.1	235	255(80)	Daniel et al. (2013)
N ₂ H ⁺	Prestellar	I16923E	353.9, 15.8	125	365(135)	Daniel et al. (2016)
N ₂ H ⁺	Prestellar	L1544	178.0, -9.7	150	1080(160)	Bizzocchi et al. (2013)
CN	Disk	TW Hya	278.7, 23.0	59.5	323(30)	This work
CN	–	Interpolation [‡]	–	0	290 ± 40	Adande & Ziurys (2012)

Notes. Uncertainties are at the 1σ level. These data correspond to Fig. 4. ^(†) Two velocity components were detected towards this source. ^(‡) Galactic gradient obtained from several source types.

The main reservoir of nitrogen in the dense ISM is not known, although it is likely that one of the main reservoirs of nitrogen in the dense ISM are NH_3 ices. The abundance of NH_3 in ices is estimated to be between 5 and 20% the abundance of water in the ice mantles of grains. However the nitrogen isotopic ratio has never been measured in them. Which means that the isotopic ratio of one the main reservoirs of nitrogen in the ISM remains to be measured. The fact that comets preserve at least part of their interstellar heritage (Section 1.3) means that the nitrogen isotopic ratios we see in comets today may be a reflexion of the isotopic ratios of nitrogen in the ices at the PSN.

With this in mind we set out to measure the nitrogen isotopic ratio of interstellar ices by observing the sublimation of ices that occurs at the protostellar phase (Section 1.1.2). In the warm region close to the protostar, the abundances of NH_3 and NH_2D are expected to be greatly enhanced due to evaporation from the ices (Aikawa et al., 2012) and the $^{14}\text{N}/^{15}\text{N}$ isotopic ratio in gas-phase NH_2D is thus essentially that in the ice. Under the assumption that gas-phase fractionation takes place on a timescale longer than the desorption from the ices. This is a most likely assumption given that the timescale of the protostar phase ($< 10^5$ yr Section 1.1.2) is much shorter than the chemical timescale, $\sim 3 \times 10^6$ yr Hily-Blant et al., 2013b.

We targeted three well studied protostars IRAS 03282 + 3035 (Tobin et al., 2015), IRAS 16293 – 2422 (Zapata et al., 2013; Favre et al., 2014; Jørgensen et al., 2016) and VLA 1623 – 2417 (Murillo et al., 2015) (henceforth IRAS03282, IRAS16293 and VLA1623). Towards this three protostars we observed the $1_{1,1} \rightarrow 1_{1,0}$ transition of singly deuterated ammonia (NH_2D) along with the same transition of the ^{15}N substituted isotopologue, $o\text{-}^{15}\text{NH}_2\text{D}$. We also observed in parallel the H^{13}CN and HC^{15}N $J = 1 \rightarrow 0$ transitions thanks to the proximity in frequency of this transitions to the $o\text{-}\text{NH}_2\text{D}$ $1_{1,1} \rightarrow 1_{1,0}$ transition at 85.926 GHz.

The choice of NH_2D was motivated by the fact three facts: ammonia is the major known ice-repository of nitrogen Boogert, Gerakines, and Whittet, 2015, the transitions of NH_2D can be observed with both ALMA and NOEMA and NH_2D has already been used to derive nitrogen isotopic ratios successfully (Gerin et al., 2009; Daniel et al., 2013). Also of help is the hyperfine structure of NH_2D which gives rise to spectrally resolved hyperfine components in its transitions, that can be used to gauge its opacity. In the following two sections we present preliminary results of this project.

Table 6.1 – Detected species and transitions with NOEMA towards IRAS 03282.

Species	Transition	detected
H^{13}CN	$J = 1 \rightarrow 0$	Yes
HC^{15}N	$J = 1 \rightarrow 0$	Yes
$o - \text{NH}_2\text{D}$	$1_{1,1} \rightarrow 1_{0,1}$	Yes
$o - ^{15}\text{NH}_2\text{D}$	$1_{1,1} \rightarrow 1_{0,1}$	No

6.1 NH_2D IN IRAS03282

The observations of IRAS03282 were conducted with the NOEMA interferometer under project W15AH. W15AH was a result of a proposal with V. S. Magalhães as the P.I. (Table C.1). The data reduction was executed at the IRAM headquarters at Grenoble using the interferometric data reduction software CLIC (*GILDAS software*). Self-calibration of this data set has proved difficult due to the low signal to noise ratio of the continuum (~ 60). Due to time constraints the data has been fully reduced up to the cleaned images, but has not yet been completely analysed. The integrated intensity clean images of $o - \text{NH}_2\text{D}$ and H^{13}CN are presented in Figures 6.1 and 6.2 along with their integrated spectra. The integrated spectrum of $o - ^{15}\text{NH}_2\text{D}$, a non detection, is shown in Figure 6.1 while the integrated spectrum of HC^{15}N is shown in Figure 6.2. Table 6.1 presents a summary on the detections towards IRAS03282.

6.2 THE NITROGEN ISOTOPIC RATIO IN VLA1623 AND IRAS16293

The observations of VLA1623 and IRAS16293 were conducted with the ALMA interferometer under project 2016.1.01468.S, P.I. V. S. Magalhães (Table C.1). This project with ALMA targeted the same transitions as the project with NOEMA but also included the $p - \text{NH}_2\text{D}$ $1_{1,1} \rightarrow 1_{1,0}$ transition to enable us to also measure the ortho to para ratio of NH_2D in these two protostars. The data reduction of this project was the subject of the M1 stage of Mark Brionne, under my supervision. The stage consisted in then calibration followed by the self-calibration of the data sets from ALMA. The stage was successful and M. Brionne was capable of delivering the self-calibrated data sets. Due to time constraints this data set has not been completely analysed yet.

In Figure 6.3 we display the integrated intensity map of $o - \text{NH}_2\text{D}$ $1_{1,1} \rightarrow 1_{1,0}$ towards VLA1623. Figure 6.4 displays the spatially integrated spectra of $o - \text{NH}_2\text{D}$ $1_{1,1} \rightarrow 1_{1,0}$, $p - \text{NH}_2\text{D}$ $1_{1,1} \rightarrow 1_{1,0}$

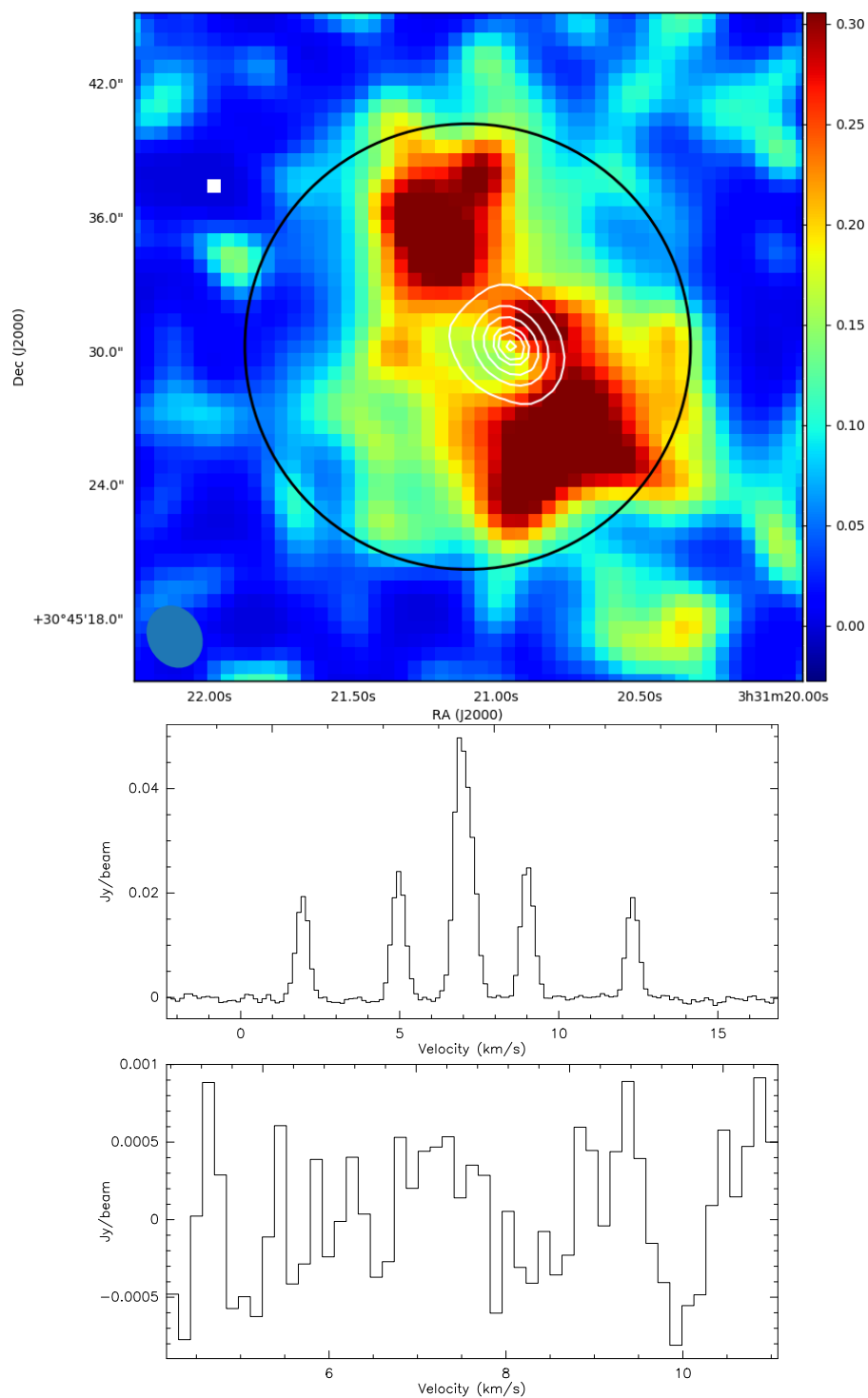


Figure 6.1 – Top panel: $o\text{-NH}_2\text{D } 1_{1,1} \rightarrow 1_{1,0}$ integrated intensity map towards IRAS03282 along with contours indicating the continuum emission of IRAS03282 at 86 GHz. Intensity of the integrated intensity map in Jy/beam. The continuum contours start at 2 mJy/Beam and go up to 18 mJy/beam in 4 mJy/beam intervals. Middle panel: $o\text{-NH}_2\text{D } 1_{1,1} \rightarrow 1_{1,0}$ spatially integrated spectrum inside the black circle in the top panel. Bottom panel: $o\text{-}^{15}\text{NH}_2\text{D } 1_{1,1} \rightarrow 1_{1,0}$ spatially integrated spectrum inside the black circle in the top panel.

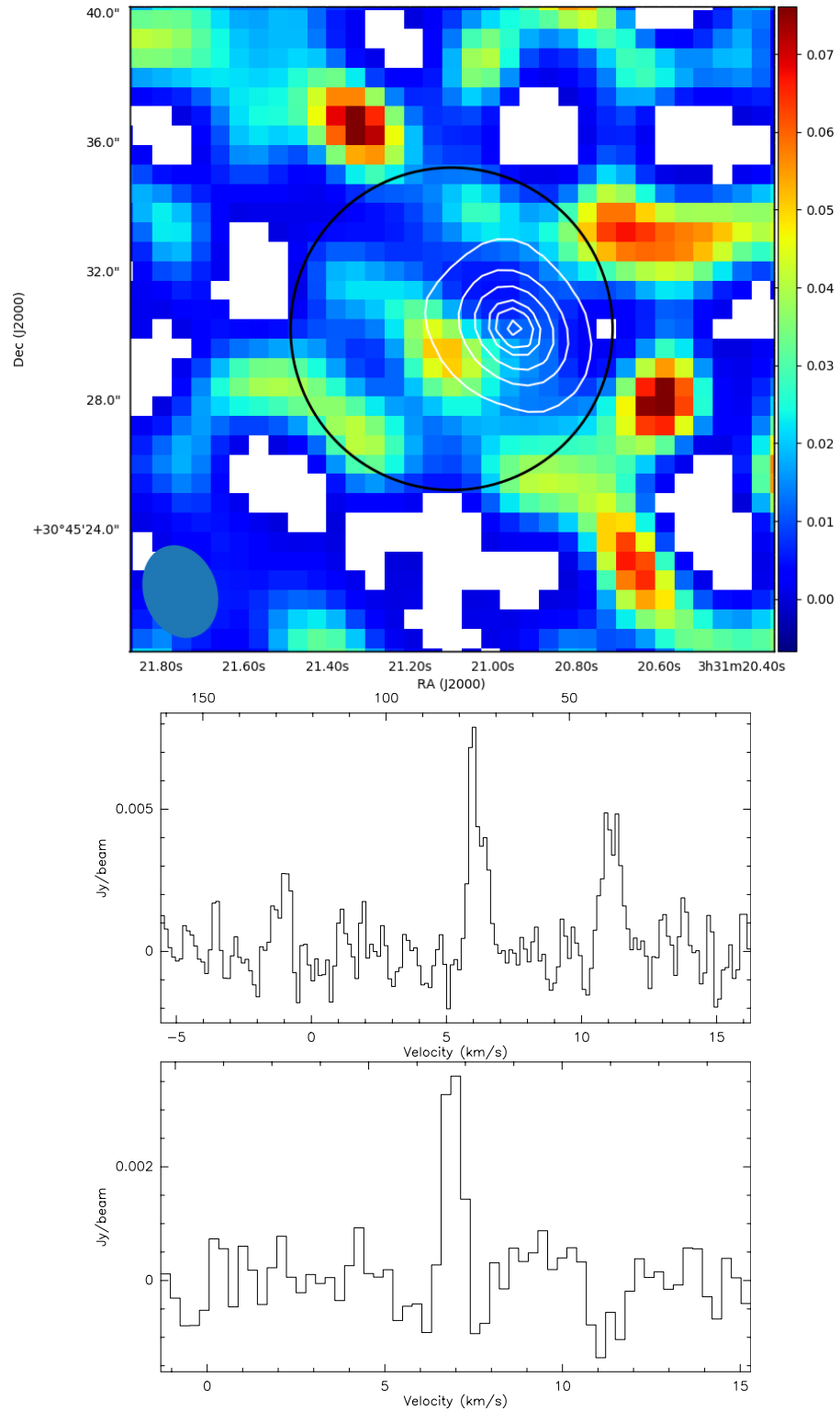


Figure 6.2 – Top panel: $\text{H}^{13}\text{CN } J = 1 \rightarrow 0$ integrated intensity map towards IRAS03282 along with contours indicating the continuum emission of IRAS03282 at 86 GHz. Intensity of the integrated intensity map in Jy/beam. The continuum contours start at 2 mJy/Beam and go up to 18 mJy/beam in 4 mJy/beam intervals. Middle panel: $\text{H}^{13}\text{CN } J = 1 \rightarrow 0$ spatially integrated spectrum inside the black circle in the top panel. Bottom panel: $\text{HC}^{15}\text{N } J = 1 \rightarrow 0$ spatially integrated spectrum inside the black circle in the top panel.

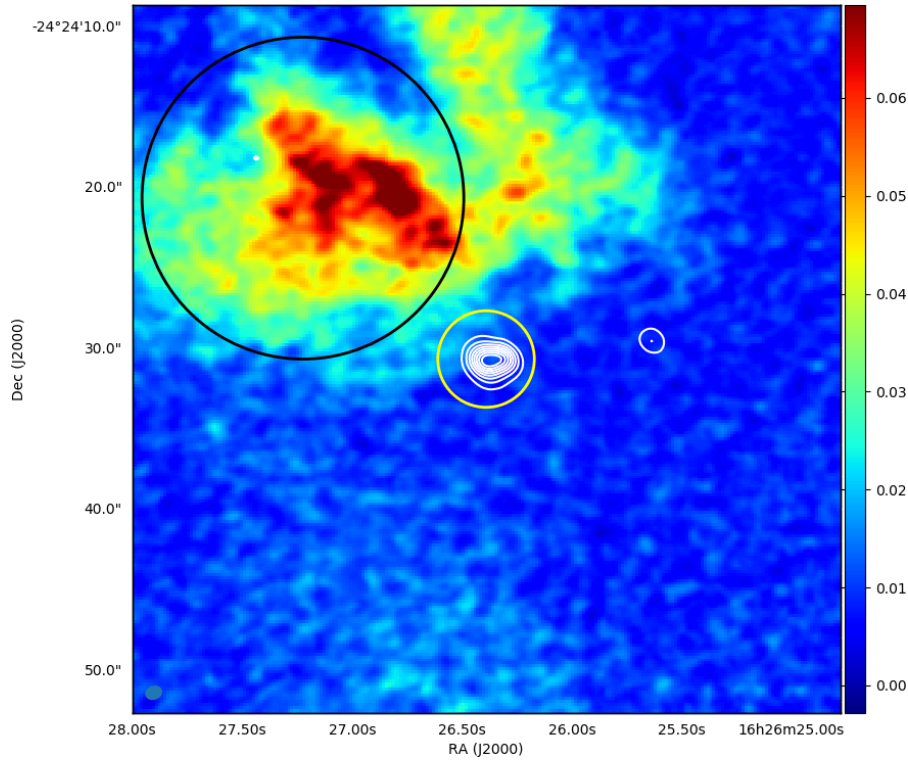


Figure 6.3 – o – $\text{NH}_2\text{D } 1_{1,1} \rightarrow 1_{1,0}$ integrated intensity map towards VLA 1623 along with contours indicating the continuum emission of VLA 1623 at 110 GHz. Intensity of the integrated intensity map in Jy/beam. The continuum contours start at 5 mJy/Beam and go up to 40 mJy/beam in 5 mJy/beam intervals. The black circle indicates the region of strong NH_2D emission in the envelope of VLA 1623, over which spectra of NH_2D and $^{15}\text{NH}_2\text{D}$ were integrated. The black circle indicates the region around VLA 1623 where ice sublimation is expected, over which spectra of NH_2D and $^{15}\text{NH}_2\text{D}$ were integrated.

and o – $^{15}\text{NH}_2\text{D } 1_{1,1} \rightarrow 1_{1,0}$ towards VLA1623 and the point of peak o – $\text{NH}_2\text{D } 1_{1,1} \rightarrow 1_{1,0}$ emission in the envelope. Table 6.2 summarises the detections made towards VLA1623.

In Figure 6.6 we display the integrated intensity map of o – $\text{NH}_2\text{D } 1_{1,1} \rightarrow 1_{1,0}$ towards IRAS16293 along with its spatially integrated spectra towards three positions, the A component, the B component and the envelope. Also shown in Figure 6.6 is the $^{15}\text{NH}_2\text{D}$ towards the envelope. Figure 6.7 displays the integrated intensity map of p – $\text{NH}_2\text{D } 1_{1,1} \rightarrow 1_{1,0}$ towards IRAS16293 along with its spatially integrated spectra towards three positions, the A component, the B component and the envelope. Figures 6.8 and 6.9 display the integrated intensity maps of the H^{13}CN and $\text{HC}^{15}\text{N } J = 1 \rightarrow 0$ transitions respectively. Figures 6.8 and 6.9 also display the spatially integrated spectra of these two species towards three different positions: the A component,

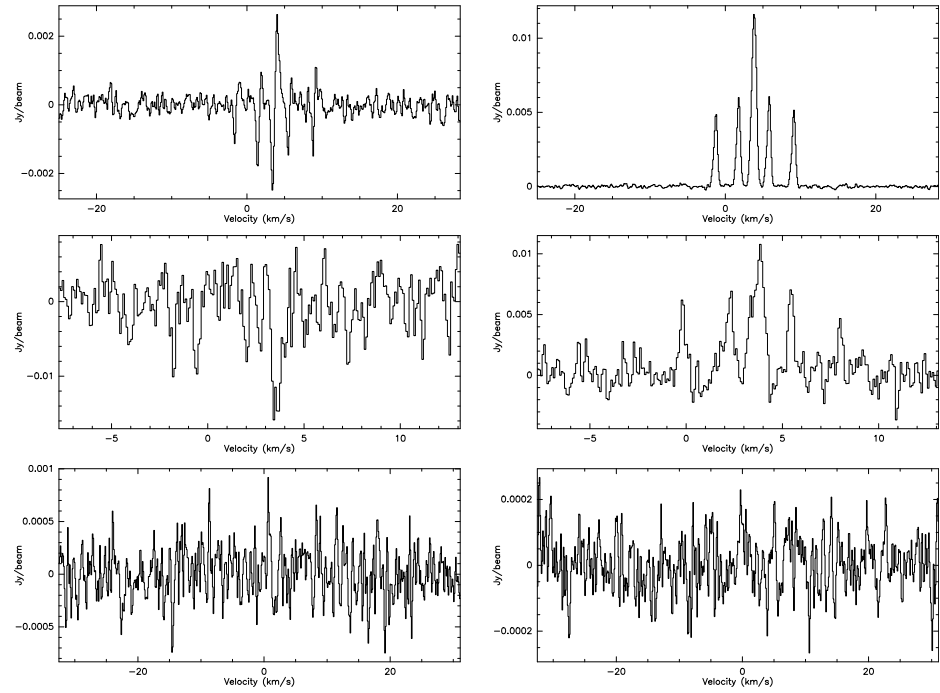


Figure 6.4 – Left panels: spatially integrated spectra towards the sublimation region of VLA 1623. Right: spatially integrated spectra towards NH_2D emission peak in the envelope of VLA 1623. Top: o – $\text{NH}_2\text{D } 1_{1,1} \rightarrow 1_{1,0}$. Middle: p – $\text{NH}_2\text{D } 1_{1,1} \rightarrow 1_{1,0}$. Bottom: o – $^{15}\text{NH}_2\text{D } 1_{1,1} \rightarrow 1_{1,0}$.

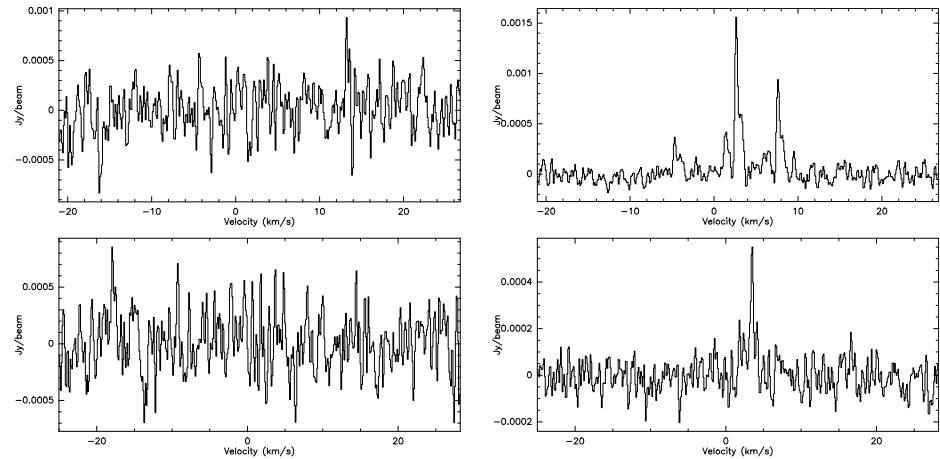


Figure 6.5 – Left panels: spatially integrated spectra towards the sublimation region of VLA 1623. Right: spatially integrated spectra towards NH_2D emission peak in the envelope of VLA 1623. Top: $\text{H}^{13}\text{CN } J = 1 \rightarrow 0$. Bottom: $\text{HC}^{15}\text{N } J = 1 \rightarrow 0$.

Table 6.2 – Detected species and transitions with ALMA towards VLA1623.

Species	Transition	detected
H^{13}CN	$J = 1 \rightarrow 0$	Yes (envelope)
HC^{15}N	$J = 1 \rightarrow 0$	Yes (envelope)
$o - \text{NH}_2\text{D}$	$1_{1,1} \rightarrow 1_{0,1}$	Yes
$o - ^{15}\text{NH}_2\text{D}$	$1_{1,1} \rightarrow 1_{0,1}$	No
$p - \text{NH}_2\text{D}$	$1_{1,1} \rightarrow 1_{0,1}$	Yes (envelope)

Table 6.3 – Detected species and transitions with ALMA towards IRAS16293.

Species	Transition	detected
H^{13}CN	$J = 1 \rightarrow 0$	Yes
HC^{15}N	$J = 1 \rightarrow 0$	Yes
$o - \text{NH}_2\text{D}$	$1_{1,1} \rightarrow 1_{0,1}$	Yes
$o - ^{15}\text{NH}_2\text{D}$	$1_{1,1} \rightarrow 1_{0,1}$	Yes (envelope)
$p - \text{NH}_2\text{D}$	$1_{1,1} \rightarrow 1_{0,1}$	Yes

the B component and the envelope. Table 6.3 summarises the detections made towards IRAS16293.

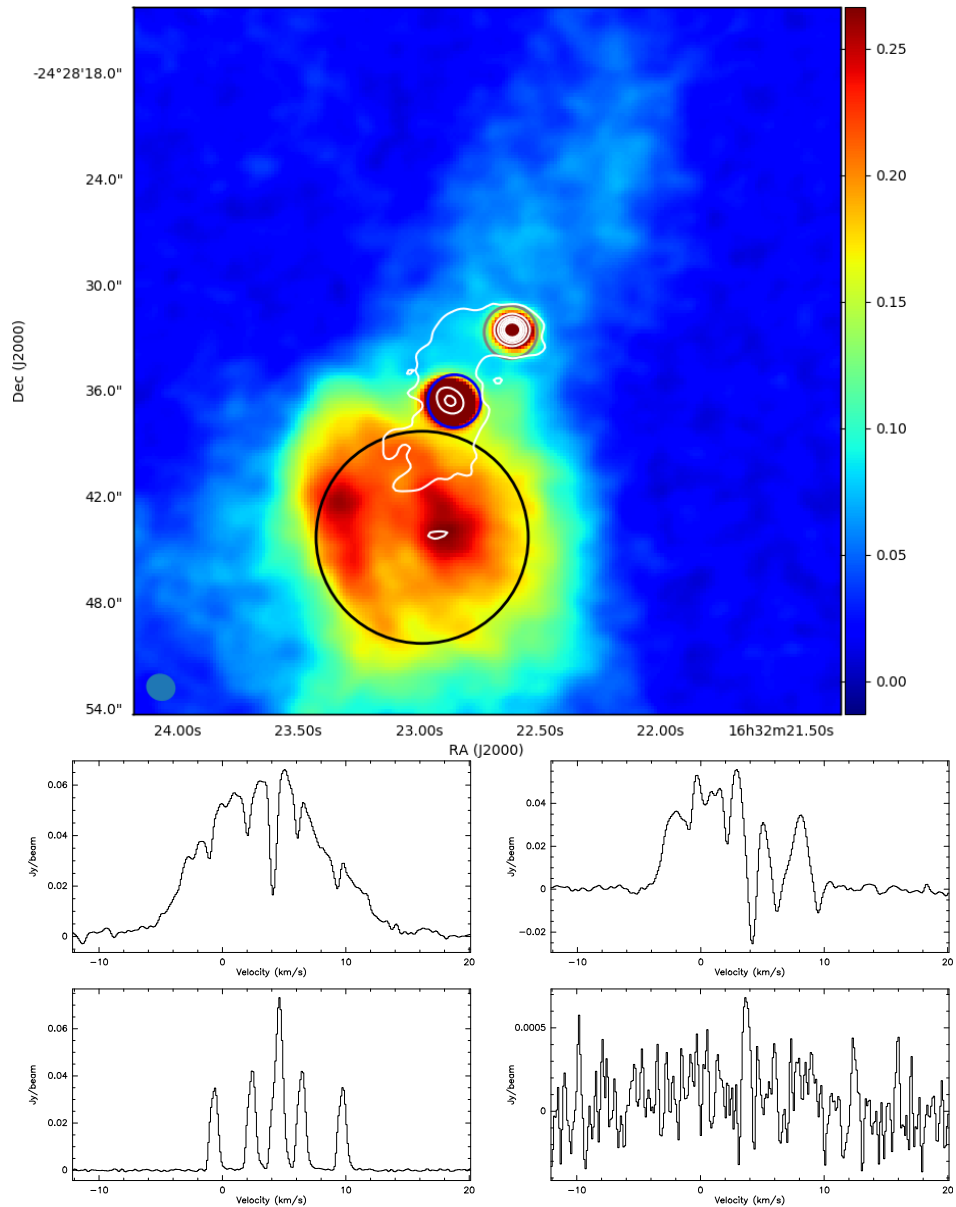


Figure 6.6 – Top panel Integrated intensity map of $o\text{-NH}_2\text{D } 1_{1,1} \rightarrow 1_{1,0}$ towards IRAS16293. Middle left panel: spatially integrated spectrum of $o\text{-NH}_2\text{D } 1_{1,1} \rightarrow 1_{1,0}$ towards the A component of IRAS16293 (blue circle in the top panel). Middle right panel: spatially integrated spectrum of $o\text{-NH}_2\text{D } 1_{1,1} \rightarrow 1_{1,0}$ towards the B component of IRAS16293 (yellow circle in the top panel). Bottom left panel: spatially integrated spectrum of $o\text{-NH}_2\text{D } 1_{1,1} \rightarrow 1_{1,0}$ towards the NH₂D peak in the envelope of IRAS16293 (black circle in the top panel). Bottom right panel: spatially integrated spectrum of $o\text{-}^{15}\text{NH}_2\text{D } 1_{1,1} \rightarrow 1_{1,0}$ towards the NH₂D peak in the envelope of IRAS16293.

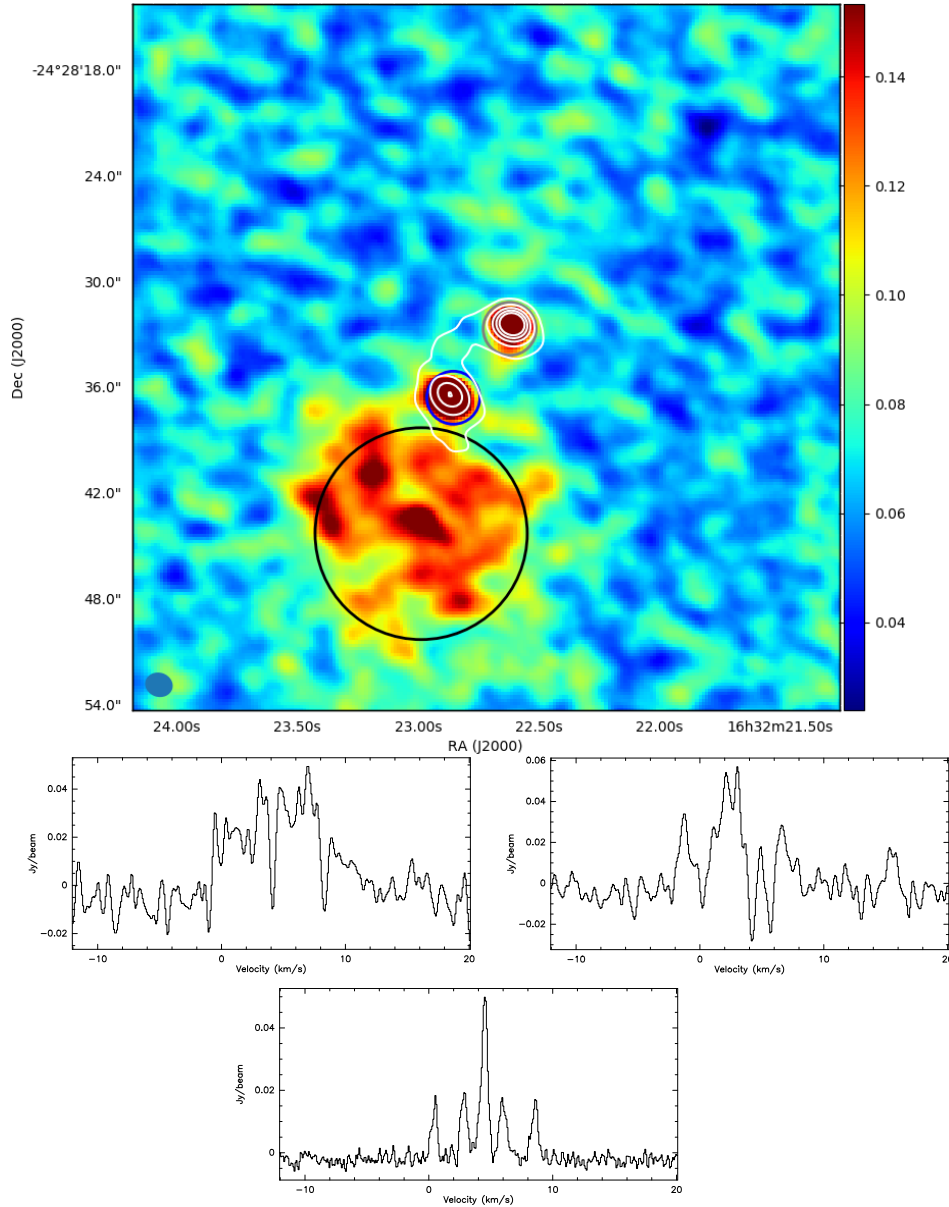


Figure 6.7 – Top panel Integrated intensity map of $p - \text{NH}_2\text{D } 1_{1,1} \rightarrow 1_{1,0}$ towards IRAS16293. Middle left panel: spatially integrated spectrum of $p - \text{NH}_2\text{D } 1_{1,1} \rightarrow 1_{1,0}$ towards the A component of IRAS16293 (blue circle in the top panel). Middle right panel: spatially integrated spectrum of $p - \text{NH}_2\text{D } 1_{1,1} \rightarrow 1_{1,0}$ towards the B component of IRAS16293 (yellow circle in the top panel). Bottom panel: spatially integrated spectrum of $p - \text{NH}_2\text{D } 1_{1,1} \rightarrow 1_{1,0}$ towards the NH_2D peak in the envelope of IRAS16293 (black circle in the top panel).

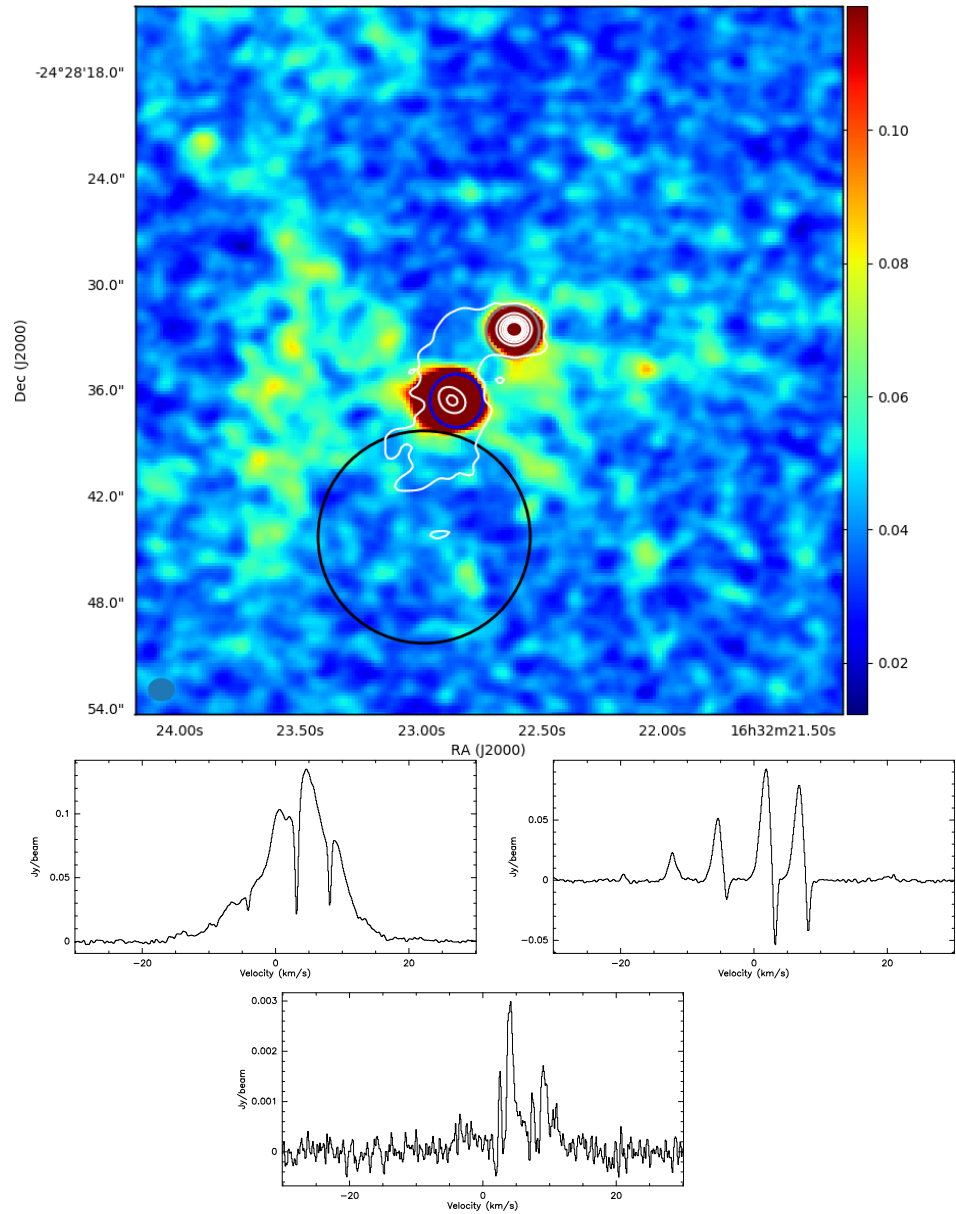


Figure 6.8 – Top panel Integrated intensity map of $\text{H}^{13}\text{CN } J = 1 \rightarrow 0$ towards IRAS16293. Middle left panel: spatially integrated spectrum of $\text{H}^{13}\text{CN } J = 1 \rightarrow 0$ towards the A component of IRAS16293 (blue circle in the top panel). Middle right panel: spatially integrated spectrum of $\text{H}^{13}\text{CN } J = 1 \rightarrow 0$ towards the B component of IRAS16293 (yellow circle in the top panel). Bottom panel: spatially integrated spectrum of $\text{H}^{13}\text{CN } J = 1 \rightarrow 0$ towards the NH_2D peak in the envelope of IRAS16293 (black circle in the top panel).

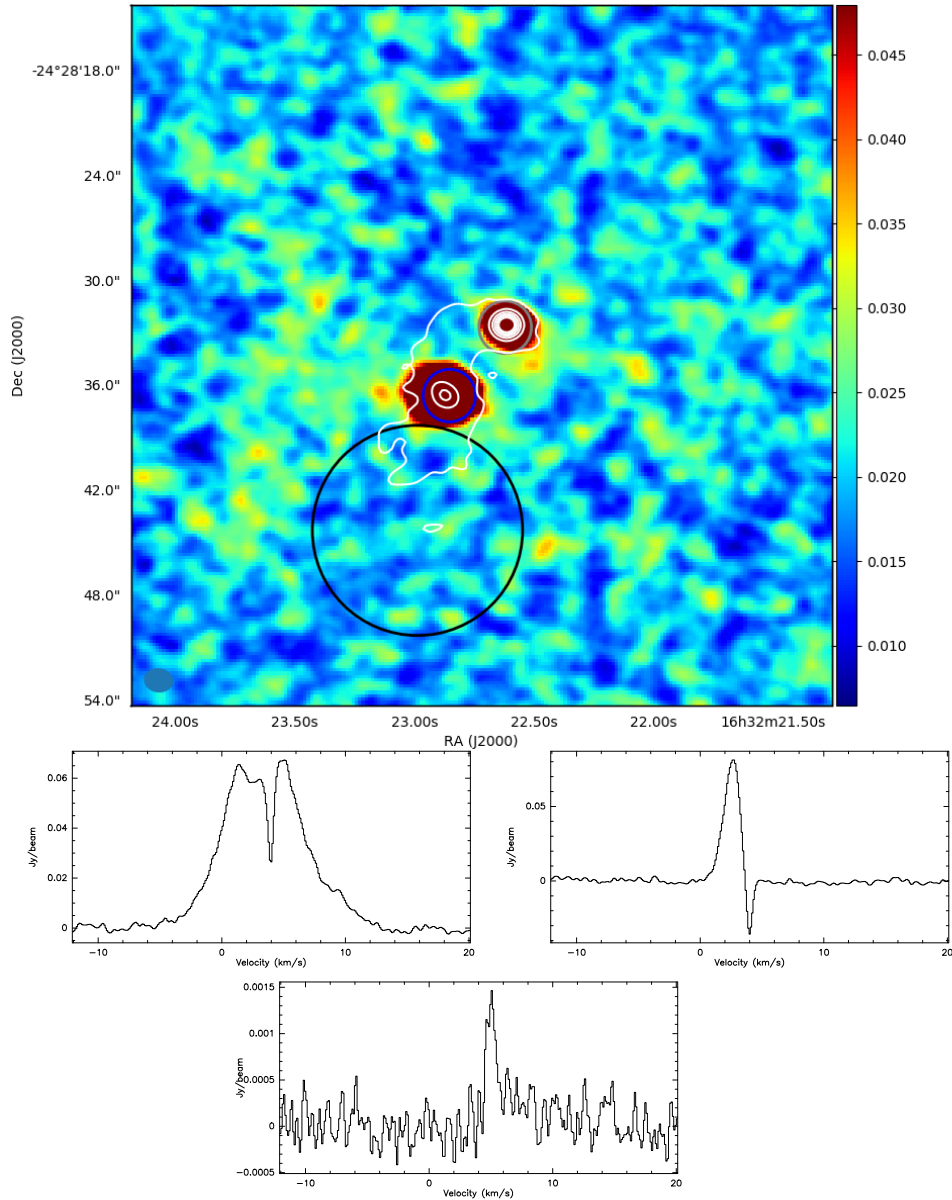


Figure 6.9 – Top panel Integrated intensity map of $\text{HC}^{15}\text{N } J = 1 \rightarrow 0$ towards IRAS16293. Middle left panel: spatially integrated spectrum of $\text{HC}^{15}\text{N } J = 1 \rightarrow 0$ towards the A component of IRAS16293 (blue circle in the top panel). Middle right panel: spatially integrated spectrum of $\text{HC}^{15}\text{N } J = 1 \rightarrow 0$ towards the B component of IRAS16293 (yellow circle in the top panel). Bottom panel: spatially integrated spectrum of $\text{HC}^{15}\text{N } J = 1 \rightarrow 0$ towards the NH_2D peak in the envelope of IRAS16293 (black circle in the top panel).

DISCUSSION AND PERSPECTIVES

The main objective of this thesis was to identify the different isotopic reservoirs of nitrogen at different stages of star formation. To accomplish this objective we aimed to obtain accurate measurements of the nitrogen isotopic ratio in a variety of environments and species. This aim was fulfilled as we have successfully identified different isotopic reservoirs of nitrogen at two different stages of star formation, prestellar cores where we have measured $\text{HCN}/\text{HC}^{15}\text{N} = 338 \pm 23$ (L1498) and $\text{HC}_3\text{N}/\text{HC}_3^{15}\text{N} = 400 \pm 20$ (L1544), and protoplanetary disks where two reservoirs have been identified, $\text{HCN}/\text{HC}^{15}\text{N} = 111 \pm 19$ and $\text{CN}/\text{C}^{15}\text{N} = 323 \pm 30$. We also obtained data that will lead to a study of the isotopic ratios of nitrogen in the protostellar stage of star formation.

To obtain the results in L1498 we had to reach a good understanding of the mechanisms governing the hyperfine anomalies of HCN, revisit the physical structure of prestellar cores and develop a way to efficiently explore the parameter space and thus obtain meaningful and non arbitrary uncertainties in our measurements. Here we demonstrate that the main mechanism needed to create the hyperfine anomalies of HCN is that described in Guilloteau and Baudry (1981). We studied this mechanism in detail in order to understand the effects of each physical quantity on the hyperfine anomalies. We studied in detail the effects of kinematics and excitation temperature on the hyperfine anomalies going one step further from Gonzalez-Alfonso and Cernicharo (1993) who used constant collapse velocities and two values for the non thermal dispersion of velocities. This is also a step further from (Daniel et al., 2013) who did not explore the effects of kinematics on the spectra of HCN. Using multi-wavelength continuum analysis we have obtained an improved density profile for L1498 that also takes into account the variation of the dust temperature. This is a step further from what was done by Tafalla et al. (2004) who had only one continuum wavelength (1.25 mm) to work with and therefore had to assume a constant dust temperature. This simplistic assumption led to an implausible physical model where the density at large radii varied with $r^{-3.5}$.

From our study we reach the conclusions that to accurately measure the $\text{HCN}/\text{HC}^{15}\text{N}$ ratio in prestellar cores we need to combine spatial information on the spectral lines, multiple rotational transitions, collisional excitation rates at the hyperfine level, a precise density profile, a detailed study of the non thermal velocity and collapse velocity profiles and finally a non biased way to explore the parame-

ter space and therefore obtain meaningful non arbitrary uncertainties. Spatial information on the spectral lines are essential as variations on the line profiles along a cut provide clues on the parameter space. The HCN $J = 3 \rightarrow 2$ transition is the best choice a good signal to noise ratio can be achieved with the IRAM-30m in a short time. 50 mK RMS can be reach in less than 2 hours under average winter conditions at the IRAM-30m with a channel spacing of 20 kHz. The late Malcolm Walmsley pointed us in the correct direction in this matter and we would like to profoundly thank him for his help. The non thermal velocity and collapse velocity profiles change the escape probability of the photons and therefore have a big impact on hyperfine anomalies.

7.1 HCN HYPERFINE ANOMALIES

In Section 4.1 we have presented a comprehensive analysis of the HCN hyperfine anomalies. In this analysis we present a complete explanation of the pumping mechanism that leads to the hyperfine anomalies thanks to new and precise HCN hyperfine collisional rates (Lique et al. in preparation). As part of this analysis we have also explored the parameter space that controls the hyperfine anomalies in great detail. The main conclusions of this analysis are:

- The radiative pumping through hyperfine overlap mechanism to explain the hyperfine anomalies of Guilloteau and Baudry (1981) is confirmed.
- A gradient of excitation temperature is needed to accurately reproduce the hyperfine ratios seen in prestellar, confirming the conclusions of Gonzalez-Alfonso and Cernicharo (1993).
- The HCN $J = 1 \rightarrow 0$ hyperfine anomalies are very sensitive to the velocity field and line widths, therefore the hyperfine anomalies become a new tool to study the kinematics of cores.
- High J rotational transitions, such as HCN $J = 3 \rightarrow 2$ are essential to constrain the excitation of HCN, and also helps to constrain the velocity as it probes the velocity field deep inside the core.
- The hyperfine anomalies are very sensitive to the HCN column density, thus becoming a reliable tool to measure the HCN column density provided that the kinematics parameter space is properly explored.

The addition of the HCN $J = 2 \rightarrow 1$ to the analysis would help to constraint the radiative pumping leading to the hyperfine anomalies. This was not done since atmospheric absorption due to water does not allow the HCN $J = 2 \rightarrow 1$ transition to be observed with a good signal to noise ratio in a reasonable amount of time. Reaching a 50 mK RMS noise would take 6.4 hours per position under average winter conditions at the IRAM-30m with a channel spacing of 20 kHz.

This study also led to a better understand of the kinematics of L1498. The absence of collapse signatures in the line profiles of the HCN $J = 3 \rightarrow 2$ transition rules out the presence of collapse in the inner parts of L1498. This transition is moderately optically thick and presents a sharp gradient of excitation temperature. If the collapse were to be taking place in the regions probed by this transition, red-blue asymmetries would be seen in the $F = 3 \rightarrow 3$ hyperfine component, but this is not the case. The collapse signatures seen in HCN $J = 1 \rightarrow 0$ are more prominent in the more optically thick hyperfine components, suggesting that the collapse takes places in the very outermost parts of the core. This is consistent with the collapse profile used by Lee et al. (2007) to reproduce HCN $J = 1 \rightarrow 0$. It is also consistent with theoretical works on core dynamics (Foster and Chevalier, 1993; Lesaffre et al., 2005; Keto and Caselli, 2010). All this points to the conclusion that L1498 is in a less advanced state of evolution compared to L1544, since it has a lower central density, $n_0 = 10^5 \text{ cm}^{-3}$ while it is $\sim 10^7 \text{ cm}^{-3}$ in L1544 (Keto and Caselli, 2010). Moreover, the collapse only happens in the outer part of the core (Lesaffre et al., 2005).

The main mechanisms behind the hyperfine anomalies leads us to anticipate that HCN hyperfine anomalies may not be very prominent in the spectra of protoplanetary disks. The large velocity shear seen in protoplanetary disks would increase the escape probability of photons thus damping the radiative pumping through hyperfine overlaps leading to hyperfine populations closer to the expected LTE values. Nevertheless the HCN transitions are still expected to have large optical depths which would hamper the accurate determination of its column density. This means that resolving the hyperfine components of the HCN rotational transitions is essential to accurately determine its column density in disks. This is probably impossible for disks seen with large inclinations as the Keplerian motion of the disk would merge the narrowly separated hyperfine components of HCN rotational transitions, but it may still be feasible in inclined disks in the HCN $J = 1 \rightarrow 0$ transition. The best prospect for measuring accurate HCN column densities in protoplanetary disk rely on face on disks such as the disk around TW Hya. To do this we need a radiative transfer code capable of dealing with all the complexities of hyperfine structures in 2 dimensions. This will be the starting point for ALICO 2D.

7.2 ACCURATE MEASUREMENTS OF ISOTOPIC RATIOS

There are only small differences between the HCN/H¹³CN measured in L1498 with three different methods: LTE, escape probability with RADEX+N_{SLAB}+MCMC and complete radiative transfer with ALICO/MCMC. The main difference being on the uncertainties. This in-

icates that LTE derived $\text{H}^{13}\text{CN}/\text{HC}^{15}\text{N}$ ratios can be trusted up to a certain degree. In the case of L1498 the $\text{H}^{13}\text{CN}/\text{HC}^{15}\text{N}$ ratio obtained through LTE analysis is consistent with the values obtained with the non LTE methods. The disagreement between the LTE derived ratio and the non-LTE derived ratios is close to 10% (8 and 7.5 ± 0.8 respectively). In any case it is difficult to ascribe uncertainties to LTE measurements and also they are not reliable to measure absolute column densities. The total rotational opacity measured for $\text{H}^{13}\text{CN } J = 1 \rightarrow 0$ in LTE is 3.72 which is 33% lower than the opacities derived with the non LTE methods (5.9 in both cases). The good agreement between the opacities derived from RADEX+N_{SLAB}+MCMC and those derived with ALICO/MCMC suggest that RADEX+N_{SLAB}+MCMC is a reliable method to determine the column density of rare isotopologues.

For the case of the main isotopologue the picture is less promising for escape probability methods. The inability to treat hyperfine overlaps at the excitation level precludes them from being capable of accurately reproducing the HCN line profiles. The agreement is especially poor when we consider the higher J transitions such as $J = 3 \rightarrow 2$ which are indeed very poorly reproduced by RADEX+N_{SLAB}+MCMC.

To completely reproduce the HCN line profiles and consequently derive accurate measurements of the HCN column density we need to resort to more complicated radiative transfer analysis, involving physical structures, such as what is done with ALICO. The problem here is that there are degeneracies between the physical parameters. Kinetic temperature, density and abundance all affect the emission in non-linear ways, as they are coupled with each other through the excitation and radiative transfer. In such a case χ^2 statistics fails to properly measure the uncertainties of the parameters, as it is not intended to deal with non linear correlations between parameters. Here the Affine Invariant Markov Chain Monte Carlo Ensemble sampler provides a more efficient way to sample the parameter space (Goodman and Weare, 2010), and thus obtain meaningful non arbitrary uncertainties.

The two main sources of uncertainty that affect measurements of isotopic ratios are: the calibration uncertainties, of the order of 5 to 10% and the uncertainties on the collisional excitation rates, which is of the order of 20% (Stoecklin et al., 2017). The impact of the uncertainties on the collisional excitation rates is still not understood and need to be studied further. The calibration uncertainties may be mitigated if isotopologues are observed simultaneously. This is not always possible, and depends on the available receiver setups and observational performances of these setups. At the IRAM-30m telescope HCN $J = 1 \rightarrow 0$ can not be observed simultaneously with $\text{H}^{13}\text{CN } J = 1 \rightarrow 0$ or $\text{HC}^{15}\text{N } J = 1 \rightarrow 0$. The frequency spacing between the transitions of the main isotopologue and that of the rare isotopologues is larger than 2 GHz. The only spectrometer at the IRAM-30m

telescope capable of covering such a wide interval of frequencies is the Fourier Transform Spectrometer (FTS) in the 200 kHz spectral resolution mode. The problem is that this spectral resolution is not enough to spectrally resolve HCN $J = 1 \rightarrow 0$ in cold environments which have line widths smaller than that (the FWHM of HC¹⁵N in L1498 is ~ 60 kHz). One possible solution is to cross-calibrate spectra obtained in different runs with the aid of strong spectral lines that can be observed simultaneously with different setups.

But for now the goals are to obtain calibration-limited accuracy. This is achieved here by using an MCMC approach to sample the parameter space. Araki et al. (2016) claim to have gone beyond calibration-limited accuracy by observing all carbon isotopologues of HC₃N simultaneously. However, the caveat of their method is that the column density of the HC₃N isotopologues was determined from LTE considerations using only one rotational transition. They most likely underestimated the uncertainties of the method by ignoring the possible excitation temperature differences between the HC₃N carbon isotopologues and the main isotopologue.

7.3 HCN ISOTOPIC RATIOS IN L1498

HCN/HC¹⁵N is measured to be 338 ± 28 in L1498. This value is consistent with the bulk nitrogen isotopic ratio in the local ISM, 323 ± 30 (Hily-Blant et al., 2017). Hence HCN is not fractionated in nitrogen, which agrees with Roueff, Loison, and Hickson (2015). HCNH¹³CN is measured to be 45 ± 3 which is not consistent with the bulk local ISM value, $^{12}\text{C}/^{13}\text{C} = 68 \pm 15$ (Milam et al., 2005). If we apply the HCN/H¹³CN ratio of the present study, to previous HCN/HC¹⁵N double isotopic measurements we get: HCN/HC¹⁵N in protoplanetary disks becomes 71 ± 13 ($\text{H}^{13}\text{CN}/\text{HC}^{15}\text{N} = 1.6 \pm 0.3$, Guzmán et al., 2017), HCN/HC¹⁵N in L1544 becomes 157 ± 37 ($\text{H}^{13}\text{CN}/\text{HC}^{15}\text{N} = 3.5 \pm 0.8$, Hily-Blant et al., 2013a) and HCN/HC¹⁵N in L183 becomes 131 ± 29 ($\text{H}^{13}\text{CN}/\text{HC}^{15}\text{N} = 2.9 \pm 0.6$, Hily-Blant et al., 2013a). These values are consistent with the directly measured HCN/HC¹⁵N ratio in B1 (165^{+30}_{-25}) but that were discarded by Daniel et al. (2013). The authors consider that the column density of HCN could not be reliably estimated in B1. In this study we have reliably estimated the column density of HCN and therefore are confident of our direct isotopic ratios. The new values for HCN/HC¹⁵N are consistent with a secondary reservoir of nitrogen in the gas phase in L1544 and L183. Moreover, this secondary reservoir would be consistent with the expected cometary value, which is approximately one third of the bulk value (Hily-Blant et al., 2017). Nevertheless, confirmation of these low isotopic ratios require further studies, as a confirmation of the existence of a secondary reservoir of nitrogen in the gas phase would have profound significance for the formation of comets. We

intend to proceed our studies by using ALICO to measure the HCN isotopic ratios in L183 and L1544.

However HCN is fractionated in carbon with $\text{HCN}/\text{H}^{13}\text{CN} = 45 \pm 3$. Such a low ratio was also found by Daniel et al. (2013) $\text{HCN}/\text{H}^{13}\text{CN} = 30^{+7}_{-4}$. In both case HCN is enriched in ^{13}C when compared to the bulk of carbon $^{12}\text{C}/^{13}\text{C} = 68 \pm 15$ (measured in CO, H_2CO and CN, with similar results by Milam et al., 2005). This is not consistent with Roueff, Loison, and Hickson (2015) who predict $\text{HCN}/\text{H}^{13}\text{CN} = 93\text{-}168$, a impoverishment in ^{13}C .

The ratio between the two rare isotopologues, $\text{H}^{13}\text{CN}/\text{HC}^{15}\text{N} = 7.5 \pm 0.8$, is also in disagreement with Roueff, Loison, and Hickson (2015) being twice the predicted value (2.6-4.3). This ratio is also $\sim 40\%$ larger than the value measured by Daniel et al. (2013) ($\text{HCN}/\text{H}^{13}\text{CN} = 5.5 \pm 1$). This could be easily checked for a large sample of sources including cores and protostellar envelopes at different stages of evolution This will be done in the near future using RADEX+NSLAB+MCMC.

7.4 WHERE WHEN AND HOW ARE THE TWO RESERVOIRS OF NITROGEN SEEN IN PROTOPLANETARY DISKS SEPARATED?

The answer for this question is still not known but there are four main possibilities:

- In the gas phase of prestellar cores through fractionation reactions during the collapse.
- In the circumstellar material around protostars during the hot core/corino phase.
- During the planet formation epoch in protoplanetary disks.
- Through isotopic exchange reactions during the star formation process.

The answer to this question may lie in the isotopic ratio of nitrogen in ices. Therefore is of fundamental importance to conduct the analysis of our ALMA and NOEMA data on the isotopic ratio of nitrogen in the circumstellar environments of IRAS03282, IRAS16293 and VLA1623. The James Webb Space Telescope slated to be launched in 2019 may also contribute to these measurements. Although it is uncertain if it will be capable of measuring the abundance of rare isotopologues in ices. The picture will also be clearer when we have a direct measurement of the nitrogen isotopic ratio in protoplanetary disks. Which may be feasible with ALMA towards the face on disk of TW Hya. The answer may also be found in the spatial variation of isotopic ratios in prestellar cores. To do such a measurement we need to assume a radial profile of abundance that varies independently with radius for each isotopologue. One possible parametrisation would be to assume a power law like abundance profile such as that in Lee et al. (2007).

Part I

APPENDIX



SOFTWARE WRITTEN AND EXAMPLE INPUT FILES

A.1 NSLAB

A.1.1 *Source code for Nslab*

```
#!/opt/local/bin/python
import argparse
import numpy as np
import num_lte as nl
import pyfi as fh
#from matplotlib import pyplot as plt

def gauss(x,tau_atcenter,fwhm,lcenter):
    a = tau_atcenter
    sigma = fwhm/2.355
    gaussian = a*np.exp(-1.*(x-lcenter)**2/(2.*sigma**2))
    return gaussian

def emergingTb(tex,tau,nu):
    return nl.jnu(texl,nu)*(1-np.exp(-1*tau))

parser = argparse.ArgumentParser(description="N Slabs
emergent spectrum")
parser.add_argument("input", type=str, help="File containing
the parameters for the N slabs. Format:\n"
    +"#nu in GHz, ex:\n88.631\n"
    +"#for line 1 2 etc\n#Tex1 Tau1 Vel1 FWHM1 Tex2
    Tau2 Vel2 FWHM2 etc\n"
    +"#Layer1\n3.4 1.0 0.0 0.3 5.0 1.5 1.2 0.3\n"
    +"#Layer2\n4.0 1.0 0.0 0.3 2.5 1.5 1.2 0.3\n"
    )

parser.add_argument("output", type=str, help="File for
outputting the spectrum")
parser.add_argument("-b", "--bgspec", type=str, help="
Background spectrum")
parser.add_argument("-v", "--velres", type=float, default
=0.01, help="Change spectral resolution (km/s) Default = 0.01
km/s")
```

```

parser.add_argument("-l", "--vlims", type=str, default=None,
                    help="Velocity limits for spectrum, Default = -6*fw hm,6*
                    fwhm")
parser.add_argument("-c", "--tbg", type=float, default
                    =2.7325, help="Temperature of the background radiation (K)
                    Default = 2.7325 K")
parser.add_argument("-s", "--show", action="store_true",
                    default=False, help="Show the spectrum at the end")
parser.add_argument("-n", "--nopl ot", action="store_true",
                    default=False, help="Does not mak plots of the spectra.")
parser.add_argument("-i", "--nspec", type=int, default=1, help
                    ="number of spectra in BG spectrum file.")

args = parser.parse_args()
if not args.nopl ot:
    from matplotlib import pyplot as plt

with open(args.input) as filein:
    striped = fh.strip_off_comm(filein)
    fllines = fh.float_file(striped)
    striped = None
nu = fllines[0][0]
nlines = 0

if len(fllines[1])%4 == 0:
    nlines = int(len(fllines[1])/4)
else:
    print "Incorrect number of parameters for the desired number
    of spectral "
    "lines.\nExpected 4 per spectral line."
    exit()
vel,sig,tau,tex=[],[],[],[]
for i in range(nlines):
    tex.append([item[0+4*i] for item in fllines[1:]])
    tau.append([item[1+4*i] for item in fllines[1:]])
    vel.append([item[2+4*i] for item in fllines[1:]])
    sig.append([item[3+4*i] for item in fllines[1:]])
minvel = np.min(vel)
maxvel = np.max(vel)
maxsig = np.max(sig)

if args.bgspec != None: ## Using background spectrum
    rx = np.loadtxt(args.bgspec, unpack=True, usecols=[0,])
    velims = [rx[0], rx[-1]]
    nvel = len(rx)

```

```

vaxis = rx
rx = None
# exit()
else: ## starting from CMB
    if args.vlims is None:
        velims = [minvel - 6 * maxsig, maxvel + 6 * maxsig]
    else:
        velims = [float(lim) for lim in args.vlims.split()]
    nvel = int((velims[1] - velims[0]) / args.velres) + 1
    vaxis = np.linspace(velims[0], velims[1], num=nvel,
                        endpoint=True)
    yaxis = np.empty(len(vaxis))
    yaxis.fill(nl.jnu(args.tbg, nu))

nspec = args.nspec
outyaxis=[]
for l in range(1,nspec+1):
    if args.bgspec != None: ## Using background spectrum
        ry = np.loadtxt(args.bgspec,unpack=True,usecols=[l])
        yaxis = ry
        ry = None

    else: ## starting from CMB
        yaxis = np.copy(vaxis)
        yaxis.fill(nl.jnu(args.tbg,nu))

    for layer in flines[1:]:
        tausum = np.zeros(nvel)
        lineemi = np.zeros(nvel)
        for j in range(nlines):
            linepar = layer[4*j:4+4*j]
            texl,taul,vell,sigl = linepar
            taunu = gauss(vaxis,taul,sigl,vell)
            tausum += taunu
            jethline = nl.jnu(texl,nu)*(1-np.exp(-1*taunu))
            lineemi += jethline
        yaxis = lineemi+yaxis*np.exp(-tausum)
    outyaxis.append(yaxis)

outstr = ""
for i in range(len(vaxis)):
    outstr+= "{0:.4e}".format(vaxis[i])
    for j in range(nspec):
        outstr += "\t{0:.4e}".format(outyaxis[j][i])
    outstr += "\n"

```

```

strout = "#V(nu={0:.5f} GHz) (km/s) Intensity (K)\n".format(nu)
strout += outstr
filout = open(args.output,'w')
filout.write(strout)
filout.close()

if not args.noplot:
    plt.step(vaxis,yaxis,where='mid')
    plt.xlabel("Velocity (km/s)")
    plt.ylabel("Intensity (K)")
    idot = args.output.rfind(".")
    plt.savefig(args.output[:idot]+'png')

    layers = range(1,len(fllines[1:])+1)
    fig2 = plt.figure(figsize=(10, 8))
    plt.subplot(221)
    plt.xlabel("Layer")
    plt.ylabel("Opacity")
    plt.xlim([layers[0]-0.2, layers[-1]+0.2])
    plt.ylim([np.min(tau)-0.1*np.max(tau), np.max(tau)+0.1*
              np.max(tau)])
    for i in range(len(tau)):
        plt.step(layers,tau[i],where='mid',label='Line {0:d}'.
                format(i+1))
    plt.legend()

    plt.subplot(222)
    plt.xlabel("Layer")
    plt.ylabel("Excitation Temperature (K)")
    plt.xlim([layers[0]-0.2, layers[-1]+0.2])
    plt.ylim([np.min(tex)-0.1*np.max(tex), np.max(tex)+0.1*
              np.max(tex)])
    for i in range(len(tex)):
        plt.step(layers,tex[i],where='mid',label='Line {0:d}'.
                format(i+1))
    plt.legend()

    plt.subplot(223)
    plt.xlabel("Layer")
    plt.ylabel("Velocity (km/s)")
    plt.xlim([layers[0]-0.2, layers[-1]+0.2])
    plt.ylim([np.min(vel)-0.1*np.abs(np.max(vel)), np.max(
              vel)+0.1*np.abs(np.max(vel))])
    for i in range(len(vel)):

```

```

plt.step(layers, vel[i], where='mid', label='Line {0:d}'.
         format(i+1))
plt.legend()

plt.subplot(224)
plt.xlabel("Layer")
plt.ylabel("FWHM")
plt.xlim([layers[0]-0.2, layers[-1]+0.2])
plt.ylim([np.min(sig)-0.1*np.max(sig), np.max(sig)+0.1*
         np.max(sig)])
for i in range(len(sig)):
    plt.step(layers, sig[i], where='mid', label='Line {0:d}'.
            format(i+1))
plt.legend()

fig2.set_tight_layout(True)
plt.savefig(args.output[:idot]+'_struct.png')
if args.show:
    plt.show()

```

A.1.2 Nslab input

```

### Frequency on which to compute the spectrum (in GHz)
88.6310
### Parameters corresponded to three lines in each slab:
### Tex1 Tau1 V0_1 DV1 Tex2 Tau2 V0_2 DV2 Tex3 Tau3 V0_3
DV3
### Slab 1
3.58 2.13 -7.1759 0.23 3.02 3.25 -0.11 0.23 3.02 2.69
4.7303 0.23
### Slab 2
5.32 0.71 -7.1959 0.19 5.03 2.34 -0.13 0.19 4.9 0.98
4.7103 0.19
### Slab 3
5.32 0.71 -6.9359 0.19 5.03 2.34 0.13 0.19 4.9 0.98
4.9703 0.19
### Slab 4
3.58 2.13 -6.9559 0.23 3.02 3.25 0.11 0.23 3.02 2.69
4.9503 0.23

```

A.1.3 Nslab output

```

#V(nu=88.63100 GHz) (km/s) Brightness temperature (K)

```

```
-8.5759e+00 1.1364e+00
-8.4757e+00 1.1364e+00
-8.3755e+00 1.1364e+00
-8.2754e+00 1.1364e+00
-8.1752e+00 1.1364e+00
-8.0750e+00 1.1364e+00
-7.9748e+00 1.1364e+00
-7.8747e+00 1.1364e+00
-7.7745e+00 1.1364e+00
-7.6743e+00 1.1364e+00
-7.5741e+00 1.1368e+00
-7.4740e+00 1.1553e+00
-7.3738e+00 1.4417e+00
-7.2736e+00 2.3113e+00
-7.1734e+00 2.5010e+00
-7.0733e+00 1.9981e+00
-6.9731e+00 1.9233e+00
-6.8729e+00 1.9173e+00
-6.7727e+00 1.5025e+00
-6.6726e+00 1.1669e+00
-6.5724e+00 1.1372e+00
-6.4722e+00 1.1364e+00
-6.3720e+00 1.1364e+00
-6.2719e+00 1.1364e+00
-6.1717e+00 1.1364e+00
-6.0715e+00 1.1364e+00
-5.9713e+00 1.1364e+00
-5.8712e+00 1.1364e+00
-5.7710e+00 1.1364e+00
-5.6708e+00 1.1364e+00
-5.5706e+00 1.1364e+00
-5.4704e+00 1.1364e+00
-5.3703e+00 1.1364e+00
-5.2701e+00 1.1364e+00
-5.1699e+00 1.1364e+00
-5.0697e+00 1.1364e+00
-4.9696e+00 1.1364e+00
-4.8694e+00 1.1364e+00
-4.7692e+00 1.1364e+00
-4.6690e+00 1.1364e+00
-4.5689e+00 1.1364e+00
-4.4687e+00 1.1364e+00
-4.3685e+00 1.1364e+00
-4.2683e+00 1.1364e+00
-4.1682e+00 1.1364e+00
-4.0680e+00 1.1364e+00
```

-3.9678e+00	1.1364e+00
-3.8676e+00	1.1364e+00
-3.7675e+00	1.1364e+00
-3.6673e+00	1.1364e+00
-3.5671e+00	1.1364e+00
-3.4669e+00	1.1364e+00
-3.3668e+00	1.1364e+00
-3.2666e+00	1.1364e+00
-3.1664e+00	1.1364e+00
-3.0662e+00	1.1364e+00
-2.9661e+00	1.1364e+00
-2.8659e+00	1.1364e+00
-2.7657e+00	1.1364e+00
-2.6655e+00	1.1364e+00
-2.5653e+00	1.1364e+00
-2.4652e+00	1.1364e+00
-2.3650e+00	1.1364e+00
-2.2648e+00	1.1364e+00
-2.1646e+00	1.1364e+00
-2.0645e+00	1.1364e+00
-1.9643e+00	1.1364e+00
-1.8641e+00	1.1364e+00
-1.7639e+00	1.1364e+00
-1.6638e+00	1.1364e+00
-1.5636e+00	1.1364e+00
-1.4634e+00	1.1364e+00
-1.3632e+00	1.1364e+00
-1.2631e+00	1.1364e+00
-1.1629e+00	1.1364e+00
-1.0627e+00	1.1364e+00
-9.6254e-01	1.1364e+00
-8.6236e-01	1.1364e+00
-7.6218e-01	1.1364e+00
-6.6201e-01	1.1364e+00
-5.6183e-01	1.1364e+00
-4.6166e-01	1.1386e+00
-3.6148e-01	1.2394e+00
-2.6131e-01	2.1709e+00
-1.6113e-01	2.8834e+00
-6.0954e-02	2.1239e+00
3.9222e-02	1.4915e+00
1.3940e-01	1.4495e+00
2.3957e-01	1.6390e+00
3.3975e-01	1.3097e+00
4.3993e-01	1.1420e+00
5.4010e-01	1.1365e+00

```
6.4028e-01 1.1364e+00
7.4045e-01 1.1364e+00
8.4063e-01 1.1364e+00
9.4080e-01 1.1364e+00
1.0410e+00 1.1364e+00
1.1412e+00 1.1364e+00
1.2413e+00 1.1364e+00
1.3415e+00 1.1364e+00
1.4417e+00 1.1364e+00
1.5419e+00 1.1364e+00
1.6420e+00 1.1364e+00
1.7422e+00 1.1364e+00
1.8424e+00 1.1364e+00
1.9426e+00 1.1364e+00
2.0427e+00 1.1364e+00
2.1429e+00 1.1364e+00
2.2431e+00 1.1364e+00
2.3433e+00 1.1364e+00
2.4434e+00 1.1364e+00
2.5436e+00 1.1364e+00
2.6438e+00 1.1364e+00
2.7440e+00 1.1364e+00
2.8441e+00 1.1364e+00
2.9443e+00 1.1364e+00
3.0445e+00 1.1364e+00
3.1447e+00 1.1364e+00
3.2448e+00 1.1364e+00
3.3450e+00 1.1364e+00
3.4452e+00 1.1364e+00
3.5454e+00 1.1364e+00
3.6456e+00 1.1364e+00
3.7457e+00 1.1364e+00
3.8459e+00 1.1364e+00
3.9461e+00 1.1364e+00
4.0463e+00 1.1364e+00
4.1464e+00 1.1364e+00
4.2466e+00 1.1364e+00
4.3468e+00 1.1368e+00
4.4470e+00 1.1550e+00
4.5471e+00 1.4460e+00
4.6473e+00 2.2154e+00
4.7475e+00 2.1122e+00
4.8477e+00 1.5192e+00
4.9478e+00 1.4428e+00
5.0480e+00 1.5048e+00
5.1482e+00 1.3201e+00
```

```

5.2484e+00 1.1474e+00
5.3485e+00 1.1366e+00
5.4487e+00 1.1364e+00
5.5489e+00 1.1364e+00
5.6491e+00 1.1364e+00
5.7492e+00 1.1364e+00
5.8494e+00 1.1364e+00
5.9496e+00 1.1364e+00
6.0498e+00 1.1364e+00
6.1499e+00 1.1364e+00
6.2501e+00 1.1364e+00
6.3503e+00 1.1364e+00

```

A.1.4 *Nslab help*

```

$ns slab.py -h
usage: ns slab.py [-h] [-b BGSPEC] [-v VELRES] [-l VLIMS] [-c
    TBG] [-s] [-n] [-i NSPEC] input output

N Slabs emergent spectrum

positional arguments:
  input File containing the parameters for the N slabs.
          Format: #nu in GHz, ex: 88.631 #for line 1
                2 etc #Tex1
                Tau1 Vel1 FWHM1 Tex2 Tau2 Vel2 FWHM2 etc #
                Layer1 3.4
                1.0 0.0 0.3 5.0 1.5 1.2 0.3 #Layer2 4.0
                1.0 0.0 0.3
                2.5 1.5 1.2 0.3
  output File for outputting the spectrum

optional arguments:
  -h, --help show this help message and exit
  -b BGSPEC, --bgspec BGSPEC
                Background spectrum
  -v VELRES, --velres VELRES
                Change spectral resolution (km/s) Default
                = 0.01 km/s
  -l VLIMS, --vlims VLIMS
                Velocity limits for spectrum, Default =
                -6*fwhm,6*fwhm
  -c TBG, --tbg TBG Temperature of the background radiation
    (K) Default =
                2.7325 K

```

```
-s, --show Show the spectrum at the end
-n, --noplot Does not mak plots of the spectra.
-i NSPEC, --nspec NSPEC
                number of spectra in BG spectrum file.
```

A.2 ALICO/1DART

A.2.1 1DART input files

A.2.1.1 Physical model input file

```
!-----
!-----!
!!
! Parameter file for the MTCsRE code a.k.a mali !
! The Commented lines must be kept !
! The blank Lines must be kept !
! The physical model an other parameters are described by
! the variables in this file !
!!
!-----
!-----!
! Output files for final and intermediate results !
!-----
!-----!

'r7_185_hcn.pop'
'r7_185_hcn.dat'

!-----
!-----!
! Helium and atomic hydrogen abundance !
!-----
!-----!

0.0000E+00 ! XHe Helium abundance
0.0000E+00 ! XHI Atomic hydrogen abundance

!-----
!-----!
! Molecule selection parameters !
!-----
!-----!

1 ! Number of vibrational Levels
```

```

8 0 0 0 0 ! Number of rotational levels per vibrational
      level
0 1.D-12 1.0 !
'HCN_hyp', 5 ! Molecule, Collisional rates selection
1.0 ! Abundance factor, proxy for isotopic ratios

!-----
      -----!
! Source distance and angular size !
!-----
      -----!

140.0 ! Distance [pc]
16.000000000000000 ! Angular diameter of the source in arc
      minutes

!-----
      -----!
! Numerical parameters for the code !
!-----
      -----!

1 ! LI: 0, ALI-J: 1, ALI-GSu: 2, ALI-GSud: 3
0 ! Interpolation type : Linear 0, Parabolic 1 ! obsolete
1, 200 ! ?NG? Acceleration No: 0; Yes 1, First application
1 ! Take hyperfine overlap into account
50 ! Number of layers in the model
1 1 50 ! Additional layers | Number | every N layer | Total
      number
0 0 0 ! Include Dust (0 No, 1 yes)
1.D-1, 500 ! Stop criteria, Maximal relative variation and
      number of iterations
2 ! Number of LVG iterations to inicialize populations !
      Obsolete
1 0 ! Output info to screen ! Obsolete

!-----
      -----!
! Iterations in which the counter are voided (Obsolete) !
!-----
      -----!

1
1000000,

```

```

!-----
!-----!
! Parameters for the numerical Monte Carlo solution !
!-----
!-----!

20 ! Number of radiative directions
30 ! Number of velocity bins in a line

!-----
!-----!
! Radius of the central source and its temperatures !
!-----
!-----!

0.000000 ! Central source radius in unitary radius
3 ! 1 = 1 temp. per line; 2 = Single temp.; 3 = Grey body (
    Central temp., Opacity, Freq?, ?)
1.0,100.,150.,1.

!-----
!-----!
! Cosmic microwave background temperature !
!-----
!-----!

2
2.728

!-----
!-----!
! Velocity field V(R)=VLSR+gradient*R**exponent !
!-----
!-----!

2
-0.000000 -0.000002 -0.000007 -0.000024 -0.000078 -0.000234
  -0.000647 -0.001651 -0.003898 -0.008507 -0.017164
  -0.032017 -0.055219 -0.088046 -0.129796 -0.176903
  -0.222912 -0.259690 -0.279706 -0.278530 -0.256428
  -0.218265 -0.171762 -0.124966 -0.084059 -0.052275
  -0.030056 -0.015977 -0.007852 -0.003568 -0.001499
  -0.000582 -0.000209 -0.000069 -0.000021 -0.000006
  -0.000002 -0.000000 -0.000000 -0.000000 -0.000000
  -0.000000 -0.000000 -0.000000 -0.000000 -0.000000
  -0.000000 -0.000000 -0.000000 -0.000000 -0.000000

```

```

!-----
!-----!
! Physical Model: Unit. Rad. | Density | Kin. Temp. | Turb.
  Vel. | Abun. | dust Temp. !
!-----
!-----!

0.0196078431373 8.80128066E+04 10.000 0.05048 5.146E-09
  10.0 0. 0. 0. 10.0
0.0392156862745 8.71477094E+04 10.000 0.05071 5.146E-09
  10.0 0. 0. 0. 10.0
0.0588235294118 8.32577915E+04 10.000 0.05095 5.537E-09
  10.0 0. 0. 0. 10.0
0.0784313725490 7.38031662E+04 10.000 0.05121 5.537E-09
  10.0 0. 0. 0. 10.0
0.0980392156863 5.89975223E+04 10.000 0.05148 5.537E-09
  10.0 0. 0. 0. 10.0
0.1176470588235 4.28244840E+04 10.000 0.05176 5.537E-09
  10.0 0. 0. 0. 10.0
0.1372549019608 2.92833260E+04 10.000 0.05207 5.537E-09
  10.0 0. 0. 0. 10.0
0.1568627450980 1.96317962E+04 10.000 0.05240 5.537E-09
  10.0 0. 0. 0. 10.0
0.1764705882353 1.32616182E+04 10.000 0.05274 5.537E-09
  10.0 0. 0. 0. 10.0
0.1960784313725 9.15908778E+03 10.000 0.05312 5.537E-09
  10.0 0. 0. 0. 10.0
0.2156862745098 6.50900179E+03 10.000 0.05352 5.537E-09
  10.0 0. 0. 0. 10.0
0.2352941176471 4.76989864E+03 10.000 0.05395 5.537E-09
  10.0 0. 0. 0. 10.0
0.2549019607843 3.60461407E+03 10.000 0.05441 5.537E-09
  10.0 0. 0. 0. 10.0
0.2745098039216 2.80641087E+03 10.000 0.05491 5.537E-09
  10.0 0. 0. 0. 10.0
0.2941176470588 2.24776458E+03 10.000 0.05546 5.537E-09
  10.0 0. 0. 0. 10.0
0.3137254901961 1.84879239E+03 10.000 0.05605 5.537E-09
  10.0 0. 0. 0. 10.0
0.3333333333333 1.55848506E+03 10.000 0.05669 5.537E-09
  10.0 0. 0. 0. 10.0
0.3529411764706 1.34360350E+03 10.000 0.05740 5.537E-09
  10.0 0. 0. 0. 10.0
0.3725490196078 1.18204988E+03 10.000 0.05818 5.537E-09
  10.0 0. 0. 0. 10.0

```

```
0.3921568627451 1.05884887E+03 10.000 0.05905 5.537E-09
 10.0 0. 0. 0. 10.0
0.4117647058824 9.63667258E+02 10.000 0.06001 5.537E-09
 10.0 0. 0. 0. 10.0
0.4313725490196 8.89253968E+02 10.000 0.06109 5.537E-09
 10.0 0. 0. 0. 10.0
0.4509803921569 8.30440592E+02 10.000 0.06230 5.537E-09
 10.0 0. 0. 0. 10.0
0.4705882352941 7.83489451E+02 10.000 0.06367 5.537E-09
 10.0 0. 0. 0. 10.0
0.4901960784314 7.45661015E+02 10.000 0.06523 5.537E-09
 10.0 0. 0. 0. 10.0
0.5098039215686 7.14922196E+02 10.000 0.06703 5.537E-09
 10.0 0. 0. 0. 10.0
0.5294117647059 6.89746646E+02 10.000 0.06913 5.537E-09
 10.0 0. 0. 0. 10.0
0.5490196078431 6.68976085E+02 10.000 0.07159 5.537E-09
 10.0 0. 0. 0. 10.0
0.5686274509804 6.51722708E+02 10.000 0.07452 5.537E-09
 10.0 0. 0. 0. 10.0
0.5882352941176 6.37299646E+02 10.000 0.07805 5.537E-09
 10.0 0. 0. 0. 10.0
0.6078431372549 6.25170844E+02 10.000 0.08236 5.537E-09
 10.0 0. 0. 0. 10.0
0.6274509803922 6.14914510E+02 10.000 0.08771 5.537E-09
 10.0 0. 0. 0. 10.0
0.6470588235294 6.06196218E+02 10.000 0.09444 5.537E-09
 10.0 0. 0. 0. 10.0
0.6666666666667 5.98748896E+02 10.000 0.10300 5.537E-09
 10.0 0. 0. 0. 10.0
0.6862745098039 5.92357812E+02 10.000 0.11394 5.537E-09
 10.0 0. 0. 0. 10.0
0.7058823529412 5.86849216E+02 10.000 0.12770 5.537E-09
 10.0 0. 0. 0. 10.0
0.7254901960784 5.82081666E+02 10.000 0.14425 5.537E-09
 10.0 0. 0. 0. 10.0
0.7450980392157 5.77939366E+02 10.000 0.16255 5.537E-09
 10.0 0. 0. 0. 10.0
0.7647058823529 5.74327004E+02 10.000 0.18064 5.537E-09
 10.0 0. 0. 0. 10.0
0.7843137254902 5.71165726E+02 10.000 0.19669 5.537E-09
 10.0 0. 0. 0. 10.0
0.8039215686275 5.68389978E+02 10.000 0.20989 5.537E-09
 10.0 0. 0. 0. 10.0
0.8235294117647 5.65945010E+02 10.000 0.22032 5.537E-09
 10.0 0. 0. 0. 10.0
```

```

0.8431372549020 5.63784894E+02 10.000 0.22849 5.537E-09
 10.0 0. 0. 0. 10.0
0.8627450980392 5.61870944E+02 10.000 0.23492 5.537E-09
 10.0 0. 0. 0. 10.0
0.8823529411765 5.60170442E+02 10.000 0.24004 5.537E-09
 10.0 0. 0. 0. 10.0
0.9019607843137 5.58655611E+02 10.000 0.24419 5.537E-09
 10.0 0. 0. 0. 10.0
0.9215686274510 5.57302785E+02 10.000 0.24759 5.537E-09
 10.0 0. 0. 0. 10.0
0.9411764705882 5.56091729E+02 10.000 0.25042 5.537E-09
 10.0 0. 0. 0. 10.0
0.9607843137255 5.55005084E+02 10.000 0.25280 5.537E-09
 10.0 0. 0. 0. 10.0
0.9803921568627 5.54027910E+02 10.000 0.25484 5.537E-09
 10.0 0. 0. 0. 10.0
1.0000000000000 5.53147314E+02 10.000 0.25659 5.537E-09
 10.0 0. 0. 0. 10.0

!-----
!-----!
! Population initialization method (1:LTE, 2:LVG, 4:File) !
!-----
!-----!

2

```

A.2.1.2 *Beam convolution input file*

```

1 !Iteration to use
318 !Number of velocity channels
3 !Integration steps in RMAX units
-3.5,3.48097 !Velocity limits
1 !Number of rotational transitions
10 15 12 ! Transition indexes initial | Final | zero
reference
6 !Number of pointings in the cloud
0.0
11.18
22.36
44.72
67.08
89.44
5 !Number of impact parameters per layer
3 9 1.0 350 !main beam HPBW & Main beam efficiency & error
beam HPBW

```

A.2.2 *Model cloud input file*

```
###Name for the associated files
teste_largura
###Provided physical structure? 0|1 if 1 supply
0
###Run MALI? 0|1
1
###Generate perfil hyp input 0|1
1
###Run perfil-hyp
1
###Number of velocity points
1000
###Lower and Upper velocity limits
-10,10
###Number of lines computed
3
###Line numbers according to NAME.dat 1 per line
1 3 2
4 9 6
10 15 12
###Observational parameters 1 per line
### Id Beam_FWHM_sec MB_eff first_side_lobe_dist_sec
1 28 0.81 350
2 14 0.68 350
3 9 0.52 350
### Pointings in sec from center (space separated)
0
### Number of layers, number of additional layers in
    between layers , [layer sampling: Lin(def), zen, log]
30,1,zen
### Angular Diameter in arc min
3
### Distance in pc
200
### Number of included rotational levels
8
### Molecule, collisional coefficient selector
HCN_HYP,1
### Abundance factor (can be used as isotopic ratio)
1
### temperatures (space separated)
10
### radius for previous temperatures (space separated)
0
```

```

### Molecular abundance relative to H2
1e-9
### Initial density for power law
0
### Plateau position in fraction of the radius
1
### Turbulent velocity
0.0
### Exponent of the power law *-1
1000
### Exterior density
10000.0
### velocity law
0 0 0 0 1.0 0 0

```

A.2.2.1 *Model cloud help*

```

$model_cloud.py -h
usage: model_cloud.py [-h] [-q] [-b] [-n] [-c] [-o] parfile

Python Wrapper for 1DART.

positional arguments:
  parfile Name of the parameter file to be used for the
          model.

optional arguments:
  -h, --help show this help message and exit
  -q, --quiet Quiet mode, no output from 1DART.
  -b, --bench Produce benchmarking plots.
  -n, --no_overlap Ignore Hyperfine structure overlap
          effects.
  -c, --save_space saves disk space by throwing away
          superfluous files and compressing the output.
  -o, --override Override abundances in provided physical
          structure, does nothing if there is no provided
          physical structure

```

A.2.3 *ALICO gridding software*

A.2.3.1 *Source file*

```

# alpha
3.8
# n0

```

```

0.65E+05
# next
1e3
#plateau
0.305555555555556
### x???
1.0
#distance
140
# size
12
Layers
100,1,lin
## Tk = 10 K from Tafalla et al 2004, NH3 measurements.
10
0.0

```

A.2.3.2 *Molecular file*

```

# molecule
H13CN_hyp,5
# n rot levels
4
#vel bins
727
#vel lims
-10,10
# hf lines
1 3 2
# telescope
1 28 1.0 350
# pointing
0.0 22.36 44.72 67.08 89.44

```

A.2.3.3 *Grid file*

```

## non thermal dispe
j 0.005 0.265 0.500 0.150; j 0.005 0.265 0.5 0.2; j 0.005
  0.265 0.60 0.20; j 0.005 0.265 0.55 0.20
## velocities
a,-0.05; a,-0.06; a,-0.07; a,-0.08
## abundances
1.0000e-11; 1.3335e-11; 1.7783e-11; 2.3714e-11; 3.1623e-11;
  4.2170e-11; 5.6234e-11; 7.4989e-11; 1.0000e-10; 1.3335e
-10; 1.7783e-10; 2.3714e-10; 3.1623e-10; 4.2170e-10;
  5.6234e-10; 7.4989e-10; 1.0000e-09

```

```

## abundance ratios
1
## XXX?
1
###
### initial turbulent broadening from  $K_b \cdot 8 / (28 \cdot \text{amu})$ 

```

A.2.3.4 Gridding software help

```

$ali_gridder_simple.py -h
usage: ali_gridder_simple.py [-h] [-b] [-s] [-n NTHREADS] [-t] [-c]
                               [-p PROVIDED] [-o]
                               root source mol grid

Simple gridder for ALICO.

positional arguments:
  root Root name for the grid run.
  source File containing the information to construct the source model.
  mol File containing the molecule used and the related spectroscopy.
  grid File containing the grid parameters.

optional arguments:
  -h, --help show this help message and exit
  -b, --benchmarking
  -s, --serial Run grid in serial mode instead of parallel mode. Resource saving in case of multiple grids.
  -n NTHREADS, --nthreads NTHREADS
                        Defines number of threads to be used by the grid, if negative, not given, or larger than Ncpu, it is assumed as Ncpu-1, in this machine: 7.
  -t, --testRun Test run, nothing is done.
  -c, --save_space saves disk space by throwing away superfluous files and compressing the output.
  -p PROVIDED, --provided PROVIDED Uses provided physical structure
  -o, --override Overrides abundances in provided physical structure file, only relevant if provided != None

```

A.2.4 ALICO classes

A.2.4.1 Model class

```

import subprocess
import numpy as np
import subprocess as sp
import os
from matplotlib import pyplot as plt

class Model:

    listuseless = ["TB","CFL","FLU"]

    def __init__(self,name,velopars,turbpars,denspars,
                 abunpars,temperature,molecule,layerinfo,distance,size
                 ):
        if len(velopars) != 3:
            print "Velocity parameters should be 3 and in this order:"
            "
            print "1 – Peak collapse velocity (km/s)"
            print "2 – Position of the collapse peak (Urad)"
            print "3 – Width of the collapse profile (Urad)"
            raise Exception("Incorrect number of arguments in call"
                             )
        if len(turbpars) != 4:
            print "Turbulence parameters should be 4 and in this
                  order:"
            print "1 – Turbulence in the interior (km/s)"
            print "2 – Turbulence in the exterior (km/s)"
            print "3 – Position of the turbulence jump (Urad)"
            print "4 – Width of the turbulence jump (Urad)"
            raise Exception("Incorrect number of arguments in call"
                             )
        if len(denspars) != 4:
            print "Density parameters should be 4 and in this order:"
            print "1 – Central density (cm-3)"
            print "2 – External density (cm-3)"
            print "3 – Plateau size (Urad)"
            print "4 – Slope of density profile"
            raise Exception("Incorrect number of arguments in call"
                             )
        if len(abunpars) != 2:
            print "Abundance parameters should be 2 and in this
                  order:"
            print "1 – HCN abundance string x0,r0 x1,r1 x2,r2 etc"
            print "2 – Abundance factor"

```

```

        raise Exception("Incorrect number of arguments in call"
            )
    if not isinstance(molecule,Molecule):
        print "Molecule not correctly defined"
        raise Exception("Incorrect instantiation")

    self.velopars = velopars
    self.turbpars = turbpars
    self.denspars = denspars
    self.abunpars = abunpars
    self.molecule = molecule
    self.layerinfo = layerinfo
    self.distance = distance
    self.temperature = temperature
    self.size = size
    self.name = name
    self.inpname = []

    if not os.path.isdir(self.name):
        os.mkdir(self.name)
    self.ran = False
    self.inpwrit = False
    self.loaded = False
    self.chi2 = 0.0

def write_mcloudinp(self,dry=False):
    if dry:
        return
    for iline in range(self.molecule.nlines):

        line = self.molecule.line[iline]
        mol = self.molecule
        outstr = self.name
        if iline == 0:
            outstr += "\no\ni\ni\ni\n" # Run mali and
                perfil_hyp.
        else:
            outstr += "\no\no\ni\ni\n" # Run mali and
                perfil_hyp.
        ### line information
        outstr += "{0:s}\n{1:s}\n".format(line.nvels, line.
            velims)
        outstr += "{0:s}\n{1:s}\n".format(line.hypsel, line.
            telpars)
        outstr += "{0:s}\n".format(line.pos)
        ### distance + size

```

```

        outstr += "{0:s}\n{1:s}\n{2:s}\n".format(self.
            layerinfo, self.size, self.distance)
    ### Molecule info
    outstr += "{0:s}\n{1:s},{2:s}\n".format(mol.nrot, mol.
        name, mol.colssel)
    outstr += "{0:2f}\n".format(self.abunpars[1])
    outstr += "{0:s}\no\n".format(self.temperature)
    ## abundance changed to abundance string VSM
    12/09/2017
    ## Allowing for depletion holes
    outstr += "{0:s}\n".format(self.abunpars[0])
    outstr += "{0:3e}\n".format(self.denspars[0])
    outstr += "{0:5f}\n".format(self.denspars[2])
    outstr += "j {0:4f} {1:4f} {2:4f} {3:4f}\n".format(*self.
        turbpars)
    outstr += "{0:3e}\n".format(self.denspars[3])
    outstr += "{0:3e}\n".format(self.denspars[1])
    outstr += "l {0:4f} {1:4f} {2:4f}\n".format(*self.
        velopars)

    if iline == 0:
        fileout = open(self.name + "/" + self.name + ".
            par", 'w')
        self.inpname.append(self.name + ".par")
    else:
        fileout = open(self.name + "/" + self.name + "
            _lin{o:d}.par".format(iline+1), 'w')
        self.inpname.append(self.name + "_lin{o:d}.par".
            format(iline+1))
    fileout.write(outstr)
    fileout.close()

    self.inpwrit = True
    return

def run(self,dry=False):
    if dry:
        self.ran=True
        return
    if not self.inpwrit:
        print "Input file not written"
        raise Exception("A computer only follow orders, if you
            give none, I can't procede")
    flags = "-q"
    with open(os.devnull, 'w') as devnull:
        predir = os.getcwd()

```

```

os.chdir(self.name)
if os.access(self.name+".INP", os.F_OK):
    os.system("rm "+self.name+".INP")
for name in self.inpname:
    sp.call(["model_cloud.py " + name + flags],
           shell=True, stdout=devnull,stderr=devnull)
os.chdir(predir)
self.ran = True

def clean_up(self):
    if self.ran:
        predir = os.getcwd()
        os.chdir(self.name)
        for useless in self.listuseless:
            os.system("rm -f *."+useless)
        os.system("rm -f fort*")
        os.chdir(predir)
        self.clean = True
    else:
        print "Cannot clean up, model not run!"
        raise Exception("Cannot clean what is not dirty!")

def load(self):
    if self.ran:
        predir = os.getcwd()
        os.chdir(self.name)
        alltrans = []
        for i in range(self.molecule.nlines):
            transid = self.molecule.line[i].transid
            noffs = self.molecule.line[i].noffs
            data = np.loadtxt(self.name+'_o'+transid+'.CTB',
                             unpack =True)
            for j in range(noffs):
                data[j+1] -= data[j+1][0]
            alltrans.append(data)
        self.alltrans = alltrans
        os.chdir(predir)
        self.loaded = True
    else:
        print "Model not run, nothing to load"

def plot(self):
    if self.loaded:
        predir = os.getcwd()
        os.chdir(self.name)
        size = 10

```

```

    for i in range(self.molecule.nlines):
        plt.clf()
        transid = self.molecule.line[i].transid
        figure = plt.figure(figsize=(14,10))
        noffs = self.molecule.line[i].noffs
        nlines,ncolumns = plotfactors(noffs)
        for j in range(noffs):
            ax = plt.subplot(nlines, ncolumns, j + 1)
            for item in ([ax.title, ax.xaxis.label, ax.
                yaxis.label]+ax.get_xticklabels() + ax.
                get_yticklabels()):
                item.set_fontsize(size)
            plt.step(self.alltrans[i][0],self.alltrans[i
                ][j+1])
            plt.xlabel("Velocity (km/s)",fontsize=size)
            plt.ylabel("Intensity (Tmb)",fontsize=size)
            figure.set_tight_layout(True)
            plt.savefig(self.name+'_'+transid+'.png')
        os.chdir(predir)
        return
    else:
        print "Model not loaded nothing to plot"

def eval(self, obs,weight=None):
    if weight is None:
        weight = np.ndarray([len(obs)])
        weight.fill(1.0)
    chi2sum = 0
    if not self.prepared:
        print "Model not prepared nothing to evaluate"
        raise Exception("How can I evaluate something if it is
            not prepared????")
    for i in range(len(obs)):
        iobs = obs[i]
        if not isinstance(iobs,Observation):
            print "{0:d} observation is not an observation".format
                (i)
            raise Exception("Your observation is not an
                observation...")
        elif not iobs.prepared:
            print "Observation not prepared, nothing to evaluate"
            raise Exception("How can I grade your homework if
                the answer sheet is not prepared????")
        else:
            if iobs.type=='direct':
                for j in range(iobs.noffs):

```

```

        for k in range(iobs.nwindows):
            chiarr = (self.cutspec[i][j][k]-iobs.
                    cutspec[j][k])**2/iobs.sigmas[j]
            chi2sum += weight[i]*np.sum(chiarr)
        elif iobs.type=='quantified':
            chiarr = (self.quantified[i]-iobs.quantified)
                    **2/iobs.quantifiederrs**2
            chi2sum += weight[i]*np.sum(chiarr)
    self.chi2 = chi2sum
    return chi2sum

def prepare(self,obs):
    if not self.loaded:
        print "Model not loaded nothing to prepare"
        raise Exception("How can I prepare something if I don't
            have the materials?")
    cutspec=[]
    quantified=[]
    for i in range(len(obs)):
        iobs = obs[i]
        cut_spectra = []
        nwindows = iobs.nwindows
        noffs = iobs.noffs
        for j in range(noffs):
            off = []
            for k in range(nwindows):
                liminf, limsup = iobs.windows[k]
                sel = (self.alltrans[i][0] >= liminf) & (self
                    .alltrans[i][0] <= limsup)
                off.append(self.alltrans[i][j+1][sel])
            cut_spectra.append(np.array(off))
        cut_spectra = cut_spectra

        if iobs.type == 'direct':
            cutspec.append(cut_spectra)
            quantified.append(False)
        elif iobs.type == 'quantified':
            quant = np.empty([noffs,nwindows,3])
            for j in range(noffs):
                for k in range(nwindows):
                    nums = np.arange(len(cut_spectra[j][k]))
                    sum = np.sum(cut_spectra[j][k])
                    max = np.max(cut_spectra[j][k])
                    posmax = nums[cut_spectra[j][k] == max][0]
                    quant[j,k,:] = sum, max, posmax
            quantified.append(quant)

```

```

        cutspec.append(False)
self.cutspec = cutspec
self.quantified = quantified
self.prepared = True
return

def plot_with_obs(self, obs):
    if self.loaded:
        predir = os.getcwd()
        os.chdir(self.name)
        size = 10
        for i in range(self.molecule.nlines):
            iobs = obs[i]
            plt.clf()
            transid = self.molecule.line[i].transid
            figure = plt.figure(figsize=(14,10))
            noffs = self.molecule.line[i].noffs
            nlines, ncolumns = plotfactors(noffs)
            for j in range(noffs):
                ax = plt.subplot(nlines, ncolumns, j + 1)
                for item in ([ax.title, ax.xaxis.label, ax.
                    yaxis.label]+ax.get_xticklabels() + ax.
                    get_yticklabels()):
                    item.set_fontsize(size)
                residuals = iobs.specs[j] - self.alltrans[i][
                    j + 1]
                plt.plot(iobs.velaxis, iobs.specs[j], color='
                    blue', label="Observation", linewidth=1.5,
                    drawstyle='steps')
                plt.plot(self.alltrans[i][0], self.alltrans[i]
                    [j + 1], '--', color='red', label="Model"
                    ,
                    linewidth=1.5, drawstyle='steps')
                maxres = np.max(residuals)
                plt.plot(iobs.velaxis, residuals-1.5*maxres, ':
                    ', color='orange', label="Residuals", linewidth
                    =1.5, drawstyle='steps')
                plt.xlabel("Velocity (km/s)", fontsize=size)
                plt.ylabel("Intensity (Tmb)", fontsize=size)
                plt.text(0.1, 0.75, "$\sigma=$" + "{0:1f}".
                    format(iobs.sigmas[j] * 1000) + " mK",
                    transform=ax.transAxes, fontsize=size)
                plt.legend(loc="upper left", fontsize=size)
            figure.set_tight_layout(True)
            plt.savefig(self.name+'_with_obs_'+transid+'.png',
                dpi=900)

```

```

        os.chdir(predir)
        return
    else:
        print "Model not loaded nothing to plot"

class Molecule:
    def __init__(self,name,line,nrot,colsel):
        self.name = name
        if isinstance(line,Line):
            self.nlines = 1
            self.line = [line]
        else:
            self.nlines = len(line)
            self.line = line
        self.nrot = nrot
        self.colsel = colsel

class Line:
    def __init__(self,positions,velims,nvels,hypsel,telpars):

        self.pos = positions
        poswrds = positions.split()
        self.noffs = len(poswrds)
        self.velims = velims
        self.nvels = nvels
        self.hypsel = hypsel
        self.telpars = telpars
        telwrds = telpars.split()
        self.transid = telwrds[0]

```

A.2.4.2 *Observation class*

```

from matplotlib import pyplot as plt
import numpy as np

class Observation:

    def __init__(self,obsfile,noffs,windows,type):
        data = np.loadtxt(obsfile,unpack=True)
        self.velaxis = data[0][1:]
        specs = []
        sigmas = []
        for i in range(noffs):
            specs.append(data[i+1][1:])
            sigmas.append(data[i+1][0])
        self.windows = windows

```

```

self.nwindows = len(windows)
self.type = type
self.specs = np.array(specs)
self.sigmas = np.array(sigmas)
self.prepared = False
self.noffs = noffs
self.dvel = abs(self.velaxis[1]-self.velaxis[0])
return

def prepare(self):
    cut_spectra = []
    nwindows = len(self.windows)
    for j in range(self.noffs):
        off = []
        for i in range(nwindows):
            liminf, limsup = self.windows[i]
            sel = (self.velaxis >= liminf) & (self.velaxis
                <= limsup)
            off.append(self.specs[j][sel])
            cut_spectra.append(np.array(off))
        cut_spectra = np.array(cut_spectra)

    if self.type == 'direct':
        self.cutspec = cut_spectra
        self.prepared = True
    elif self.type == 'quantified':
        quantified = np.empty([self.noffs,nwindows,3])
        quantifiederrs = np.copy(quantified)
        for j in range(self.noffs):
            for i in range(nwindows):
                nums = np.arange(len(cut_spectra[j][i]))
                sum = np.sum(cut_spectra[j][i])
                max = np.max(cut_spectra[j][i])
                if max<3*self.sigmas[j]:
                    max = 0
                    posmax = len(nums)/2
                else:
                    posmax = nums[cut_spectra[j][i]==max][0]
                errsum = self.sigmas[j]*np.sqrt(len(
                    cut_spectra[j][i]))
                quantified[j,i,:] = sum,max,posmax
                quantifiederrs[j,i,:] = errsum,self.sigmas[j
                    ],self.dvel

    self.quantified = np.copy(quantified)
    self.quantifiederrs = (quantifiederrs)

```

```

        self.prepared = True
    else:
        print("unknow type "+self.type)
        self.prepared = False

    def plot(self,name):
        size = 10
        nlines,ncolumns = plotfactors(self.noffs)
        figure = plt.figure(figsize=(14,10))
        for j in range(self.noffs):
            plt.clf()
            ax = plt.subplot(nlines, ncolumns, j + 1)
            for item in ([ax.title, ax.xaxis.label, ax.yaxis.
                label] + ax.get_xticklabels() + ax.
                get_yticklabels()):
                item.set_fontsize(size)
            plt.step(self.velaxis, self.specs[j])
            plt.xlabel("Velocity (km/s)",fontsize=size)
            plt.ylabel("Intensity (Tmb)",fontsize=size)
            plt.text(0.1, 0.75, "$\sigma=$" + "{0:.1f}".format(
                self.sigmas[j] * 1000) + " mK",
                transform=ax.transAxes)
            figure.set_tight_layout(True)
        plt.savefig(name+'.png')

    return

```

A.2.4.3 Example code using observation and model classes

```

from ali_general import Model
from ali_general import Molecule
from ali_general import Line
from ali_general import Observation

name = "example_model"
### density as n0 next r0 and alpha
denspars = [8.8e4, 507, 0.09, 2.84]
### Non thermal dispersion as sig0 sigext rj deltarj
turbpars = [0.0488, 0.28, 0.71, 0.042]
### Velocity field as Vc rv deltarv
velopars = [-0.19, 0.55, 0.12]
### Abundance relative to H2, and abundance factor
abunpars = ["6.2e-9",1]

### Telescope pointings in distance from the model center
in arcseconds

```

```

pointings = "0.0 22.36 44.72 67.08 89.44 111.8"
### selecting the HCN 10 hfs components
hfs10selec = '1 3 2'
### Telescope properties for HCN 10, number, HPBW, Beff, 1
  st side lobe
telescope10 = "1 28 1.0 350"
### selecting the HCN 32 hfs components
hfs32selec = "10 15 12"
### Telescope properties for HCN 32, number, HPBW, Beff, 1
  st side lobe
telescope32 = "3 9 1.0 350"
### Number of rotational levels
nrot = '8'
### Selecting collisional coefficients (For HCN, 5 =
  Hernandez-vera 2017)
collisionselector = '5'

temp = "10" ### assuming constant temperature = 10 Kelvin
layers = "50,1,lin" ### Number of layers of the model
dist = "140" # distance in parsec
size = "16" ## Diameter of the model in arcminutes

### HCN10 hyperfine components
hcn1001 = -7.0659
hcn1021 = 0.0
hcn1011 = 4.8403

# Windows to compute chi2
hcn10win = [[hcn1001-0.5,hcn1001],[hcn1001,hcn1001+0.5],[
  hcn1021-0.5,hcn1021],[hcn1021,hcn1021+0.5],[hcn1011-0.5,
  hcn1011],[hcn1011,hcn1011+0.5]]
hcn32win =
  [[-2.6612,-2.0222],[-0.6225,-0.0444],[-0.0444,0.2751],
  [0.2751,0.6022],[1.2944,1.7356],[1.7356,2.1312]]

## Initiliaze HCN observations
hcn10_obs = Observation("hcn10_ascii.dat",6,hcn10win,"
  quantified")
hcn32_obs = Observation("hcn32_ascii.dat",6,hcn32win,"
  quantified")
## Prepare the HCN observations in the chunks defined by
  the windows
hcn10_obs.prepare()
hcn32_obs.prepare()
## Bundle HCN observations together

```

```

hcn_obs = [hcn10_obs,hcn32_obs]

## Defining Spectral axis for models
hcn10npoints = str(int((9. + 7.) / 6.6036e-2)+1)
hcn32npoints = str(int((3.5 + 3.5) / 2.2022e-2) + 1)
hcn10velims = "-9,{0:.5f}".format(-9.+(float(hcn10npoints)-1)
    *6.6036e-2)
hcn32velims = "-3.5,{0:.5f}".format(-3.5 + (float(hcn32npoints)
    -1)*2.2022e-2)

## Creating the two line objects with the aforementioned
    spectral axis
hcn10 = Line(pointings,hcn10velims,hcn10npoints,hfs10selec,
    telescope10)
hcn32 = Line(pointings,hcn32velims,hcn32npoints,hfs32selec,
    telescope32)

## Using the aforementioned lines to create the complete
    molecular spectroscopy used in the model
hcn = Molecule("HCN_hyp",[hcn10,hcn32],nrot,
    collisionselector)

## Initialise model
hcn_model = Model(name+"_hcn",velopars,turbpars,denspars,
    abunpars,temp,
                    hcn,layers,dist,size)

## Write model cloud input file
hcn_model.write_mcloudinp()
## Run model cloud
hcn_model.run()
## Clean up superflous files
hcn_model.clean_up()
## Load the spectra into numpy arrays
hcn_model.load()
## Cut and prepare the observation in chunks just as the
    ones in the observations in obs_hcn
hcn_model.prepare(obs_hcn)
## Compute the Chi^2 between the observations and the model
    with weights 1.0 and 1.0
hcn_chi2 = hcn_model.eval(obs_hcn,[1.0,1.0])
## Plot the model against the observations for visual
    inspection
hcn_model.plot_with_obs(obs_hcn)

```

A.3 MCMC TOOLKIT

A.3.1 MCMC toolkit code

```

from astropy.io import fits
import numpy as np
import corner
from matplotlib import pyplot as plt
import string
import random
import time

def run_corner(prefix, burn_in, legend, savevals=False,
              plotlims=1.0):
    hdulist = fits.open(prefix + '.fits')
    # chains
    chain = hdulist[1].data
    # likelihood
    ndim = len(legend)
    answers = []
    try:
        len(plotlims)
    except:
        plotlims = np.zeros(ndim)+plotlims
    for n in burn_in:
        # We need to cut the first steps so that we use the '
        # stationary state'
        samples = chain[:, n:, :].reshape((-1, ndim))
        fig, answer = corner.corner(samples, labels=legend,
                                   quantiles=[0.16, 0.5, 0.84], show_titles=True,
                                   title_kwargs={"fontsize": 28}, title_fmt
                                   =None, range=plotlims)
        answers.append(answer)
        fig.savefig(prefix + '_' + str(n) + '_corner.png')
    if savevals:
        outstr = "#Parameters for the run: {0:s}\n".format(
            prefix)
        outstr += "#Burn in: {0:d}\n".format(n)
        for i in range(len(answer)):
            outstr+="{0:s} = {1:.4f} {2:.4f} +{3:.4f}\n".format(
                legend[i], answer[i][1], answer[i][0] -
                answer[i][1],
                answer[i]
                ][2] -
                answer

```

```

        [i
        ][1])
    outfile = open("{0:s}_{1:d}.dat".format(prefix,n),'w')
    outfile.write(outstr)
    outfile.close()
    return answers

def plot_walkers(prefix, legend):
    """
    Plot and save the evolution of the remainingtimeerent
    parameters through the markov chain
    """
    hdulist = fits.open(prefix+".fits")
    chain = hdulist[1].data
    adim = chain.shape
    nwalkers = adim[0]
    nit = adim[1]
    ndim = adim[2]
    nlines,ncolumn = plotfactors(ndim)
    if nlines * ncolumn >= ndim:
        X = np.linspace(1, nit, nit)
        fig = plt.figure(figsize=(20,20))

        if len(legend) != ndim:
            print('Watch out for your legend! \n')
        else:
            for j in range(ndim):
                plt.subplot(nlines, ncolumn, j + 1)
                for i in range(nwalkers):
                    plt.plot(X, chain[i, 0:nit , j])
                    plt.ylabel(legend[j])
                    plt.xlabel('number of steps')
                fig.set_tight_layout(True)
                fig.savefig(prefix + '_walkers.png')
    else:
        print('I need more place to plot\n')

def savechain(chain,name,steps,totsteps,initial=None):
    if initial is None:
        if steps == totsteps:
            outputchain = chain
        else:
            adim = chain.shape
            nwalkers = adim[0]
            ndim = adim[2]
            outputchain = np.ndarray([nwalkers,steps,ndim])

```

```

        for i in range(nwalkers):
            for j in range(steps):
                for k in range(ndim):
                    outputchain[i,j,k] = chain[i,j,k]
    else:
        adim = initial.shape
        nwalkers = adim[0]
        isteps = adim[1]
        ndim = adim[2]
        totalsteps = steps+isteps
        outputchain = np.ndarray([nwalkers,totalsteps,ndim])
        for i in range(nwalkers):
            for j in range(isteps):
                for k in range(ndim):
                    outputchain[i, j, k] = initial[i, j, k]
            for j in range(isteps,totalsteps):
                for k in range(ndim):
                    outputchain[i, j, k] = chain[i, j-isteps, k]
    hdul = fits.HDUList()
    hdul.append(fits.PrimaryHDU())
    hdul.append(fits.ImageHDU(data=outputchain)) # save the
        markov chain in an array (nwalkers, nit,ndim)
    fits_name = name + '.fits'
    hdul.writeto(fits_name, overwrite=True)

def get_pos_and_chain(fitsfile):
    hdulist = fits.open(fitsfile)
    chain = hdulist[1].data
    adim = chain.shape
    nwalkers = adim[0]
    pos = [chain[i][-1] for i in range(nwalkers)] # initial
        positions for each walker form fits file
    return pos,chain

def cut_fits(ifits,ofits,limit):
    pos,chain = get_pos_and_chain(ifits)
    savechain(chain,ofits,limit,1e20,None)

def plotfactors(ndim):
    if ndim == 1:
        return 1, 1
    elif ndim == 2:
        return 2, 1
    elif ndim == 3:
        return 3, 1
    for i in range(int(np.sqrt(ndim)),1,-1):

```

```

    for j in range(int(np.sqrt(ndim)),1,-1):
        if (i*j)==ndim:
            return i,j
        elif (i*j)<ndim:
            if i*(j+1)>=ndim:
                return i,j+1
            else:
                return i+1, j + 1

    return -1,-1

def read_input_sel(filein):
    pars,printf,prsup=np.loadtxt(filein,usecols=[0,1,2],unpack
        =True)
    fix,log = np.loadtxt(filein,usecols=[3,4],unpack=True,
        dtype=bool)
    itheta = pars[~fix]
    fixed = pars[fix]
    priorinf = printf[~fix]
    priorsup = prsup[~fix]
    ndim = len(itheta)
    return itheta,priorinf,priorsup,ndim,fixed,fix,log

def read_legend(filein):
    legends = np.loadtxt(filein, usecols=[1], unpack=True,
        dtype=str,delimiter="|")
    fix= np.loadtxt(filein, usecols=[3], unpack=True, dtype=
        bool)
    legends = legends[~fix]
    return legends

def completepset(theta,fixed,fix,log):
    ifix = 0
    ipar = 0
    modelpars = []
    for i in range(len(fix)):
        if fix[i]:
            pars = fixed[ifix]
            ifix += 1
        else:
            pars = theta[ipar]
            ipar += 1
        if log[i]:
            pars = 10 ** (pars)
        modelpars.append(pars)
    return modelpars

```

```

def random_str(size=6, chars=string.ascii_uppercase +
    string.digits):
    return "".join(random.choice(chars) for x in range(size))

def etf(start,nit,ntotal):
    now = time.time()
    duration = now-start
    tottime = ntotal*duration/nit
    remainingtime = (1.0-1.0*nit/ntotal)*tottime
    if remainingtime < 60:
        return "will end in: {0:5.2f} seconds".format(remainingtime
            )
    elif remainingtime < 3600:
        return "will end in: {0:5.2f} minutes".format(remainingtime
            /60.)
    elif remainingtime < 86400:
        return "will end in: {0:5.2f} hours".format(remainingtime
            /3600.)
    else:
        return "will end in: {0:5.2f} days".format(remainingtime
            /86400.)

def took(ref):
    now = time.time()
    diff = now - ref
    if diff < 60:
        print "it took: {0:.4f} seconds.\n".format(diff)
    elif diff < 3600:
        print "it took: {0:.2f} minutes.\n".format(diff/60.)
    elif diff < 86400:
        print "it took: {0:.2f} hours.\n".format(diff/3600.)
    else:
        print "it took: {0:.3f} days.\n".format(diff/86400.)

def progress(ref):
    now = time.time()
    diff = now - ref
    if diff < 60:
        return "Time since start: {0:5.2f} seconds".format(diff)
    elif diff < 3600:
        return "Time since start: {0:5.2f} minutes".format(diff/60.)
    elif diff < 86400:
        return "Time since start: {0:5.2f} hours".format(diff/3600.)
    else:
        return "Time since start: {0:5.2f} days".format(diff/86400.)

```

A.3.2 MCMC toolkit example input file

```
### Example input file for MCMC toolkit
### structure:
### Par name
### initial[0] Priorinf[1] Priorsup[2] Fix[3] logscale[4] |
    Legend[5]
### Parameters for the gaussian
-----
### Peak intensity
20 0 100 0 0 |$A$
### Center
-30 -50 50 0 0 |$x_0$
### Dispersion
50 1 60 0 0 |$\sigma$
```


B

DATA TABLES

Table B.1 – Integrated intensities for the hyperfine components of the HCN $J = 1 \rightarrow 0$ transition along with the ratios between them, $R_{02} = F = 0 \rightarrow 1/F = 2 \rightarrow 1$, $R_{12} = F = 1 \rightarrow 1/F = 2 \rightarrow 1$. Data extracted from Sohn et al. (2007).

Source	$F = 0 \rightarrow 1$ (K km/s)	$F = 2 \rightarrow 1$ (K km/s)	$F = 1 \rightarrow 1$ (K km/s)	R_{01}	R_{12}
L1498	0.171±0.014	0.175±0.014	0.147±0.012	0.977±0.114	0.840±0.114
L1495AN	0.218±0.017	0.305±0.024	0.184±0.015	0.715±0.111	0.603±0.113
L1521B	0.185±0.015	0.224±0.018	0.196±0.016	0.826±0.114	0.875±0.115
B217-2	0.336±0.027	0.495±0.040	0.306±0.024	0.679±0.114	0.618±0.113
L1521F	0.272±0.022	0.296±0.024	0.237±0.019	0.919±0.115	0.801±0.114
TMC-2	0.234±0.019	0.518±0.041	0.332±0.027	0.452±0.113	0.641±0.113
CB22	0.150±0.012	0.259±0.021	0.157±0.013	0.579±0.114	0.606±0.116
TMC-1	0.390±0.031	0.355±0.028	0.304±0.024	1.099±0.112	0.856±0.112
L1527B-1	0.260±0.021	0.240±0.019	0.180±0.014	1.083±0.113	0.750±0.111
CB23	0.122±0.010	0.198±0.016	0.124±0.010	0.616±0.115	0.626±0.114
L1507A	0.190±0.015	0.224±0.018	0.139±0.011	0.848±0.113	0.621±0.113
L1517B	0.167±0.013	0.237±0.019	0.124±0.010	0.705±0.112	0.523±0.114
L1544	0.305±0.024	0.258±0.021	0.275±0.022	1.182±0.113	1.066±0.114
L1512a	0.128±0.010	0.202±0.016	0.125±0.010	0.634±0.111	0.619±0.113
L1552	0.139±0.011	0.137±0.011	0.117±0.009	1.015±0.113	0.854±0.111
L1622A2	0.336±0.027	0.496±0.040	0.243±0.019	0.677±0.114	0.490±0.112
L1622A1	0.322±0.026	0.406±0.032	0.252±0.020	0.793±0.113	0.621±0.112
L1696A	0.310±0.025	0.444±0.036	0.302±0.024	0.698±0.114	0.680±0.114
L1696B	0.242±0.019	0.322±0.026	0.211±0.017	0.752±0.113	0.655±0.114
L204C-2b	0.251±0.020	0.604±0.048	0.332±0.027	0.416±0.113	0.550±0.114
L234E-Sb	0.183±0.015	0.343±0.027	0.248±0.020	0.534±0.114	0.723±0.113
L462-2b	0.185±0.015	0.256±0.020	0.307±0.024	0.723±0.113	1.199±0.111
L492	0.279±0.022	0.384±0.031	0.286±0.023	0.727±0.113	0.745±0.114
L673-7	0.200±0.016	0.490±0.039	0.249±0.020	0.408±0.113	0.508±0.113
L694-2	0.108±0.009	0.095±0.010	0.107±0.009	1.137±0.134	1.126±0.135
L1155C1	0.135±0.011	0.182±0.015	0.131±0.010	0.742±0.116	0.720±0.112
L944-2	0.076±0.006	0.165±0.013	0.089±0.007	0.461±0.112	0.539±0.111
L1197	0.125±0.010	0.132±0.011	0.105±0.008	0.947±0.116	0.795±0.113
CB246-2b	0.123±0.010	0.261±0.021	0.163±0.013	0.471±0.114	0.625±0.113

APPROVED TELESCOPE TIME PROPOSALS

Table C.1 – Approved telescope time proposals submitted by V. S. Magalhães during this thesis.

Proposal ID	Epoch	Observatory
041-15	Summer 2015	IRAM-30m
W15AH	Winter 2015	IRAM-NOEMA
007-16	Summer 2016	IRAM-30m
2016.1.01468.S	Cycle 4	ALMA
105-16	Winter 2016	IRAM-30m

D

HC₃N/HC₃¹⁵N IN L1544

Nitrogen isotopic ratio of HC₃N towards the L1544 prestellar core

P. Hily-Blant,^{1,2*} A. Faure,² C. Vastel,^{3,4} V. Magalhaes,² B. Lefloch,² R. Bachiller⁵

¹*Institut Universitaire de France*

²*Université Grenoble Alpes, CNRS, IPAG, F-38000 Grenoble, France*

³*Université de Toulouse, UPS-OMP, IRAP, 31400 Toulouse, France*

⁴*CNRS, IRAP, 9 Av. Colonel Roche, BP 44346, 31028 Toulouse Cedex 4, France*

⁵*Observatorio Astronómico Nacional (OAN, IGN), Calle Alfonso XII 3, E-28014 Madrid, Spain*

Accepted XXX. Received YYY; in original form ZZZ

ABSTRACT

The origin of the heavily fractionated reservoir of nitrogen in comets is a key question in the theory of formation of comets and hence of the solar system. This question was put on a more general footing by the detection of a similar fractionated reservoir in nearby protoplanetary disks, suggesting that similar processes, either in the parent prestellar core, in the protostellar core, or in the disk itself, are responsible for the enriched reservoir of nitrogen traced by comets. So far, observations of isotopic ratios of nitrogen in protostars or prestellar cores have not securely identify such a fractionated reservoir owing to the intrinsic difficulty of direct isotopic ratios measurements. In this article, we report the detection of 5 rotational lines of HC₃N and two rotational lines of its ¹⁵N isotopologue, toward the L1544 prestellar core obtained in the context of the ASAI/IRAM-30m large program. The excellent sensitivity of the observations also allows the detection of the hyperfine structure of the HC₃N lines. Based on a multiline analysis at the hyperfine level, we derive the column densities of HC₃N and HC₃¹⁵N and derive an isotopic ratio of 400±20. Uncertainties were obtained using a MCMC approach to explore the parameter space. The comparison of this value with those obtained in CN and HCN in the same core suggest that the formation of HC₃N involves two debated pathways, one through CN + C₂H₂ and another through dissociative recombination of HC₃NH⁺. The present observations do not allow to constrain the relative importance of the two pathways.

Key words: Prestellar cores (L1544) – Astrochemistry – Nitrogen isotopic ratios

1 INTRODUCTION

From an observational perspective, measuring isotopic ratios from remote observations is a challenging and intrinsically time-demanding task (Taniguchi & Saito 2017). Deriving isotopic ratios generally rests upon several assumptions, some of which being questionable—such as the co-spatial distribution of isotopologues—while others may be difficult to assess—e.g. identical excitation temperature. From interstellar medium standards, true accuracies are usually larger than the calibration uncertainties, typically 10%, and more likely around 50%. In contrast, laboratory or *in situ* measurements of cosmomaterial samples have accuracies at the percent level (Bonal et al. 2010; Marty et al. 2011). Yet, isotopic ratios are so far the best tool to follow the volatile

content of molecular clouds in their evolution towards the formation of stars, planets, and planetary systems bodies. Observations of sublimating ices from comet 67P/C-G with spectrometers onboard the ESA/ROSETTA satellite provide *in situ* measurements of isotopic ratios of xenon and hydrogen, and abundances of S₂ and O₂ molecules which consistently support a presolar origin for cometary ices (Altwegg et al. 2015; Rubin et al. 2015; Calmonte et al. 2016; Marty et al. 2017). On the other hand, *Herschel* observations of water towards protostars suggest that only a few percents of interstellar ices may actually sublime (van Dishoeck et al. 2014), leaving important amounts of pristine interstellar material available to build up planetary systems. These findings motivate the search for an interstellar heritage within the solar system while providing insights in the composition of primitive planetary systems in general. Understanding the link between the chemical composition of prestellar and pro-

* E-mail: pierre.hily-blant@univ-grenoble-alpes.fr

tostellar cores and that of comets, which form at the earliest stages of the planetary formation sequence, is therefore of paramount importance. From this perspective, the origin of nitrogen in the solar system remains elusive. In particular, the $^{14}\text{N}/^{15}\text{N}$ isotopic ratio of nitrogen in comets is an unsolved problem. Its average value of 144 ± 3 (Jehin et al. 2009; Bockelée-Morvan et al. 2015; Shinnaka et al. 2016; Hily-Blant et al. 2017) is three times lower than the bulk ratio of 441 ± 6 in the solar system as measured in the solar wind (Marty et al. 2011), a sharp discrepancy which questions our understanding of the formation of comets and of the origin of nitrogen in the solar system (Füri & Marty 2015). Several possibilities could explain the discrepancy: *i*) the main repository of cometary nitrogen has not been observed yet, *ii*) efficient fractionation processes in the protosolar nebula at the time of comet formation, *iii*) efficient fractionation processes in the parent interstellar cloud, or *iv*) exchange processes within cometary ices since their formation. Recently, it was shown that protoplanetary disks—or equivalently protosolar nebula analogs—carry at least two isotopic reservoirs of nitrogen, which are found to be in a 1:3 ratio, similar to the comets-to-bulk ratio (144:441) in the protosolar nebula, thus ruling out the need for exchange process in comets.

In this work, we wish to explore the interstellar scenario for the origin of the heavily fractionated cometary nitrogen. From an astrophysical perspective, the main issue is observational in that the main repositories of nitrogen, N or N_2 , are not directly observable in cold interstellar clouds. The bulk isotopic ratio is therefore only measurable indirectly, using trace species such as CN or HNC (Adande & Ziurys 2012). To which extent the isotopic ratio in these molecules is representative of the bulk depends on their formation pathways and molecule-specific fractionation processes which may, or may not, favour one of ^{14}N or ^{15}N in those species leading to isotopic ratios distinct from the bulk. In cold and dense clouds, such processes reduce to mass fractionation associated to zero-point energy differences between the two isotopologues (Watson et al. 1976; Terziewa & Herbst 2000) may be efficient (Heays et al. 2014). Therefore, to infer the bulk isotopic ratio from trace species, chemical models including detailed fractionation reactions must be used. Yet, the chemical mass fractionation decreases with temperature and observations of warmer gas may then provide better probes of the bulk ratio. Indeed, consistent isotopic ratios were obtained in nitrile and hydride species in Barnard 1b (Daniel et al. 2013), contrary to expectations based on chemical calculations in cold gas (Hily-Blant et al. 2013a). Furthermore, the B1b ratios are in harmony with the directly measured CN/ C^{15}N ratio of 323 ± 30 in the TW Hya protoplanetary disk (Hily-Blant et al. 2017) and it is argued this ratio is indeed representative of the bulk ratio in the present-day local interstellar medium.

Models of chemical fractionation of nitrogen have been developed and applied to dense gas, from the typical 10^4cm^{-3} of prestellar clouds where mild effects are predicted (Terziewa & Herbst 2000), to the much higher density, 10^7cm^{-3} , of protostars (Charnley & Rodgers 2002) where high degrees of fractionation are promoted by the heavy depletion of carbon monoxide. Nevertheless, this picture is not well established. Indeed, chemical calculations based on the fractionation network of Terziewa & Herbst

(2000) used in combination with the chemical network of Hily-Blant et al. (2010), significant variations of the isotopic ratios are predicted for most of the observable nitrogenated species, especially HCN (Hily-Blant et al. 2013b). More recently, the set of fractionation reactions was revised (Roueff et al. 2015), and the dominant fractionation route $^{15}\text{N} + ^{14}\text{N} \text{ } ^{14}\text{NH}^+ \rightleftharpoons ^{14}\text{N} + ^{14}\text{N} \text{ } ^{15}\text{N}_2\text{H}^+$ was disqualified on energetical grounds. As a consequence, steady-state isotopic ratios of all trace species fairly well reflect the elemental ratio. To put these results on a firmer ground, observations are needed not only to accurately measure isotopic ratios but also to test the chemical fractionation models. In particular, isotopic ratios of species containing equivalent atoms can identify the dominant formation routes (Sakai & Yamamoto 2013). However, measurements of interstellar isotopic ratios are complicated by the large difference in opacities among the various isotopologues. Detailed model calculations (Roueff et al. 2015) have emphasized the pitfalls of the so-called double isotopic ratios—namely the use of $\text{H}^{13}\text{C}^{14}\text{N}/\text{H}^{12}\text{C}^{15}\text{N}$ ratio and the assumption that $\text{H}^{12}\text{C}^{14}\text{N}/\text{H}^{13}\text{C}^{14}\text{N} = ^{12}\text{C}/^{13}\text{C}$ —to circumvent the large optical depth of the primary isotopologue (Hily-Blant et al. 2013a; Guzmán et al. 2017). Direct ratios may be achieved in some instances, e.g. with doubly substituted molecules such as NH_2D Gerin et al. (2009), or with weak hyperfine lines (CN, HCN) at high signal-to-noise (Hily-Blant et al. 2017).

In this work, we provide a direct measurement of the isotopic ratio of the HC_3N cyanopolyne toward the L1544 prestellar core. The obtained ratio is compared to that in related species (CN, HCN) in L1544 to derive some conclusions on the formation route of HC_3N in this source. Our ratio is also put in perspective with that in HC_3N and other species towards prestellar cores.

Origin of ^{15}N anomalies in the Solar System. Review of values in the ISM and protoplanetary disks. HC_3^{15}N detected recently toward L1527, with $[\text{HC}_3\text{N}]/[\text{HC}_3^{15}\text{N}]=338\pm 12$ (Araki et al. 2016).

2 OBSERVATIONS

The observations for all transitions quoted in Table 1 were performed at the IRAM-30m toward the dust peak emission of the L1544 prestellar core ($\alpha_{2000} = 05^{\text{h}}04^{\text{m}}17.21^{\text{s}}$, $\delta_{2000} = 25^{\circ}10'42.8''$) in the framework of the ASAI Large Program¹ (Lefloch et al. 2017). Observations at frequencies lower than 80 GHz have been performed in December 2015. The EMIR receivers (Carter et al. 2012) were used in combination with the Fast Fourier Transform Spectrometer in its so-called 50 kHz configuration, providing us with 49 kHz spectral resolution, or typically 0.15 to 0.20 kms^{-1} at the frequency discussed in this paper. Further details on the observations can be found in Vastel et al. (2014) and Quénard et al. (2017). The forward and beam efficiencies of the radiotelescope are 0.95 and 0.81 respectively, and all antenna temperatures were brought into the main-beam temperature scale by assuming no spatial dilution, namely $T_{\text{mb}} = F_{\text{eff}}/B_{\text{eff}} \times T_{\text{A}}^*$. Contributions from error-beams were considered negligible for

¹ Astrochemical Surveys At IRAM: <http://www.oan.es/asai>

Table 1. Properties of the HC_3N and HC_3^{15}N lines obtained through Gaussian fitting.

Molecule	$N' \rightarrow N$	Frequency GHz	σ_T^\S mK	T^\ddagger K	ν_0 kms $^{-1}$	FWHM kms $^{-1}$	W_{main}^\dagger mK kms $^{-1}$	W_{hf}^\dagger mK kms $^{-1}$	W_{tot}^\dagger mK kms $^{-1}$
HC_3N	8-7	72.78382	5	3.78	7.22	0.51	2053	77	2120
	9-8	81.88147	5	2.87	7.24	0.53	1633	34	1664
	10-9	90.97902	3	2.66	7.32	0.50	1404	30	1430
	11-10	100.07639	3	1.84	7.23	0.49	956	16	971
	12-11	109.17363	3	1.28	7.22	0.46	626	–	627
HC_3^{15}N	9-8	79.50005	6	0.072	7.19	0.18	–	–	14(2)
	10-9	88.33300	2	0.020	7.23	0.42	–	–	9.0(7)
	11-10	97.16583	3	–	–	–	–	–	<1.4
	12-11	105.99852	3	–	–	–	–	–	<1.0
	13-12	114.83109	14	–	–	–	–	–	<4.3

§ Statistical uncertainty, at the 1σ level, on the main-beam temperature (in K).

‡ Peak intensity (main beam temperature).

† For HC_3N , three integrated intensity values are provided: main component, sum of the two weaker hf lines, and the total (main+hf) flux. For HC_3^{15}N , only the main component is detected. Upper limits are 1σ .

HC_3N . All the following analysis is performed in this T_{mb} scale. The spectra were reduced and analysed with the CLASS package of the GILDAS software².

Charlotte: TSYS ; TREC ; weather ; ... ; integration time ; periodes d’observation — important pour l’incertitude de calibration ; quelles raies ont ete observees simultanement ?.

3 RESULTS

3.1 Spectra

The HC_3N and HC_3^{15}N spectra are shown in Figs. 3.1 and 3.1 respectively. The signal-to-noise ratio of the HC_3N lines ranges from a few hundreds up to more than a thousand. Indeed, the hyperfine structure of HC_3N has been detected in most cases (see Fig. 3.1), although only the most widely separated frequencies are resolved leading to essentially three lines instead of 6. The main line thus consists of 3 overlapping transitions (see Table A1), taking into account that one hf transition is too low to contribute to the emission. Hyperfine lines were also reported for the 5-4 transition of HC_3N (Araki et al. 2016). Intensities of the HC_3^{15}N lines are typically a hundred times weaker than the main isotopologue, and only two lines (9-8 and 10-9) have been detected. This also explains why no hyperfine structure was detected in the case of HC_3^{15}N . The observed line properties are summarized in Table 1, including the upper limits on the three undetected HC_3^{15}N lines. The integrated intensities of the hyperfine lines are given in Table 4.

Although our chief objective is to directly determine the isotopic ratio of nitrogen in HC_3N , the physical conditions of the emitting gas must also be known to some extent. One important feature of the present study is the availability of several rotational lines of each isotopologue, which we analyse simultaneously, providing strong constraints on the physical conditions and derived column densities.

3.2 Methodology

Our analysis presented below is based on non-equilibrium radiative transfer calculations. We have used dedicated collisional rate coefficients for both HC_3N and HC_3^{15}N (Faure et al. 2016), extended down to 5 K. For HC_3N , two sets of rates have been used, describing the collisions at the rotational and hyperfine levels respectively. For HC_3^{15}N , only the rotational set is needed. The calculations were performed using the public code RADEX program (van der Tak et al. 2007).

The efficiency of this type of numerical code makes it possible to perform large grids to explore the four-dimensional parameter space (density, kinetic temperature, column densities of both species). Such a frequentist approach allows minima (both local and global) to be found. However, determining uncertainties based on a simple χ^2 approach usually fails because these parameters are indeed not independent from each other. Instead, they are coupled with each other through the complex interplay of the collisional and radiative excitation processes. To explore and quantify the correlations between the parameters, we adopted the widely-used Markov chain Monte Carlo approach to explore the parameter space in a meaningful and efficient way. In practice, we used the emcee Python implementation an affine invariant sampling algorithm, which is freely available and widely used in the astrophysical community³. We also used the corner Python library to produce plots of the parameter distribution and correlation matrix.

In this approach, the parameter space is explored using several Markov chains which are run in parallel (although not entirely from a numerical point of view), for typically $\sim 10^3$ steps. In our case, the prior probability was a uniform distribution for each parameter, with boundaries inferred from physical and chemical considerations. The kinetic temperature T_{kin} varies between 6 to 15 K, the log10 of the density, HC_3N column density, and isotopic ratio, were taken in the intervals [4 : 7], [11 : 15], and [2 : 3] respectively. To

² <http://www.iram.fr/IRAMFR/GILDAS>

³ The code is available online at <http://dan.iel.fm/emcee> under the MIT License.

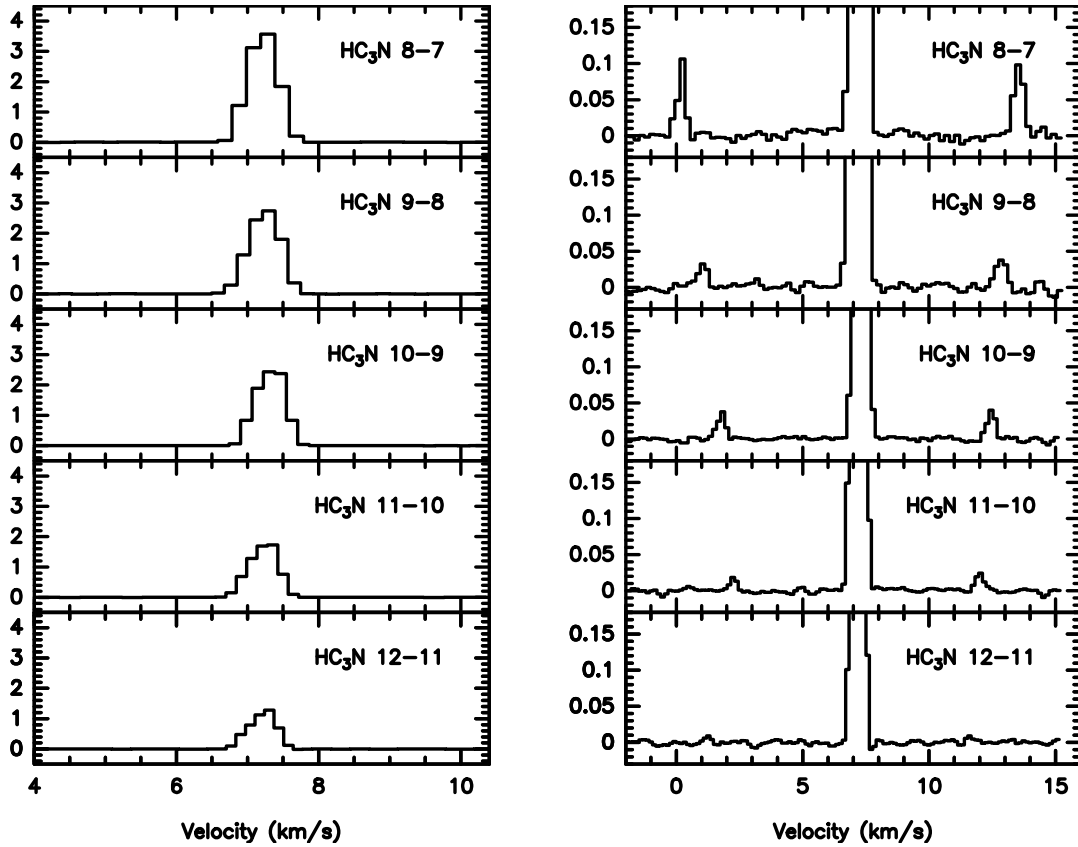


Figure 1. Spectra of HC_3N towards L1544 in main-beam temperature scale (left panels). The scale is magnified in the right panels to show the hyperfine structure.

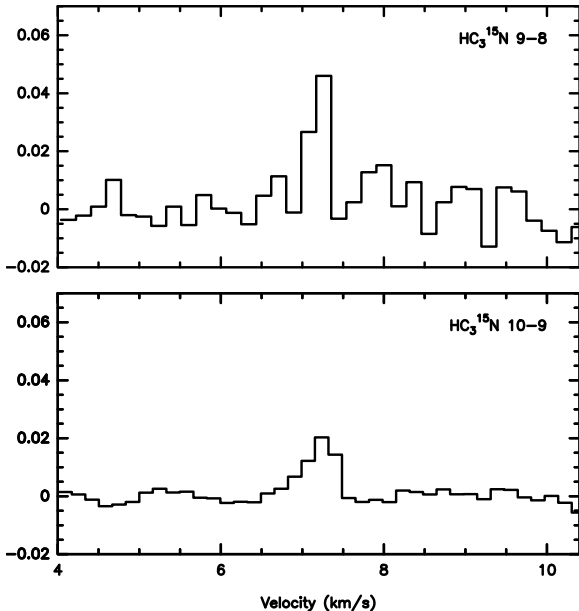


Figure 2. Spectra of the detected HC_3^{15}N lines in main-beam temperature scale (left panels).

compute the likelihood of each sample, the uncertainties on the integrated intensities were taken to be at least 5%, much larger than the statistical uncertainties obtained from Gaussian fitting. In performing MCMC parameter space explo-

ration, the number of chains —also called walkers— and the number of steps of each chain, are critically important to ensure that the parameter space has been correctly sampled. It is also important to begin with a physically acceptable solution, although we have successfully tested that various initial conditions lead to the same final distributions. By using multithreading on a 4 CPU laptop, the typical execution time was 20 min for 10^5 samples.

3.3 Assumptions

The basic assumption is that both isotopologues are co-spatial, not only in terms of abundance, but also in terms of their excitation, such that their emissions come from the same regions within the core. Based on chemical arguments, the two species are expected to be formed by the same pathways, apart from some potential active specific fractionation routes. In addition, these two molecules have very similar spectroscopic properties (spontaneous decay and collision rates), and hence are most likely to emit from the same locations in the cloud.

3.4 Physical conditions from the HC_3N lines

3.4.1 Rotational analysis

In a first set of calculations, only the high-SNR HC_3N lines are used to determine the physical conditions. The integrated intensity of the main hyperfine (hf) transitions listed

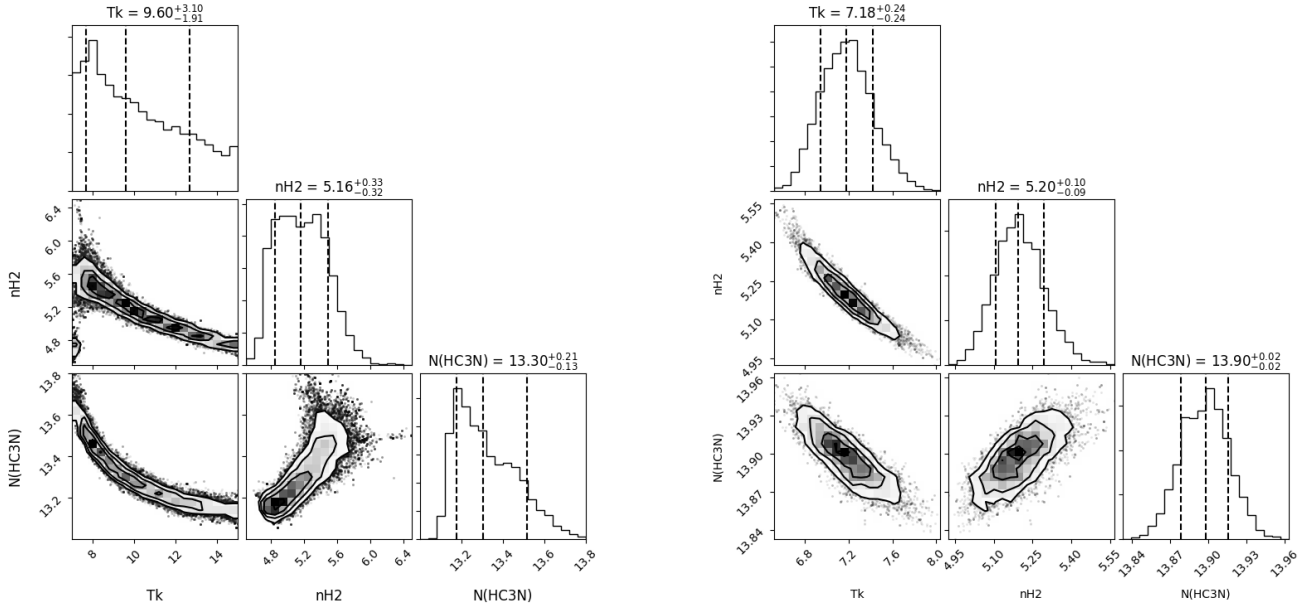


Figure 3. Physical conditions and column density of HC_3N derived from the rotational (left) and hyperfine (right) fluxes (see Section 3.4.2 and Table 2) In each histogram panel, the median value of the parameter, with the $\pm 1\sigma$ boundaries (16% and 84% quantiles), are quoted and indicated by vertical dashed-lines.

in Table 1 were used. Since this component represents $\approx 99\%$ of the intensity (Table A1), it should be directly compared to the non-LTE predictions based on the rotational collisional rates only. However, Gaussian fitting of the three sets of hf lines separately suggest departure from a single excitation temperature among the hf multiplets, and the two weak hf lines indeed carry 1.6 to 3.6% of the total flux. The flux predictions based on rotational collisional rate coefficients were thus compared to the total observed flux of each rotational transition.

The results are shown in Fig. 3. As is evident, the set of 5 rotational lines does not point towards a single solution but to an ensemble of parameters. Basically, and not surprisingly, the physical conditions are slightly degenerated, with dense gas corresponding to cold temperatures, while warmer gas have lower density. The density is constrained within an order of magnitude, from 10^5 to 10^6 cm^{-3} , and the kinetic temperature within 7 to 14 K. In contrast, the column density is relatively well constrained within 0.4dex, and $N(HC_3N) = (2.3 \pm 1.0) \times 10^{13} \text{ cm}^{-2}$. This column density agrees well with previous analysis (Quénard et al. 2017). The presently determined physical conditions also confirm those reported by these authors although they broaden the range of solutions.

3.4.2 Hyperfine analysis

The physical conditions were also derived by including the hyperfine fluxes into the set of observational constraints. The analysis was performed using the same tools although with rotational collision rate coefficients replaced with rates at the hyperfine level. The analysis is, however, not as straightforward as in the rotational case, because several hf transitions are blended within the strongest line. To perform the comparison with the RADEX calculations, we thus

added the opacities of the overlapping lines and computed the flux assuming a single excitation temperature, namely $W_{\text{main}} = [J_V(T_{\text{ex}}) - J_V(2.73)] \times [1 - \exp(-\sum_k \tau_k)] \times FWHM \times 1.064$. A Gaussian line profile was adopted, an assumption supported by the opacity of the strongest hf transitions which remains smaller than 0.5 in all models. We also checked that the excitation temperatures of the various hf lines within each rotational transition were effectively equal to within 5%.

The results of the hyperfine analysis are summarized in Table 2 (model hfs) and shown in Fig. 3. The correlation between the kinetic temperature and H_2 density is tighter than in the rotational analysis. Kinetic temperatures ranging from 6.5 to 8 K are associated with H_2 densities from 2.5 to $1.0 \times 10^5 \text{ cm}^{-3}$ respectively. The physical conditions are therefore consistent with those from the rotational analysis, although with a smaller dispersion around the median values (see Table 2). Nevertheless, the derived column density of HC_3N is larger, at the 1σ level, in the hyperfine analysis than from the rotational one, with a value of $(8.0 \pm 0.4) \times 10^{13} \text{ cm}^{-2}$. The parameters show similar correlations with each others in both analysis, and in particular the HC_3N column density increases with the density, and decreases with the kinetic temperature.

The excitation temperatures of the best solutions from the rotational analysis are within 7 to 8 K for all transitions, while somewhat lower values (5–7 K) are obtained from the hyperfine analysis.

3.5 Nitrogen isotopic ratio in HC_3N

To determine the isotopic ratio, the two isotopologues of HC_3N were analyzed simultaneously, using either the total rotational fluxes or the hyperfine fluxes. The upper limits

Table 2. Results from the MCMC runs applied to the HC_3N and HC_3^{15}N fluxes from Table 1. Results for different number of steps and/or initial conditions are compared.

RunId	Walkers	Steps	Initial conditions [†]				Results [‡]			
			T_{kin}	$\log n_{\text{H}_2}$	$\log N$	$\log \mathcal{R}$	T_{kin}	$\log n_{\text{H}_2}$	$\log N$	$\log \mathcal{R}$
rot [§]	24	5000	8.0	5.0	13.1	–	9.60(-191,+310)	5.16(-32,+33)	13.30(-13,+21)	
hfs [§]	24	1000	8.0	5.0	13.1	–	7.18(-24,+24)	5.20(-9,+10)	13.90(-2,+2)	
w24s5000rot	24	5000	8.0	5.6	13.4	2.3	9.44(-183,+339)	5.24(-36,+35)	13.30(-14,+22)	2.32(-5,+ 7)
w24s5000hfs	24	5000	8.0	5.0	13.1	2.2	7.18(-22,+25)	5.19(-9,+ 9)	13.89(-2,+ 2)	2.60(-2,+ 2)

[†] N is the total column density of HC_3N and \mathcal{R} is the $\text{HC}_3\text{N}/\text{HC}_3^{15}\text{N}$ isotopic ratio.

[‡] The median value is given with the 16% and 84 % quantiles indicated within brackets in units of the last digit.

[§] Physical conditions derived from the HC_3N lines only, using either the rotational (rot) or hyperfine (hyp) intensities and the corresponding collision rate coefficients (see also Fig.3).

on the HC_3^{15}N lines were taken at the 5σ level, while the uncertainties for the 5 HC_3N and 2 HC_3^{15}N detected lines were, as before, at least 5% of the integrated intensity. Several MCMC runs were performed (not shown), with various numbers of steps and initial parameters, to check for parameter space exploration and for convergence towards a consistent set of physical conditions and column densities. The hyperfine analysis was conducted in the same way as before, namely by summing the opacities to compute the flux of the overlapping hyperfine transitions.

The results of the rotational and hyperfine analysis are shown in Fig. 4 and summarized in Table 2. The corresponding walkers are shown in Appendix (Fig. A2). Overall, the parameters show similar correlation patterns as in the previous analysis. In particular, the physical conditions are consistent with the above HC_3N analysis, and the difference between the HC_3N column densities from the rotational and hyperfine analysis is confirmed. This difference translates into the isotopic ratios: the rotational and hyperfine analysis lead to $\mathcal{R}=216\pm30$ and 400 ± 20 respectively. The corresponding HC_3^{15}N column densities differ by a factor two, being 9.6 and $19.5\times10^{10}\text{cm}^{-2}$ respectively.

To compare the two sets of solutions, we computed the hyperfine fluxes associated with the most probable parameters from each analysis (Table 2). These predictions are then compared to the observed fluxes by considering their algebraic distance from the observed flux measured in units of the 1σ rms. The results are shown in Fig. 5. The flux of the strongest HC_3N lines are well reproduced, within $\pm3\sigma$, by both analysis. The fluxes and upper limits of HC_3^{15}N are also well matched. However, the flux of the two weaker hyperfine lines of the 8-7 transition are underpredicted by more than 10σ by the rotational analysis. Similar discrepancies are also found for the 10-9 and 11-10 transitions. In comparison the hyperfine analysis solution is able to reproduce all fluxes to within $\pm5\sigma$. This suggests that the hyperfine analysis may be preferred. The underestimate of the weak hyperfine lines by the rotational analysis is the origin of the discrepancy on the column density between the rotational and hyperfine analysis: since these weak lines are optically thin, the rotational analysis also underestimates the column density of HC_3N although the excitation temperatures in the rotational analysis are larger ($\approx 7-8$ K) than in the hyperfine solutions.

Another difference between the two analysis is the cor-

Table 3. Compilation of nitrogen isotopic ratios in cyanopolyynes and the directly related species CN and HCN.

Source	Species	\mathcal{R}	Method [§]	Reference
TMC1(CP)	HC_3N	270 ± 57	Direct	(1–3)
	HC_3^{15}N	257 ± 54	Indirect	(1–2)
	HC_5N	323 ± 80	Direct	(1)
	HC_5^{15}N	344 ± 80	Indirect	(1)
L1527	HC_3N	338 ± 12	Indirect	(4)
L1544	HC_3N	400 ± 20	Direct	This work
	HCN	140–350	Indirect	(5)
	CN	500 ± 75	Indirect	(6)
TW Hya	CN	323 ± 30	Direct	

[§] Direct methods measure the $X^{15}\text{N}/X^{14}\text{N}$ abundance ratio; indirect methods use double isotopic ratios.

References: (1) [Taniguchi & Saito \(2017\)](#) (2) ? (3) [Takano et al. \(1998\)](#) (4) [Araki et al. \(2016\)](#) (5) [Hily-Blant et al. \(2013a\)](#) (6) [Hily-Blant et al. \(2013b\)](#)

relation between $N(\text{HC}_3\text{N})$ and \mathcal{R} obtained in the rotational fitting but not in the hyperfine analysis. Instead, the isotopic ratio presents no clear correlation with any other parameter. This difference suggests that handling separately the hyperfine fluxes adds significant constraints which forces the system towards higher HC_3N column densities and removes the low values. Finally, we note that the excitation temperatures are similar to those obtained in the previous analysis of HC_3N only. In particular, the excitation temperatures are very close for both isotopologues.

The hyperfine MCMC analysis shows that, despite the degeneracy among the physical conditions, the HC_3N column density and isotopic ratio are well constrained. The resulting \mathcal{R} isotopic ratio is

$$\mathcal{R} = 400 \pm 20. \quad (1)$$

4 DISCUSSION

4.1 Nitrogen fractionation in HC_3N

When compared to the elemental ratio of 323 ± 30 in the solar neighbourhood ([Hily-Blant et al. 2017](#)), the present direct determination of the $[\text{HC}_3\text{N}]/[\text{HC}_3^{15}\text{N}]$ ratio in L1544 shows that HC_3N is, at the 1σ level, enriched in ^{15}N . Recently, the nitrogen isotopic ratio of HC_3N was measured towards the cyanopolyynes peak (CP) in TMC-1 and a value of

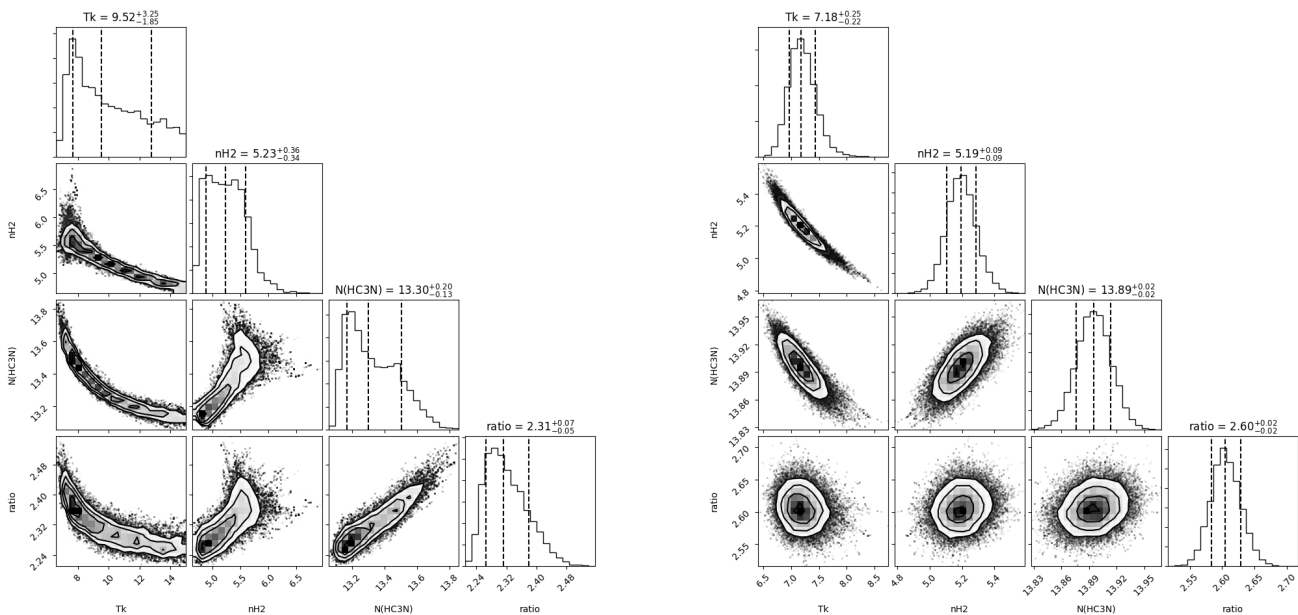


Figure 4. Same as Fig. 3 for the simultaneous analysis of the HC_3N and HC_3^{15}N lines summarized in Table 2. Left: rotational analysis (w24s5000rot). Right: hyperfine analysis (w24s5000hfs).

257 ± 54 was obtained (Taniguchi & Saito 2017), not consistent with our present determination. However, we note that the TMC1-CP measurement relies on the double isotopic ratio using ^{13}C isotopologues of HC_3N , and assumes a single excitation temperature. Nevertheless, the two ratios are not consistent. Because both cores are located within the solar neighbourhood, the elemental isotopic ratio of nitrogen should be identical, and different isotopic ratios in L1544 and TMC-1 CP thus indicate different dominant chemical formation pathways in both cores.

The isotopic ratio in HC_3N can also be compared to ratios derived for the other nitrogen bearing molecules in L1544, namely CN, HCN and N_2H^+ . In CN and HCN, the ratios were derived indirectly using the $^{13}\text{C}^{14}\text{N}/^{12}\text{C}^{15}\text{N}$ double isotopic ratios, leading to 500 ± 75 for CN and within 140 to 360 for HCN (Hily-Blant et al. 2013a,b).

is marginally thus suggest that HC_3N could sample the same pool of nitrogen atoms as CN, but a different one HCN and HC_3N could share a common nitrogen reservoir. In N_2H^+ towards L1544, the ratio is 1000 ± 200 , which is also the largest ratio found in any species towards prestellar cores (Hily-Blant et al. 2017). The ratios in N_2H^+ and HC_3N are therefore significantly different, at the 3σ level, indicating that they either sample different pools of nitrogen atoms, or that so-far unknown fractionation reactions are unevenly partitioning ^{14}N and ^{15}N among these two species.

HC_3N depletion was observed towards the L1498 prestellar core (Tafalla et al. 2006). However, the present analysis points towards dense and cold physical conditions which may not be compatible with the depletion scenario. Indeed, the central density towards L1498 is $\approx 10^5 \text{ cm}^{-3}$, which is of the order of the density traced by HC_3N as the present analysis suggests. Therefore, one might expect significant depletion of HC_3N as such densities in L1544 as well. Nevertheless, the dynamical state of L1544 is likely more evolved

towards collapse than for L1498, as evidenced by the two orders of magnitude lower central density in L1498. Definitive conclusion require maps of the HC_3N emission towards L1544 and radiative transfer calculations taking into account the density profile of the source (e.g Daniel et al. 2013).

In turn this indicates that some fractionation process must be at work in the cold and dense gas of prestellar cores. Whether HC_3N inherits the fractionation from a parent molecule or not can only be elucidated by an analysis for the formation pathways of HC_3N (see below). In the inheritance scenario, our result would contrast with the latest chemical model predictions Roueff et al. (2015) in which the dominant nitrogen fractionation routes were found to have activation barriers hence being inefficient at low kinetic temperature. However, other chemical models (Terzieva & Herbst 2000; Charnley & Rodgers 2002; Hily-Blant et al. 2013b) do predict fractionation effects in cold cores.

In the following, we examine into further details the different formation pathways of HC_3N , in the light of the present ratio and recent measurements using ^{13}C and ^{15}N isotopologues.

4.2 Uncertainties

Obtaining reliable and as small as possible uncertainties on column density ratios is certainly one of the main challenge in remote isotopic ratio measurements such as the one presented here.

Although the statistical uncertainties on the observed HC_3N integrated intensities are extremely small (Table 1), they hardly reflect the total uncertainty which must take into account the influence of the weather, pointing, focus, and chopper wheel calibration method. At the IRAM-30m telescope, the overall calibration uncertainty is generally taken to be 5% to 10%. Given the fact that all lines in

Table 4. Model predictions for the most probable solutions from the rotational and hyperfine (fluxes and flux ratios) analysis.

Species	Transition [§]	Observations [†]		w24s5000rot [‡]		w24s5000hfs	
		W	σ	\bar{W}	$ \bar{W} - W /\sigma$	\bar{W}	$ \bar{W} - W /\sigma$
HC ₃ N	8-7	37.9	1.9	17.8	-10.6	46.4	4.5
		2053.0	102.7	1971.3	-0.8	1982.4	-0.7
		50.3	2.7	17.8	-12.1	46.9	-1.3
	9-8	15.9	2.2	10.9	-2.3	25.2	4.2
		1633.0	81.7	1662.4	0.4	1756.9	1.5
		21.2	2.2	10.9	-4.7	25.5	2.0
	10-9	16.4	0.8	6.2	-12.5	12.3	-5.0
		1404.0	70.2	1295.9	-1.5	1474.3	1.0
		16.3	0.8	6.2	-12.4	12.4	-4.7
	11-10	6.4	0.7	3.2	-4.5	5.4	-1.4
		956.2	47.8	915.6	-0.8	1091.6	2.8
		10.3	0.8	3.2	-9.0	5.5	-6.2
HC ₃ ¹⁵ N	12-11	626.1	31.3	571.9	-1.7	670.7	1.4
	9-8	14.1	2.1	12.4	-0.8	14.8	0.4
	10-9	9.0	0.7	8.8	-0.3	9.1	0.1
	11-10	<7	1.4	5.8	3.7	5.0	3.2
	12-11	<5	1.0	3.4	1.0	2.5	0.0
	13-12	<22	4.3	1.8	-0.8	1.1	-1.0

[§] Hyperfine transitions of HC₃N are those of Table A1, starting with the main hf group, followed by the other two hf lines, sorted by increasing frequency.

[†] The adopted uncertainties are at least 5% of the flux. Upper limits are at 5σ . All integrated intensities are in mK kms⁻¹.

[‡] \bar{W} is the predicted flux.

our survey were observed in a consistent way and over a relatively short period of time, we adopt a lower limit of 5% on the flux. Our conservative approach differs from that of other authors who use the statistical uncertainties (Araki et al. 2016). Moreover, in their study, these authors use three lines obtained with different telescopes (GBT and NRO) to determine the excitation temperature under the SET approximation. Strictly speaking, the uncertainty on the derived excitation temperature should be propagated into the column densities and column density ratios. As such, the 5–10% calibration accuracy would certainly dominate the final uncertainty on the isotopic ratio. In fact, the excitation temperatures of the three ¹³C isotopologues are only consistent at the 20% level (their Table 2). **ALEX: est-ce que tu peux relire leur article, parce que c'est leur methode est difficile a suivre...?**

Although our conclusions would not be affected by such a choice, uncertainties are crucially important when the isotopic ratios are used to infer the existence of fractionated reservoirs. We thus adopted a conservative value of 5% for the calibration uncertainty at 1σ .

In addition to the flux calibration, the analysis method also carries its own sources of uncertainties. The single excitation temperature (SET) assumption⁴, allows to compute column densities from single lines (Hily-Blant et al. 2013a; Araki et al. 2016; Taniguchi & Saito 2017). If the uncertainty associated to the assumed value of the excitation temperature can be quantified—and is actually generally small when

dealing with column density ratios, the uncertainty associated to the SET assumption itself is much more difficult to estimate.

4.3 Formation of HC₃N

The chemistry of HC₃N in dense prestellar cores is still a matter of debate although it has been studied in great details especially using carbon isotopic ratios. In particular, isotopic anomalies were observed for HC₃N in the Taurus Molecular Cloud-1 (TMC-1) starless core towards the so-called Cyanopolyne Peak (CP) (Takano et al. 1998). The column densities of H¹³CCCN, HC¹³CCN, and HCC¹³CN follow the ratios 1:0:1.0:1.4, respectively, which was interpreted as a result of the production pathway of HC₃N rather than isotope exchange reactions. The latter are unlikely because the zero-point energy differences between the three carbon isotopologues would not produce predict H¹³CCCN/HC¹³CCN close to 1. Instead, HC₃N is thought to form primarily from a parent molecule having two equivalent carbon atoms in order to explain [H¹³CCCN]=[HC¹³CCN]. Currently, three potential formation routes are considered, through CN, HCN, and HNC (for a review, see e.g. Taniguchi et al. 2016).

4.3.1 The HC₃NH⁺ route

In this route, the two equivalent carbons are provided by C₂H₂⁺:



This reaction is known to be rapid at room temperature with a rate coefficient $k_3 = 3.78 \times 10^{-11} \text{ cm}^3 \text{ s}^{-1}$ (Iraqi et al.

⁴ This assumption is usually called the LTE assumption, although it only states that a single excitation temperature describes the level population of a given molecule or of a set of molecules. The SET is thus a weaker, and sufficient, instance of the LTE assumption.

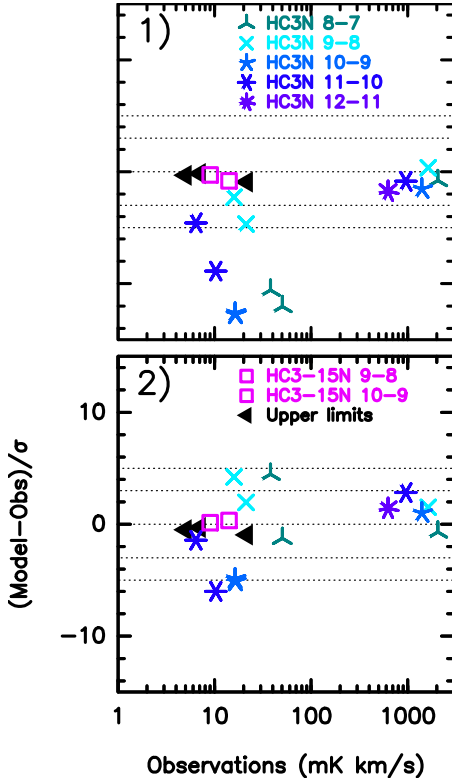


Figure 5. Distance of the best solutions from the models in units of the 1σ uncertainty as obtained in the two complete analysis reported in Tables 2 and 4 (panels 1 and 2 for w24s5000rot and w24s5000hfs resp.). In each panel, the fluxes of the hyperfine components are given for all HC_3N lines except the 12-11 transition for which only the main hf line was detected (see Table 1). The filled triangles indicate the 5σ upper limits on the $HC_3^{15}N$ rotational transitions.

1990). This reaction is followed by the dissociative recombination (DR) between HC_3NH^+ and electrons. The rate coefficient and the branching ratios of this DR process have not been measured but quantum calculations indicate that all isomers of HC_3N , namely HNC_3 , $HCCNC$ and $HCNCC$ can be produced at low temperature. If reaction (2) is a major pathway to produce HC_3N , then HC_3N and HNC_3 are expected to have similar abundances since both products result from a direct hydrogen elimination of the parent ion HC_3NH^+ (Osamura et al. 1999). The observation of HC_3N and its isomers $HCCNC$ and HNC_3 , however, indicates that the three species have very different abundances in the cold conditions of TMC-1 (Ohishi & Kaifu 1998). Assuming that HC_3N and HNC_3 have a similar reactivity, this suggests that reaction (2) is not a major pathway to HC_3N .

4.3.2 The CN route

Here, the two equivalent carbons come from C_2H_2 :



This reaction is also rapid at room temperature with a rate coefficient $k_1 = 2.5 \times 10^{-10} \text{ cm}^3 \text{ s}^{-1}$ (Sims et al. 1993). Reaction (3) has even been found to accelerate down to 25 K (Sims et al. 1993). The current consensus is that HC_3N is mainly produced through the neutral-neutral reaction (3).

In addition the larger abundance of $HCC^{13}CN$ relative to $H^{13}CCCN$ and $HC^{13}CCN$ can be easily explained by different $^{12}C/^{13}C$ ratios in C_2H_2 and CN , since the triple $-CN$ bond is conserved in reaction (3). This scenario has been recently supported by observations of $H^{13}CCCN$, $HC^{13}CCN$, $HCC^{13}CN$, and HC_3N towards the L1527 protostar, which were found to follow the ratios 1.00:1.01:1.35:86.4, respectively (Araki et al. 2016). This corresponds to a $^{12}C/^{13}C$ ratio of 64 for $[HCC^{13}CN]/[HC_3N]$, in good agreement with the local ISM elemental $^{12}C/^{13}C$ ratio of 68 (Milam et al. 2005). This in turn seems to indicate that CN is not fractionated in carbon, which would support either early-time chemistry in typical core condition or late time chemistry in denser ($n_H = 10^5 \text{ cm}^{-3}$) gas (Roueff et al. 2015). On the other hand, the significantly higher $^{12}C/^{13}C$ ratios in $H^{13}CCCN$ and $HC^{13}CCN$ of ≈ 86 is consistent with ^{13}C depletion in C_2H_2 , as observed in other carbon-chain molecules (see Roueff et al. 2015; Araki et al. 2016, and references therein).

4.3.3 The HNC route

In this route, the two equivalent carbons are provided by C_2H :



This reaction proceeds at a rate $k = XXX$ **ALEX: REVIEW**. In this reaction, the H atom is removed from HNC , and we thus expect $H^{13}CCCN/HC^{13}CCN = C^{13}CH/^{13}CCH$, at odds with the observations which find $C^{13}CH/^{13}CCH$ abundance ratios significantly larger than 1 (Sakai et al. 2010). The origin of the departure of $C^{13}CH/^{13}CCH$ from unity is likely associated to the neutral-neutral fractionation reaction $^{13}CCH + H \longrightarrow C^{13}CH + H + 8.1K$. Indeed, at a kinetic temperature of 15 K, this steady-state abundance ratio due to this reaction is $\exp(8.1/15) = 1.7$, which is in harmony with the observed ratio of 1.6 ± 0.1 . At the lower temperature of TMC-1 (CP), where the steady-state ratio would be 2.2, chemical model calculations show that the $1.6 \pm 0.4(3\sigma)$ ratio can be obtained at earlier times, when carbon is still mostly neutral (Furuya et al. 2011). As a consequence of the different $H^{13}CCCN/HC^{13}CCN$ and $C^{13}CH/^{13}CCH$ ratios, the HNC route was discarded (Taniguchi et al. 2016).

However, most recently, the $H^{13}CCCN/HC^{13}CCN$ abundance ratio was measured towards two cold prestellar cores, L1521B and L134N, with values of 0.98 ± 0.14 and 1.5 ± 0.2 (1σ uncertainties), respectively, suggesting different formation pathways for HC_3N in these two sources (Taniguchi et al. 2017). In particular, the ratio in L134N could indicate that HC_3N is primarily formed from C_2H , while C_2H_2 would be the main precursor in L1521B. In fact, the $H^{13}CCCN/HC^{13}CCN$ abundance ratio in L134N closely matches the observed ratio in TMC1 (Sakai et al. 2010).

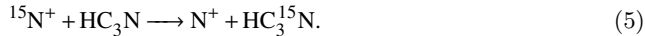
The competition between the CN and HNC routes was interpreted as reflecting different CN/HNC abundance ratios in the two prestellar cores. Observations of the $C^{13}CH/^{13}CCH$ in both sources should bring valuable informations.

4.4 Consequences on the nitrogen isotopic ratio of HC₃N

Which of the CN or HNC routes dominates has consequences for the nitrogen isotopic ratio in HC₃N which would be inherited from CN or HNC.

Araki et al. (2016) also determined a HCC¹³CN/HC₃¹⁵N ratio of 5.26±0.19, resulting in a [HC₃N]/[HC₃¹⁵N] ratio of 338±12. This value is again close to the elemental ¹⁴N/¹⁵N ratio in the local ISM (Adande & Ziurys 2012; Hily-Blant et al. 2017). To our knowledge, however, the ¹²C/¹³C and ¹⁴N/¹⁵N ratios of CN in L1527 are unknown so that a firm conclusion regarding the link between CN and HC₃N cannot be established in this source.

The present determination of the [HC₃N]/[HC₃¹⁵N] ratio in L1544 brings a new piece of the HC₃N puzzle. The [CN]/[C¹⁵N] ratio in this source was determined by Hily-Blant et al. (2013b) as 510±70, assuming a [CN]/[¹³CN] ratio of 68. The ¹⁴N/¹⁵N ratio in HC₃N is thus a factor of 2-3 lower than [CN]/[C¹⁵N] in L1544. This contradicts a production of HC₃N *via* reaction (3) except if the [CN]/[¹³CN] ratio in L1544 is much lower than 68⁵. This possibility seems unlikely as it would translate in HC₃N:H¹³CCCN and HC₃N:HC¹³CCN isotopic ratios lower than the elemental value. Another possibility is that isotope exchange reactions occur after the formation of HC₃N, e.g. through



To our knowledge, however, this reaction has not been studied so far. On the other hand, the [HCN]/[HC¹⁵N] ratio in the central position of L1544 was found to be ~257, again assuming a value of 68 for the [HCN]/[H¹³CN] ratio (Hily-Blant et al. 2013a). This value is close to the present determination of the ¹⁴N/¹⁵N ratio in HC₃N which would *a priori* favor reaction (2) for the production of HC₃N in L1544. The determination of the ¹⁴N/¹⁵N ratio in HC₃NH⁺ would provide a crucial test of this scenario. We note that the main isotopologue HC₃NH⁺ has been observed recently in L1544 (Quénard et al. 2017). The detection of HC₃N isomers in L1544, in particular HNC₃, would be also useful, especially if the complete branching ratios for the DR of HC₃NH⁺ could be determined in the laboratory.

In summary, from the previous studies and the present result, both CN and HCN can be the parent molecules of HC₃N through reactions (3) and (2), respectively. More observations and laboratory works are necessary before we can possibly exclude one of the two chemical pathways. It will be particularly important to properly determine the ¹²C/¹³C ratio in CN and HCN (in order to avoid the double isotope method) with the best possible spatial resolution.

ACKNOWLEDGEMENTS

We wish to thank Martin Legrand and Luc Lefort who participated into the multiline analysis and the implementation of the MCMC/Radex code, during their internship in

⁵ We note that ¹²C/¹³C ratios as low as 20 have been measured, e.g. in HNC toward the Barnard 1 molecular cloud (Daniel et al. 2013).

our group in May-July 2017. PHB acknowledges the *Institut Universitaire de France* for financial support.

References

- Adande G. R., Ziurys L. M., 2012, *ApJ*, 744-758, 194
 Altwegg K., et al., 2015, *Science*, 347
 Araki M., Takano S., Sakai N., Yamamoto S., Oyama T., Kuze N., Tsukiyama K., 2016, *ApJ*, 833, 291
 Bockelée-Morvan D., et al., 2015, *Space Sci Rev*, 197, 47
 Bonal L., Huss G. R., Krot A. N., Nagashima K., Ishii H. A., Bradley J. P., 2010, *Geochim. Cosmochim. Ac.*, 74, 6590
 Calmonte U., et al., 2016, *MNRAS*, 462, S253
 Carter M., et al., 2012, *A&A*, 538, A89
 Charney S. B., Rodgers S. D., 2002, *ApJL*, 569, L133
 Daniel F., et al., 2013, *A&A*, 560, A3
 Faure A., Lique F., Wiesenfeld L., 2016, *MNRAS*, 460, 2103
 Füre E., Marty B., 2015, *Nature Geosc.*, 8, 515
 Furuya K., Aikawa Y., Sakai N., Yamamoto S., 2011, *ApJ*, 731, 38
 Gerin M., Marcelino N., Biver N., Roueff E., Coudert L. H., Elkeurti M., Lis D. C., Bockelée-Morvan D., 2009, *A&A*, 498, L9
 Guzmán V. V., Öberg K. I., Huang J., Loomis R., Qi C., 2017, *ApJ*, 836, 30
 Heays A. N., Visser R., Gredel R., Ubachs W., Lewis B. R., Gibson S. T., van Dishoeck E. F., 2014, *A&A*, 562, A61
 Hily-Blant P., Walmsley M., Pineau des Forêts G., Flower D., 2010, *A&A*, 513, A41
 Hily-Blant P., Bonal L., Faure A., Quirico E., 2013a, *Icarus*, 223, 582
 Hily-Blant P., Pineau des Forêts G., Faure A., Le Gal R., Padovani M., 2013b, *A&A*, 557, A65
 Hily-Blant P., Magalhaes V., Kastner J., Faure A., Forveille T., Qi C., 2017, *A&A*, 603, L6
 Iraqi M., Petrank A., Peres M., Lifshitz C., 1990, *International Journal of Mass Spectrometry and Ion Processes*, 100, 679
 Jehin E., Manfroid J., Hutsemékers D., Arpigny C., Zucconi J.-M., 2009, *Earth Moon and Planets*, 105, 167
 Marty B., Chaussidon M., Wiens R. C., Jurewicz A. J. G., Burnett D. S., 2011, *Science*, 332, 1533
 Marty B., et al., 2017, *Science*, 356, 1069
 Milam S. N., Savage C., Brewster M. A., Ziurys L. M., Wyckoff S., 2005, *ApJ*, 634, 1126
 Ohishi M., Kaifu N., 1998, *Faraday Discussions*, 109, 205
 Osamura Y., Fukuzawa K., Terzieva R., Herbst E., 1999, *ApJ*, 519, 697
 Quénard D., Vastel C., Ceccarelli C., Hily-Blant P., Lefloch B., Bachiller R., 2017, preprint, ([arXiv:1706.00647](https://arxiv.org/abs/1706.00647))
 Roueff E., Loison J. C., Hickson K. M., 2015, *A&A*, 576, A99
 Rubin M., et al., 2015, *Science*, 348, 232
 Sakai N., Yamamoto S., 2013, *Chemical Reviews*, 113, 8981
 Sakai N., Saruwatari O., Sakai T., Takano S., Yamamoto S., 2010, *A&A*, 512, A31
 Shinnaka Y., Kawakita H., Jehin E., Decock A., Hutsemékers D., Manfroid J., Arai A., 2016, *MNRAS*, 462, S195
 Sims I. R., Queffelec J.-L., Travers D., Rowe B. R., Herbert L. B., Karthäuser J., Smith I. W. M., 1993, *Chemical Physics Letters*, 211, 461
 Tafalla M., Santiago-García J., Myers P. C., Caselli P., Walmsley C. M., Crapsi A., 2006, *A&A*, 455, 577
 Takano S., et al., 1998, *A&A*, 329, 1156
 Taniguchi K., Saito M., 2017, preprint, ([arXiv:1706.08662](https://arxiv.org/abs/1706.08662))
 Taniguchi K., Saito M., Ozeki H., 2016, *ApJ*, 830, 106
 Taniguchi K., Ozeki H., Saito M., 2017, *ApJ*, 846, 46
 Terzieva R., Herbst E., 2000, *MNRAS*, 317, 563

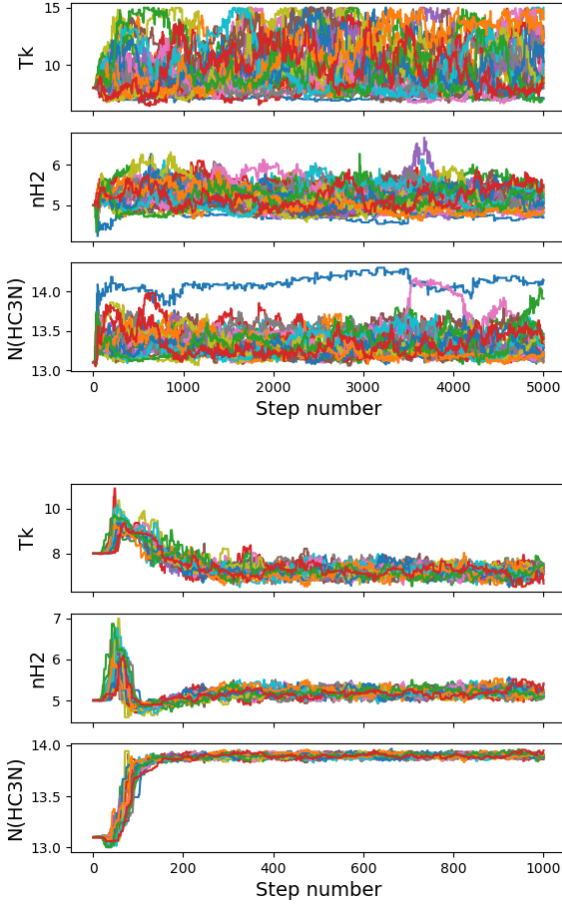


Figure A1. The 24 walkers along their 5000 and 1000 steps evolution associated with the rotational and hyperfine analysis (resp.) of the HC_3N lines (see Fig. 3 and Table 2).

Vastel C., Ceccarelli C., Lefloch B., Bachiller R., 2014, *ApJL*, 795, L2
 Watson W. D., Anicich V. G., Huntress W. T., 1976, *ApJL*, 205, L165
 van Dishoeck E. F., Bergin E. A., Lis D. C., Lunine J. I., 2014, *Protostars & Planets VI*, pp 835–858
 van der Tak F. F. S., Black J. H., Schöier F. L., Jansen D. J., van Dishoeck E. F., 2007, *A&A*, 468, 627

APPENDIX A: MCMC CALCULATIONS

A1 Physical conditions

A2 Best model predictions

A3 Hyperfine fitting of HC_3N

This paper has been typeset from a $\text{\TeX}/\text{\LaTeX}$ file prepared by the author.

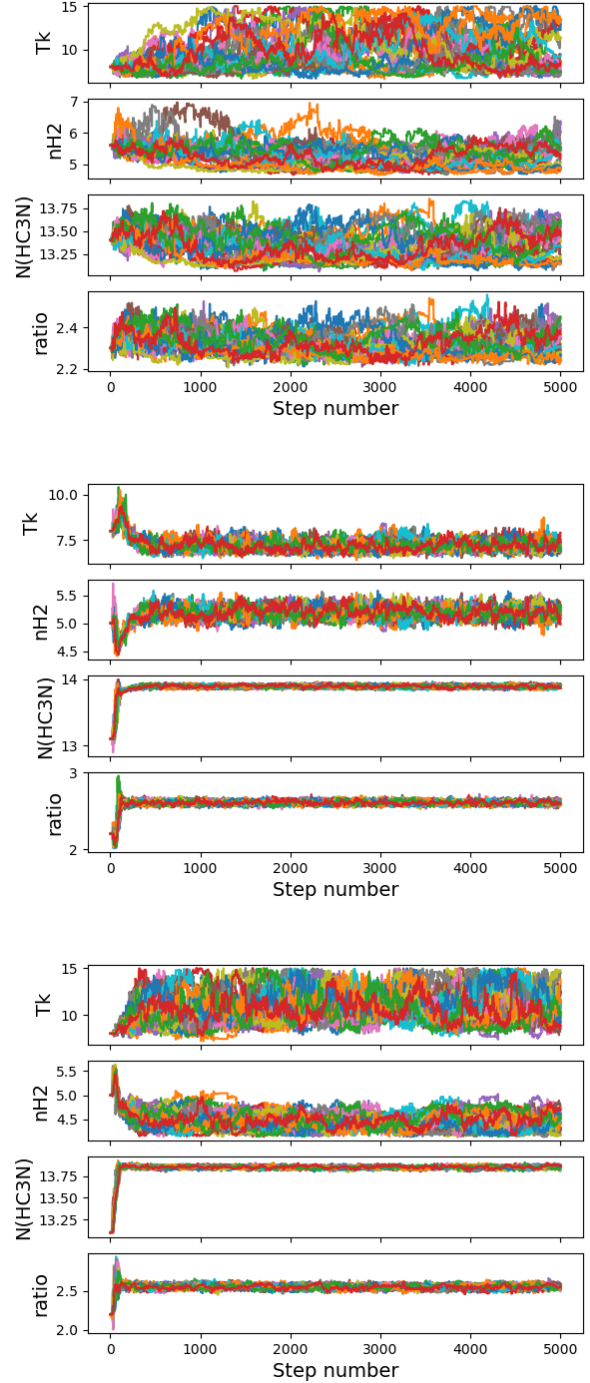


Figure A2. Markov chains of the runs used to measure the nitrogen isotopic ratio of HC_3N . From top to bottom: w24s5000rot, w24s5000hfs, and w24s5000ratio. For the sake of clarity, the legends do not specify that the density and column density are on a log10 scale. Note that the prior probabilities are uniform for each parameter, within 6 to 15 for the temperature, 10^4 to 10^{12} cm^{-3} for the H_2 density, and 10^{12} to 10^{15} for the column density of HC_3N .

Table A1. Theoretical relative intensities of the various hf components of each multiplet.

Frequency MHz	A_{ul}^\dagger s ⁻¹	R.I. [‡] %
72782.291100	1.421E-05	0.52
72783.805200	7.881E-04	–
72783.822800	8.952E-04	99.02
72783.833700	1.016E-03	–
72785.542800	1.421E-05	0.46
81879.924900	1.579E-05	0.41
81881.453900	1.128E-03	–
81881.467500	1.263E-03	99.22
81881.476600	1.414E-03	–
81883.174000	1.579E-05	0.37
90977.443100	1.730E-05	0.33
90978.983800	1.548E-03	–
90978.994800	1.713E-03	99.37
90979.002400	1.895E-03	–
90980.690300	1.730E-05	0.30
100074.832100	1.874E-05	0.27
100076.382400	2.052E-03	–
100076.391400	2.249E-03	99.47
100076.398000	2.465E-03	–
100078.077800	1.874E-05	0.25
109172.078500	2.011E-05	0.23
109173.636700	2.644E-03	–
109173.644400	2.875E-03	99.55
109173.650100	3.127E-03	–
109175.323200	2.011E-05	0.21

† Einstein coefficient for spontaneous decay.

‡ Relative intensities normalized to a sum of one. For the sake of clarity, one hf transition within each multiplet was omitted for having a negligible relative intensity.

BIBLIOGRAPHY

- Adande, G. R. and L. M. Ziurys (2012). « Millimeter-wave Observations of CN and HNC and Their ^{15}N Isotopologues: A New Evaluation of the $^{14}\text{N}/^{15}\text{N}$ Ratio across the Galaxy. » In: *ApJ* 744, 194, p. 194. DOI: [10.1088/0004-637X/744/2/194](https://doi.org/10.1088/0004-637X/744/2/194).
- Agency, European Space. *The Herschel Science Archive*. URL: <http://archives.esac.esa.int/hsa/whsa/>.
- Ahrens, V., F. Lewen, S. Takano, G. Winnewisser, Š. Urban, A. A. Negirev, and A. N. Koroliev (2002). « Sub-Doppler Saturation Spectroscopy of HCN up to 1 THz and Detection of $J = 3 \rightarrow 2$ ($4 \rightarrow 3$) Emission from TMC1. » In: *Zeitschrift Naturforschung Teil A* 57, pp. 669–681. DOI: [10.1515/zna-2002-0806](https://doi.org/10.1515/zna-2002-0806).
- Aikawa, Y. et al. (2012). « AKARI observations of ice absorption bands towards edge-on young stellar objects. » In: *A&A* 538, A57, A57. DOI: [10.1051/0004-6361/201015999](https://doi.org/10.1051/0004-6361/201015999).
- Alexander, C. M. O. '., M. Fogel, H. Yabuta, and G. D. Cody (2007). « The origin and evolution of chondrites recorded in the elemental and isotopic compositions of their macromolecular organic matter. » In: *Geochim. Cosmochim. Acta* 71, pp. 4380–4403. DOI: [10.1016/j.gca.2007.06.052](https://doi.org/10.1016/j.gca.2007.06.052).
- Alexander, C. M. O. '., R. Bowden, M. L. Fogel, K. T. Howard, C. D. K. Herd, and L. R. Nittler (2012). « The Provenances of Asteroids, and Their Contributions to the Volatile Inventories of the Terrestrial Planets. » In: *Science* 337, p. 721. DOI: [10.1126/science.1223474](https://doi.org/10.1126/science.1223474).
- Alpher, R. A., H. Bethe, and G. Gamow (1948). « The Origin of Chemical Elements. » In: *Physical Review* 73, pp. 803–804. DOI: [10.1103/PhysRev.73.803](https://doi.org/10.1103/PhysRev.73.803).
- André, P. et al. (2010). « From filamentary clouds to prestellar cores to the stellar IMF: Initial highlights from the Herschel Gould Belt Survey. » In: *A&A* 518, L102, p. L102. DOI: [10.1051/0004-6361/201014666](https://doi.org/10.1051/0004-6361/201014666). arXiv: [1005.2618](https://arxiv.org/abs/1005.2618).
- Araki, M., S. Takano, N. Sakai, S. Yamamoto, T. Oyama, N. Kuze, and K. Tsukiyama (2016). « Precise Observations of the $^{12}\text{C}/^{13}\text{C}$ Ratios of HC_3N in the Low-mass Star-forming Region L1527. » In: *ApJ* 833, 291, p. 291. DOI: [10.3847/1538-4357/833/2/291](https://doi.org/10.3847/1538-4357/833/2/291). arXiv: [1610.02793](https://arxiv.org/abs/1610.02793) [astro-ph.SR].
- Asplund, M., N. Grevesse, A. J. Sauval, and P. Scott (2009). « The Chemical Composition of the Sun. » In: *ARA&A* 47, pp. 481–522. DOI: [10.1146/annurev.astro.46.060407.145222](https://doi.org/10.1146/annurev.astro.46.060407.145222). arXiv: [0909.0948](https://arxiv.org/abs/0909.0948) [astro-ph.SR].

- Barone, V., C. Latouche, D. Skouteris, F. Vazart, N. Balucani, C. Ceccarelli, and B. Lefloch (2015). « Gas-phase formation of the prebiotic molecule formamide: insights from new quantum computations. » In: *MNRAS* 453, pp. L31–L35. DOI: [10.1093/mnrasl/slv094](https://doi.org/10.1093/mnrasl/slv094). arXiv: [1507.03741](https://arxiv.org/abs/1507.03741).
- Belloche, A., B. Parise, F. Schuller, P. André, S. Bontemps, and K. M. Menten (2011). « Will the starless cores in Chamaeleon I and III turn prestellar? » In: *A&A* 535, A2, A2. DOI: [10.1051/0004-6361/201117276](https://doi.org/10.1051/0004-6361/201117276). arXiv: [1106.5064](https://arxiv.org/abs/1106.5064).
- Ben Abdallah, D., F. Najjar, N. Jaidane, F. Dumouchel, and F. Lique (2012). « Hyperfine excitation of HCN by H₂ at low temperature. » In: *MNRAS* 419, pp. 2441–2447. DOI: [10.1111/j.1365-2966.2011.19896.x](https://doi.org/10.1111/j.1365-2966.2011.19896.x).
- Bergin, E. A. (2014). « Astrobiology: An astronomer's perspective. » In: *American Institute of Physics Conference Series*. Vol. 1638. American Institute of Physics Conference Series, pp. 5–34. DOI: [10.1063/1.4904143](https://doi.org/10.1063/1.4904143). arXiv: [1309.4729](https://arxiv.org/abs/1309.4729) [astro-ph.EP].
- Best image of Alpha Centauri A and B* (2016). URL: <http://www.spacetelescope.org/images/potw1635a/>.
- Bethe, H. A. (1939). « Energy Production in Stars. » In: *Physical Review* 55, pp. 434–456. DOI: [10.1103/PhysRev.55.434](https://doi.org/10.1103/PhysRev.55.434).
- Bieler, A. et al. (2015). « Abundant molecular oxygen in the coma of comet 67P/Churyumov-Gerasimenko. » In: *Nature* 526, pp. 678–681. DOI: [10.1038/nature15707](https://doi.org/10.1038/nature15707).
- Bizzocchi, L., P. Caselli, E. Leonardo, and L. Dore (2013). « Detection of ¹⁵NNH⁺ in L1544: non-LTE modelling of dyazenilium hyperfine line emission and accurate ¹⁴N/¹⁵N values. » In: *A&A* 555, A109, A109. DOI: [10.1051/0004-6361/201321276](https://doi.org/10.1051/0004-6361/201321276). arXiv: [1306.0465](https://arxiv.org/abs/1306.0465) [astro-ph.SR].
- Bockelée-Morvan, D. et al. (1998). « Deuterated Water in Comet C/1996 B2 (Hyakutake) and Its Implications for the Origin of Comets. » In: *Icarus* 133, pp. 147–162. DOI: [10.1006/icar.1998.5916](https://doi.org/10.1006/icar.1998.5916).
- Bockelée-Morvan, D. et al. (2015). « Cometary Isotopic Measurements. » In: *Space Sci. Rev.* 197, pp. 47–83. DOI: [10.1007/s11214-015-0156-9](https://doi.org/10.1007/s11214-015-0156-9).
- Bok, B. J. and E. F. Reilly (1947). « Small Dark Nebulae. » In: *ApJ* 105, p. 255. DOI: [10.1086/144901](https://doi.org/10.1086/144901).
- Bonal, L., G. R. Huss, A. N. Krot, K. Nagashima, H. A. Ishii, and J. P. Bradley (2010). « Highly ¹⁵N-enriched chondritic clasts in the CB/CH-like meteorite Isheyev. » In: *Geochim. Cosmochim. Acta* 74, pp. 6590–6609. DOI: [10.1016/j.gca.2010.08.017](https://doi.org/10.1016/j.gca.2010.08.017).
- Boogert, A. C. A., P. A. Gerakines, and D. C. B. Whittet (2015). « Observations of the icy universe. » In: *ARA&A* 53, pp. 541–581. DOI: [10.1146/annurev-astro-082214-122348](https://doi.org/10.1146/annurev-astro-082214-122348). arXiv: [1501.05317](https://arxiv.org/abs/1501.05317).
- Bourke, T. L., A. R. Hyland, and G. Robinson (1995). « Studies of star formation in isolated small dark clouds - I. A catalogue of south-

- ern BOK globules: optical and IRAS properties. » In: *MNRAS* 276, pp. 1052–1066. DOI: [10.1093/mnras/276.4.1052](https://doi.org/10.1093/mnras/276.4.1052).
- Brünken, S. et al. (2014). « H_2D^+ observations give an age of at least one million years for a cloud core forming Sun-like stars. » In: *Nature* 516, pp. 219–221. DOI: [10.1038/nature13924](https://doi.org/10.1038/nature13924).
- Busemann, H., A. F. Young, C. M. O'D. Alexander, P. Hoppe, S. Mukhopadhyay, and L. R. Nittler (2006). « Interstellar Chemistry Recorded in Organic Matter from Primitive Meteorites. » In: *Science* 312, pp. 727–730. DOI: [10.1126/science.1123878](https://doi.org/10.1126/science.1123878).
- Caselli, P. et al. (2012). « First Detection of Water Vapor in a Pre-stellar Core. » In: *ApJ* 759, L37, p. L37. DOI: [10.1088/2041-8205/759/2/L37](https://doi.org/10.1088/2041-8205/759/2/L37). arXiv: [1208.5998](https://arxiv.org/abs/1208.5998) [astro-ph.GA].
- Cazaux, S., A. G. G. M. Tielens, C. Ceccarelli, A. Castets, V. Wakelam, E. Caux, B. Parise, and D. Teyssier (2003). « The Hot Core around the Low-mass Protostar IRAS 16293-2422: Scoundrels Rule! » In: *ApJ* 593, pp. L51–L55. DOI: [10.1086/378038](https://doi.org/10.1086/378038).
- Cernicharo, J., A. Castets, G. Duvert, and S. Guilloteau (1984). « Large-scale HCN hyperfine anomalies. » In: *A&A* 139, pp. L13–L15.
- Chacón-Tanarro, A., P. Caselli, L. Bizzocchi, J. E. Pineda, J. Harju, M. Spaans, and F.-X. Désert (2017). « Search for grain growth towards the center of L1544. » In: *ArXiv e-prints*. arXiv: [1707.00005](https://arxiv.org/abs/1707.00005).
- Chapillon, E. et al. (2012a). « Chemistry in Disks. VII. First Detection of HC_3N in Protoplanetary Disks. » In: *ApJ* 756, 58, p. 58. DOI: [10.1088/0004-637X/756/1/58](https://doi.org/10.1088/0004-637X/756/1/58). arXiv: [1207.2682](https://arxiv.org/abs/1207.2682) [astro-ph.SR].
- Chapillon, E., S. Guilloteau, A. Dutrey, V. Piétu, and M. Guélin (2012b). « Chemistry in disks. VI. CN and HCN in protoplanetary disks. » In: *A&A* 537, A60, A60. DOI: [10.1051/0004-6361/201116762](https://doi.org/10.1051/0004-6361/201116762). arXiv: [1109.5595](https://arxiv.org/abs/1109.5595).
- Clayton, D. (2003). *Handbook of Isotopes in the Cosmos*, p. 326.
- Cleeves, L. I., E. A. Bergin, C. M. O. ' . Alexander, F. Du, D. Graninger, K. I. Öberg, and T. J. Harries (2014). « The ancient heritage of water ice in the solar system. » In: *Science* 345, pp. 1590–1593. DOI: [10.1126/science.1258055](https://doi.org/10.1126/science.1258055). arXiv: [1409.7398](https://arxiv.org/abs/1409.7398) [astro-ph.SR].
- Coutens, A., C. Vastel, E. Caux, C. Ceccarelli, S. Bottinelli, L. Wiesenfeld, A. Faure, Y. Scribano, and C. Kahane (2012). « A study of deuterated water in the low-mass protostar IRAS 16293-2422. » In: *A&A* 539, A132, A132. DOI: [10.1051/0004-6361/201117627](https://doi.org/10.1051/0004-6361/201117627). arXiv: [1201.1785](https://arxiv.org/abs/1201.1785).
- Dahmen, G., T. L. Wilson, and F. Matteucci (1995). « The nitrogen isotope abundance in the galaxy. 1: The galactic disk gradient. » In: *A&A* 295, pp. 194–198.
- Daniel, F. and J. Cernicharo (2008). « Solving radiative transfer with line overlaps using Gauss-Seidel algorithms. » In: *A&A* 488, pp. 1237–1247. DOI: [10.1051/0004-6361:200810103](https://doi.org/10.1051/0004-6361:200810103). arXiv: [0807.1845](https://arxiv.org/abs/0807.1845).
- Daniel, F., M. Gérin, E. Roueff, J. Cernicharo, N. Marcelino, F. Lique, D. C. Lis, D. Teyssier, N. Biver, and D. Bockelée-Morvan (2013).

- « Nitrogen isotopic ratios in Barnard 1: a consistent study of the N_2H^+ , NH_3 , CN , HCN , and HNC isotopologues. » In: *A&A* 560, A3, A3. DOI: [10.1051/0004-6361/201321939](https://doi.org/10.1051/0004-6361/201321939). arXiv: [1309.5782](https://arxiv.org/abs/1309.5782).
- Daniel, F., C. Rist, A. Faure, E. Roueff, M. Gérin, D. C. Lis, P. Hily-Blant, A. Bacmann, and L. Wiesenfeld (2016). « Collisional excitation of doubly and triply deuterated ammonia ND_2H and ND_3 by H_2 . » In: *MNRAS* 457, pp. 1535–1549. DOI: [10.1093/mnras/stw084](https://doi.org/10.1093/mnras/stw084). arXiv: [1601.02386](https://arxiv.org/abs/1601.02386).
- Dartois, E., W.-F. Thi, T. R. Geballe, D. Deboffle, L. d'Hendecourt, and E. van Dishoeck (2003). « Revisiting the solid $\text{HDO}/\text{H}_2\text{O}$ abundances. » In: *A&A* 399, pp. 1009–1020. DOI: [10.1051/0004-6361:20021558](https://doi.org/10.1051/0004-6361:20021558).
- Denis-Alpizar, O., T. Stoecklin, P. Halvick, and M.-L. Dubernet (2013). « A four-dimensional potential energy surface for the He - HCN complex. » In: *ArXiv e-prints*. arXiv: [1305.5465](https://arxiv.org/abs/1305.5465) [[physics.chem-ph](https://arxiv.org/archive/physics)].
- Draine, B. T. (2011). *Physics of the Interstellar and Intergalactic Medium*.
- Ebenstein, W. L. and J. S. Muenter (1984). « Dipole moment and hyperfine properties of the ground state and the C-H excited vibrational state of HCN. » In: *J. Chem. Phys.* 80, pp. 3989–3991. DOI: [10.1063/1.447269](https://doi.org/10.1063/1.447269).
- Eberhardt, P., M. Reber, D. Krankowsky, and R. R. Hodges (1995). « The D/H and $^{18}\text{O}/^{16}\text{O}$ ratios in water from comet P/Halley. » In: *A&A* 302, p. 301.
- Eddington, A. S. (1920). « The Internal Constitution of the Stars. » In: *Nature* 106, pp. 14–20. DOI: [10.1038/106014a0](https://doi.org/10.1038/106014a0).
- Elst, E. W., O. Pizarro, C. Pollas, J. Ticha, M. Tichy, Z. Moravec, W. Offutt, and B. G. Marsden (1996). « Comet P/1996 N2 (Elst-Pizarro). » In: *IAU Circ.* 6456.
- Faure, A., M. Faure, P. Theulé, E. Quirico, and B. Schmitt (2015). « Hydrogen isotope exchanges between water and methanol in interstellar ices. » In: *A&A* 584, A98, A98. DOI: [10.1051/0004-6361/201526499](https://doi.org/10.1051/0004-6361/201526499). arXiv: [1511.00894](https://arxiv.org/abs/1511.00894) [[astro-ph.SR](https://arxiv.org/archive/astro-ph)].
- Favre, C., J. K. Jørgensen, D. Field, C. Brinch, S. E. Bisschop, T. L. Bourke, M. R. Hogerheijde, and W. W. F. Frieswijk (2014). « Dynamical Structure of the Inner 100 AU of the Deeply Embedded Protostar IRAS 16293-2422. » In: *ApJ* 790, 55, p. 55. DOI: [10.1088/0004-637X/790/1/55](https://doi.org/10.1088/0004-637X/790/1/55). arXiv: [1406.0709](https://arxiv.org/abs/1406.0709) [[astro-ph.SR](https://arxiv.org/archive/astro-ph)].
- Floss, C., F. J. Stadermann, J. P. Bradley, Z. R. Dai, S. Bajt, G. Graham, and A. S. Lea (2006). « Identification of isotopically primitive interplanetary dust particles: A NanoSIMS isotopic imaging study. » In: *Geochim. Cosmochim. Acta* 70, pp. 2371–2399. DOI: [10.1016/j.gca.2006.01.023](https://doi.org/10.1016/j.gca.2006.01.023).
- Foreman-Mackey, D., D. W. Hogg, D. Lang, and J. Goodman (2013). « emcee: The MCMC Hammer. » In: *PASP* 125, p. 306. DOI: [10.1086/670067](https://doi.org/10.1086/670067). arXiv: [1202.3665](https://arxiv.org/abs/1202.3665) [[astro-ph.IM](https://arxiv.org/archive/astro-ph)].

- Foreman-Mackey, Daniel (2016). « corner.py: Scatterplot matrices in Python. » In: *The Journal of Open Source Software* 24. DOI: [10.21105/joss.00024](https://doi.org/10.21105/joss.00024). URL: <http://dx.doi.org/10.5281/zenodo.45906>.
- Foster, P. N. and R. A. Chevalier (1993). « Gravitational Collapse of an Isothermal Sphere. » In: *ApJ* 416, p. 303. DOI: [10.1086/173236](https://doi.org/10.1086/173236).
- Fouchet, T., E. Lellouch, B. Bézard, T. Encrenaz, P. Drossart, H. Feuchtgruber, and T. de Graauw (2000). « ISO-SWS Observations of Jupiter: Measurement of the Ammonia Tropospheric Profile and of the $^{15}\text{N}/^{14}\text{N}$ Isotopic Ratio. » In: *Icarus* 143, pp. 223–243. DOI: [10.1006/icar.1999.6255](https://doi.org/10.1006/icar.1999.6255). eprint: [astro-ph/9911257](https://arxiv.org/abs/astro-ph/9911257).
- Foundation, Python Software. *Python Language Reference, version 2.7*. URL: <http://www.python.org>.
- Füri, E., M. Chaussidon, and B. Marty (2015). « Evidence for an early nitrogen isotopic evolution in the solar nebula from volatile analyses of a CAI from the CV3 chondrite NWA 8616. » In: *Geochim. Cosmochim. Acta* 153, pp. 183–201. DOI: [10.1016/j.gca.2015.01.004](https://doi.org/10.1016/j.gca.2015.01.004). *GILDAS software*. URL: <http://www.iram.fr/IRAMFR/GILDAS/>.
- Gerin, M., N. Marcelino, N. Biver, E. Roueff, L. H. Coudert, M. Elkeurti, D. C. Lis, and D. Bockelée-Morvan (2009). « Detection of $^{15}\text{NH}_2\text{D}$ in dense cores: a new tool for measuring the $^{14}\text{N}/^{15}\text{N}$ ratio in the cold ISM. » In: *A&A* 498, pp. L9–L12. DOI: [10.1051/0004-6361/200911759](https://doi.org/10.1051/0004-6361/200911759). arXiv: [0903.3155](https://arxiv.org/abs/0903.3155) [[astro-ph](https://arxiv.org/abs/astro-ph).GA].
- Gonzalez-Alfonso, E. and J. Cernicharo (1993). « HCN hyperfine anomalies in dark clouds. » In: *A&A* 279, pp. 506–520.
- Goodman, J. and J. Weare (2010). « Ensemble samplers with affine invariance. » In: *Communications in Applied Mathematics and Computational Science, Vol. 5, No. 1, p. 65-80, 2010* 5, pp. 65–80. DOI: [10.2140/camcos.2010.5.65](https://doi.org/10.2140/camcos.2010.5.65).
- Gottlieb, C. A., C. J. Lada, E. W. Gottlieb, A. E. Lilley, and M. M. Litvak (1975). « Observations of millimeter-wave HCN in four prototype clouds. » In: *ApJ* 202, pp. 655–672. DOI: [10.1086/154021](https://doi.org/10.1086/154021).
- Guilloteau, S. and A. Baudry (1981). « Thermal overlap effects and collision models - HCN. » In: *A&A* 97, pp. 213–217.
- Guzmán, V. V., K. I. Öberg, R. Loomis, and C. Qi (2015). « Cyanide Photochemistry and Nitrogen Fractionation in the MWC 480 Disk. » In: *ApJ* 814, 53, p. 53. DOI: [10.1088/0004-637X/814/1/53](https://doi.org/10.1088/0004-637X/814/1/53). arXiv: [1511.03313](https://arxiv.org/abs/1511.03313) [[astro-ph](https://arxiv.org/abs/astro-ph).SR].
- Guzmán, V. V., K. I. Öberg, J. Huang, R. Loomis, and C. Qi (2017). « Nitrogen Fractionation in Protoplanetary Disks from the $\text{H}^{13}\text{CN}/\text{HC}^{15}\text{N}$ Ratio. » In: *ApJ* 836, 30, p. 30. DOI: [10.3847/1538-4357/836/1/30](https://doi.org/10.3847/1538-4357/836/1/30). arXiv: [1701.07510](https://arxiv.org/abs/1701.07510).
- Henning, T. and D. Semenov (2013). « Chemistry in Protoplanetary Disks. » In: *Chemical Reviews* 113, pp. 9016–9042. DOI: [10.1021/cr400128p](https://doi.org/10.1021/cr400128p). arXiv: [1310.3151](https://arxiv.org/abs/1310.3151) [[astro-ph](https://arxiv.org/abs/astro-ph).GA].

- Herbst, E. and W. Klemperer (1973). « The Formation and Depletion of Molecules in Dense Interstellar Clouds. » In: *ApJ* 185, pp. 505–534. DOI: [10.1086/152436](https://doi.org/10.1086/152436).
- Herbst, E., J. G. Schubert, and P. R. Certain (1977). « The radiative association of CH₂/+/. » In: *ApJ* 213, pp. 696–704. DOI: [10.1086/155199](https://doi.org/10.1086/155199).
- Herbst, E., R. Terzieva, and D. Talbi (2000). « Calculations on the rates, mechanisms, and interstellar importance of the reactions between C and NH₂ and between N and CH₂. » In: *MNRAS* 311, pp. 869–876. DOI: [10.1046/j.1365-8711.2000.03103.x](https://doi.org/10.1046/j.1365-8711.2000.03103.x).
- Hernández Vera, M., F. Lique, F. Dumouchel, P. Hily-Blant, and A. Faure (2017). « The rotational excitation of the HCN and HNC molecules by H₂ revisited. » In: *MNRAS* 468, pp. 1084–1091. DOI: [10.1093/mnras/stx422](https://doi.org/10.1093/mnras/stx422).
- Hily-Blant, P. and E. Falgarone (2007). « Dissipative structures of diffuse molecular gas. II. The translucent environment of a dense core. » In: *A&A* 469, pp. 173–187. DOI: [10.1051/0004-6361:20054565](https://doi.org/10.1051/0004-6361:20054565).
- Hily-Blant, P., M. Walmsley, G. Pineau Des Forêts, and D. Flower (2010). « Nitrogen chemistry and depletion in starless cores. » In: *A&A* 513, A41, A41. DOI: [10.1051/0004-6361/200913200](https://doi.org/10.1051/0004-6361/200913200). arXiv: [1001.3930](https://arxiv.org/abs/1001.3930) [astro-ph.SR].
- Hily-Blant, P., L. Bonal, A. Faure, and E. Quirico (2013a). « The ¹⁵N-enrichment in dark clouds and Solar System objects. » In: *Icarus* 223, pp. 582–590. DOI: [10.1016/j.icarus.2012.12.015](https://doi.org/10.1016/j.icarus.2012.12.015). arXiv: [1302.6318](https://arxiv.org/abs/1302.6318) [astro-ph.GA].
- Hily-Blant, P., G. Pineau des Forêts, A. Faure, R. Le Gal, and M. Padovani (2013b). « The CN/C¹⁵N isotopic ratio towards dark clouds. » In: *A&A* 557, A65, A65. DOI: [10.1051/0004-6361/201321364](https://doi.org/10.1051/0004-6361/201321364). arXiv: [1308.4380](https://arxiv.org/abs/1308.4380) [astro-ph.GA].
- Hily-Blant, P., V. Magalhaes, J. Kastner, A. Faure, T. Forveille, and C. Qi (2017). « Direct evidence of multiple reservoirs of volatile nitrogen in a protosolar nebula analogue. » In: *A&A* 603, L6, p. L6. DOI: [10.1051/0004-6361/201730524](https://doi.org/10.1051/0004-6361/201730524). arXiv: [1706.10095](https://arxiv.org/abs/1706.10095).
- Hocuk, S., L. Szűcs, P. Caselli, S. Cazaux, M. Spaans, and G. B. Esplugues (2017). « Parameterizing the interstellar dust temperature. » In: *A&A* 604, A58, A58. DOI: [10.1051/0004-6361/201629944](https://doi.org/10.1051/0004-6361/201629944). arXiv: [1704.02763](https://arxiv.org/abs/1704.02763).
- Högbom, J. A. (1974). « Aperture Synthesis with a Non-Regular Distribution of Interferometer Baselines. » In: *A&AS* 15, p. 417.
- Hoyle, F. (1946). « The synthesis of the elements from hydrogen. » In: *MNRAS* 106, p. 343. DOI: [10.1093/mnras/106.5.343](https://doi.org/10.1093/mnras/106.5.343).
- Hoyle, F., W. A. Fowler, G. R. Burbidge, and E. M. Burbidge (1956). « Origin of the Elements in Stars. » In: *Science* 124, pp. 611–614. DOI: [10.1126/science.124.3223.611](https://doi.org/10.1126/science.124.3223.611).

- Hsieh, H. H. and D. Jewitt (2006). « Main Belt Comets: Ice in the Inner Solar System. » In: *AAS/Division for Planetary Sciences Meeting Abstracts #38*. Vol. 38. Bulletin of the American Astronomical Society, p. 492.
- Hunter, John D. (2007). « Matplotlib: A 2D Graphics Environment. » In: *Computing in Science & Engineering 9*, pp. 90–95.
- Ikeda, M., T. Hirota, and S. Yamamoto (2002). « The $\text{H}^{13}\text{CN}/\text{HC}^{15}\text{N}$ Abundance Ratio in Dense Cores: Possible Source-to-Source Variation of Isotope Abundances? » In: *ApJ* 575, pp. 250–256. DOI: [10.1086/341287](https://doi.org/10.1086/341287).
- Jehin, E., J. Manfroid, D. Hutsemékers, C. Arpigny, and J.-M. Zucconi (2009). « Isotopic Ratios in Comets: Status and Perspectives. » In: *Earth Moon and Planets* 105, pp. 167–180. DOI: [10.1007/s11038-009-9322-y](https://doi.org/10.1007/s11038-009-9322-y).
- Jørgensen, J. K. et al. (2016). « The ALMA Protostellar Interferometric Line Survey (PILS). First results from an unbiased submillimeter wavelength line survey of the Class 0 protostellar binary IRAS 16293-2422 with ALMA. » In: *A&A* 595, A117, A117. DOI: [10.1051/0004-6361/201628648](https://doi.org/10.1051/0004-6361/201628648). arXiv: [1607.08733](https://arxiv.org/abs/1607.08733) [astro-ph.SR].
- Juvela, M. et al. (2015). « Galactic cold cores. V. Dust opacity. » In: *A&A* 584, A93, A93. DOI: [10.1051/0004-6361/201423788](https://doi.org/10.1051/0004-6361/201423788). arXiv: [1501.07092](https://arxiv.org/abs/1501.07092).
- Kastner, J. H., P. Hily-Blant, D. R. Rodriguez, K. Punzi, and T. Forveille (2014). « Unbiased Millimeter-wave Line Surveys of TW Hya and V4046 Sgr: The Enhanced C_2H and CN Abundances of Evolved Protoplanetary Disks. » In: *ApJ* 793, 55, p. 55. DOI: [10.1088/0004-637X/793/1/55](https://doi.org/10.1088/0004-637X/793/1/55). arXiv: [1408.5918](https://arxiv.org/abs/1408.5918) [astro-ph.SR].
- Keto, E. and A. Burkert (2014). « From filaments to oscillating starless cores. » In: *MNRAS* 441, pp. 1468–1473. DOI: [10.1093/mnras/stu379](https://doi.org/10.1093/mnras/stu379). arXiv: [1402.3558](https://arxiv.org/abs/1402.3558).
- Keto, E. and P. Caselli (2010). « Dynamics and depletion in thermally supercritical starless cores. » In: *MNRAS* 402, pp. 1625–1634. DOI: [10.1111/j.1365-2966.2009.16033.x](https://doi.org/10.1111/j.1365-2966.2009.16033.x). arXiv: [0908.2400](https://arxiv.org/abs/0908.2400).
- Keto, E., P. Caselli, and J. Rawlings (2015). « The dynamics of collapsing cores and star formation. » In: *MNRAS* 446, pp. 3731–3740. DOI: [10.1093/mnras/stu2247](https://doi.org/10.1093/mnras/stu2247). arXiv: [1410.5889](https://arxiv.org/abs/1410.5889) [astro-ph.SR].
- Keto, E., G. B. Rybicki, E. A. Bergin, and R. Plume (2004). « Radiative Transfer and Starless Cores. » In: *ApJ* 613, pp. 355–373. DOI: [10.1086/422987](https://doi.org/10.1086/422987). eprint: [astro-ph/0407433](https://arxiv.org/abs/astro-ph/0407433).
- Knauth, D. C., B.-G. Andersson, S. R. McCandliss, and H. Warren Moos (2004). « The interstellar N_2 abundance towards HD 124314 from far-ultraviolet observations. » In: *Nature* 429, pp. 636–638. DOI: [10.1038/nature02614](https://doi.org/10.1038/nature02614).
- Kurtz, S., R. Cesaroni, E. Churchwell, P. Hofner, and C. M. Walmsley (2000). « Hot Molecular Cores and the Earliest Phases of High-Mass Star Formation. » In: *Protostars and Planets IV*, pp. 299–326.

- Kwan, J. and N. Z. Scoville (1974). « Radiative trapping and hyperfine structure: HCN (11). » In: *NASA STI/Recon Technical Report N 75*.
- Langer, W. D., R. W. Wilson, P. S. Henry, and M. Guelin (1978). « Observations of anomalous intensities in the lines of the HCO/plus/isotopes. » In: *ApJ* 225, pp. L139–L142. DOI: [10.1086/182812](https://doi.org/10.1086/182812).
- Larson, R. B. (1969). « Numerical calculations of the dynamics of collapsing proto-star. » In: *MNRAS* 145, p. 271. DOI: [10.1093/mnras/145.3.271](https://doi.org/10.1093/mnras/145.3.271).
- Lécuyer, Christophe, Philippe Gillet, and François Robert (1998). « The hydrogen isotope composition of seawater and the global water cycle. » In: *Chemical Geology* 145.3, pp. 249–261. ISSN: 0009-2541. DOI: [https://doi.org/10.1016/S0009-2541\(97\)00146-0](https://doi.org/10.1016/S0009-2541(97)00146-0). URL: <http://www.sciencedirect.com/science/article/pii/S0009254197001460>.
- Lee, C. W., P. C. Myers, and M. Tafalla (2001). « A Survey for Infall Motions toward Starless Cores. II. CS (2-1) and N₂H⁺ (1-0) Mapping Observations. » In: *ApJS* 136, pp. 703–734. DOI: [10.1086/322534](https://doi.org/10.1086/322534). eprint: [astro-ph/0105515](https://arxiv.org/abs/astro-ph/0105515).
- Lee, S. H., Y.-S. Park, J. Sohn, C. W. Lee, and H. M. Lee (2007). « Velocity Distribution of Collapsing Starless Cores, L694-2 and L1197. » In: *ApJ* 660, pp. 1326–1331. DOI: [10.1086/513682](https://doi.org/10.1086/513682). eprint: [astro-ph/0702330](https://arxiv.org/abs/astro-ph/0702330).
- Lesaffre, P., A. Belloche, J.-P. Chièze, and P. André (2005). « The dynamical influence of cooling in the envelope of prestellar and protostellar cores. » In: *A&A* 443, pp. 961–971. DOI: [10.1051/0004-6361:20053388](https://doi.org/10.1051/0004-6361:20053388). eprint: [astro-ph/0508161](https://arxiv.org/abs/astro-ph/0508161).
- Lewis, J. S. (1997). *Physics and chemistry of the solar system*.
- Li, X., A. N. Heays, R. Visser, W. Ubachs, B. R. Lewis, S. T. Gibson, and E. F. van Dishoeck (2013). « Photodissociation of interstellar N₂. » In: *A&A* 555, A14, A14. DOI: [10.1051/0004-6361/201220625](https://doi.org/10.1051/0004-6361/201220625). arXiv: [1305.1781](https://arxiv.org/abs/1305.1781).
- Lis, D. C., A. Wootten, M. Gerin, and E. Roueff (2010). « Nitrogen Isotopic Fractionation in Interstellar Ammonia. » In: *ApJ* 710, pp. L49–L52. DOI: [10.1088/2041-8205/710/1/L49](https://doi.org/10.1088/2041-8205/710/1/L49). arXiv: [1001.0744](https://arxiv.org/abs/1001.0744).
- Lissauer, J. J. and D. J. Stevenson (2007). « Formation of Giant Planets. » In: *Protostars and Planets V*, pp. 591–606.
- Liszt, H. and R. Lucas (2001). « Comparative chemistry of diffuse clouds. II. CN, HCN, HNC, CH₃CN & N₂H⁺. » In: *A&A* 370, pp. 576–585. DOI: [10.1051/0004-6361:20010260](https://doi.org/10.1051/0004-6361:20010260). eprint: [astro-ph/0103247](https://arxiv.org/abs/astro-ph/0103247).
- Loughnane, R. M., M. P. Redman, M. A. Thompson, N. Lo, B. O'Dwyer, and M. R. Cunningham (2012). « Observations of HCN hyperfine line anomalies towards low- and high-mass star-forming cores. » In: *MNRAS* 420, pp. 1367–1383. DOI: [10.1111/j.1365-2966.2011.20121.x](https://doi.org/10.1111/j.1365-2966.2011.20121.x). arXiv: [1305.1303](https://arxiv.org/abs/1305.1303) [[astro-ph](https://arxiv.org/abs/astro-ph).SR].

- Lucas, R. and H. Liszt (1998). « Interstellar isotope ratios from mm-wave molecular absorption spectra. » In: *A&A* 337, pp. 246–252.
- Mahaffy, P. R. (2016). « Organics, Isotopes, and Volatiles in Gale Crater Sedimentary Rocks. » In: *AGU Fall Meeting Abstracts*.
- Makiwa, G., D. A. Naylor, M. H. D. van der Wiel, D. Ward-Thompson, J. M. Kirk, S. Eyres, A. Abergel, and M. Köhler (2016). « Far-infrared/submillimetre properties of pre-stellar cores L1521E, L1521F and L1689B as revealed by the Herschel SPIRE instrument - I. Central positions. » In: *MNRAS* 458, pp. 2150–2160. DOI: [10.1093/mnras/stw428](https://doi.org/10.1093/mnras/stw428). arXiv: [1602.06927](https://arxiv.org/abs/1602.06927).
- Marti-Vidal, I. (2017). « APSYNSIM: An Interactive Tool To Learn Interferometry. » In: *ArXiv e-prints*. arXiv: [1706.00936](https://arxiv.org/abs/1706.00936) [[astro-ph.IM](#)].
- Marty, B. (2012). « The origins and concentrations of water, carbon, nitrogen and noble gases on Earth. » In: *Earth and Planetary Science Letters* 313, pp. 56–66. DOI: [10.1016/j.epsl.2011.10.040](https://doi.org/10.1016/j.epsl.2011.10.040). arXiv: [1405.6336](https://arxiv.org/abs/1405.6336) [[astro-ph.EP](#)].
- McKellar, A. (1940). « Evidence for the Molecular Origin of Some Hitherto Unidentified Interstellar Lines. » In: *PASP* 52, p. 187. DOI: [10.1086/125159](https://doi.org/10.1086/125159).
- Meibom, A., A. N. Krot, F. Robert, S. Mostefaoui, S. S. Russell, M. I. Petaev, and M. Gounelle (2007). « Nitrogen and Carbon Isotopic Composition of the Sun Inferred from a High-Temperature Solar Nebular Condensate. » In: *ApJ* 656, pp. L33–L36. DOI: [10.1086/512052](https://doi.org/10.1086/512052).
- Milam, S. N., C. Savage, M. A. Brewster, L. M. Ziurys, and S. Wyckoff (2005). « The $^{12}\text{C}/^{13}\text{C}$ Isotope Gradient Derived from Millimeter Transitions of CN: The Case for Galactic Chemical Evolution. » In: *ApJ* 634, pp. 1126–1132. DOI: [10.1086/497123](https://doi.org/10.1086/497123).
- Morbideilli, A., J. I. Lunine, D. P. O'Brien, S. N. Raymond, and K. J. Walsh (2012). « Building Terrestrial Planets. » In: *Annual Review of Earth and Planetary Sciences* 40, pp. 251–275. DOI: [10.1146/annurev-earth-042711-105319](https://doi.org/10.1146/annurev-earth-042711-105319). arXiv: [1208.4694](https://arxiv.org/abs/1208.4694) [[astro-ph.EP](#)].
- Mousis, O. et al. (2016a). « A Protosolar Nebula Origin for the Ices Agglomerated by Comet 67P/Churyumov-Gerasimenko. » In: *ApJ* 819, L33, p. L33. DOI: [10.3847/2041-8205/819/2/L33](https://doi.org/10.3847/2041-8205/819/2/L33). arXiv: [1604.08827](https://arxiv.org/abs/1604.08827) [[astro-ph.EP](#)].
- Mousis, O. et al. (2016b). « Origin of Molecular Oxygen in Comet 67P/Churyumov-Gerasimenko. » In: *ApJ* 823, L41, p. L41. DOI: [10.3847/2041-8205/823/2/L41](https://doi.org/10.3847/2041-8205/823/2/L41). arXiv: [1604.08831](https://arxiv.org/abs/1604.08831) [[astro-ph.EP](#)].
- Mousis, O., O. Ozgurel, J. I. Lunine, A. Luspay-Kuti, T. Ronnet, F. Pauzat, A. Markovits, and Y. Ellinger (2017). « Stability of Sulphur Dimers (S_2) in Cometary Ices. » In: *ApJ* 835, 134, p. 134. DOI: [10.3847/1538-4357/aa5279](https://doi.org/10.3847/1538-4357/aa5279). arXiv: [1612.01579](https://arxiv.org/abs/1612.01579) [[astro-ph.EP](#)].
- Mullins, A. M., R. M. Loughnane, M. P. Redman, B. Wiles, N. Guegan, J. Barrett, and E. R. Keto (2016). « Radiative transfer of HCN:

- interpreting observations of hyperfine anomalies. » In: *MNRAS* 459, pp. 2882–2892. DOI: [10.1093/mnras/stw835](https://doi.org/10.1093/mnras/stw835).
- Mumma, M. J. and S. B. Charnley (2011). « The Chemical Composition of Comets - Emerging Taxonomies and Natal Heritage. » In: *ARA&A* 49, pp. 471–524. DOI: [10.1146/annurev-astro-081309-130811](https://doi.org/10.1146/annurev-astro-081309-130811).
- Murillo, N. M., S. Bruderer, E. F. van Dishoeck, C. Walsh, D. Harsono, S.-P. Lai, and C. M. Fuchs (2015). « A low-mass protostar’s disk-envelope interface: disk-shadowing evidence from ALMA DCO⁺ observations of VLA1623. » In: *A&A* 579, A114, A114. DOI: [10.1051/0004-6361/201425118](https://doi.org/10.1051/0004-6361/201425118). arXiv: [1505.07761](https://arxiv.org/abs/1505.07761) [astro-ph.SR].
- Nieva, M.-F. and N. Przybilla (2012). « Present-day cosmic abundances. A comprehensive study of nearby early B-type stars and implications for stellar and Galactic evolution and interstellar dust models. » In: *A&A* 539, A143, A143. DOI: [10.1051/0004-6361/201118158](https://doi.org/10.1051/0004-6361/201118158). arXiv: [1203.5787](https://arxiv.org/abs/1203.5787) [astro-ph.SR].
- O’Brien, D. P., K. J. Walsh, A. Morbidelli, S. N. Raymond, A. M. Mandell, and J. C. Bond (2010). « Early Giant Planet Migration in the Solar System: Geochemical and Cosmochemical Implications for Terrestrial Planet Formation. » In: *AAS/Division for Planetary Sciences Meeting Abstracts #42*. Vol. 42. Bulletin of the American Astronomical Society, p. 948.
- Öberg, K. I., R. T. Garrod, E. F. van Dishoeck, and H. Linnartz (2009). « Formation rates of complex organics in UV irradiated CH₃OH-rich ices. I. Experiments. » In: *A&A* 504, pp. 891–913. DOI: [10.1051/0004-6361/200912559](https://doi.org/10.1051/0004-6361/200912559). arXiv: [0908.1169](https://arxiv.org/abs/0908.1169).
- Öberg, K. I., S. Bottinelli, J. K. Jørgensen, and E. F. van Dishoeck (2010). « A Cold Complex Chemistry Toward the Low-mass Protostar B1-b: Evidence for Complex Molecule Production in Ices. » In: *ApJ* 716, pp. 825–834. DOI: [10.1088/0004-637X/716/1/825](https://doi.org/10.1088/0004-637X/716/1/825). arXiv: [1005.0637](https://arxiv.org/abs/1005.0637).
- Öberg, K. I., V. V. Guzmán, K. Furuya, C. Qi, Y. Aikawa, S. M. Andrews, R. Loomis, and D. J. Wilner (2015). « The comet-like composition of a protoplanetary disk as revealed by complex cyanides. » In: *Nature* 520, pp. 198–201. DOI: [10.1038/nature14276](https://doi.org/10.1038/nature14276). arXiv: [1505.06347](https://arxiv.org/abs/1505.06347).
- Observatory, National Radio Astronomy. *The Common Astronomy Software Applications package*. URL: <https://casa.nrao.edu/index.shtml>.
- Olson, G. L., L. H. Auer, and J. R. Buchler (1986). « A rapidly convergent iterative solution of the non-LTE line radiation transfer problem. » In: *J. Quant. Spectr. Rad. Transf.* 35, pp. 431–442. DOI: [10.1016/0022-4073\(86\)90030-0](https://doi.org/10.1016/0022-4073(86)90030-0).
- Owen, T., P. R. Mahaffy, H. B. Niemann, S. Atreya, and M. Wong (2001). « Protosolar Nitrogen. » In: *ApJ* 553, pp. L77–L79. DOI: [10.1086/320501](https://doi.org/10.1086/320501).

- Padovani, M., C. M. Walmsley, M. Tafalla, P. Hily-Blant, and G. Pineau Des Forêts (2011). « Hydrogen cyanide and isocyanide in prestellar cores. » In: *A&A* 534, A77, A77. DOI: [10.1051/0004-6361/201117134](https://doi.org/10.1051/0004-6361/201117134). arXiv: [1108.5073](https://arxiv.org/abs/1108.5073).
- Persson, M. V., J. K. Jørgensen, and E. F. van Dishoeck (2012). « Subarcsecond resolution observations of warm water toward three deeply embedded low-mass protostars. » In: *A&A* 541, A39, A39. DOI: [10.1051/0004-6361/201117917](https://doi.org/10.1051/0004-6361/201117917). arXiv: [1203.4969](https://arxiv.org/abs/1203.4969) [[astro-ph.SR](#)].
- Persson, M. V., J. K. Jørgensen, E. F. van Dishoeck, and D. Harsono (2014). « The deuterium fractionation of water on solar-system scales in deeply-embedded low-mass protostars. » In: *A&A* 563, A74, A74. DOI: [10.1051/0004-6361/201322845](https://doi.org/10.1051/0004-6361/201322845). arXiv: [1402.1398](https://arxiv.org/abs/1402.1398) [[astro-ph.SR](#)].
- Prantzos, N. (2003). « Evolution of CNO Abundances in the Universe (invited review). » In: *CNO in the Universe*. Ed. by C. Charbonnel, D. Schaerer, and G. Meynet. Vol. 304. Astronomical Society of the Pacific Conference Series, p. 361.
- (2011). « Topics on Galactic Chemical Evolution. » In: *ArXiv e-prints*. arXiv: [1101.2108](https://arxiv.org/abs/1101.2108).
- Pringle, J. E. (1981). « Accretion discs in astrophysics. » In: *ARA&A* 19, pp. 137–162. DOI: [10.1146/annurev.aa.19.090181.001033](https://doi.org/10.1146/annurev.aa.19.090181.001033).
- Qi, C., K. I. Öberg, D. J. Wilner, P. D'Alessio, E. Bergin, S. M. Andrews, G. A. Blake, M. R. Hogerheijde, and E. F. van Dishoeck (2013). « Imaging of the CO Snow Line in a Solar Nebula Analog. » In: *Science* 341, pp. 630–632. DOI: [10.1126/science.1239560](https://doi.org/10.1126/science.1239560). arXiv: [1307.7439](https://arxiv.org/abs/1307.7439) [[astro-ph.SR](#)].
- Ritchey, A. M., S. R. Federman, and D. L. Lambert (2015). « The C¹⁴N/C¹⁵N Ratio in Diffuse Molecular Clouds. » In: *ApJ* 804, L3, p. L3. DOI: [10.1088/2041-8205/804/1/L3](https://doi.org/10.1088/2041-8205/804/1/L3). arXiv: [1503.08221](https://arxiv.org/abs/1503.08221).
- Romano, D. and F. Matteucci (2003). « Nova nucleosynthesis and Galactic evolution of the CNO isotopes. » In: *MNRAS* 342, pp. 185–198. DOI: [10.1046/j.1365-8711.2003.06526.x](https://doi.org/10.1046/j.1365-8711.2003.06526.x). eprint: [astro-ph/0302233](https://arxiv.org/abs/astro-ph/0302233).
- Roueff, E., J. C. Loison, and K. M. Hickson (2015). « Isotopic fractionation of carbon, deuterium, and nitrogen: a full chemical study. » In: *A&A* 576, A99, A99. DOI: [10.1051/0004-6361/201425113](https://doi.org/10.1051/0004-6361/201425113). arXiv: [1501.01141](https://arxiv.org/abs/1501.01141).
- Rybicki, G. B. and D. G. Hummer (1992). « An accelerated lambda iteration method for multilevel radiative transfer. II - Overlapping transitions with full continuum. » In: *A&A* 262, pp. 209–215.
- Sakai, N. and S. Yamamoto (2013). « Warm Carbon-Chain Chemistry. » In: *Chemical Reviews* 113, pp. 8981–9015. DOI: [10.1021/cr4001308](https://doi.org/10.1021/cr4001308).
- Sakai, N., O. Saruwatari, T. Sakai, S. Takano, and S. Yamamoto (2010). « Abundance anomaly of the ¹³C species of CCH. » In: *A&A* 512, A31, A31. DOI: [10.1051/0004-6361/200913098](https://doi.org/10.1051/0004-6361/200913098).

- Sandell, G., B. Hoglund, and A. G. Kisliakov (1983). « HCN J = 1-0 observations in L 673 and S 235B - Two different cases of hyperfine anomalies. » In: *A&A* 118, pp. 306–312.
- Seo, Y. M., S. S. Hong, and Y. L. Shirley (2013). « On the Internal Dynamics of Starless Cores: Stability of Starless Cores with Internal Motions and Collapse Dynamics. » In: *ApJ* 769, 50, p. 50. DOI: [10.1088/0004-637X/769/1/50](https://doi.org/10.1088/0004-637X/769/1/50). arXiv: [1304.3037](https://arxiv.org/abs/1304.3037).
- Seo, Y. M., S. S. Hong, S. H. Lee, Y. S. Park, J. Sohn, and C. W. Lee (2011). « On the Internal Dynamics of the Starless Core L694-2. » In: *ApJ* 736, 153, p. 153. DOI: [10.1088/0004-637X/736/2/153](https://doi.org/10.1088/0004-637X/736/2/153).
- Sephton, M. A., K. Amor, I. A. Franchi, P. B. Wignall, R. Newton, and J.-P. Zonneveld (2002). « Carbon and nitrogen isotope disturbances and an end-Norian (Late Triassic) extinction event. » In: *Geology* 30, p. 1119. DOI: [10.1130/0091-7613\(2002\)030<1119:CANIDA>2.0.CO;2](https://doi.org/10.1130/0091-7613(2002)030<1119:CANIDA>2.0.CO;2).
- Shinnaka, Y., H. Kawakita, E. Jehin, A. Decock, D. Hutsemékers, J. Manfroid, and A. Arai (2016). « Nitrogen isotopic ratios of NH₂ in comets: implication for ¹⁵N-fractionation in cometary ammonia. » In: *MNRAS* 462, S195–S209. DOI: [10.1093/mnras/stw2410](https://doi.org/10.1093/mnras/stw2410).
- Shu, F. H. (1977). « Self-similar collapse of isothermal spheres and star formation. » In: *ApJ* 214, pp. 488–497. DOI: [10.1086/155274](https://doi.org/10.1086/155274).
- Snow, T. P. and B. J. McCall (2006). « Diffuse Atomic and Molecular Clouds. » In: *ARA&A* 44, pp. 367–414. DOI: [10.1146/annurev.astro.43.072103.150624](https://doi.org/10.1146/annurev.astro.43.072103.150624).
- Sohn, J., C. W. Lee, H. M. Lee, Y.-S. Park, P. C. Myers, Y. Lee, and M. Tafalla (2004). « HCN(1-0) Observations of Starless Cores. » In: *Journal of Korean Astronomical Society* 37, pp. 261–263. DOI: [10.5303/JKAS.2004.37.4.261](https://doi.org/10.5303/JKAS.2004.37.4.261).
- Sohn, J., C. W. Lee, Y.-S. Park, H. M. Lee, P. C. Myers, and Y. Lee (2007). « Probing Inward Motions in Starless Cores Using the HCN(J = 1-0) Hyperfine Transitions: A Pointing Survey toward Central Regions. » In: *ApJ* 664, pp. 928–941. DOI: [10.1086/519159](https://doi.org/10.1086/519159). arXiv: [0704.2930](https://arxiv.org/abs/0704.2930).
- Spezzano, S., P. Caselli, L. Bizzocchi, B. M. Giuliano, and V. Lattanzi (2017). « The observed chemical structure of L1544. » In: *ArXiv e-prints*. arXiv: [1707.06015](https://arxiv.org/abs/1707.06015).
- Stahler, S. W. and F. Palla (2005). *The Formation of Stars*, p. 865.
- Stoeklin, T., A. Faure, P. Jankowski, S. Chefdeville, A. Bergeat, C. Naulin, S. B. Morales, and M. Costes (2017). « Comparative experimental and theoretical study of the rotational excitation of CO by collision with ortho- and para-D₂ molecules. » In: *Phys. Chem. Chem. Phys.* 19 (1), pp. 189–195. DOI: [10.1039/C6CP06404C](https://doi.org/10.1039/C6CP06404C). URL: <http://dx.doi.org/10.1039/C6CP06404C>.
- Swings, P. and L. Rosenfeld (1937). « Considerations Regarding Interstellar Molecules. » In: *ApJ* 86, pp. 483–486. DOI: [10.1086/143880](https://doi.org/10.1086/143880).

- Tafalla, M., P. C. Myers, P. Caselli, C. M. Walmsley, and C. Comito (2002). « Systematic Molecular Differentiation in Starless Cores. » In: *ApJ* 569, pp. 815–835. DOI: [10.1086/339321](https://doi.org/10.1086/339321). eprint: [astro-ph/0112487](https://arxiv.org/abs/astro-ph/0112487).
- Tafalla, M., P. C. Myers, P. Caselli, and C. M. Walmsley (2004). « On the internal structure of starless cores. I. Physical conditions and the distribution of CO, CS, N₂H⁺, and NH₃ in L1498 and L1517B. » In: *A&A* 416, pp. 191–212. DOI: [10.1051/0004-6361:20031704](https://doi.org/10.1051/0004-6361:20031704).
- Tafalla, M., J. Santiago-García, P. C. Myers, P. Caselli, C. M. Walmsley, and A. Crapsi (2006). « On the internal structure of starless cores. II. A molecular survey of L1498 and L1517B. » In: *A&A* 455, pp. 577–593. DOI: [10.1051/0004-6361:20065311](https://doi.org/10.1051/0004-6361:20065311). eprint: [astro-ph/0605513](https://arxiv.org/abs/astro-ph/0605513).
- Taniguchi, K. and M. Saito (2017). « First detection of HC₅¹⁵N in the interstellar medium. » In: *PASJ* 69, L7, p. L7. DOI: [10.1093/pasj/psx065](https://doi.org/10.1093/pasj/psx065). arXiv: [1706.08662](https://arxiv.org/abs/1706.08662).
- Taniguchi, K., H. Ozeki, M. Saito, N. Sakai, F. Nakamura, S. Kamenno, S. Takano, and S. Yamamoto (2016). « Implication of Formation Mechanisms of HC₅N in TMC-1 as Studied by ¹³C Isotopic Fractionation. » In: *ApJ* 817, 147, p. 147. DOI: [10.3847/0004-637X/817/2/147](https://doi.org/10.3847/0004-637X/817/2/147). arXiv: [1512.05783](https://arxiv.org/abs/1512.05783) [[astro-ph.SR](https://arxiv.org/abs/1512.05783)].
- Terzieva, R. and E. Herbst (2000). « The possibility of nitrogen isotopic fractionation in interstellar clouds. » In: *MNRAS* 317, pp. 563–568. DOI: [10.1046/j.1365-8711.2000.03618.x](https://doi.org/10.1046/j.1365-8711.2000.03618.x).
- Tobin, J. J., L. W. Looney, D. J. Wilner, W. Kwon, C. J. Chandler, T. L. Bourke, L. Loinard, H.-F. Chiang, S. Schnee, and X. Chen (2015). « A Sub-arcsecond Survey Toward Class 0 Protostars in Perseus: Searching for Signatures of Protostellar Disks. » In: *ApJ* 805, 125, p. 125. DOI: [10.1088/0004-637X/805/2/125](https://doi.org/10.1088/0004-637X/805/2/125). arXiv: [1503.05189](https://arxiv.org/abs/1503.05189) [[astro-ph.SR](https://arxiv.org/abs/1503.05189)].
- Usui, T., C. M. O. Alexander, J. Wang, J. I. Simon, and J. H. Jones (2012). « Origin of water and mantle-crust interactions on Mars inferred from hydrogen isotopes and volatile element abundances of olivine-hosted melt inclusions of primitive shergottites. » In: *Earth and Planetary Science Letters* 357, pp. 119–129. DOI: [10.1016/j.epsl.2012.09.008](https://doi.org/10.1016/j.epsl.2012.09.008).
- Walmsley, C. M., E. Churchwell, A. Nash, and E. Fitzpatrick (1982). « Hyperfine anomalies of HCN in cold dark clouds. » In: *ApJ* 258, pp. L75–L78. DOI: [10.1086/183834](https://doi.org/10.1086/183834).
- Walsh, K. J., A. Morbidelli, S. N. Raymond, D. P. O’Brien, and A. M. Mandell (2011). « A low mass for Mars from Jupiter’s early gas-driven migration. » In: *Nature* 475, pp. 206–209. DOI: [10.1038/nature10201](https://doi.org/10.1038/nature10201). arXiv: [1201.5177](https://arxiv.org/abs/1201.5177) [[astro-ph.EP](https://arxiv.org/abs/1201.5177)].
- Walt, S Stéfan van der, Chris Colbert, and Gaël Varoquaux (2011). « The NumPy Array: A Structure for Efficient Numerical Computation. » In: *Computing in Science & Engineering* 13, pp. 22–30.

- Wampfler, S. F., J. K. Jørgensen, M. Bizzarro, and S. E. Bisschop (2014). « Observations of nitrogen isotope fractionation in deeply embedded protostars. » In: *A&A* 572, A24, A24. DOI: [10.1051/0004-6361/201423773](https://doi.org/10.1051/0004-6361/201423773). arXiv: [1408.0285](https://arxiv.org/abs/1408.0285) [[astro-ph.SR](https://arxiv.org/abs/1408.0285)].
- Whittet, D. C. B., P. F. Goldsmith, and J. L. Pineda (2010). « The Uptake of Interstellar Gaseous CO Into Icy Grain Mantles in a Quiescent Dark Cloud. » In: *ApJ* 720, pp. 259–265. DOI: [10.1088/0004-637X/720/1/259](https://doi.org/10.1088/0004-637X/720/1/259).
- Whittet, D. C. B., C. A. Poteet, J. E. Chiar, L. Pagani, V. M. Bajaj, D. Horne, S. S. Shenoy, and A. J. Adamson (2013). « Ice and Dust in the Prestellar Dark Cloud Lynds 183: Preplanetary Matter at the Lowest Temperatures. » In: *ApJ* 774, 102, p. 102. DOI: [10.1088/0004-637X/774/2/102](https://doi.org/10.1088/0004-637X/774/2/102).
- Wiescher, M., J. Görres, E. Uberseder, G. Imbriani, and M. Pignatari (2010). « The Cold and Hot CNO Cycles. » In: *Annual Review of Nuclear and Particle Science* 60, pp. 381–404.
- Wilson, T. L. and R. Rood (1994). « Abundances in the Interstellar Medium. » In: *ARA&A* 32, pp. 191–226. DOI: [10.1146/annurev.aa.32.090194.001203](https://doi.org/10.1146/annurev.aa.32.090194.001203).
- Zapata, L. A., L. Loinard, L. F. Rodríguez, V. Hernández-Hernández, S. Takahashi, A. Trejo, and B. Parise (2013). « ALMA 690 GHz Observations of IRAS 16293-2422B: Infall in a Highly Optically Thick Disk. » In: *ApJ* 764, L14, p. L14. DOI: [10.1088/2041-8205/764/1/L14](https://doi.org/10.1088/2041-8205/764/1/L14). arXiv: [1301.3105](https://arxiv.org/abs/1301.3105).
- Zucconi, A., C. M. Walmsley, and D. Galli (2001). « The dust temperature distribution in prestellar cores. » In: *A&A* 376, pp. 650–662. DOI: [10.1051/0004-6361:20010778](https://doi.org/10.1051/0004-6361:20010778). eprint: [astro-ph/0107055](https://arxiv.org/abs/astro-ph/0107055).
- de Vries, C. H. and P. C. Myers (2005). « Molecular Line Profile Fitting with Analytic Radiative Transfer Models. » In: *ApJ* 620, pp. 800–815. DOI: [10.1086/427141](https://doi.org/10.1086/427141). eprint: [astro-ph/0410748](https://arxiv.org/abs/astro-ph/0410748).
- van Dishoeck, E. F. (2014). « Astrochemistry of dust, ice and gas: introduction and overview. » In: *Faraday Discussions* 168, p. 9. DOI: [10.1039/C4FD00140K](https://doi.org/10.1039/C4FD00140K). arXiv: [1411.5280](https://arxiv.org/abs/1411.5280).
- van der Tak, F. F. S., J. H. Black, F. L. Schöier, D. J. Jansen, and E. F. van Dishoeck (2007). « A computer program for fast non-LTE analysis of interstellar line spectra. With diagnostic plots to interpret observed line intensity ratios. » In: *A&A* 468, pp. 627–635. DOI: [10.1051/0004-6361:20066820](https://doi.org/10.1051/0004-6361:20066820). arXiv: [0704.0155](https://arxiv.org/abs/0704.0155).